Development of Enhanced Performance Luminescence-based Optical Sensor Systems for Single-analyte and Multi-analyte Applications

by

John Moore M.Sc.

A thesis presented to Dublin City University
for the Degree of Doctor of Philosophy

Research supervisor:
Prof. Brian MacCraith
School of Physical Sciences
National Centre for Sensor Research
Dublin City University

July 2010

Declaration

I hereby certify that this material, which I now submit for assessment on the programme of study leading to the award of Doctor of Philosophy is entirely my own work, that I have exercised reasonable care to ensure that the work is original, and does not to the best of my knowledge breach any law of copyright, and has not been taken from the work of others save and to the extent that such work has been cited and acknowledged within the text of my work.

Signed: ______________________ (Candidate) ID No.: _______________

Date: _______________

To Dad

Acknowledgements

First of all, I would like to thank my supervisor Prof. Brian MacCraith for giving me the opportunity to carry out this work and for all of the much appreciated help and advice, not to mention painstakingly reviewing various drafts of this thesis. I must also offer my sincere thanks to Prof. Colette McDonagh for all the help she has provided at various stages along the way.

I'd like to thank everyone at the Optical Sensors Laboratory for all of the invaluable help, friendship and encouragement when it was needed, especially the coffee room gang. Dorota deserves a special mention for tolerating my endless stream of no doubt silly chemistry questions. Many thanks to the people who proof-read and corrected earlier drafts of the thesis, Rob C in particular. And to those who provided all of the extremely useful thesis writing tips and advice. I would have been lost without it.

Outside DCU I have to single out Steph and Derek, who have been great throughout. Whenever things piled up they were always there.

Most of all I have to thank my family, who, as always, have been fantastic. They have been a great support over the last few months and right back to my days as an undergraduate. Without their never-ending support and encouragement I would not be where I find myself today.

Contents

Abstract

Luminescence-based sensors are widely used and are the subject of considerable attention from both a research and a commercial perspective. This work details the development of enhanced-performance luminescence-based sensor systems. Development efforts have focussed on three areas: instrumentation electronics, enhanced luminescence capture-based optical platforms, and multi-parameter sensing using numerical techniques.

Three instrumentation electronics systems were developed using a progressive design process that culminated in the development of a DSP-based system which is capable of multi-frequency operation and can be used to obtain intensity, phase or ratiometric-intensity measurements.

When a luminophore is placed close to a dielectric interface it exhibits an anisotropic emission profile. An optical probe that exploits this phenomenon to achieve enhanced luminescence capture was designed previously, however, it suffered from a number of shortcomings. A range of design improvements were developed and implemented which addressed a number of robustness and reliability related issues and which facilitated ratiometric mode operation. In addition, an enhanced capture element that was optimised for general sensing as opposed to bio-sensing applications was designed using a combined ray tracing/optimisation approach.

The detection of multiple parameters using a single luminescent sensor element is desirable in many applications. A multi-parameter technique was developed that achieves this through the use of numerical techniques. This approach addresses a number of limitations that are associated with alternative techniques.

A key part of this work was the development of sensor systems for a number of specific applications. Sensor systems were developed for the following: real-time measurement of oxygen concentration in breath, measurement of dissolved oxygen and dissolved carbon dioxide, and the simultaneous measurement of oxygen and temperature using a single sensor element.

Chapter 1

Introduction

1.1 Luminescence

Luminescence is the general term used to describe the emission of light from a substance due to the de-excitation of electrons from an excited state. It typically refers to so called “cold-light” [1] processes, where the electrons are excited by a means other than heating, such as chemical and biological reactions, radioactivity, and the absorption of light. This work is based on luminescence that is induced by the absorption of light, or photoluminescence as it is sometimes referred to [2].

The existence of the phenomena now referred to as luminescence was known for centuries. It was not until the middle of the nineteenth century, however, that it received attention from a scientific perspective. In 1852, Stokes [3] provided the first scientific explanation of luminescence in relation to the behaviour exhibited by quinine sulphate solution when exposed to sunlight. This phenomenon had earlier been reported by Herschel [4]. Stokes later recognised the possibility that optical properties, including luminescence, could be used in the identification of organic substances in what appears to be the first reference to the concept of luminescence sensing. The term “luminescence” was reportedly coined by Wiedemann in 1889 [5].

1.2 Luminescence-based Sensing

Luminescence-based optical sensors have seen increasing use in recent years in a wide range of application areas. Examples include the measurement of gases such as oxygen [6–8] and carbon dioxide [9–11], the detection of halides [12–14] and metal ions [15–17], and the measurement of physical parameters such as pH [18–20] and temperature [21–23]. Luminescence based-sensors are also used extensively in the area of bio-sensing, for applications such as the detection of various types of bio-molecules [24, 25]. The field of luminescence-based sensing has progressed rapidly over the last two decades. This can be attributed to a range of factors including the availability of suitable low-cost LED- and laser-diode (LD)-based light sources [26], the development of robust encapsulation strategies, such as those based around the use of solgel materials [27], and the development of a diverse range of luminophores. The development of luminescence-based sensors has also been driven by the potential advantages offered by luminescence-based sensors over other sensing techniques, which include increased robustness and lifespan, reduced cost and immunity to electro-magnetic interference. (A more detailed discussion of the advantages of optical sensors over their counterparts, e.g. electrochemical sensors, can be found in chapters 6 and 7). The field has progressed to the point that there are now a range of luminescence based sensors available commercially for a variety of applications including oxygen [28, 29], carbon-dioxide [30, 31] and pH [30, 31] sensing that boast significantly improved performance over that of the competing techniques. Despite this, there is still considerable room for improvement in terms of both functionality and performance.

The primary aim of this work was the development of luminescence-based sensor systems and subsystems that exhibited improved performance and/or functionality when compared to the current state of the art. One of the specific requirements that had to be fulfilled was the development of sensor systems for a range of applications. Sensor systems that display improved performance and/or functionality over the current state of the art have been developed for the following:

- Real-time measurement of oxygen in breath
- Measurement of dissolved oxygen and carbon dioxide
- Simultaneous measurement of oxygen concentration and temperature

While the majority of the design enhancements that have been developed are generic in nature, they were guided in the first instance by the requirements of each of these applications. The work that was completed was focussed primarily along three distinct but complementary strands. The three focus areas were as follows:

- Instrumentation electronics
- Enhanced luminescence capture-based optical sensor platforms
- Multi-parameter sensing using numerical techniques

An overview of each of these areas and the work that has been completed is presented in the following sections.

1.2.1 Instrumentation Electronics

This term encompasses all of the electronic components and subsystems that are found in a luminescence sensor system. Their primary function is to control the illumination of the luminescent sensor material and measure the resulting luminescence emission.

Three instrumentation electronics systems were developed over the course of this work. The first system that was developed is an analog phase fluorometry system that was designed for use in breath oxygen measurement and dissolved gas sensing. The second system is a digital phase fluorometry system that was designed for use in the measurement of breath oxygen levels. It was required to be belt-mountable and battery powered. The third system, which is based around a high performance digital signal processor (DSP), was designed to have significantly increased functionality and performance when compared to that of the two previous designs and the systems that represented the current state of the art. It is equipped with multiple excitation and emission channels, can be operated in intensity, phase or ratiometric mode, and is capable of multi-frequency operation.

A detailed description of the various types of instrumentation electronics that can be used, and a review of the current state of the art, is presented in section 2.4.1.

1.2.2 Optical Sensor Platforms

The optical components that are used in the excitation and collection of luminescence are an important part of all luminescence-based sensor systems and have a significant impact on sensor performance. The function of the optical components that are used is to deliver excitation light to the luminescent material, collect the resulting luminescence emission, and in some cases to act as a physical support for the luminescent material.

There are many different types of optical configurations that can be used in luminescence-based sensor systems, e.g. fibre-optic [21, 32] and waveguide-based [33, 34], and cell-based [35]. This work, however, has focussed on the use of probe-based systems, in which the sensor film, optical and optoelectronic components are all housed in a single sensor "probe". Cell-based setups are generally limited to benchtop systems and material characterisation applications, and while fibre and waveguide-based systems have seen extensive use in the area of luminescence sensing, they were deemed unsuitable for the various projects that this work encompassed. In work carried out by the author and others at this laboratory using fibre-based systems [36], considerable problems were encountered due to autofluorescence and poor levels of robustness. The use of probe-based optical platforms allowed these problems to be avoided and also facilitated the use of paraboloid-based luminescence capture elements that were developed previously at this laboratory [37]. The parabolic elements exploit the anisotropic emission profile exhibited by luminophores in certain situations to achieve increased luminescence capture, which can potentially lead to increases in sensor sensitivity of up to a factor of 100 [38].

The optical sensor platform strand of this work can be divided into two areas. The first involved the development and implementation of a range of design improvements to the original enhanced capture-based optical probe that led to increased robustness and which addressed a number of key useability-related issues. A modified optical configuration that facilitated ratiometric mode operation was developed, which allowed the advantages associated with the use of the enhanced capture element to be applied to ratiometric-based luminescent sensors.

The second part of this work was modelling-related. Although the parabolic enhanced capture element performed well, it was recognised that there was scope to improve upon its design for certain applications. Custom ray tracing software was written that allowed the behaviour of a range of element geometries to be assessed. The ray tracing algorithms were interfaced with optimisation routines that facilitated automated identification of the optimum capture structure designs.

1.2.3 Multi-parameter Sensing

The ability to sense multiple parameters simultaneously is desirable in many luminescence sensing applications [39]. Examples include in-vivo monitoring of blood gases, inline bio-process monitoring, realtime breath gas measurement, and air and water quality monitoring to name but a few.

A number of multi-parameter systems and techniques have been reported in the literature. The earliest reference which could be found dates from 1983, where Wolfbeis and Urbano [40] presented a technique for simultaneously measuring the concentration of bromine, iodine and chloride in solution using frequency domain techniques. A number of techniques have been published that are based on the use of multiple sensor elements [41, 42], including that which was developed by Orla McGaughey at this laboratory [43]. While good results have been reported with the multi-element approach, the most desirable implementation in many cases is arguably that which facilitates multi-parameter measurement using a single sensor element and single excitation source. A number of single-element systems have been developed that are based on the use of two luminophores that emit at different wavelengths [44, 45]. This approach requires that the emission spectra of the chosen luminophores display no overlap or else spectroscopic techniques must be used to resolve the signal from each. Dye combinations that do not display overlap are limited, which means that spectroscopic techniques would have to be used in most cases, resulting in high system costs. An alternative single-element approach has been developed by Borisov and co-workers [46] that is based on multi-frequency excitation of a sensor element that contains two luminophores with different lifetimes. The technique, which is sometimes referred to as the m-DLR technique, was initially developed to eliminate the effect of short-lived background fluorescence in experiments involving long-lived luminophores [47]. The technique has been applied to a number of applications, including the simultaneous sensing of oxygen and pH, and oxygen and temperature [48, 49]. A time domain analog of this approach has also been developed [50, 51], and has also been applied to a number of applications. A potential failing of the techniques developed by Wolfbeis and Borisov is that expressions that are invertible and/or solvable analytically must be used to describe the response of the luminophores to the analytes or parameters in question. This limits the expressions that can be used, which may affect the accuracy with which the response of the luminophores is described. If this were to occur it would have a knock-on effect on the accuracy of the measurements obtained using the technique.

A numerical technique was developed over the course of this work that overcomes these limitations through the use of numerical data processing techniques and the use of curve-fitting techniques to describe sensor response.

1.3 Research Objectives

The specific objectives of this work, expressed in terms of the three main focus areas were as follows:

Instrumentation Electronics The primary objective from an instrumentation electronics perspective was that the systems be designed to meet the specified functionality requirements and at the same time display maximised resolution and drift performance. The key functionality requirements that were to be accommodated were dictated by the target applications and were as follows:

- Sampling rates compatible with breath measurement ($\sim 10Sa/s$)
- A system capable of portable, battery powered operation
- A single system capable of multi-channel and multi-frequency operation and of measuring both intensity and lifetime

Optical Platforms The primary objectives in this strand of the work were as follows:

- Develop enhanced capture probe capable of ratiometric operation
- Address robustness and useability shortcomings of original design
- Design an element for general sensing applications that achieves improved performance by relaxing the bio-sensing related design constraints imposed on the current design.

Multi-parameter sensing The primary objectives of this work was to investigate the feasibility of using a numerical approach to implement multi-parameter sensing using a single sensor element. A key element of this work was the development of the required numerical algorithms.

Sensor System Development The system development objectives of this work were to utilise the relevant subset of the enhanced systems that had been developed to:

- Develop a system capable of measuring true breath-by-breath oxygen uptake, which would see the oxygen sensor placed directly in the subjects airstream.
- Develop dissolved oxygen and dissolved carbon dioxide sensor systems that display improved resolution/LOD performance over the state of the art
- Develop a simultaneous oxygen and temperature measurement system that could be used to validate the functionality of the numerical multi-parameter technique and determine if it could be used to obtain accurate temperature compensated oxygen measurements.

Maximum acceptable resolution values were defined for each of the systems that were developed. These are listed in Table 1.1. The minimum required resolution performance of the DO and DCO_2 systems was set at that which was achieved by systems developed previously at the OSL. Details of the performance of these systems are given in chapter 7. To the best of the author's knowledge,

System	Resolution
DO	$6\mu g/L$
DCO_2	0.017%
Breath oxygen	0.4%

Table 1.1: Largest acceptable resolution values for the systems that were developed.

there are no “in breath” breath by breath oxygen measurement systems available commercially or reported in the literature. As a result, it was not possible to define a precise resolution target for the system. It was deemed that a target resolution of 0.4% was acceptable in the first instance and that the performance of the system could be used to define a value with physical relevance at a later stage. 0.4% corresponds to 10% of the oxygen concentration range typically observed in a human breath cycle (see chapter 6).

1.4 Thesis Structure

This chapter provides a general introduction to luminescence sensing and illustrates the context in which this work has been completed.

Chapter 2 introduces the relevant theoretical aspects of luminescence and then goes on to cover the necessary background material.

The remainder of the thesis can be considered as being broadly divided into two sections. The first includes a chapter on each of the focus areas, and is followed by three chapters that detail the sensor systems that were developed.

Chapter 3 describes each of the electronic instrumentation systems that were developed. A concept-based approach has been used to describe the design rationale and resulting functionality of each of the systems, with circuit diagrams being confined to the appendices. The relevant performance characteristics of each of the systems are also presented.

Chapter 4 details the work that was carried out in the area of optical sensor platform development. It begins by presenting the probe design that served as the starting point for this element of the work and goes on to detail the various design enhancements that have been implemented. This includes the development of a ray tracing-based modelling system that was used to identify the design criteria of enhanced capture elements that would lead to optimised luminescence capture in certain applications

Chapter 5 describes the numerical multi-parameter technique that has been developed as part of this work. It begins with a description of the technique from a mathematical perspective, and then goes on to detail the algorithms that have been developed. It finishes with an assessment of the performance of the technique using simulated sensor data.

Chapter 6 marks the start of the applications section of the thesis and details the realtime breath monitoring system that has been developed.

Chapter 7 is concerned with the dissolved gas sensor systems that have been developed. The chapter begins with a description of the dissolved oxygen sensor system that has been developed and then moves on to detail the ratiometric dissolved carbon dioxide sensor.

Chapter 8 reports on the application of the multi-parameter technique to the simultaneous measurement of dissolved oxygen and temperature. The chapter begins with a description of the multi-element based implementation and the results it produced and then goes on to describe the single-element implementation. The chapter concludes with a discussion of the results that were obtained and the future work that is planned in this area.

Chapter 9 details the overall conclusions that were drawn from the work and discusses some possible areas of future work.

Bibliography

[1] David Rendell. *Fluorescence and phosphorescence spectroscopy.* Wiley, Chichester, 1997.

[2] George G. Guilbault. *Practical fluorescence; theory, methods, and techniques,.* M. Dekker, New York, 1973.

[3] G. G. Stokes. On the change of refrangibility of light. *Philosophical Transactions of the Royal Society of London*, 142:463–562, 1852.

[4] John Frederick William Herschel. On a case of superficial colour presented by a homogeneous liquid internally colourless. *Philosophical Transactions of the Royal Society of London*, 135:143–145, 1845.

[5] B. I. Stepanov and V. P. Gribkovskii. *Theory of luminescence.* Iliffe, London, 1968.

[6] C. McDonagh, C. Kolle, A. K. McEvoy, D. L. Dowling, A. A. Cafolla, S. J. Cullen, and B. D. MacCraith. Phase fluorometric dissolved oxygen sensor. *Sensors and Actuators B: Chemical*, 74(1-3):124–130, 2001.

[7] D. Xiao, Y. Y. Mo, and M. M. F. Choi. A hand-held optical sensor for dissolved oxygen measurement. *Measurement Science & Technology*, 14(6):862–867, 2003.

[8] Sergey Borisov and Ingo Klimant. Luminescent nanobeads for optical sensing and imaging of dissolved oxygen. *Microchimica Acta*, 164(1):7–15, 2009.

[9] Sergey M. Borisov, Magdalena Ch Waldhier, Ingo Klimant, and Otto S. Wolfbeis. Optical carbon dioxide sensors based on silicone-encapsulated room-temperature ionic liquids. *Chemistry of Materials*, 19(25):6187–6194, 2007.

[10] Conor S. Burke, Adam Markey, Robert I. Nooney, Patrick Byme, and Colette McDonagh. Development of an optical sensor probe for the detection of dissolved carbon dioxide. *Sensors and Actuators B-Chemical*, 119(1):288–294, 2006.

[11] M. Cajlakovic, A. Bizzarri, and V. Ribitsch. Luminescence lifetime-based carbon dioxide optical sensor for clinical applications. *Analytica Chimica Acta*, 573:57–64, 2006.

[12] Chris D. Geddes. Halide sensing using the spq molecule. *Sensors and Actuators B: Chemical*, 72(2):188–195, 2001.

[13] Cheng-Gang Niu, Ai-Ling Guan, Guang-Ming Zeng, Yun-Guo Liu, Guo-He Huang, Pan-Feng Gao, and Xiao-Qin Gui. A ratiometric fluorescence halide sensor based on covalently immobilization of quinine and benzothioxanthene. *Analytica Chimica Acta*, 547(2):221–228, 2005.

[14] R. H. Yang, K. M. Wang, D. Xiao, and X. H. Yang. Development of an iodine sensor based on fluorescence energy transfer. *Analyst*, 125(8):1441–1445, 2000.

[15] B. C. Barja, A. Remorino, and P. F. Aramendia. Luminescence quenching of eu(iii) carboxylates by cu(ii) in a composite polymer xerogel film. *Photochemistry and photobiology*, 82(1):43–49, 2006.

[16] A. A. A. Gaber. A novel pvc membrane sensor for selective determination of cerium(iii) ions. *Analytical Letters*, 36(12):2585–2596, 2003.

[17] O. Guney, Y. Yilmaz, and O. Pekcan. Metal ion templated chemosensor for metal ions based on fluorescence quenching. *Sensors and Actuators B-Chemical*, 85(1-2):86–89, JUN 20 2002.

[18] Aron Hakonen and Stefan Hulth. A high-precision ratiometric fluorosensor for ph: Implementing time-dependent non-linear calibration protocols for drift compensation. *Analytica Chimica Acta*, 606(1):63–71, 2008.

[19] Ramachandram Badugu, Yordan Kostov, Govind Rao, and Leah Tolosa. Development and application of an excitation ratiometric optical ph sensor for bioprocess monitoring. *Biotechnology progress*, 24(6):1393–1401, 2008.

[20] D. Wencel, B. D. MacCraith, and C. McDonagh. High performance optical ratiometric solgel-based ph sensor. *Sensors and Actuators B: Chemical*, 139(1):208–213, 2009.

[21] K. T. V. Grattan and Z. Y. Zhang. *Fiber optic fluorescence thermometry*. Chapman & Hall, London [etc.], 1995.

[22] Jeong-Ha Yoo, Sang Joon Park, and Jong Sung Kim. Fabrication and characterization of quantum dot-based optical fiber temperature sensor. *Molecular Crystals and Liquid Crystals*, 519:62–68, 2010.

[23] T. Sun, Z. Y. Zhang, and K. T. V. Grattan. Erbium/ytterbium fluorescence based fiber optic temperature sensor system. *Review of Scientific Instruments*, 71(11):4017–4022, 2000.

[24] Richard B. Thompson. *Fluorescence sensors and biosensors.* CRC/Taylor & Francis, Boca Raton, 2006.

[25] Frances S. Ligler and Chris Taitt. *Optical biosensors : present and future.* Elsevier, Amsterdam ;Oxford, 2002.

[26] D. Kieslinger, S. Draxler, K. Trznadel, and M. E. Lippitsch. Lifetime-based capillary waveguide sensor instrumentation. *Sensors and Actuators B-Chemical*, 39(1-3):300–304, 1997.

[27] B. D. MacCraith and C. McDonagh. Enhanced fluorescence sensing using sol-gel materials. *Journal of Fluorescence*, 12(3-4):333–342, 2002.

[28] *D-Opto Dissolved Oxygen Sensor.* Zebra-Tech Ltd., `http://www.d-opto.com/`.

[29] *FOXY/neoFox Oxygen Sensor.* Ocean Optics Inc., `http://www.oceanoptics.com/Products/neofox.asp`.

[30] *CellPhase pH, DO and DCO2 non-invasive sensors.* Fluorometrix Inc., `http://www.fluorometrix.com`.

[31] *Carbon Dioxide Sensors.* PreSens Precision Sensing GmbH, `http://www.presens.de`.

[32] M. A. Chan, J. L. Lawless, S. K. Lam, and D. Lo. Fiber optic oxygen sensor based on phosphorescence quenching of erythrosin b trapped in silica-gel glasses. *Analytica Chimica Acta*, 408(1-2):33–37, 2000.

[33] C. S. Burke, O. McGaughey, J. M. Sabattie, H. Barry, A. K. McEvoy, C. McDonagh, and B. D. MacCraith. Development of an integrated optic oxygen sensor using a novel, generic platform. *Analyst*, 130(1):41–45, 2005.

[34] Chris Rowe Taitt, George P. Anderson, and Frances S. Ligler. Evanescent wave fluorescence biosensors. *Biosensors and Bioelectronics*, 20(12):2470–2487, 2005.

[35] W. Trettnak, W. Gruber, F. Reininger, and I. Klimant. Recent progress in optical oxygen sensor instrumentation. *Sensors and Actuators B-Chemical*, 29(1-3):219–225, 1995.

[36] John P. Moore, Conor S. Burke, and Michael Todd. Performance of fibre bundle-based oxygen sensors. Unpublished.

[37] Conor S. Burke, Thomas Ruckstuhl, and John P. Moore. *Optical Probe*. Patent, 2008. WO2008029298.

[38] C. McDonagh, C. S. Burke, and B. D. MacCraith. Optical chemical sensors. *Chemical reviews*, 108(2):400–422, 2008.

[39] S. Nagl and O. S. Wolfbeis. Optical multiple chemical sensing: status and current challenges. *Analyst*, 132(6):507–511, 2007.

[40] O. S. Wolfbeis and E. Urbano. Fluorescence quenching method for determination of 2 or 3 components in solution. *Analytical Chemistry*, 55(12):1904–1906, 1983.

[41] L. Li and D. R. Walt. Dual-analyte fiberoptic sensor for the simultaneous and continuous measurement of glucose and oxygen. *Analytical Chemistry*, 67(20):3746–3752, 1995.

[42] S. M. Barnard and D. R. Walt. A fiberoptic chemical sensor with discrete sensing sites. *Nature*, 353(6342):338–340, 1991.

[43] Orla McGaughey. *Development of a generic multi-analyte optical sensor platform for fluorescence-based sensing*. Ph.D. Thesis, Dublin City University, 2006.

[44] Chen-Shane Chu and Yu-Lung Lo. A plastic optical fiber sensor for the dual sensing of temperature and oxygen. *Ieee Photonics Technology Letters*, 20(1-4):63–65, 2008.

[45] O. S. Wolfbeis, L. J. Weis, M. J. P. Leiner, and W. E. Ziegler. Fiber-optic fluorosensor for oxygen and carbon-dioxide. *Analytical Chemistry*, 60(19):2028–2030, 1988.

[46] S. M. Borisov, G. Neurauter, C. Schroeder, I. Klimant, and O. S. Wolfbeis. Modified dual lifetime referencing method for simultaneous optical determination and sensing of two analytes. *Applied Spectroscopy*, 60(10):1167–1173, 2006.

[47] G. Neurauter. *Frequency Domain pCO2 Sensing*. Ph.D. Thesis, University of Regensburg, 2000.

[48] A. S. Kocincova, S. Nagl, S. Arain, C. Krause, S. M. Borisov, M. Arnold, and O. S. Wolfbeis. Multiplex bacterial growth monitoring in 24-well microplates using a dual optical sensor for dissolved oxygen and ph. *Biotechnology and bioengineering*, 100(3):430–438, 2008.

[49] Anna S. Kocincova, Sergey M. Borisov, Christian Krause, and Otto S. Wolfbeis. Fiber-optic microsensors for simultaneous sensing of oxygen and ph, and of oxygen and temperature. *Analytical Chemistry*, 79(22):8486–8493, 2007.

[50] C. R. Schroeder, G. Neurauter, and I. Klimant. Luminescent dual sensor for time-resolved imaging of pco(2) and po(2) in aquatic systems. *Microchimica Acta*, 158(3-4):205–218, 2007.

[51] Claudia R. Schroeder, Lubos Polerecky, and Ingo Klimant. Time-resolved pH/pO(2) mapping with luminescent hybrid sensors. *Analytical Chemistry*, 79(1):60–70, 2007.

Chapter 2

Theory and Background

This chapter details a number of relevant theory and background-related items that are not included elsewhere in this thesis. From a theory perspective, it includes a brief overview of the fundamental concepts that underlie luminescence and the physical mechanisms that allow luminescence to be used for sensing purposes. A brief overview of anisotropic luminescence emission is also provided.

The background material consists of two main components. The first is a description of the various luminescence sensor techniques and a review of the current state of the art in terms of the techniques that were employed in this work. The second discusses the basic features that are common to virtually all luminescence-based optical sensor platforms.

2.1 Luminescence Theory

Photoluminescence can be divided into two categories (fluorescence and phosphorescence), which are distinguished based on the electronic properties of the excited state from which the emission occurs [1]. The luminescence emission that occurs when an electron decays from an excited singlet state is called fluorescence, whereas if the emission occurs due to electron decay from an excited triplet state, then it is described as phosphorescence. From a practical perspective, the main difference between fluorescence and phosphorescence is the timescale in which the decay occurs. Fluorescence emission typically occurs on a timescale of the order of $10^{-8}s$, while phosphorescence occurs much more slowly, on a timescale of 10^{-3} to $> 10^{0}s$. The difference in lifetimes is due to the relative stability of singlet and triplet states. A simplified energy level (commonly known as a Jablonski diagram) [1, 2] diagram of the processes involved in fluorescence and phosphorescence is shown in Fig. 2.1. It is noted in [1] that for certain luminophores, such as metal-ligand complexes, there is no clear distinction between fluorescence and phosphorescence. Ruthenium-based metal-ligand complexes were used ex-

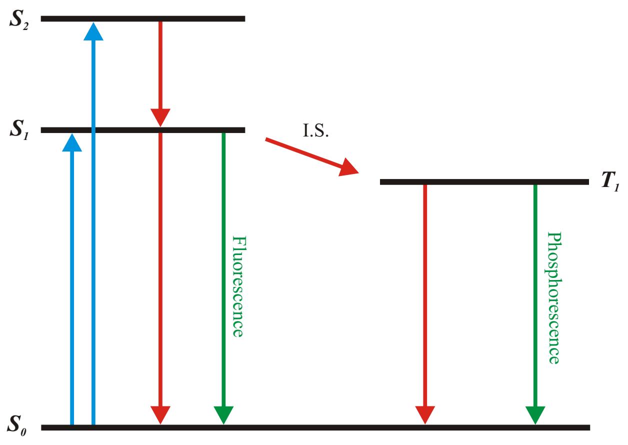

Figure 2.1: Simplified energy level diagram of the processes involved in fluorescence and phosphorescence. The excitation pathways are shown in blue and the non-radiative decay pathways in red. The excited triplet state, T_1, is populated by inter-system crossing (I.S.) from an excited singlet state.

tensively during this work and, in line with the convention that appears to have been adopted in the literature, their emission has been referred to as fluorescence.

2.1.1 Stokes Shift

The wavelength of fluorescence emission is typically longer than that of the excitation light. This phenomenon is referred to as Stokes Shift, after the Irish physicist who discovered it, and plays an important role in the use of luminescent materials for sensing purposes. The wavelength separation allows the excitation and emission light to be distinguished through the use of optical filters. It can be seen from Fig. 2.1 that the Stokes shift of a particular fluorescent molecule, or fluorophore, is dependent on the energy levels that are associated with it, which in turn are a function of its molecular structure. As a result, different fluorophores display widely different Stokes shift values, ranging from a few nm in some cases to several hundred nm in others.

2.1.2 Quantum Efficiency

The quantum efficiency of fluorescent materials is important from a sensing perspective. The quantum efficiency, Q, of a fluorophore, or quantum yield to which it is sometimes referred, is the ratio of the number of photons emitted to the number of photons absorbed [1]. It is described in terms of the radiative and non-radiative decay rate-constants, k_r and k_{nr}, and is given by the expression:

$$Q = \frac{k_r}{k_{nr} + k_r} \tag{2.1}$$

Fluorescence emission intensity is directly related to quantum efficiency, with high quantum efficiency values corresponding to large emission intensities. As will be discussed in more detail later, emission intensity has a direct impact on the performance of a luminescence-based sensor and results in quantum efficiency being a key consideration when selecting a fluorophore for a particular sensing application.

2.2 Luminescent Materials as Sensors

Although there are a variety of physical mechanisms that facilitate the use of luminescent materials for sensing purposes, only two of these are relevant to this work. The first is fluorescence quenching and the second is the fact that altering the chemical composition of a luminescent material affects its luminescent properties. Comprehensive details of the various additional mechanisms that facilitate the use of luminescence-based materials as sensors can be found in [1].

2.2.1 Fluorescence Quenching

Fluorescence quenching is the term used to describe processes that lead to a decrease in the emission intensity of a fluorophore. There are a variety of possible causes, including energy transfer, complex formation, and collisional quenching [1]. Collisional quenching is the only type of quenching that is relevant in this case. Collisional quenching occurs when a fluorophore in the excited state comes into contact with a quencher that returns it to the ground state, without a photon being emitted. It is a purely physical process and does not result in a chemical change in the fluorophore. Collisional quenching is described theoretically by the Stern-Volmer equations:

$$\frac{I_0}{I} = \frac{\tau_0}{\tau} = 1 + K_{SV}[Q] \tag{2.2}$$

$$K_{SV} = \tau_0 k \tag{2.3}$$

where $[Q]$ is the quencher concentration, I and τ are the fluorescence intensity and lifetime, respectively, I_0 and τ_0 are the unquenched intensity and lifetime, and k is the bimolecular quenching constant. The quantity K_{SV} is referred to as the Stern-Volmer constant. The derivation of equations 2.2 and 2.3 can be found in [3] and [1]. As the quencher concentration increases, the non-radiative decay rate increases , thereby reducing the emission intensity and lifetime of the fluorophore.

A range of substances act as fluorescence quenchers, with one of the best known being molecular oxygen. As a result, there are a considerable number of optical oxygen sensors that make use of the principle of luminescence quenching (e.g. [4–6]).

Two types of sensors have been used over the course of this work: a number of collisional quenching-based oxygen sensors and a luminescence-based pH sensor that was used in a dissolved carbon dioxide sensor.

2.2.2 Oxygen Sensing Using Fluorescence Quenching

If an oxygen sensitive fluorophore comes into contact with molecular oxygen, then collisional quenching will occur. The process can be described theoretically by the Stern-Volmer equations with equation 2.2 becoming:

$$\frac{I_0}{I} = \frac{\tau_0}{\tau} = 1 + K_{SV}\rho O_2 \tag{2.4}$$

where ρO_2 is the partial pressure of the oxygen in the environment that the fluorophore is exposed to. In virtually all oxygen sensing applications, with the exception of cellular measurements [7, 8], the oxygen sensitive fluorophore is immobilised in a porous support matrix, for a variety of reasons, which are detailed in a later section. Immobilising the fluorescence material has a significant impact on sensitivity as it affects the accessibility of the dye molecules. As a result, the sensitivity of collisional quenching-based sensors is highly dependent on the properties of the encapsulation matrix that is used. In the Stern-Volmer equation, this is reflected by the fact that the Stern-Volmer coefficient, K_{SV}, is dependent on the encapsulation material.

Although the Stern-Volmer equations adequately describes sensor response from a theoretical perspective, it has been found that the behaviour of fluorescence-based oxygen sensors often deviates significantly from that which is predicted by equation 2.4 [9, 10]. A number of alternative models have been developed, including the widely used Demas two-site model [11], that seek to accurately describe the response of such sensors from a theoretical perspective. This work was not concerned with the theoretical principles underlying the response of the collisional quenching-based sensors that were used, but required that their response was described as accurately as possible. As a result of this, empirical, curve-fitting-based techniques, which were not linked to any of the various theoretical models, were used to accurately describe sensor response.

2.2.3 Luminescence-Based pH Sensing

The operating principle of luminescence-based pH sensors is that the protonated and deprotonated versions of the dye have different luminescence properties. The ratio of protonated to deprotonated dye molecules varies as a function of pH, resulting in a corresponding change in the luminescent intensity and lifetime of the dye. The luminophore that was chosen, 8-hydroxy-1,3,6-pyrene trisulfonic acid (HPTS), displays quite complex photochemistry [12, 13], which is dependent on the properties of its environment. In the dissolved carbon dioxide films that were used in this work two absorption (excitation) peaks, corresponding to the protonated and deprotonated forms of the dye, and a single emission peak are exhibited. The excitation and emission spectra of HPTS are shown in Fig. 2.2. If the excitation source is chosen such that it coincides with one of the excitation peaks, the emission intensity and lifetime will vary as a function of pH. The fact that the dye possesses two excitation peaks allows for the possibility of ratiometric operation, a referencing strategy that is discussed in section 2.4.4.

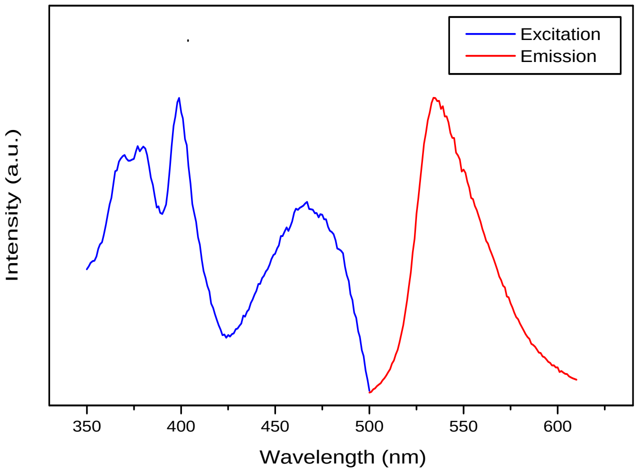

Figure 2.2: The excitation and emission spectra of HPTS when immobilised in a carbon dioxide sensor film [14].

2.3 Immobilisation/Encapsulation Techniques

As mentioned in the previous section, luminescent sensor materials are almost invariably immobilised in a porous support matrix of some kind. The primary functions of this matrix are to provide physical support for the luminescent material and to prevent leaching, which is the term used to describe unwanted migration of the luminescent molecules. The majority of luminescence sensors make use of either silica- or polymer-based support/encapsulation materials. All of the luminescence sensors fabricated at this laboratory make use of silica-based encapsulation materials that are produced using a solgel process. Silica-based materials have been chosen over their polymer counterparts as they are considered to be the better choice for a number of reasons, including porosity control, ease of fabrication, and robustness [15–17].

The solgel process, which is described in detail in [3], [10] and [18], provides a means of producing glasses, ceramics and gels at low temperatures. There are a number of distinct solgel techniques. The most popular of these sees the preparation of the required solgel material through the hydrolysis and poly-condensation of semi-metal or metal alkoxides. In this process, a solution of the alkoxide, usually a silicon alkoxide, water, a suitable solvent, and an acid or base catalyst, is prepared. This mixture, which is termed a "sol" then undergoes hydrolysis and poly-condensation, which leads to the formation of a rigid network, which is 'referred to as a "gel". The gel is then dried, usually in an oven, leaving behind a porous silica-based matrix. The luminescent material that is to be encapsulated is added to the sol. In this manner the luminescent dye becomes entrapped in the porous network. One of the key advantages of the solgel process is that the material can be coated onto almost any surface while at the sol stage and subsequently cured in situ.

All of the sensors that have been used in the work reported here employed organically modified silicate (ORMOSIL)-based [19, 20] solgel materials, that were prepared using silicon alkoxide precursors that contained an organic group. Some of the commonly-used ORMOSIL precursors are listed in Table 2.1. In ORMOSIL films the organic group of the precursor that is used has a significant impact on the properties of the resulting solgel. For example, it has an impact on the degree and nature of the cross-linking that takes place during the formation of the gel, which introduces the possibility of tailoring the physical properties of the solgel matrix through the selection of the precursor that is used.

Precursor	Abbreviation
Methyltriethoxysilane	MTEOS
Ethyltriethoxysilane	ETEOS
n-Propylyltriethoxysilane	PTEOS

Table 2.1: Common ORMOSIL precursors.

2.4 Interrogation Techniques and Systems

Luminescent sensor materials can be interrogated using either intensity- or lifetime-based techniques. Both are discussed in detail in the following sections.

2.4.1 Luminescence Intensity Measurement

Intensity-based interrogation techniques are based on the measurement of the intensity of the emission from the luminescent source in question. Intensity-based systems can be divided into two main categories: spectrometer-based, in which the emission spectrum is recorded, and lumped systems, in which the full emission spectrum, or a portion thereof, is summed to obtain a single intensity value. Spectrometer-based systems (e.g. [21, 22]), are typically found in laboratory settings, where they are used primarily for characterisation and early stage sensor development. Systems designed specifically for sensing would generally use the lumped approach.

The main elements of a lumped system are an excitation source, a suitable detector, and one or more optical filters that serve to prevent any of the excitation light from reaching the detector. A high level diagram that shows the main elements of a lumped measurement system is presented in Fig. 2.3. In intensity-based systems where ambient light is excluded, steady state or dc measurement of the luminescence intensity can be carried out. An example of such an approach is in commercially available fluorescence slide scanners (e.g. [23]). If ambient light can enter the system and reach the detector then it will interfere with the luminescence intensity measurements. The standard technique that is used to overcome this problem is lock-in amplifier-based detection.

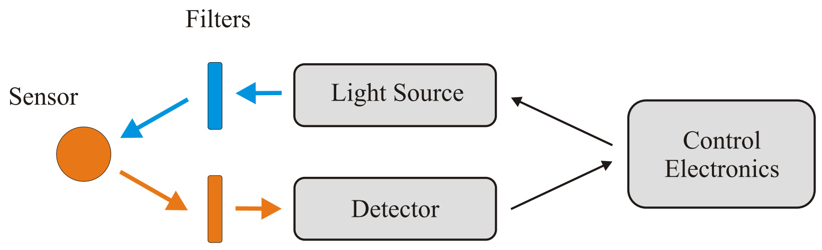

Figure 2.3: The main elements of a lumped measurement system.

2.4.1.1 Lock in Amplifier Detection

The lock-in amplifier technique is discussed in detail in chapter 3 in the context of synchronous demodulation. Therefore, only a cursory high level overview will be provided here. Lock-in amplification is a technique that is used extensively in a wide range of application areas [24, 25]. It allows a modulated signal to be measured in the presence of large background signals or to be extracted from large levels of background noise. In the case of luminescence intensity measurement, if the excitation source is modulated at a frequency other than $100Hz$, then lock-in amplification can be used to differentiate the resulting luminescence signal from unmodulated background light and artificial light, which is typically "mains-modulated" at $50Hz$ or $100Hz$. Even in cases where high background signals or levels of noise are not present, the use of lock-in detection results in an improvement in signal-to-noise ratio due to the inherent bandwidth reduction associated with its operation. Some examples of the use of lock-in detection for the measurement of luminescence intensity include [26, 27] and [28].

2.4.2 Luminescence Lifetime Measurement

Lifetime-based interrogation techniques are based on the measurement of the luminescence lifetime of the luminescent material. For a luminophore that displays single exponential decay the luminescence lifetime is defined as the time taken for the excited state population to fall to $1/e$ of the starting population.

2.4.2.1 Time Domain

There are two distinct families of lifetime measurement techniques: time domain and frequency domain. The time domain techniques are based on the excitation of the luminophore with a pulsed light source that has a rapid on-off transition when compared to the lifetime of the luminophore. When the excitation source is switched off, the resulting luminescence decay profile is recorded and analysed to determine the lifetime properties of the luminophore.

2.4.2.2 Frequency Domain

If the excitation source is modulated at a suitable frequency, then the time delay caused by the lifetime of the luminophore will result in the luminescence emission being phase-shifted relative to the excitation waveform. This forms the basis of the frequency domain measurement techniques. A diagrammatic representation of the process that occurs is shown in Fig. 2.4. The time delay due to the lifetime of the luminophore also causes demodulation of the luminescence emission. For a luminophore that exhibits single exponential decay, the phase shift, Φ, and the modulation, m, of the luminescence emission are given by the expressions [1]:

$$\Phi = \tan^{-1} \omega\tau \tag{2.5}$$

$$m = \frac{1}{\sqrt{1 + \omega^2\tau^2}} \tag{2.6}$$

where ω is the angular modulation frequency and τ is the lifetime of the luminophore. Equations 2.5 and 2.6 are plotted as a function of modulation frequency in Fig. 2.5. The phase angle increases, and the modulation factor de-

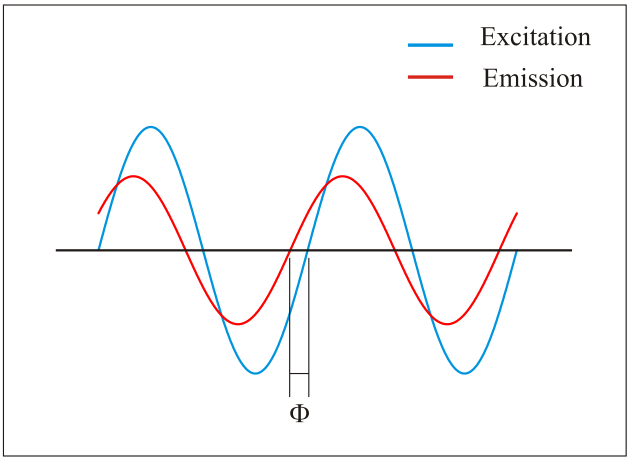

Figure 2.4: Excitation and emission waveforms in a frequency domain luminescence system.

creases as a function of frequency. This behaviour has implications from a perfor-

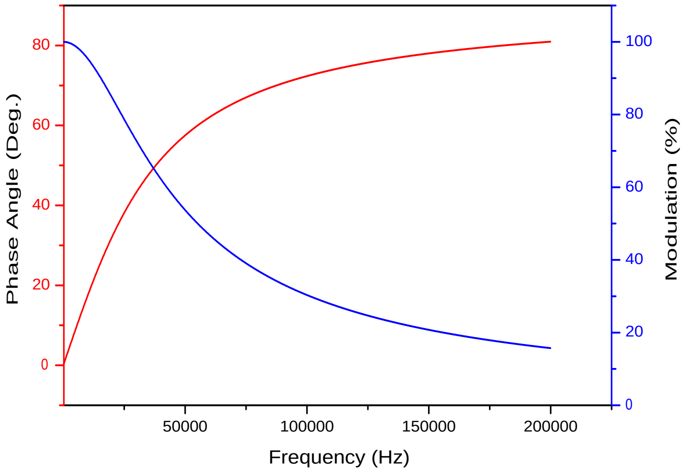

Figure 2.5: The phase angle and modulation factor of a luminophore with a lifetime of $5\mu s$ as a function of frequency.

mance perspective, as it results in the noise-related performance characteristics of the sensor system (e.g. resolution, LOD) varying as a function of frequency. This phenomenon is discussed in more detail in section 5.3.3.

The fact that both phase angle and modulation frequency vary as a function of lifetime provides two means of determining the lifetime of the luminophore. Measurement of the modulation factor requires the measurement of both the excitation and emission intensities, which, as will be seen in the next section, is not desirable in many cases. As a result, the phase measurement-based approach was used throughout this work.

Lifetime-based sensors have been developed using both time-domain [29–31] and frequency-domain [1, 4, 32] based techniques. This work has focussed on the use of frequency-domain techniques for a number of reasons. The measurement "duty cycle" associated with time-domain measurements is limited by the time taken for the luminophore to decay to close to zero intensity. There is no such fundamental limitation with frequency-domain measurements, however, and a measurement duty cycle of unity can be achieved if the instrumentation electronics are designed correctly. The net effect of this is that, from a theoretical perspective at least, the use of frequency-domain techniques will result in improved noise-related performance. An additional advantage is that the data processing routines required for frequency-domain measurements are less complex than those that are typically used with time-domain techniques.

Phase Fluorometry The use of phase measurements to determine the lifetime of a luminophore is generally referred to as phase fluorometry. A comprehensive history of phase fluorometry instrumentation is provided in [1]. There is a range of laboratory-based phase fluorometry equipment available(e.g. [33, 34]), however, in this case the focus is on systems that were designed specifically for sensing applications.

One of the earliest examples of a sensing specific phase-based system that could be found was developed for lifetime-based temperature measurement using optical fibres [35]. The advent of LEDs and LDs with suitable emission wavelengths [30] saw the development of a number of sensing-specific phase fluorometry systems that were designed for use in optical chemical sensing applications, such as oxygen and pH measurement. A number of researchers, including [36], developed bench-top systems that made use of commercially available dual-phase lock-in amplifiers for phase measurement. This approach is still used today for early stage development work. The first fully-integrated system that was reported was that of Trettnak *et al.* [37], which used a zero-crossing-based phase measurement technique. The system was developed for the measurement of oxygen using a porphyrin-based luminophore. An improved version of this design was developed by Kolle [38] while working at this laboratory and was used as part of a dissolved oxygen sensor system [4].

Over the last number of years, the focus in terms of phase fluorometry instrumentation development appears to have been primarily commercial in nature. A number of sensor systems that make use of phase fluorometry techniques have appeared on the market. These include the "Cellphase" system from Fluorometrix Inc, USA [39], the various systems from PreSens-Precision Sensing GmbH, Germany [40], and the Foxy and NeoFox oxygen sensors from OceanOptics Inc., USA [41]. A difficulty emerged when attempting to determine the baseline performance of the various commercially available instruments that represented the current state of the art in phase fluorometry. With the exception of the modules produced by PreSens, the manufacturers did not provide performance information for the instrumentation electronics by itself. Instead, they provided information on the performance of the sensor system in which it was used. The phase measurement resolution of the PreSens module intended for oxygen sensing, the "EOM O_2 Mini", is 0.05°, and as will be seen in chapter 3, is significantly improved upon by each of the three systems that were developed during this work. The sensing-related performances of all of the other commercially available systems were compared to those of the sensor systems that was developed during this work. The results, which are presented in the relevant chapters, were favourable in all cases.

From a functionality perspective, two of the systems that were developed during this work display significant increases over the state of the art. The wearable breath oxygen measurement system that was developed is, to the best of the authors knowledge, unrivalled in terms of form-factor, while still possessing the performance required to obtain realtime breath oxygen measurements. The functionality of the DSP based system also appears to be unmatched. It is equipped with multiple excitation and emission channels, can operate with multiple simultaneous excitation frequencies, and is capable of obtaining intensity, phase and ratiometric intensity measurements. PreSens produces systems that are capable of multi-channel operation, and the NeoFox system from Ocean Optics is capable of obtaining both intensity and phase measurements. None of the commercially available systems, however, have the same breath of functionality as the system that was developed during this work.

Despite the predominant commercial focus in the area of phase fluorometry instrumentation development in recent times, there have been a number of interesting developments reported in the literature. These relate primarily to the development of highly miniaturised systems. Bright *et al.* [32] have developed a phase fluorometry system that makes use of a single element CMOS-based collection and processing unit. A similar, although not as sophisticated approach has been adopted by Vallvey *et al.* [42] who have coated oxygen sensitive films directly onto photodiode detectors. Neither have provided noise-related performance information such as resolution or limit of detection, however a subjective determination of their performance relative to that of the systems that have been developed is possible. This can be achieved by comparing the noise in the calibration step responses that have been provided in both cases to those obtained using the systems developed during this work. This process reveals that these systems, while promising from a size perspective, lag well behind the systems that have been developed here from a performance point of view.

2.4.3 Comparison Between Intensity and Lifetime-based Techniques

Both intensity and lifetime interrogation techniques have been presented in the previous sections. It is generally accepted [43, 44], that the use of lifetime-based techniques is preferable for sensing applications for a number of reasons. A key requirement of most sensor systems is stability. It has been found, however, that the use of intensity-based techniques often results in poor stability. In an intensity-based system, the measurement that is obtained is dependent on the intensity of the excitation source and the number of excitable dye molecules that are present. As a result, any occurrence of excitation source intensity drift and/or photobleaching of the luminescent material will lead to drift in the sensor measurements that are obtained. Unfortunately, both of these phenomena are widely observed in luminescent sensor systems and are typically found to be limiting factors in the case of intensity-based measurements. An additional issue with intensity measurements is that good sensor to sensor repeatability requires that every sensor element contain the same amount of luminescent material, which can be quite difficult to achieve.

Lifetime-based measurements are, in theory, unaffected by the intensity of the source and the amount of luminescent material that is present. As a result, they represent a more attractive option than their intensity-based counterparts for sensing applications. Real-world limitations, such as excitation light leakage and sensor matrix heterogeneity(see section 3.2.2.3), mean that lifetime measurements typically display some amount of sensitivity to intensity-based effects. This sensitivity is typically much less than if direct intensity measurements were used, however.

Although lifetime-based techniques are the preferred choice for the reasons that have been outlined, their use is not practical in certain situations. There is a direct correlation between the cost and complexity of phase fluorometry equipment and the smallest lifetime it is capable of measuring. Low cost instrumentation can be developed for obtaining lifetime measurements in the μs to ms range [37, 45, 46]. Many commonly used fluorophores have lifetimes in the low ns region, however. The measurement of lifetimes in this region requires the use of complex and expensive equipment, which is generally not feasible for sensing applications. This has led to considerable interest in the synthesis of long-lifetime luminophores in recent years, and while there are now a considerable number of long-lifetime dyes available, many situations still require the use of dyes with lifetimes in the *ns* region. In such cases, intensity-based techniques are generally used. A number of other techniques have been developed to overcome the problems that are associated with direct intensity measurements. These include dual luminophore referencing (DLR) [47, 48] and ratiometric operation.

DLR sees the co-immobilisation of a short lifetime analyte-sensitive luminophore with a long-lifetime luminophore that is insensitive to the analyte. If this dye combination is excited using modulated light then the phase of the resulting aggregate emission will vary as a function of the intensity of the short lifetime luminophore. Successful operation of the DLR technique has been demonstrated in a range of applications. the technique was developed by Klimant *et al.*, and as a result of IP protection, there is not "freedom to operate" with this technology.

2.4.4 Ratiometric Sensing

The ratiometric technique is widely used for compensation purposes in many areas of sensing. When applied to luminescence-based sensing, it allows many of the problems associated with direct intensity measurements to be eliminated. The basic concept behind ratiometric operation is that the sensor is designed such that it has two responses that display unequal responses to the analyte in question. Taking the ratio of both responses will result in a quantity that is sensitive to the analyte but insensitive to intensity changes. The principle of operation is illustrated in Fig. 2.6. There are a variety of means by which the required dual response can be achieved. The ideal situation sees the use of a

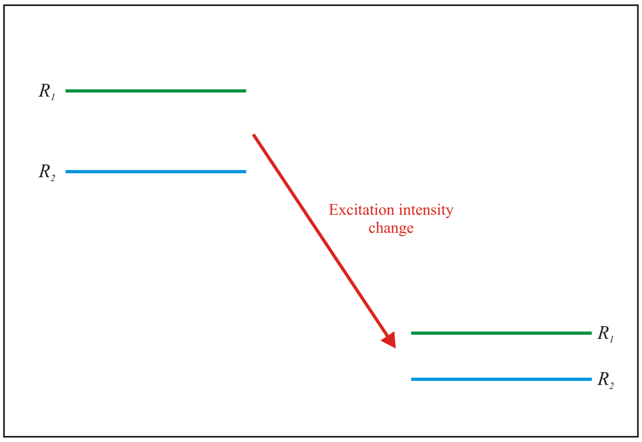

Figure 2.6: This diagram depicts the concept behind ratiometric operation. The sensor exhibits two responses, R_1 and R_2, with only one of these responses being sensitive to the analyte in question. If a change in intensity occurs (e.g. a change in excitation intensity), then both responses will change but their ratio will stay the same.

luminophore that intrinsically exhibits dual responses that are sensitive to the analyte to differing degrees. In this case, photo-bleaching-based effects can be taken into account in addition to excitation source drift and instability. Some examples of this type of implementation can be found in [49–55]. If a suitable dual response luminophore is not available, ratiometric operation can be achieved by co-immobilising a second dye in the sensor film, such as in [5, 56–58]. This approach eliminates source-based effects but requires that both dyes photobleach at the same rate in order to fully account for bleaching-based effects.

There are a range of ratiometric strategies that can be implemented in luminescence sensing applications. These are dictated by the properties of the luminophore or luminophore combination that is being used. The most commonly used configurations include dual-excitation [52, 53], dual emission, and dual-excitation/dual-emission [13, 59], where both dual-excitation and dual-emission occur simultaneously. Dual-emission can relate to emission at two wavelengths [5, 57], or two lifetimes [49]. The ratiometric sensing carried out during this work made use of the pH sensitive luminophore, HPTS, which displayed two excitation/absorption peaks and a single short-lifetime emission peak.

From an instrumentation perspective, the majority of work with ratiometric luminescence-based sensors that is reported in the literature appears to have been carried out using laboratory-based equipment such as spectrofluorometers [51–53, 55, 60]. A number of dedicated ratiometric instrumentation systems have been developed by Kostov, Rao and coworkers [26, 50, 61, 62] for various ratiometric configurations. Only the intensity-based systems [26, 61] were of interest in this case. Both of these systems make use of dual LED light sources, which are switched alternately. The resulting emission intensities are measured using a photodiode amplifier and digitisation circuitry. Lock-in techniques are used to eliminate the effects of ambient light. An obvious drawback with these systems is that the LEDs are operated alternately. This leads to a reduction in signal-to-noise ratio compared to continuous measurements. It also limits the effective response time of the system. The ratiometric sensing system that was developed during this work used the DSP-based instrumentation electronics, which was capable of operating both LEDs simultaneously through the use of multi-frequency techniques. The system that was developed also made use of an enhanced capture optical configuration which led to significant increases in signal-to-noise ratio and had a corresponding impact on sensor resolution and limit of detection.

2.5 Optical Sensor Platform General Features

2.5.1 Exploitation of Anisotropic Emission

When a radiating dipole, such as a luminescent molecule, is placed close to, or at, a dielectric interface, the resulting emission pattern is anisotropic, and results in the emission being emitted preferentially in certain directions. A rigorous analysis of this phenomenon has been performed by Polerecky *et al.* [63] in the context of luminescent sensors. It was found that if a luminescent layer was deposited on the surface of a substrate with a higher refractive index than that of the luminescent layer, then the majority of the luminescence is directed into the substrate, with a highly anisotropic profile. The 2D cross-section of a typical emission profile is shown in Fig. 2.7. The directional nature of the emission introduces the possibility of optimising luminescence capture through the use of geometrical configurations that are matched to the luminescence emission profile. A number of systems have been developed at this laboratory to this end. These included waveguide-based platforms [18, 64] and frustrated-cone-based structures [65] that exploit the circular symmetry of the emission profile. Separately, parabolic element-based structures were developed by Ruckstuhl [66, 67]. An optical sensor probe based around a parabolic element was designed by a group of researchers that included the author, and served as the starting point for the optics related strand of this work.

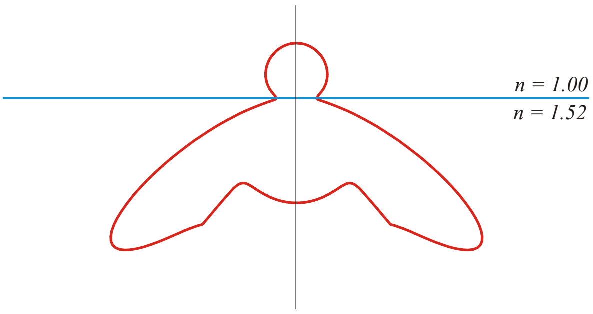

Figure 2.7: Emission profile that is observed when a luminophore is located at the interface between a material with a refractive index of 1.52 and air.

2.5.2 Excitation and Emission Filters

Optical filters are an important requirement in most luminescence sensor systems, where they serve to separate the excitation and emission light. The purpose of the emission filter is to filter the luminescence emission and remove any scattered or transmitted excitation light that would otherwise reach the detector. It must either be a long pass or bandpass filter with a suitable cut-on point.

Some excitation sources, such as LEDs have quite a broad emission, and in certain cases the long wavelength tail of their emission peak can overlap with the luminescence emission, and be transmitted by the emission filter. In such cases, the excitation must be filtered to remove the long wavelength tail. Excitation filters must either be short-pass or band-pass filters. The excitation and emission spectra and filter transmission curves of one of the systems developed during this work are shown in Fig. 2.8

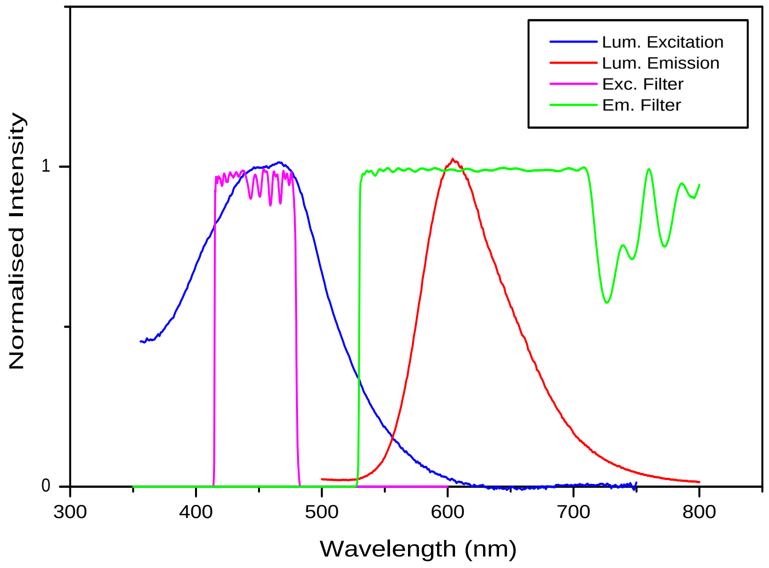

Figure 2.8: The excitation and emission spectra [14] of the oxygen sensitive fluorophore, $[Ru(dpp)_3]^{2+}$ and the transmission profiles of the emission and excitation filters [68] that were used in the breath monitoring system (see chapter 6. The excitation LED emission, which has been omitted in the interests of clarity is centred at $450nm$.

2.5.2.1 Filter Selection

The important filter parameters from a luminescence sensing point of view are the pass band and stop band transmission levels and the location and sharpness of the pass band to stop band transition. The stop band transmission of both the excitation and emission filters determines the amount of excitation light that reaches the detector. The passband transmission of both filters has an impact on the emission intensity that reaches the detector. The location and sharpness of the transition affects both of these parameters and is generally dictated by the Stokes shift of the luminophore that is being used. Luminophores with a small Stokes shift require the use of filters that display a sharp transition.

There are two main types of optical filters available commercially: absorption-based and interference-based. The absorption-based filters, such as gel filters [69] and coloured glass filters [70] are the less expensive but lower quality of the two. Interference filters [71] typically have better pass and stop band characteristics and sharper transitions. They are considerably more expensive, however, and display significant angular sensitivity [72], which must be taken into account during the design process. Interference-based filters from either Semrock Inc, USA or ThorLabs, Germany have been used during this work in order to maximise performance.

2.5.3 Excitation Source and Detector Selection

There is a wide array of light sources that can be used for luminescence excitation. Broadband sources, such as xenon and mercury arc lamps, are generally be confined to large laboratory-based systems, such as spectrofluorometers [21]. Portable systems, and systems designed with a specific luminophore in mind would typically use either LEDs or laser diodes (LDs) as the source of excitation light. Although laser diodes can generate much higher emission intensities than LEDs, they are considerably more expensive, and as a result, LEDs were chosen for this work.

The majority of luminescence sensing applications make use of one of three types of detectors: photomultiplier tubes (PMTs), photodiodes, and CCD cameras. Detector choice is typically governed by the requirements of the application in question. PMTs are the most sensitive of the three and have the highest signal-to-noise ratios but are bulky, expensive, delicate, and require the generation of high voltages [1]. Although photodiodes are much less sensitive than PMTs, they are smaller, substantially less expensive, do not require high voltage drive circuitry, and are more robust. Avalanche photodiodes (APDs), which are essentially a hybrid of the photodiode and the PMT, are seeing increasing use in sensing applications. They consist of a pn junction that is reversed biased by a large voltage. This voltage causes an amplification effect analogous to that which occurs in a PMT. APD sensitivity lies between that of the PMT and the photodiode and are an intermediate choice between PMTs and photodiodes in almost every respect. CCD cameras are also being used for luminescence sensing applications and provide the possibility of obtaining both spectral [22, 73] and spatial [74] information.

The choice of which type of excitation source and detector to use is very much system dependent. In virtually all cases, there will be trade-offs between performance, cost, and reliability and robustness. A key requirement that was placed on the systems that were developed as part of this work was the use of low-cost components, in order to maximise commercialisation potential. As a result, LEDs and photodiodes were used throughout.

2.6 Conclusion

This chapter presented theory and background information on luminescence and luminescence sensor interrogation techniques and systems. This included a review of the current state of the art in relation to the sensor techniques that were employed in this work. A brief overview of some of the general aspects concerning the optical sensor platforms that were used was also included. Any additional theoretical and background material that was deemed necessary is included in the chapter to which it is applicable.

Bibliography

[1] J. R. Lakowicz. *Principles of Fluorescence Spectroscopy, 3rd ed.* Springer, New York, 2006.

[2] David Rendell. *Fluorescence and phosphorescence spectroscopy.* Wiley, Chichester, 1997.

[3] Aisling K. McEvoy. *Development of an Optical Sol-gel-based Dissolved Oxygen Sensor.* Ph.D. Thesis, Dublin City University, 1996.

[4] C. McDonagh, C. Kolle, A. K. McEvoy, D. L. Dowling, A. A. Cafolla, S. J. Cullen, and B. D. MacCraith. Phase fluorometric dissolved oxygen sensor. *Sensors and Actuators B: Chemical*, 74(1-3):124–130, 2001.

[5] Chen-Shane Chu and Yu-Lung Lo. Ratiometric fiber-optic oxygen sensors based on solgel matrix doped with metalloporphyrin and 7-amino-4-trifluoromethyl coumarin. *Sensors and Actuators B: Chemical*, 134(2):711–717, 2008.

[6] Marta Valledor, Juan Carlos Campo, Israel Sanchez-Barragan, Juan Carlos Viera, Jose M. Costa-Fernandez, and Alfredo Sanz-Medel. Luminescent ratiometric method in the frequency domain with dual phase-shift measurements: Application to oxygen sensing. *Sensors and Actuators B-Chemical*, 117(1):266–273, 2006.

[7] Tomas C. O'Riordan, Kathleen Fitzgerald, Gelii V. Ponomarev, John Mackrill, James Hynes, Cormac Taylor, and Dmitri B. Papkovsky. Sensing intracellular oxygen using near-infrared phosphorescent probes and live-cell fluorescence imaging. *American Journal of Physiology-Regulatory Integrative and Comparative Physiology*, 292(4):R1613–R1620, 2007.

[8] E. Schmalzlin, J. T. van Dongen, I. Klimant, B. Marmodee, M. Steup, J. Fisahn, P. Geigenberger, and H. G. Lohmannsroben. An optical multifrequency phase-modulation method using microbeads for measuring intracellular oxygen concentrations in plants. *Biophysical journal*, 89(2):1339–1345, 2005.

[9] E. R. Carraway, J. N. Demas, B. A. Degraff, and J. R. Bacon. Photophysics and photochemistry of oxygen sensors based on luminescent transition-metal complexes. *Analytical Chemistry*, 63(4):337–342, 1991.

[10] Dorota Wencel. *Sol-gel-derived Optical Oxygen, pH and Dissolved Carbon Dioxide Sensors*. Ph.D. Thesis, Dublin City University, 2008.

[11] J. N. Demas, B. A. Degraff, and W. Y. Xu. Modeling of luminescence quenching-based sensors - comparison of multisite and nonlinear gas solubility models. *Analytical Chemistry*, 67(8):1377–1380, 1995.

[12] D. B. Spry and M. D. Fayer. Charge redistribution and photoacidity: Neutral versus cationic photoacids. *Journal of Chemical Physics*, 128(8):084508, 2008.

[13] Aron Hakonen and Stefan Hulth. A high-precision ratiometric fluorosensor for ph: Implementing time-dependent non-linear calibration protocols for drift compensation. *Analytica Chimica Acta*, 606(1):63–71, 2008.

[14] Dorota Wencel. Excitation and emission spectra of HPTS and Ru(dpp)3, 2010. Personal Communication.

[15] B. D. MacCraith, C. McDonagh, A. K. Mcevoy, T. Butler, G. OKeeffe, and V. Murphy. Optical chemical sensors based on sol-gel materials: Recent advances and critical issues. *Journal of Sol-Gel Science and Technology*, 8(1-3):1053–1061, 1997.

[16] G. E. Badini, K. T. V. Grattan, A. C. C. Tseung, and A. W. Palmer. Sol-gel properties for fiber optic sensor applications. *Optical Fiber Technology*, 2(4):378–386, 10 1996.

[17] Maryanne M. Collinson. Recent trends in analytical applications of organically modified silicate materials. *TrAC Trends in Analytical Chemistry*, 21(1):31–39, 2002.

[18] Orla McGaughey. *Development of a generic multi-analyte optical sensor platform for fluorescence-based sensing*. Ph.D. Thesis, Dublin City University, 2006.

[19] H. Schmidt. Organic modification of glass structure - new glasses or new polymers. *Journal of Non-Crystalline Solids*, 112(1-3):419–423, 1989.

[20] H. Schmidt. New type of non-crystalline solids between inorganic and organic materials. *Journal of Non-Crystalline Solids*, 73(1-3):681–691, 1985.

[21] *Fluoromax Compact Sprectrofluorometer.* Horiba Scientific, `http://www.horiba.com/scientific/products/fluorescence-spectroscopy/steady-state/fluoromax/fluoromax-compact-spectrofluorometer-524/`.

[22] *USB2000 FLG Spectrofluorometer.* Ocean Optics Inc., `http://www.oceanoptics.net/products/usb2000flg.asp`.

[23] *Axon GenePix400B.* Molecular Devices Inc., `http://www.moleculardevices.com/pages/instruments/gn_genepix4000.html`.

[24] Arun K. Ghosh. *Introduction to Instrumentation and Control.* Prentice-hall of India Private Limited, New delhi, 2004.

[25] M. L. Meade. *Lock-in amplifiers : principles and applications.* P. Peregrinus on behalf of the Institution of Electrical Engineers, London, 1983.

[26] Sandeep Vuppu, Yordan Kostov, and Govind Rao. Economical wireless optical ratiometric ph sensor. *Measurement Science & Technology*, 20(4):045202, 2009.

[27] A. K. McEvoy, C. M. McDonagh, and B. D. MacCraith. Dissolved oxygen sensor based on fluorescence quenching of oxygen-sensitive ruthenium complexes immobilized in sol-gel-derived porous silica coatings. *Analyst*, 121(6):785–788, 1996.

[28] Taha M. A. Razek, Michael J. Miller, Saad S. M. Hassan, and Mark A. Arnold. Optical sensor for sulfur dioxide based on fluorescence quenching. *Talanta*, 50(3):491–498, 1999.

[29] J. Hradil, C. Davis, K. Mongey, C. McDonagh, and B. D. MacCraith. Temperature-corrected pressure-sensitive paint measurements using a single camera and a dual-lifetime approach. *Measurement Science & Technology*, 13(10):1552–1557, OCT 2002.

[30] D. Kieslinger, S. Draxler, K. Trznadel, and M. E. Lippitsch. Lifetime-based capillary waveguide sensor instrumentation. *Sensors and Actuators B-Chemical*, 39(1-3):300–304, 1997.

[31] B. Konig, O. Kohls, G. Holst, R. N. Glud, and M. Kuhl. Fabrication and test of sol-gel based planar oxygen optodes for use in aquatic sediments. *Marine Chemistry*, 97(3-4):262–276, 2005.

[32] Vamsy P. Chodavarapu, Daniil O. Shubin, Rachel M. Bukowski, Albert H. Titus, Alexander N. Cartwright, and Frank V. Bright. Cmos-based phase fluorometric oxygen sensor system. *Ieee Transactions on Circuits and Systems I-Regular Papers*, 54(1):111–118, 2007.

[33] *K2 Multi-frequency cross-correlation phase and modulation fluorometer.* ISS Inc., `http://www.iss.com/products/k2/index.html`.

[34] *ChronosFD Frequency domain lifetime spectrometer.* ISS Inc., `http://www.iss.com/products/chronos/index.html`, 2010.

[35] Z. Y. Zhang, K. T. V. Grattan, and A. W. Palmer. A novel signal-processing scheme for a fluorescence based fiberoptic temperature sensor. *Review of Scientific Instruments*, 62(7):1735–1742, 1991.

[36] G. Okeeffe, B. D. Maccraith, A. K. Mcevoy, C. M. Mcdonagh, and J. F. Mcgilp. Development of a led-based phase fluorometric oxygen sensor using evanescent-wave excitation of a sol-gel immobilized dye. *Sensors and Actuators B-Chemical*, 29(1-3):226–230, 1995.

[37] W. Trettnak, C. Kolle, F. Reininger, C. Dolezal, and P. OLeary. Miniaturized luminescence lifetime-based oxygen sensor instrumentation utilizing a phase modulation technique. *Sensors and Actuators B-Chemical*, 36(1-3):506–512, 1996.

[38] Christian Kolle. *Development and evaluation of a phase fluorometric instrument for different luminescence based optical oxygen sensor applications.* Ph.D. Thesis, University of Leoben, 1999.

[39] *CellPhase pH, DO and DCO2 non-invasive sensors.* Fluorometrix Inc., `http://www.fluorometrix.com`.

[40] *Carbon Dioxide Sensors.* PreSens Precision Sensing GmbH, `http://www.presens.de`.

[41] *FOXY/neoFox Oxygen Sensor.* Ocean Optics Inc., `http://www.oceanoptics.com/Products/neofox.asp`.

[42] L. F. Capitan-Vallvey, L. J. Asensio, J. Lopez-Gonzalez, M. D. Fernandez-Ramos, and A. J. Palma. Oxygen-sensing film coated photodetectors for portable instrumentation. *Analytica Chimica Acta*, 583(1):166–173, 2007.

[43] Max E. Lippitsch and Sonja Draxler. Luminescence decay-time-based optical sensors: principles and problems. *Sensors and Actuators B: Chemical*, 11(1-3):97–101, 1993.

[44] H. Hochreiner, I. Sanchez-Barragan, J. M. Costa-Fernandez, and A. Sanz-Medel. Dual emission probe for luminescence oxygen sensing: a critical comparison between intensity, lifetime and ratiometric measurements. *Talanta*, 66(3):611–618, 2005.

[45] Y. Kostov and G. Rao. Low-cost gated system for monitoring phosphorescence lifetimes. *Review of Scientific Instruments*, 74(9):4129–4133, 2003.

[46] J. M. Costa-Fernandez, N. Bordel, J. C. Campo, F. J. Ferrero, M. A. Perez, and A. Sanz-Medel. Portable fibre optic oxygen sensor based on room-temperature phosphorescence lifetime. *Mikrochimica acta*, 134(3-4):145–152, 2000.

[47] C. Huber, I. Klimant, C. Krause, T. Werner, T. Mayr, and O. S. Wolfbeis. Optical sensor for seawater salinity. *Fresenius Journal of Analytical Chemistry*, 368(2-3):196–202, 2000.

[48] C. von Bultzingslowen, A. K. McEvoy, C. McDonagh, B. D. MacCraith, I. Klimant, C. Krause, and O. S. Wolfbeis. Sol-gel based optical carbon dioxide sensor employing dual luminophore referencing for application in food packaging technology. *Analyst*, 127(11):1478–1483, 2002.

[49] M. Valledor, J. Carlos Campo, I. Sanchez-Barragan, J. Carlos Viera, J. M. Costa-Fernandez, and A. Sanz-Medel. Luminescent ratiometric method in the frequency domain with dual phase-shift measurements: Application to oxygen sensing. *Sensors and Actuators B-Chemical*, 117(1):266–273, 2006.

[50] Y. Kostov, P. Harms, R. S. Pilato, and G. Rao. Ratiometric oxygen sensing: detection of dual-emission ratio through a single emission filter. *Analyst*, 125(6):1175–1178, 2000.

[51] Silviya Petrova, Yordan Kostov, Kim Jeffris, and Govind Rao. Optical ratiometric sensor for alcohol measurements. *Analytical Letters*, 40(4):715–727, 2007.

[52] Ramachandram Badugu, Yordan Kostov, Govind Rao, and Leah Tolosa. Development and application of an excitation ratiometric optical ph sensor for bioprocess monitoring. *Biotechnology progress*, 24(6):1393–1401, 2008.

[53] H. R. Kermis, Y. Kostov, P. Harms, and G. Rao. Dual excitation ratiometric fluorescent ph sensor for noninvasive bioprocess monitoring: Development and application. *Biotechnology progress*, 18(5):1047–1053, 2002.

[54] C. C. Overly, K. D. Lee, E. Berthiaume, and P. J. Hollenbeck. Quantitative measurement of intraorganelle pH in the endosomal lysosomal pathway in neurons by using ratiometric imaging with pyranine. *Proceedings of the National Academy of Sciences of the United States of America*, 92(8):3156–3160, 1995.

[55] D. Wencel, B. D. MacCraith, and C. McDonagh. High performance optical ratiometric solgel-based ph sensor. *Sensors and Actuators B: Chemical*, 139(1):208–213, 2009.

[56] Feng Gao, Lijuan Tang, Lu Dai, and Lun Wang. A fluorescence ratiometric nano-ph sensor based on dual-fluorophore-doped silica nanoparticles. *Spectrochimica Acta Part A-Molecular and Biomolecular Spectroscopy*, 67(2):517–521, 2007.

[57] E. J. Park, K. R. Reid, W. Tang, R. T. Kennedy, and R. Kopelman. Ratiometric fiber optic sensors for the detection of inter- and intra-cellular dissolved oxygen (vol 15, pg 2913, 2005). *Journal of Materials Chemistry*, 15(31):3246–3246, 2005.

[58] Sergey Borisov and Ingo Klimant. Luminescent nanobeads for optical sensing and imaging of dissolved oxygen. *Microchimica Acta*, 164(1):7–15, 2009.

[59] Aron Hakonen. Plasmon enhancement and surface wave quenching for phase ratiometry in coextraction-based fluorosensors. *Analytical Chemistry*, 81(11):4555–4559, 2009.

[60] Ozlem Oter, Kadriye Ertekin, and Sibel Derinkuyu. Ratiometric sensing of co2 in ionic liquid modified ethyl cellulose matrix. *Talanta*, 76(3):557–563, 2008.

[61] Y. Kostov and G. Rao. Low-cost device for ratiometric fluorescence measurements. *Review of Scientific Instruments*, 70(12):4466–4470, 1999.

[62] Y. Kostov, K. A. Van Houten, P. Harms, R. S. Pilato, and G. Rao. Unique oxygen analyzer combining a dual emission probe and a low-cost solid-state ratiometric fluorometer. *Applied Spectroscopy*, 54(6):864–868, 2000.

[63] L. Polerecki, J. Hamrle, and B. D. MacCraith. Theory of the radiation of dipoles placed within a multilayer system. *Applied Optics*, 39(22):3968–3977, 2000.

[64] C. S. Burke, O. McGaughey, J. M. Sabattie, H. Barry, A. K. McEvoy, C. McDonagh, and B. D. MacCraith. Development of an integrated optic oxygen sensor using a novel, generic platform. *Analyst*, 130(1):41–45, 2005.

[65] R. Blue, N. Kent, L. Polerecky, H. McEvoy, D. Gray, and B. D. MacCraith. Platform for enhanced detection efficiency in luminescence-based sensors. *Electronics Letters*, 41(12):682–684, 2005.

[66] T. Ruckstuhl and A. Krieg. Microscope objective for large-angle fluorescence used for rapid detection of single nucleotide polymorphisms in dna hybridization. *Analytical Chemistry*, 77(8):2656–2661, 2005.

[67] Thomas Ruckstuhl and Stefan Seeger. *Light Detecting Optical Device*. Number US6714297 (B1). U.S. Patent, 2004. US6714297 (B1).

[68] *Semrock Inc.* `http://www.semrock.com`.

[69] *LEE Filters.* `http://www.leefilters.com/lighting/`.

[70] *Optical Glass Filters.* Schott AG, `http://www.schott.com/advanced_optics/english/our_products/filters/color.html?PHPSESSID=u5ubeju3cmh91mm4cr8onca047`.

[71] P. Hariharan. *Basics of interferometry*. Elsevier Academic Press, Amsterdam; Boston, 2007.

[72] Michael Bass, Virendra N. Mahajan, Eric W. Van Stryland, Guifang Li, Carolyn Ann MacDonald, Casimer DeCusatis, and Optical Society of America. *Handbook of optics*. McGraw-Hill, New York, 2010. ID: 318409251.

[73] I. Tsagkatakis, S. Peper, and E. Bakker. Spatial and spectral imaging of single micrometer sized solvent cast fluorescent plasticized poly(vinyl chloride) sensing particles. *Analytical Chemistry*, 73(2):315–320, 2001.

[74] Qingzhi Zhu, Robert C. Aller, and Yanzhen Fan. A new ratiometric, planar fluorosensor for measuring high resolution, two-dimensional pco2 distributions in marine sediments. *Marine Chemistry*, 101(1-2):40–53, 2006.

Chapter 3

Instrumentation Electronics

3.1 Introduction

Instrumentation electronics are a key part of all sensor systems, from both a performance and functionality perspective, and as a result were one of the key focus areas in this work. Three separate systems have been developed using a progressive design process, with each subsequent system having increased functionality and/or performance compared to the previous one. The first system was an analog phase fluorometry system, for use in a range of applications. The second was a digital phase fluorometry system, that was designed for use in a breath monitoring application. The third system, representing the culmination of the design efforts, was a high performance DSP-based system, which can be used in a range of luminescence-based sensing applications. It is equipped with multiple excitation and collection channels and can be operated in a variety of measurement modes.

3.2 Analog Phase Fluorometry system

A stand-alone phase fluorometry system was required for a range of oxygen sensing applications, including real-time breath monitoring and dissolved oxygen (DO) measurement. The key design requirements for the system were:

- Measurement frequency of $\sim 10Hz$
- Minimisation of intensity sensitivity
- Maximisation of phase measurement resolution

The measurement frequency requirement was dictated by the fact that the system was to be used to obtain real-time breath oxygen concentration measurements.

An analog zero-crossing-based phase fluorometry system was developed previously at the Optical Sensors Laboratory (OSL) [1]. However, it could not operate at the required measurement frequency, for reasons that are discussed in detail in section 3.2.2.1. An improved phase fluorometry system was developed that addressed this issue and implemented a range of changes that increased functionality and improved performance. The original and improved designs are described in the following sections.

3.2.1 Original System

A block diagram of the original system, which was used as the starting point for the design, is shown in Fig. 3.1

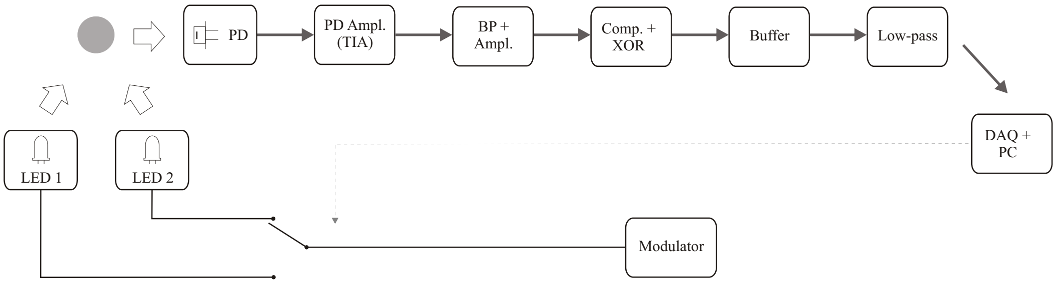

Figure 3.1: Block diagram of original Phase fluorometry Circuit

Luminescence is excited using a spectrally compatible LED and is collected using a Si-PIN photodiode or similar detector. An optimised bootstrap transimpedance-based photodiode amplifier, which was the result of considerable design effort [2], converts the photodiode photo-current into a voltage signal which is then passed through a bandpass filter and subsequently to comparator/exclusive-OR (XOR) based phase measurement circuitry. The XOR circuitry outputs a pulse-width-modulated (PWM) waveform, the duty cycle of which is determined by the phase difference between the input waveforms(A detailed explanation of comparator/exclusive-OR phase measurement technique can be found in [1]). The PWM waveform is buffered using a zener diode-powered FET bridge to enhance the temporal and thermal stability of the waveform. The stabilised waveform is lowpass-filtered to convert it to a dc signal, which is then passed to a data acquisition (DAQ) card that is installed in a PC. Optical excitation and emission filters are also included in the system but they have been omitted here in the interests of clarity.

3.2.1.1 Referencing Strategy

A sizeable temperature-dependent phase shift is introduced by the electronic circuitry and this must be taken into account in order that accurate measurements of luminescence lifetime-induced phase shift be obtained. This is achieved in this case by implementing a dual LED referencing strategy. A second LED, termed the reference LED, which does not induce fluorescence in the sensor membrane, is included in the system. The system switches between both LEDs and a phase measurement is obtained for each. Subtraction of these two phase values yields a measurement of the luminescence lifetime induced phase shift that is independent of phase changes induced in the circuitry.

3.2.2 Improved Design

A block diagram of the improved design is shown in Fig. 3.2.

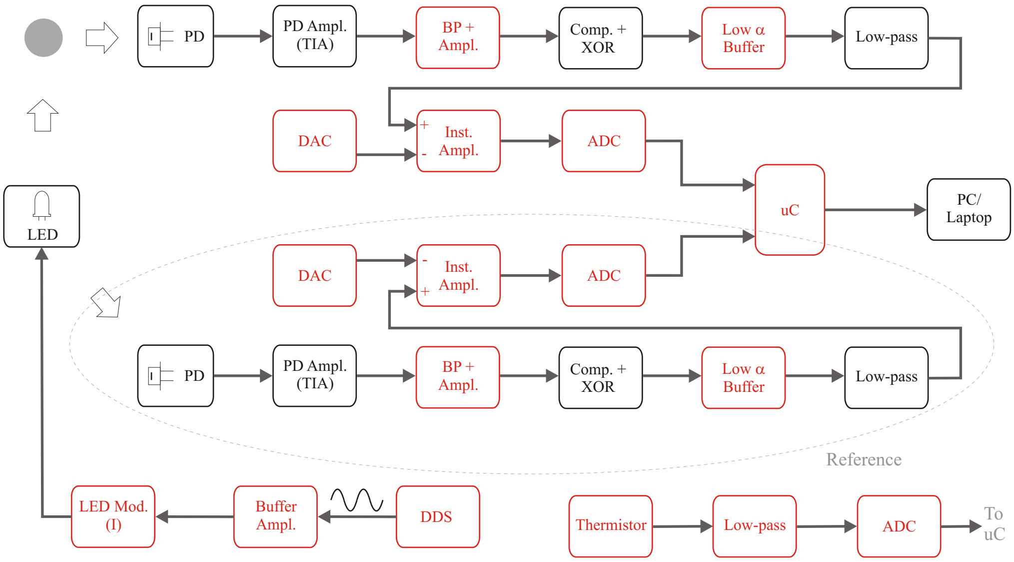

Figure 3.2: Block diagram of Improved Phase fluorometry Circuit. The system makes use of dual photodiode referencing

The major changes are shown in red, and include: the addition of digitisation circuitry to eliminate the need for a DAQ card to be included in the host PC, the use of digitally-controlled sine wave modulation circuitry that incorporates a current-based drive stage, the addition of temperature measurement circuitry, and the implementation of dual photodiode referencing. A number of improvements have also been made to other parts of the system, including the bandpass filter and XOR output buffer.

The digitisation circuitry consists of a low power microcontroller from the Microchip PIC family and separate 16-bit ADCs for the signal, reference and temperature channels. Gain- and offset-based signal conditioning circuitry is included in the signal and reference channels to scale the active range of the sensor to the full input range of the ADC, thus minimising quantisation effects. The offset level is controlled using a 12-bit digital to analog converter (DAC), which facilitates the use of high gains without restricting the dynamic range of the system, and also allows realtime user control of the operating range. Communication between the system and the host PC/laptop is implemented using a standard RS232 serial link.

The square wave-based modulation scheme used in the original design has been replaced with sine wave-based modulation to enhance system performance. Using sine wave modulation improves modulation efficiency as modulation does not take place at frequencies that are later filtered out. The improvement over square wave modulation is illustrated in Fig. 3.3, which compares the modulation power at the fundamental frequency for square and sine wave modulation waveforms with equal total power. The results presented in the figure are derived in Appendix A. The

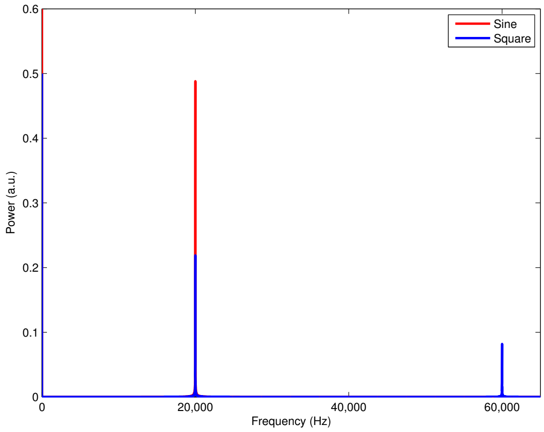

Figure 3.3: Relative power at the fundamental frequency for square and sine modulation waveforms with equal total power. Sine wave modulation is approximately 2.3 times more efficient than square wave modulation. The modulation frequency was set to 20kHz.

significance of improved modulation efficiency is that the LED intensity, which has a direct link to photo-degradation of the fluorescent dye, can be reduced while still maintaining the same overall system performance. A digital direct synthesis (DDS) IC (AD9832, Analog Devices) was chosen as the modulation source for the system primarily due to the much improved thermal stability of crystal driven DDS sources over their analog counterparts but also to minimise footprint area. The output of the DDS is buffered and then passed to a current-based drive stage that modulates the current in the LED. Direct voltage modulation of the LED is not desirable as the non-linear V-I characteristics of the LED will lead to the presence of harmonics in its output. Early stage testing also found that current modulation resulted in much reduced thermal drift, when compared to a voltage modulated system.

Simple, thermistor-based, temperature measurement circuitry was added to the system. The thermistor is connected in a half bridge configuration, and is driven using a precision voltage source with a low temperature coefficient. The output from the bridge is lowpass-filtered and sampled using a 16-bit ADC. It was determined that sufficient resolution ($0.0011^{O}C$) could be obtained without the inclusion of an amplification stage.

The bandpass filter, which is a key element in system performance, was completely redesigned and is now implemented using a state variable IC (UAF42, Burr Brown/TI). This device makes use of laser-trimmed on-chip components which facilitate the implementation of filters with higher Q factors than could be achieved using discrete components, thus reducing system bandwidth, and consequently, measurement noise. The zener diode-based power source for the XOR output buffer was replaced with a precision voltage reference, which has a substantially lower output impedance and temperature coefficient than its predecessor($20\Omega, 5ppm/°C$ vs. $1K\Omega, 200ppm/°C$). The reduced output impedance leads to improved waveform quality and the reduced temperature coefficient reduces the thermal dependence of the system.

A range of alternative photo-diode amplifiers, including a number of photodiodes with integrated amplifiers, was tested during the initial design phase. Their performance was exceeded, however, by that of the original design in all cases.

3.2.2.1 Referencing Strategy

As listed previously, one of the design requirements for the system was that it be capable of operating at a measurement frequency of $\geq 10Hz$. The original circuit implemented a dual LED temperature compensation strategy, which required that the system switch between the signal and reference LEDs to obtain a single measurement. In this configuration, when the LEDs are switched the phase value changes, resulting in a step change in the duty cycle of the lowpass filter input waveform. Sufficient time must be allowed following this step change for the output of the lowpass filter to stabilise before measurements can be obtained. This, combined with the minimum sampling rate requirement, imposes maximum limits on the lowpass corner frequency, which directly impacts system noise. When the system was modelled it was found that the maximum possible corner frequency would have led to excessive measurement noise, and consequently, it was concluded that dual LED referencing was not viable. This led to the implementation of a dual photodiode-based referencing strategy, using two parallel measurement channels. Instead of switching between a signal and a reference LED, a second photodiode and phase measurement channel that monitors the excitation LED was added to the system to obtain the reference signal. As both measurement channels can operate in parallel there is no settling-time-related restriction on the low-pass filter corner frequency, allowing the system to be operated at the required sampling rate.

Full circuit diagrams for the system can be found in appendix B.1

3.2.2.2 PCB Design and Layout

Printed circuit board (PCB) design and layout play an important role in the performance of electronic systems [3, 4]. Poor PCB design can cause a range of problems including incorrect component operation, reduced system performance, increased measurement noise and increased electromagnetic interference (EMI).

As a result, considerable attention was paid to the PCB design and circuit layout process. The final configuration, which is shown in Fig. 3.4, was the result of an iterative design process that saw the development and extensive testing of a number of revisions of the system. The current best practices in PCB design are captured as a set of guidelines that are widely available from component manufacturers in application notes and product datasheets (e.g. [5–8], and these were used as the basis for the design. They include: the use of large, unbroken, ground planes, the use of extensive power supply decoupling, keeping signal traces as short as possible, and the segregation of sensitive analog circuitry from digital and high current circuitry. The full system was implemented on a single dual layer PCB, with one side being used exclusively as a ground plane. A split plane ground topology was implemented with separate regions being used for the analog and digital sections of the board. Surface mount (SMT) components were used where possible in order to preserve ground plane integrity, minimise signal trace

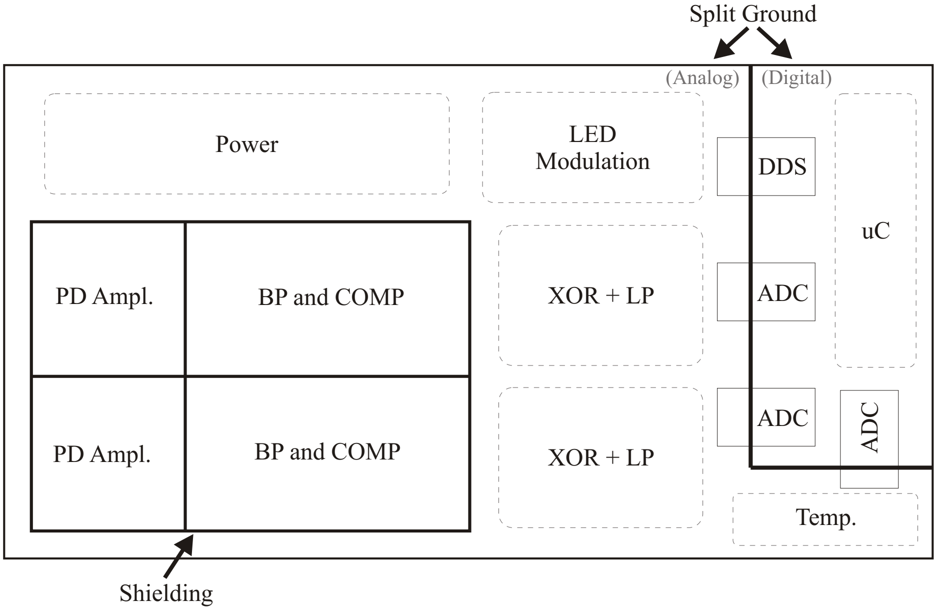

Figure 3.4: High level diagram of circuit layout

length and minimise the overall size of the PCB. The noise performance of the system was improved by adding either an RC or LC filter to the power supplies of the noise sensitive analog circuit elements (PD amplifier, bandpass filter and lowpass filter). The PD amplifier and bandpass filter shielding (see next section) that was added to the system primarily to minimise intensity sensitivity also had a positive impact on measurement noise, which was believed to be due to reduced coupling of RF noise into the system.

3.2.2.3 Intensity Sensitivity and Shielding

One of the intended applications of the system was the measurement of gaseous oxygen in a range of industrial applications, such as modified atmosphere food packaging and double glazed window assemblies, using a sensing configuration in which the fluorescent membrane was remote from the optical excitation and detection assembly. This configuration introduced the possibility of substantial distance-induced intensity changes and, as a result, one of the main design requirements of the system was that changes in measured phase angle due to fluorescence intensity changes be minimised. As discussed in section 2.4.3, one of the key advantages of lifetime-based measurement techniques over intensity-based techniques is that such measurements are theoretically independent of fluorescence intensity. However, real-world performance limitations and parasitic effects mean that all lifetime-based instrumentation displays some degree of intensity sensitivity. The mechanism by which this takes place is illustrated in Fig. 3.5. The ideal situation is represented in Fig. 3.5a, where changes in intensity do not affect the measured phase angle. In Fig. 3.5b, a second modulated signal, with

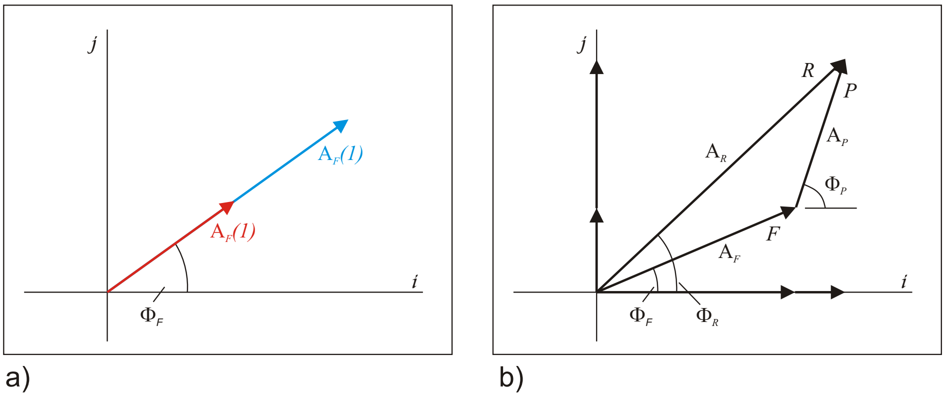

a) b)

Figure 3.5: Phasor diagram representation of modulated waveform(s). a) The ideal phase measurement situation, where intensity has no effect on measured phase angle. b) The real world situation, where the presence of a parasitic modulated signal introduces intensity sensitivity

a different phase angle, is present alongside the fluorescence signal. This second, parasitic, signal could be from a number of sources, for example the presence of excitation light at the detector, or electronic coupling of a modulated signal into the signal path prior to the comparator. Vector addition occurs between the fluorescence signal, F, and the parasitic signal, P, and the system will measure the phase angle ϕ_R of the resultant, R, instead of that of the fluorescence signal, ϕ_F. By resolving the vectors into orthogonal components (i and j), the phase angle ϕ_R of the resultant can be expressed as:

$$\phi_R = \tan^{-1}\left(\frac{A_F\sin(\phi_F) + A_R\sin(\phi_R)}{A_F\cos(\phi_F) + A_R\cos(\phi_R)}\right) \tag{3.1}$$

This expression contains a term for the amplitude, A_F, of the fluorescence signal, indicating that the presence of a parasitic modulated signal, with a different phase angle than that of the fluorescence signal, results in the measured phase angle becoming sensitive to fluorescence intensity. If the amplitude of the parasitic signal, A_P, approaches zero then then equation 3.1 becomes:

$$\phi_R \simeq \phi_F \tag{3.2}$$

which shows that intensity sensitivity can be minimised by minimising the amplitude of the parasitic signal. The electronic contribution to P could come from a variety of sources but must be coupled into the signal channel before it is digitised by the comparator. Therefore, all of the analog circuitry in the signal path before the comparator was placed inside shielding enclosures, as indicated in Fig. 3.4, in order to minimise coupling into that circuitry. The PD amplifier and bandpass filter sections were shielded from each other as the bandpass filter introduces a sizeable phase shift (120^O), which meant that both circuit elements could couple adversely into one another. The signal and reference channels were also isolated as they could generally be expected to be at different phase angles. Power supply coupling represented another avenue by which the parasitic signal could be introduced to the signal so the power supplies to the sensitive circuit elements were filtered using LC filters. In addition, the LED drive circuitry power supply was LC-filtered in order to minimise the coupling of a modulated signal onto the power supply rails by the high current LED drive stage.

It is worth noting that the scenario described in this analysis may also arise in the case of sensor dyes/sensor elements that exhibit multi-exponential decay. Multi-exponential fluorophores may be considered as having a number of discrete lifetimes [9] and if the above analysis is applied, it becomes apparent that the phase of the resultant fluorescence emission will be sensitive to the relative intensity contributions from each lifetime component. A number of situations can arise where the relative contributions at each lifetime changes: e.g. in the case of heterogenous film deposition, where different regions of the film will display different phase angles.

3.2.3 Performance

The performance of the system was assessed using two test configurations. In the first, which will be referred to as loopback mode, the output of the system was fed back into the input. This was achieved by connecting a resistor in place of the LED and feeding the voltage drop across it into the inputs. The second test configuration saw the use of a remote configuration optical front-end (see Fig. 3.6) that allowed the luminescence intensity to be changed easily.

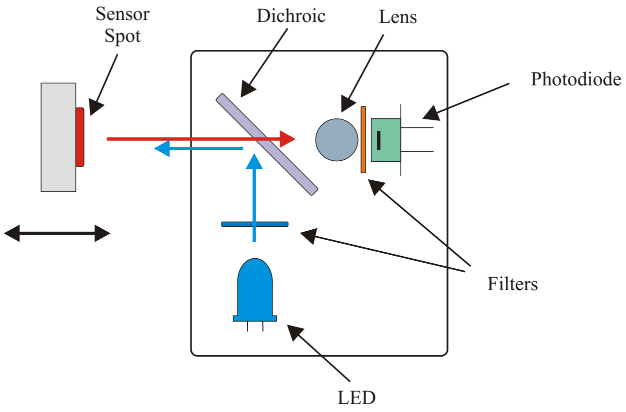

Figure 3.6: Remote configuration optical probe. Excitation light from the LED passes through the excitation filter and is reflected by the dichroic mirror. The sensor spot is fixed to a movable block and is placed in front of the probe assembly. The fluorescence emission from the spot is transmitted by the dichroic mirror and focussed onto a photodiode using a ball-lens. Changing the position of the sensor spot allows the fluorescence intensity to be controlled.

There are many performance criteria that could have been assessed when characterising the performance of the electronic systems that have been developed during this work. It was found, however, that resolution and drift, thermal drift in particular, were the most important parameters from an instrumentation perspective. Accuracy related performance was not an issue for any of the systems that were developed during this work as the response of the sensors were determined using a calibration process in all cases. Any absolute inaccuracy in the output of the system would be taken into account by the calibration process.

3.2.3.1 Resolution

The resolution of a sensor is defined as the smallest detectable change in the quantity being measured [10]. It is generally taken to be the peak-to-peak noise in the sensor output. A difficulty emerges when trying to quantify the peak-to-peak noise from a mathematical perspective due to the fact that noise is probabilistic in nature. The implication of this is that the peak-to-peak noise is infinite from a mathematical perspective. A common solution to this problem is to specify an acceptable confidence interval and use it as a measure of the peak-to-peak noise. $\pm 3\sigma$ is commonly used for this purpose [2]. If the signal has a normal distribution, then there is a 99.73% probability that a given signal value lies in the range $\pm 3\sigma$ [11]. If this convention is adopted, then the peak-to-peak noise in the signal, N_{p-p}, can be defined as:

$$N_{p-p} = 6\sigma \tag{3.3}$$

where σ is the standard deviation of the signal. The phase measurement resolution of the system, R_Φ, can then be taken to be:

$$R_\Phi = 6\sigma_\Phi \tag{3.4}$$

A full analysis of the noise characteristics of phase measurement systems, such as that carried out in [2, 12], reveals that the phase measurement standard deviation, σ_ϕ, is a function of the signal to noise ratio (SNR) of the input signal, and can be described by the expression:

$$\sigma_\Phi = \frac{\sigma_s}{A_s} = \frac{1}{SNR_s} \tag{3.5}$$

where A_s and σ_s are the amplitude and rms value of the synchronous demodulation system input signal. This result shows that the behaviour of phase measurement systems differs from that of most other sensor systems (e.g. intensity-based) in that changes in the intensity of the input signal lead to a change in the measurand noise.

The phase resolution of the system was evaluated in loopback mode, by measuring the peak-to-peak noise in the output signal. The resolution that was obtained for an input signal amplitude of $2V_{p-p}$ is listed in Table 3.1.

The resolution of the system was also measured using the remote mode optical probe for a range of signal intensity values. The results are shown in Table 3.2. The signal intensity values were varied by changing the distance of the luminescent sensor spot from the probe. It can be seen that the resolution of the system

Resolution (°)
0.011

Table 3.1: Phase measurement resolution in loopback mode with a signal amplitude of $2V_{p-p}$

Amplitude V	Resolution $Deg.$
0.01	1.158
0.02	0.512
0.05	0.195
0.10	0.054
0.20	0.053
0.50	0.040
1.00	0.029
2.00	0.018

Table 3.2: Phase resolution for a range of signal amplitudes. The amplitude was varied by changing the distance of the fluorescent spot from the optical front-end

worsens rapidly as the signal amplitude decreases, indicating the importance of maximising luminescence intensity.

3.2.3.2 Drift

Thermally induced drift was found to be the only measurable source of drift in the system output. The warm-up drift of the system was characterised by operating it in a typical environment for an extended period. The warm-up drift of the system in loopback mode is shown in Fig. 3.7.

3.3 Digital Phase Fluorometry System

3.3.1 Motivation

The analog system described previously performed well and was used in a number of applications. However, its size ($160mm \times 85mm$) meant that it was not suitable for use as a portable system. The development of a portable battery-powered phase fluorometry system was one of the requirements of the real-time breath monitoring application (see chapter 6). Therefore, it became necessary to design a system with reduced size. It was not possible to reduce the size of the existing system without sacrificing performance. Therefore, the only option in that regard was to move to a stacked, multi-board configuration, which would yield a reduction in the length and width of the system at the cost of increased

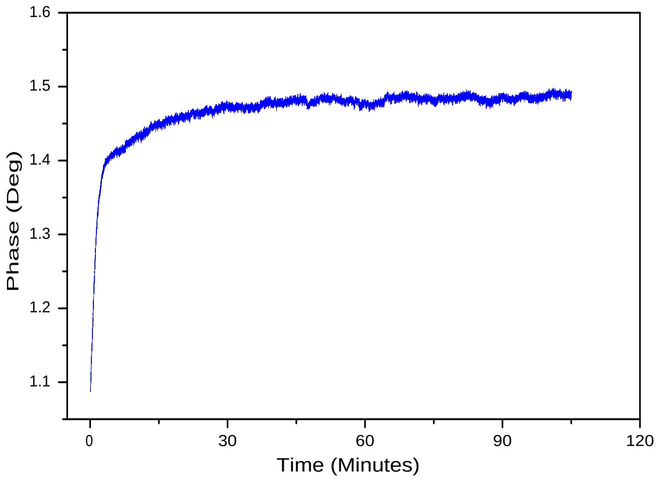

Figure 3.7: Warmup behaviour of system in loopback mode

height. Another option was to move away from the analog approach to a digital implementation, which would yield a significant reduction in size as much of the functionality performed by discrete components in the analog design could be implemented in software using a single processor. Estimates based on typical component footprint areas suggested that a reduction in board area by a factor of 2.5 - 3.5 was possible. A digital approach would also have a number of additional advantages such as insensitivity to harmonics/distortion, increased design flexibility due to software implementation and the option of performing intensity measurements if so desired. Given all of these factors, it was decided that a digital implementation was the best option.

3.3.2 Synchronous Demodulation

The standard technique for digital phase measurement, and that which is used by commercial instruments such as lock-in amplifiers (LIAs), is synchronous demodulation. The synchronous demodulation process is described in block diagram format in Fig. 3.8. The input signal is digitised using an ADC and the modulation waveform is generated using a DAC. The digitised input signal is multiplied by the reference waveform, which in this case is also the excitation waveform, and by a quadrature (90^O out of phase) copy of the reference waveform. The resulting signals are then lowpass filtered (Σ) and the outputs of the filters are used to calculate phase and/or intensity as described below.

The mathematical description of the synchronous demodulation process is as fol-

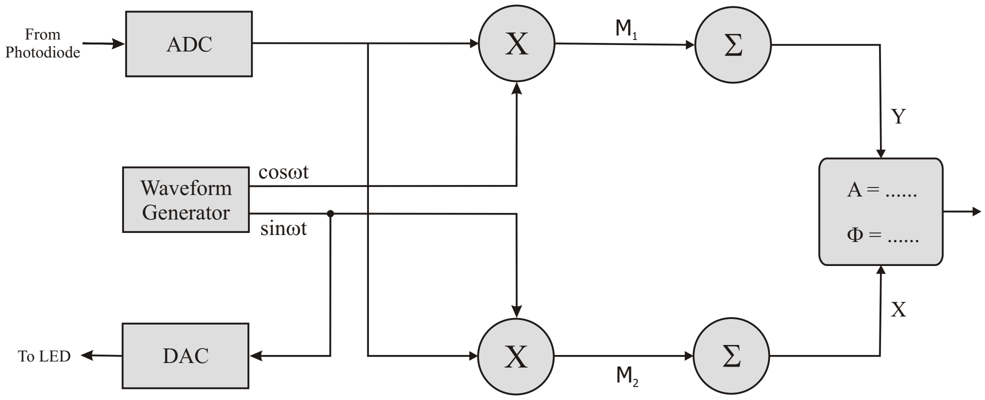

Figure 3.8: Block diagram of synchronous demodulation process.

lows: the signal waveform, $S(t)$, can be described by the expression

$$S(t) = A_s \sin(\omega t + \phi_s) + n(t) \tag{3.6}$$

where A_s and ϕ_s are the amplitude and phase of the luminescence induced signal, and $n(t)$ represents any component in the input signal that is not modulated at ω, which includes any noise present in the signal. The output of the $\sin(\omega t)$ multiplier, $M_1(t)$, is given by:

$$M_1(t) = A_s \sin\left(\omega t + \phi_s\right) \sin \omega t + n(t) \sin \omega t \tag{3.7}$$

Application of the 'product of sines' trigonometric identity yields:

$$M_1(t) = \frac{A_s}{2} \cos \phi_s - \frac{A_s}{2} \cos\left(2\omega t + \phi_s\right) + n(t) \sin \omega t \tag{3.8}$$

The lowpass filter, assuming ideal behaviour, eliminates the a.c. terms in this expression resulting in a filter output, Y, of

$$Y = \frac{A_s}{2} \cos \phi_s \tag{3.9}$$

A similar analysis on the quadrature arm yields:

$$X = \frac{A_s}{2} \sin \phi_s \tag{3.10}$$

The amplitude and phase of the luminescence-induced waveform can then be calculated from the values of X and Y using the expressions:

$$A_s = \sqrt{X^2 + Y^2} \tag{3.11}$$

$$\Phi_s = \tan^{-1}\frac{X}{Y} \tag{3.12}$$

3.3.3 System Development

The digital system was developed in conjunction with an external company (Innovada, Dublin) that had significant experience in the design and development of embedded systems.

3.3.4 System Description

A block diagram of the digital phase fluorometry system that was developed is shown in Fig. 3.9. It provides the same functionality as the analog system, including the use of a dual photodiode referencing strategy. It would have been possible to revert to dual LED referencing without sacrificing sampling rate performance through the use of multi-frequency techniques (see section 3.4). However, this would have represented a substantial change in design. It was deemed that this would have posed an unacceptable risk to the short timeline available for the development of the system, so it was decided to consider the implementation of this strategy in a future revision of the system. At the core of the system is a high performance 32-bit ARM7 micro-controller (LPC2134, NXP) capable of executing 60 million instructions per second (MIPS). This is interfaced with a dual channel, pseudo differential, 16-bit ADC (AD7655, ADI) for signal acquisition and a 12-bit DAC (AD5445, ADI) for modulation waveform generation. It was decided to place the photodiode amplifiers in a separate module that could

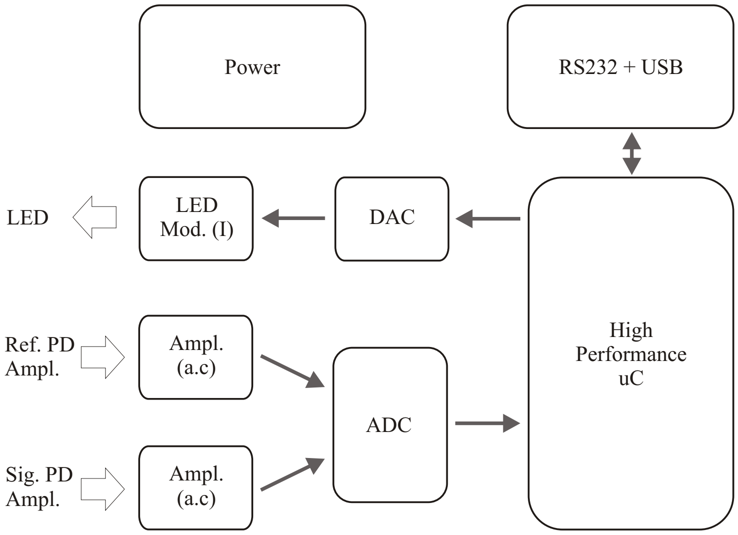

Figure 3.9: Block diagram of digital phase fluorometry system. The photodiode(PD) amplifiers are located off board.

be located in the optical assembly, thus further reducing the size of the main board. The input stage of the board consists of a pair of fully differential ac-coupled amplifiers. A differential configuration was used so that any noise that coupled into the leads connecting the photodiode amplifiers to the board would be removed by the common mode rejection action associated with differential operation. AC coupling was used to remove the potentially large dc signal caused by ambient light, thus facilitating the use of a 5V power supply system for the analog front end, which simplified system design. The system is equipped with both an RS232 and a USB interface. The USB functionality is provided by a serial to USB converter IC (TUSB3140, TI) and was included in order to avoid system compatibility issues.

3.3.4.1 System Timing and Clock Jitter

The sampling/update actions of ADCs and DACs are controlled with a clock signal that is typically derived from an external source. The jitter present in this timing clock is an important parameter from a system performance point of view as it adds in-band noise to the measurement signal that cannot be removed by the lock-in action of the synchronous demodulation process. The impact of ADC clock jitter is illustrated in Fig. 3.10. As a result, it is important that clock jitter be kept as low as possible. This precluded the option of controlling the clock directly using the processor core of the microcontroller, as precise timing of core operations cannot be guaranteed. Instead, a free running peripheral timer, which did not require core intervention, was used. Another option would have been the use of an external crystal driven clock source. However, this would have

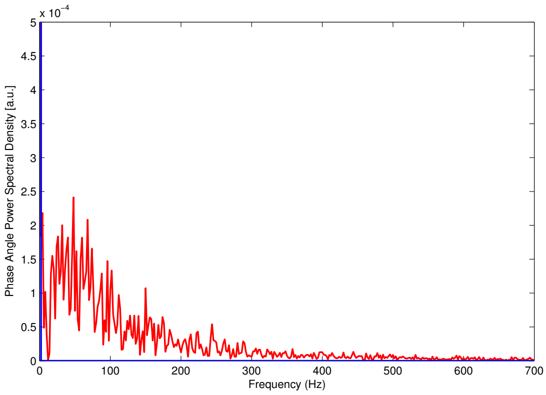

Figure 3.10: FFTs of calculated phase with and without ADC clock jitter. Random (or 'white') jitter, with a maximum value of 1 microsecond, has been added to the sampling clock. The corner frequency of the lowpass filter in the synchronous demodulation system was set to 100Hz. This data has been obtained using a fully functioning Matlab model of a synchronous demodulation-based phase measurement system.

prevented the sampling frequency from being changed easily should the need have arisen.

3.3.4.2 PCB Size and Schematics

The dimensions of the PCB are $56 \times 55mm$, which represented a factor of 4.4 reduction in board area over that of the analog system. Full circuit schematics are included in appendix B.2

3.3.5 Software and Algorithm Implementation

Software for the system was written in C and compiled using the open source GNU ARM toolchain [13]. An event-based architecture was used for high level control of the system, while time-critical actions, such as modulation signal generation and signal acquisition, were implemented using fast interrupts. The chosen microcontroller did not have hardware floating point support so all of the mathematical operations had to be carried out using fixed point arithmetic. Detailed descriptions of fixed point arithmetic can be found in [14] and [15]. Once the basic structures of a fixed point system have been put in place, the main consideration from a programming perspective is the much reduced dynamic range and associated risk of overflow of fixed point versus floating point arithmetic.

The system was designed to operate at a fixed modulation frequency of $20kHz$, with an ADC sampling rate of $100kSa/s$ and a DAC update rate of $200kSa/s$. The sampling and update rates were set as multiples of the modulation frequency to facilitate the use of look-up tables in the generation of of the required waveforms. The numerical values corresponding to one period of each of the required waveforms were calculated using Matlab and loaded into the memory of the microcontroller. The finite precision associated with fixed point arithmetic introduced distortion into the waveforms. This is not a problem for the modulation waveform. However, if the waveforms being used for the synchronous demodulation process are distorted, or in other words contain harmonics of the fundamental frequency, then the system will be sensitive at the harmonic frequencies also, which will degrade its performance. The precision-induced distortion in the waveform was found to vary as a function of waveform amplitude and phase, which implied that there were a set of optimum values of phase and intensity that would minimise distortion. A search algorithm was developed that scanned through the acceptable range of values of amplitude and phase and identified the optimum set of values. The algorithm was applied to the generation of both the excitation and synchronous demodulation waveforms, with the latter being optimised in tandem as they were required to have matching amplitude and phase values.

The synchronous demodulation algorithm described in Fig. 3.8 was implemented in discrete form, using a simple average-based lowpass filter. The multiplication and lowpass actions were carried out using the microcontroller's hardware multiply and accumulate (MAC) module, which was operated in 64 bit mode to avoid overflow problems. Discrete synchronous demodulation, with a summation-based lowpass filter can be described by the expressions:

$$M \cdot X = \sum_{n=0}^{M} A \sin\left[\frac{2\pi n}{N}\right] \cdot S\left[n\right] \tag{3.13}$$

$$M \cdot Y = \sum_{n=0}^{M} A \cos\left[\frac{2\pi n}{N}\right] \cdot S\left[n\right] \tag{3.14}$$

where M is the number of samples averaged to obtain one pair of X and Y values, thus defining the filter properties, N is the number of samples per period in the waveforms, and $S\left[\right]$ is the sample value. Division by M is not necessary as these terms cancel out when evaluating equation 3.12, thereby avoiding computationally intensive division operations, which must be carried out in software on the LPC2134. The summation-based filter is not the ideal choice from a performance perspective [16, 17]. However, it is much more computationally efficient than the other types of lowpass filters (e.g. Butterworth, Chebyshev) that could be used. The performance of the summation filter and that of a $3rd$ order type II Chebyshev lowpass filter with similar corner frequency parameters were compared using a Matlab simulation and it was found that the phase noise was approximately $12 - 15\%$ higher for the summation filter. As it will be seen later, computational efficiency was a key factor for the system so it was decided that a performance loss of this magnitude was acceptable.

Phase angle is evaluated from the lowpass filter outputs using equation 3.12. There was no library function in the gcc toolchain for evaluating $\tan^{-1}$ on fixed point systems however. Therefore, a custom function that was based on the well known CORDIC algorithm was implemented. Detailed information on the operation of the CORDIC family of algorithms can be found in [18, 19].

3.3.5.1 System Operation

As mentioned previously, the LPC2134 is capable of operating at 60MIPS. Processor overhead estimates, that were compiled during the feasibility stage, predicted that this would allow for continuous operation of the system. However, it was found during early stage testing that this was not the case. The problem was traced to an error in the overhead calculations, which saw the overhead associated with data memory access being omitted. The only means of overcoming the problem without upgrading the processor and designing a new PCB was to use discontinuous operation. Block-based operation, as described graphically in Fig. 3.11 was implemented. System operation is broken into three phases. In the first phase, blocks of sensor data are acquired for both the signal and reference channels and stored in memory. This is followed by a data processing phase in which the synchronous demodulation algorithm is applied to the stored data. In phase three, the phase angle is calculated, the temperature sensor value is obtained, and the data is transmitted via RS232/USB to the host PC. The final action in this phase is to process any commands that may have been received from the user. The blocks of data are 2000 samples long, which corresponds to a measurement window of $20ms$. The block length was chosen to correspond to an integer multiple of waveform periods to avoid increased phase measurement noise due to edge effects.

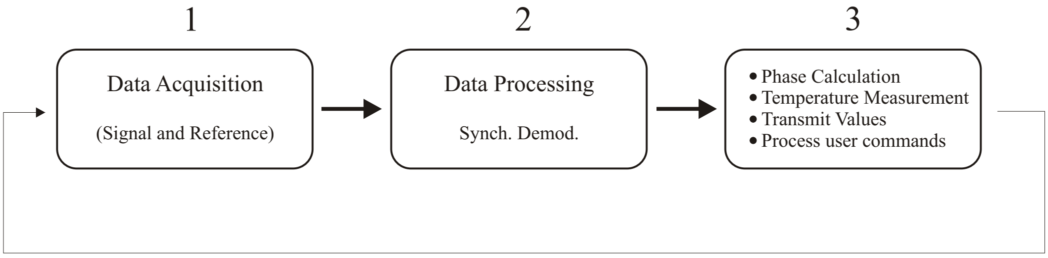

Figure 3.11: Flow diagram of high level operation of system. Block-based discontinuous operation was necessary due to processor constraints

3.3.6 Performance

The performance of the system was quantified in the same manner as was that of the previous system, namely through the use of loopback tests and tests with the remote configuration optical probe.

3.3.6.1 Resolution

The resolution of the system was evaluated in loopback mode, by measuring the peak-to-peak noise in the output signal for an input signal amplitude of $2V_{p-p}$. The value that was obtained is listed in Table 3.3. The resolution of this system shows a factor of three improvement compared to that of the analog system (see Table 3.1). This indicates that the baseline noise performance of the DSP system is superior to that of the analog system.

The resolution values obtained with the optical front-end for a range of signal intensity values are shown in Table 3.4. The range of values that was used was

Resolution (°)
0.003

Table 3.3: Phase measurement resolution in loopback mode with a signal amplitude of $2V_{p-p}$

the same as that used for testing the analog system, allowing the performance of both systems to be compared. When this data is compared to that which was obtained with the analog system it can be seen that both systems have the same resolution for high signal amplitudes but that the resolution performance of the digital system drops off more quickly than the analog system at reduced signal levels. The reason for this is not immediately clear, however, it is possible that the non-continuous operation of the digital system has a negative impact on resolution for low signal amplitudes.

Amplitude *V*	Resolution *Deg.*
0.01	6.801
0.02	3.269
0.05	1.283
0.10	0.591
0.20	0.271
0.50	0.079
1.00	0.027
2.00	0.018

Table 3.4: Phase resolution for a range of signal amplitudes. The amplitude was varied by changing the distance of the fluorescent spot from the optical front-end.

3.3.6.2 Drift

The warm-up profile of the system was evaluated in loopback mode and is shown in Fig. 3.12. In theory, the reference channel should cancel out the component-induced drift completely. However, there is still considerable warm-up drift in the measured phase angle following compensation. This can be attributed to component mismatch and non-uniform thermal gradients across the analog components of both input channels. There was scope to improve the drift performance of the system through judicious component selection. It was deemed that the warm-up drift exhibited by the system was adequate for the application for which it was intended, however, and as a result no changes were made to the components that were used.

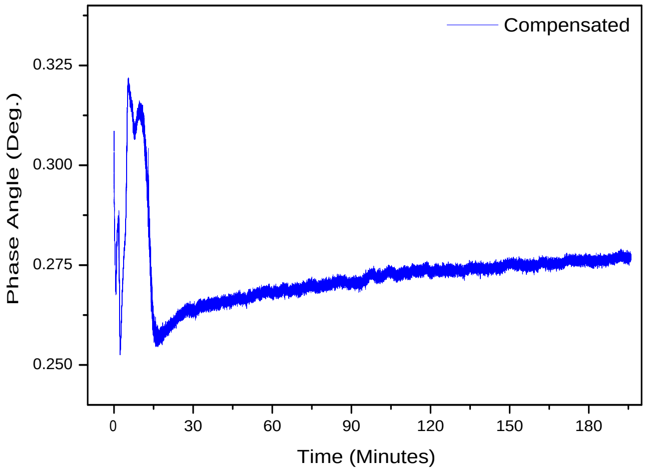

Figure 3.12: Warm-up Profile of Digital Phase Fluorometry System in Loopback Mode.

3.3.7 Module Design

The system was designed to be used as a portable battery-powered system for the measurement of oxygen in breath. To this end, a suitable enclosure for the system had to be sourced and a suitable battery had to be identified.

There are a wide range of battery technologies on the market at present, each with its own specific advantages and disadvantages. The first decision that had to be made was whether to opt for a rechargeable or non-rechargeable battery. The estimated run time from the range of battery sizes that were being considered was 4 to 6 hours. Therefore, in the interests of reducing costs, it was decided to opt for the rechargeable option. There are 4 main rechargeable battery technologies: lead acid, Nickel-Cadmium (NiCad), Nickel Metal Hydride (NiMH) and Lithium ion/Lithium polymer(Li-ion/LiPo). Lead acid batteries have the lowest energy density and were discounted on those grounds. NiCad and NiMH batteries have intermediate capacities but display significant self-discharge rates and are susceptible to memory effects. Li-ion batteries have the highest capacities of all of the technologies, and the lowest self-discharge rates, with the only drawback being that they require the use of battery supervision circuitry to ensure safe operation. Li-ion battery packs that contain built-in protection circuitry are widely available which means that they are now as convenient to use as any other battery technology and are therefore the obvious choice. The board requires an input voltage of $8V$ so a $10.8V$ battery pack was chosen. The battery pack, model no. 2008, from batteryspace.com has a capacity of $2400mAh$, which gives an operating time of approximately 6 hours. In order to avoid any problems due to varying supply voltage as the battery discharged, an $8V$ linear regulator was placed between the battery and the circuit.

As it was required that the system be wearable, a suitable, belt-mountable enclosure was sourced. The ERGO S (p/n B7005107), from OKW Enclosures, UK was found to be a suitable choice. The assembled system can be seen in Fig. 3.13. The switch that is visible on the top surface switches between “powered-on” and “charging”.

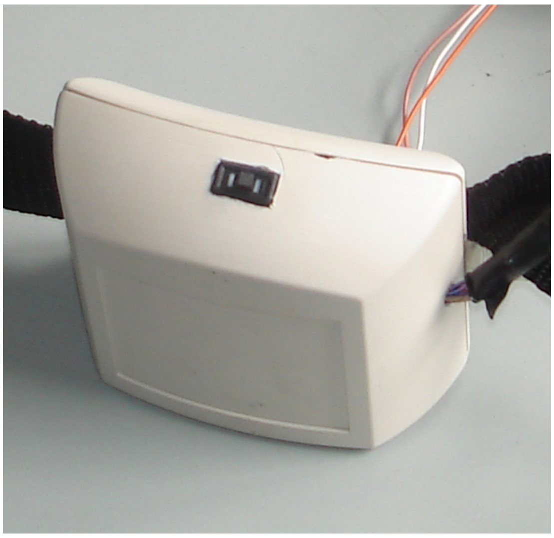

Figure 3.13: Battery powered digital phase fluorometry system in a belt-mountable housing.

3.4 High Performance DSP System

A system with added functionality was required for a range of sensing applications, all of which are described in detail in the following chapters. The required additional features were:

1. Intensity measurement capability
2. Simultaneous multi-frequency operation
3. Simultaneous operation of multiple excitation sources

A digital implementation, using the system described previously as a starting point, was the obvious choice as it would yield maximum performance and design flexibility, while minimising system size. There was considerable scope for improvements over the existing system. The use of a more powerful floating point processor would facilitate continuous operation, the use of increased ADC and DAC sample and update rates, and would allow a move away from the restrictive fixed point arithmetic that had to be used previously. Additional processing power would also allow the implementation of realtime user control of operating parameters, such as excitation frequency and intensity, and would allow the operating mode of the system to be changed easily. There was also scope to improve the system from an analog perspective through the use of higher resolution and performance ADCs and DACs, and the use of higher performance components in the signal path.

The range of target applications is quite diverse, with some requiring quite different functionality. The ideal situation would see the development of a number of small portable systems, each tailored to a particular application, as portability is desirable in all cases. This was not feasible, however, so it was decided to develop an all-in-one lab-based system and to make stripped down versions of this system, with only the required functionality, as the need arose.

3.4.1 System Description

A high level block diagram of the lab-based system, which can also be considered as a generic development platform, is shown in Fig 3.14. At the heart of the system is a high performance floating point Digital Signal Processor (DSP). The system has 4 LED modulation channels, two input channels with integrated photodiode amplifiers, extensive auxiliary sensor support, and provides support for RS232, USB and RF-based serial communications.

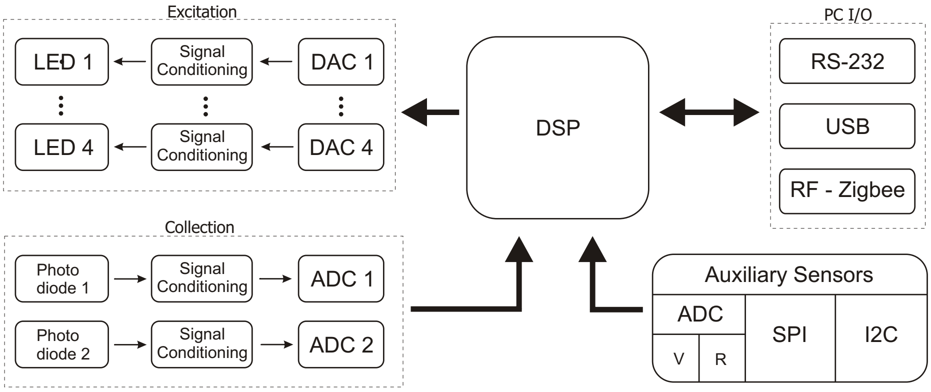

Figure 3.14: High performance laboratory-based measurement system

Digital signal processors differ from standard processors, such as those found in PCs, in that they are designed specifically to perform mathematical operations at high speeds and throughput rates, and often contain hardware accelerator modules for the most common mathematical operations found in digital signal processing applications (e.g. digital filters, FFTs). Given this and the computationally intensive nature of the synchronous demodulation algorithm, a DSP was deemed to be the best choice for the system. There are a wide range of DSPs available, with a correspondingly wide range of operating parameters. In terms of processing power, it was decided to opt for a device at the upper end of the performance spectrum in order to provide maximum design freedom and reduce the possibility of processor capacity limiting the overall performance of the system, as was the case with the previous system. It was also decided to opt for a device that possessed an extensive range of peripherals (e.g. UART, SPI, memory interface), in order to simplify the system design process by eliminating the need for companion ICs and glue logic. The chosen device, the SHARC ADSP-21369, from Analog Devices, met these criteria. It is a high-end 32/40 bit floating point device that is capable of operating at $2400MFLOPS$ (Million Floating Point Operations per Second). It possesses all of the required peripherals (SPI, UART, DSP serial ports, GPIO) as well as an external memory interface with support for multiple memory types, and a precision clock generator, which would be useful for ADC and DAC clock generation.

Detailed diagrams of the system are shown in Fig. 3.15 and Fig. 3.17. Only one excitation and collection channel are shown in the interests of clarity.

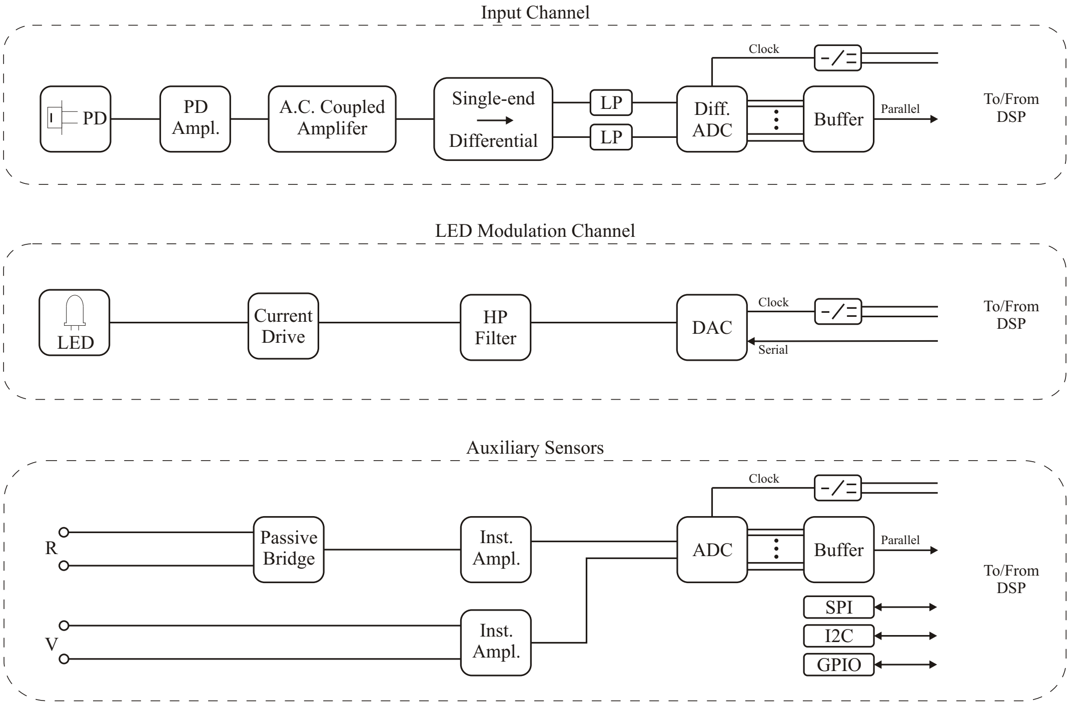

Figure 3.15: Detailed diagrams of analog interface sections of design.

3.4.1.1 Analog Circuitry

Input Channel The signal channels make use of a fully differential 18 bit ADC (AD7643, ADI). A fully differential ADC was chosen in order to reduce the thermal drift experienced by the previous design. A differential ADC has two closely matched input stages, one for each 'side' of the signal, which results in any thermally induced changes that occur being cancelled out. This is in contrast to single-ended or pseudo-differential devices, which only have a single input stage. By the same reasoning, it can be seen that anti-aliasing lowpass filters can be used without introducing additional thermal drift, as a filter must be used for each input, resulting in their effects cancelling out. The only requirement is that the components used be as closely matched as possible.

The remainder of the signal channel consists of the same photodiode amplifier that was used previously, an ac-coupled amplifier connected in ground sensing mode, and a low noise high-performance single-end to differential converter, which also acts as the ADC input buffer. A design level analysis of the analog input stage reveals that the only sections of the circuit capable of introducing significant phase changes due to thermally-induced changes in component parameters are the various RC stages, namely the ac-coupling stage at the input of the differential amplifier and the anti-aliasing filter at the input of the ADC. AS discussed above, the use of a fully differential ADC prevents the anti-aliasing filters from introducing thermal drift, which just leaves the ac-coupling RC filter. The phase shift, Φ_{HP}, introduced by the ac-coupling RC filter, which can be considered to be a simple first order high pass filter is given by:

$$\Phi_{HP} = \tan^{-1}\left(\frac{1}{\omega RC}\right) \tag{3.15}$$

while its corner frequency is given by:

$$f_c = \frac{1}{2\pi RC} \tag{3.16}$$

From equation 3.15, we see that the induced phase shift is reduced by increasing the RC value of the filter, or, in other words, by moving its corner frequency away from the modulation frequency being used by the system. Reducing Φ_{HP} also reduces the absolute magnitude of any changes in the signal phase angle caused by temperature-related changes in R and C. As a result, R and C were set to the largest values feasible. The benefit of doing this was further augmented by using low temperature coefficient components.

Excitation Channel All four excitation channels are identical and make use of a 16 bit current mode DAC (DAC8812, TI). The resolution of a DAC has a direct impact on the harmonic distortion in its output that is caused by its finite precision. This is illustrated in Fig. 3.16. Harmonic distortion in the output was of no concern in the previous system as it only used a single modulation frequency.

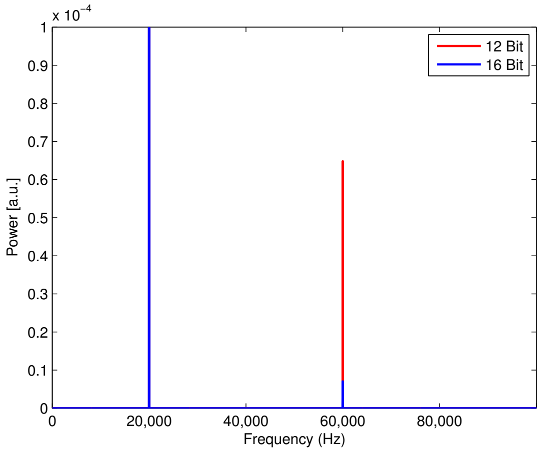

Figure 3.16: The harmonic distortion in the outputs of a 12 bit and 16 bit DAC. The distortion is caused by the finite precision of the device. This data was generated using a Matlab model. Noiseless waveforms were used in the interests of clarity.

This system, however, was required to use multiple modulation frequencies so the minimisation of harmonic distortion was desirable in order to avoid the situation where certain frequencies were 'out of bounds' due to the presence of harmonics.

Another factor that had to be taken into account was DAC settling time. DACs take a finite amount of time to settle at the final output value and this settling time introduces a phase shift in the output waveform. Minimisation of this phase shift is desirable in order to minimise thermal drift and to achieve close matching of the excitation channels in the presence of thermal gradients on the PCB. A current output DAC was chosen as it has a shorter settling time than its voltage output counterpart. The remaining components of the excitation channel are a high pass filter and a current drive stage. The high pass filter is included in order to reduce the amplitude of the DAC switching frequency component present in the LED modulation signal, as it has been found to lead to intermittent instability in the current drive stage.

Auxiliary Sensors Support is provided for a wide range of auxiliary sensors in order to maximise the useability of the system. Analog sensor support is provided using a 4 channel 16 bit ADC (AD7655, ADI), with 2 channels being used for passive resistive-type sensors, and two channels being used for active, voltage-output sensors. The resistive sensor channels use a Wheatstone bridge configuration to drive the sensor, with the resulting signal being amplified using a dual channel instrumentation amplifier. Voltage mode sensors connect directly to the inputs of a second dual channel instrumentation amplifier, with the systems analog rails being made available for powering the sensor. The DSPs SPI and I2C ports, as well as a number of general purpose input/output (GPIO) pins, were made available for use by digital sensors, which are becoming increasingly commonplace.

3.4.1.2 Digital Circuitry

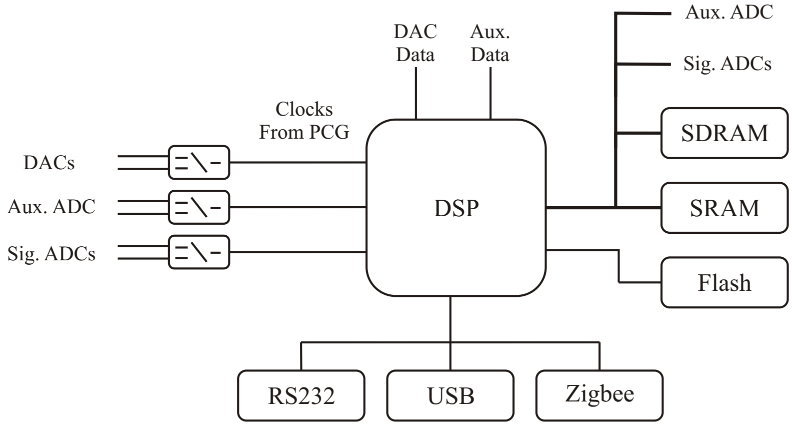

Figure 3.17: Detailed diagram of digital section of design.

The digital circuitry of the board consists of the DSP, memory (SDRAM, SRAM and Flash), the serial interface circuitry, clock distribution circuitry, and a processor supervisor IC that implements power supply-quality monitoring functionality for the DSP. SRAM and SDRAM has been included to expand upon the processors internal memory, while the flash memory is used as the boot device for the system, as well as for the storage of system configuration information. The DSP has two RS232 compatible serial ports that are used to implement serial communications. One port is provided as a dedicated RS232 port, while the other is shared between USB and Zigbee circuitry. USB support is provided using a serial to USB converter IC (TUSB3410, TI), while a connection socket is provided to allow the use of a member of the family of XBee OEM Zigbee modules to be used to implement RF communications.

Interfacing with the ADCs and DACs The DSP's external memory port is used to interface with the ADCs while two of the devices DSP serial ports are used to interface with the DACs. The external memory bus was used to connect to the ADCs to simplify the code development process as this means of connection results in the ADCs being mapped to a location in the DSPs memory, allowing for very simple data retrieval. The only negative aspect of this approach is the increased PCB area occupied by the parallel connection. A serial interface was used for the DACs partly due to the lack of availability of a suitable device, but also to reduce PCB area.

Clock Sources and Distribution As discussed in section 3.3.4.1, it is important that ADC and DAC clock jitter be kept at a minimum. The ADSP-21369 is equipped with a precision clock generator (PCG), which can be used to generate low jitter, precision clocks for demanding applications and this was used to generate all of the clock signals required by the system. The use of the PCG over a stand-alone alternative also has the advantage that clock rates can be easily changed by the user. A high accuracy temperature-compensated oscillator was used as the clock source for the PCG unit, in order to minimise drift in the modulation frequencies generated by the system. In high speed digital systems, clock distribution requires careful attention as the coupling of spurious pulses onto a clock line can dramatically reduce the performance of a sampling-based system [20, 21]. To prevent this, a differential clock distribution strategy was implemented, which saw the single-ended clock signal generated by the PCG being converted to a differential signal as close as possible to the DSP, and then being routed to the vicinity of the relevant device, where it was converted back into a single-ended signal. The use of differential transport also preserves the quality of the clock signal as it is routed across the analog and digital ground plane divide.

3.4.1.3 PCB Layout

Given the component density of the system and the high speeds of some of the signals, good PCB design and layout was critical. The PCB design process saw the application of the standard high speed design principles, which are covered extensively by Johnson [3] . The result was an 8 layer, impedance-driven design that utilised a split power and ground plane topology. Careful attention was paid to power supply decoupling and the avoidance of crosstalk. A diagram of the PCB layer-stack is shown in 3.18. The PCB has 2 ground planes, two power planes and 4 signal layers (the top and bottom of the board and 2 internal layers). Various layer configurations are possible, with this variation being chosen as it optimises crosstalk performance at the expense of having to use additional decoupling capacitors [3], which was not a problem in this design. Split power and ground planes were used, thereby providing separate regions for the analog

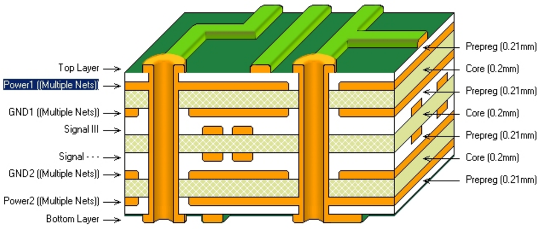

Figure 3.18: The layer-stack of the high performance DSP system PCB

and digital circuitry, and each of the LED drive stages.

Parallel Buffers Buffer ICs (see Fig. 3.15) were used to connect the ADCs to the memory bus in order to prevent high speed switching noise from the bus being coupled onto the ADC die, where its presence during the conversion process would have led to increased noise.

Full schematics of the system can be found in appendix B.3.

3.4.2 Software

Custom software was designed and written for the system by the author and a colleague at the OSL using the VisualDSP 5.0 development environment from Analog Devices. The high level structure of the software was hierarchical in nature. The highest priority, time-critical operations were implemented using interrupts with the remaining tasks to be performed by the system being arranged in decreasing order of importance. An event-based structure, as was used in the previous system, was not required.

Multi-frequency Synchronous Demodulation The system was required to be capable of performing synchronous demodulation at multiple frequencies simultaneously, using one or more excitation channels. This was possible due to the lock-in nature of the synchronous demodulation process and the resulting narrow measurement bandwidths [12]. From an implementation perspective, all that is required is that the synchronous demodulation algorithm be applied to the input signal at each of the modulation frequencies present.

To facilitate runtime user control over modulation frequency and intensity values, the modulation waveforms, and associated quadrature waveforms required for synchronous demodulation, had to be generated at runtime by the DSP. For single frequency modulation waveforms, a look-up table approach, similar to that used in the previous design, could be implemented quite easily. However, the use of multi-frequency modulation waveforms requires the construction of composite waveforms, comprised of the required modulation frequencies. A typical multi-frequency composite waveform is shown in Fig. 3.19. The use of a look-up table-based approach for modulation waveform storage was not feasible due to the potentially large size of the possible composite waveforms. Generation of the waveforms on the fly, which would involve the evaluation of multiple sine values, would have been computationally intensive and a drain on resources, so a partial look-up table-based approach was implemented. This saw the population of single period look-up tables, or wavetables, for each of the modulation waveforms constituent frequencies, with these values then being summed on the fly using

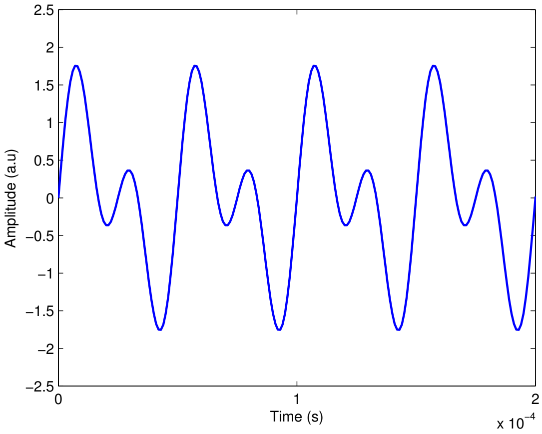

Figure 3.19: Composite waveform with equal amplitude components at 20 and $40KHz$

circular buffer techniques to produce the composite waveform. This approach represented the optimum compromise between system flexibility and computational efficiency, and had the added advantage that the wavetables could be used in the synchronous demodulation process.

As discussed in section 3.3.5, the use of an IIR filter to implement the low-pass filter operation of the synchronous demodulation process will result in a $12-15\%$ reduction in phase measurement noise compared to a summation-based approach. As a result, a range of IIR-based filters that were designed using the MAtlab filter design toolbox were implemented and tested. Good results were obtained for corner frequencies $> 100Hz$, however, corner frequencies lower than this value resulted in filter instability. This was a problem as corner frequencies of $< 1Hz$ were required for some of the applications for which the system was to be used. It was found that the issue was caused by quantisation errors in the filter coefficients. Time constraints prevented the investigation of possible work-arounds for this problem, such as down-sampling or the use of alternative filter implementations, and instead, a summation-based approach was used.

User Control From a user interface perspective, it was required that the user have full control over all of the operating parameters of the system. These are as follows:

1. Number of active input channels
2. Number of active excitation channels
3. Number of modulation frequencies (For each active channel)
4. Modulation frequency value(s)
5. Modulation intensity value(s)
6. Phase measurement status (For each modulation frequency)
7. Intensity measurement status (For each modulation frequency)

8. Synchronous demodulation corner frequency
9. Number of active auxiliary sensors

A serial parser and command line interface has been written to receive and process any commands received from the user interface. Real-time user control of all of the above parameters has been implemented successfully. The values of all of the systems parameters and configuration settings are stored to flash memory, which is non-volatile, thereby allowing the system to restart using its previous settings at power-up.

3.4.3 Performance

The performance of the system was assessed in loopback mode, as was the case with the previous analog and digital systems. The remote mode optical probe was no longer available and while data could be obtained using an alternative optical assembly, it would not have been possible to compare it to the results obtained for the previous systems. For this reason, the performance of the system at multiple luminescence intensities was not evaluated.

3.4.3.1 Resolution

The system is capable of performing phase and intensity measurements so the resolution of both were determined in loopback mode using a signal amplitude of $2V_{p-p}$. the values that were obtained are listed in Table 3.5 The phase measurement resolution of the system corresponds to a factor of three improvement over that of the previous system. Signal-to-noise ratio is commonly used to assess the quality of intensity-based measurements. The signal-to-noise ratio (SNR) of a voltage signal, in decibels, is given by the expression:

Meas. Type	Resolution
Phase	0.001°
Intensity	$41\mu V$

Table 3.5: Intensity and phase resolution in loopback mode with a signal amplitude of $2V_{p-p}$ and a measurement interval of $20ms$.

$$SNR(dB) = 20\log_{10}\frac{A_s}{A_n} \tag{3.17}$$

where A_s and A_n are the rms values of the signal amplitude and noise, respectively. Using equation 3.17 with the values presented in Table 3.5 results in a SNR value of $103dB$.

3.4.3.2 Warm-up Drift

This system is capable of operating in both dual LED or dual photodiode referencing modes. As discussed in section 7.2.4, dual LED mode is preferable, and can be used with this system without any reduction in system performance due to its multi-frequency capabilities. As a result, the performance of the system was not assessed in dual photodiode mode, as there are no circumstances under which it would be used in this manner. Dual LED mode is difficult to assess using a loopback configuration as a voltage adder would have to be used to add both signals, which would introduce noise and lead to false resolution measurements. The uncompensated warm-up drift of the system, which was obtained by connecting one output channel in loopback, is shown in Fig. 3.20. There is a substantial reduction in the amplitude of the warm-up drift compared to both of the previous systems. The uncompensated warm-up drift is a factor of fifteen lower than the compensated warm-up drift of the previous system, and the compensated drift will be even lower still. Given the degree of uncompensated warm-up drift that is present, it is possible that compensation may not even be required in certain situations.

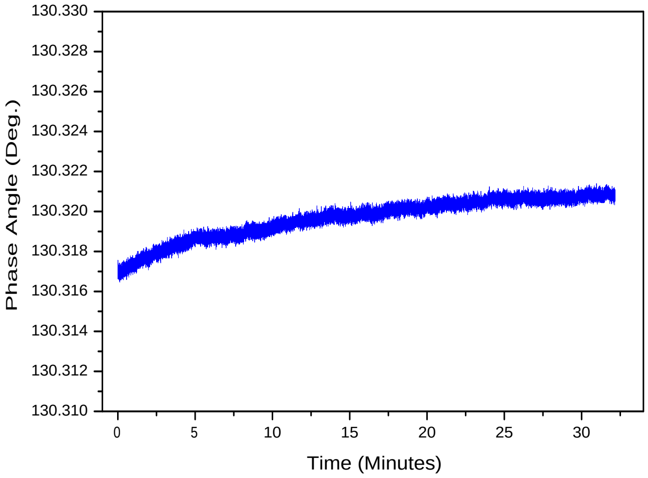

Figure 3.20: Uncompensated warmup of DSP-based system. The change in signal levels over the first 30 minutes of operation is $3mDeg$.

Warm-up Drift with Optoelectronic Components Up to this point, the warm-up drift of the electronic systems that have been developed was characterised using a loopback technique that did not involve the use of optoelectronic components. The optoelectronic components were excluded in order to obtain a measure of the warm-up drift of the system itself that was not influenced by the characteristics of the optoelectronic components that were used. This facilitates accurate comparison of the performance of each of the systems, however, it does not provide a realistic measure of the drift that will be observed in real applications. The warm-up profile of the DSP-based system using a $[Ru(dpp)_3]^{2+}$ based sensor that was exposed to ambient oxygen levels is presented in Fig. 3.21. The sensor film was located in an enhanced capture optical probe (Probe 1 - see section 4.1) and the DSP system was operated in dual-LED referencing mode. The warm-up drift is approximately 0.03°, which is a factor of ten greater than the loopback warm-up. It is likely that this is due to mismatch between the thermal properties of the signal and reference LEDs. The warm-up time is $< 1min$, which implies that the warm-up drift displayed by the system will not cause problems during operation.

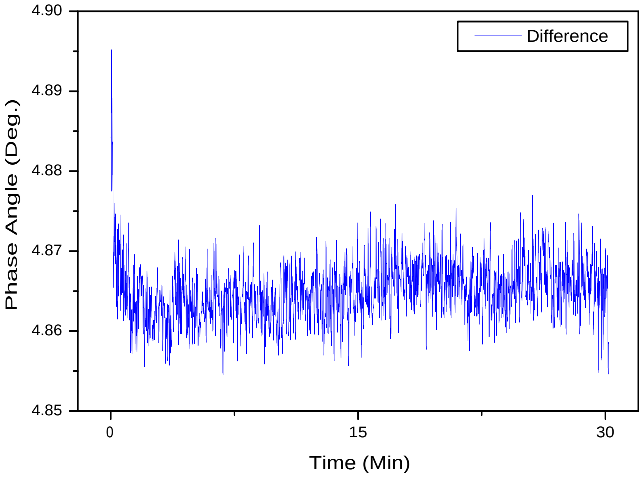

Figure 3.21: The warm-up profile of the DSP-based system for an oxygen sensor that was exposed to ambient oxygen levels. Dual-LED referencing was used.

3.5 Conclusions and Future Work

Three instrumentation electronics systems were designed over the course of this work. The first of these was an analog phase fluorometry system that was designed for use in a number of oxygen sensing applications including real-time breath oxygen measurement and dissolved oxygen measurement. One of the key design features of this system was the use of dual photodiode referencing, which facilitated the sampling rates necessary for the breath monitoring application. The second system that was developed was a digital implementation of the first and was designed with reduced size in mind. The end result was a battery powered, belt-mountable device that was suitable for use as a portable breath oxygen measurement system. The third system built on the digital foundations that were introduced with the second and was designed to have substantially increased functionality and improved performance compared to the two previous designs and any of the systems that were available commercially or reported in the literature. It is based around a high performance DSP and is capable of operating in intensity, phase and ratiometric intensity measurement modes. It has multiple excitation and emission channels and is capable of multi-frequency operation. Each of the systems have been applied to a number of sensing applications. The resulting sensor systems are described in chapters 6, 7 and 8.

A number of elements of future work are planned, all of which concern further development of the DSP-based system. The first of these is to design a reduced-functionality, reduced-size version of the system for portable use in applications such as breath monitoring. This process will include the implementation and testing of Zigbee-based wireless communications.

The possibility of using IIR-based filters in the implementation of the synchronous demodulation algorithm will be revisited. While perfectly adequate results were obtained using an averaging-based approach, the use of IIR-based filters would result in reduced noise, as was determined during the design of the digital phase fluorometry system.

Bibliography

[1] C. McDonagh, C. Kolle, A. K. McEvoy, D. L. Dowling, A. A. Cafolla, S. J. Cullen, and B. D. MacCraith. Phase fluorometric dissolved oxygen sensor. *Sensors and Actuators B: Chemical*, 74(1-3):124–130, 2001.

[2] Christian Kolle. *Development and evaluation of a phase fluorometric instrument for different luminescence based optical oxygen sensor applications.* Ph.D. Thesis, University of Leoben, 1999.

[3] Howard W. Johnson and Martin Graham. *High-speed digital design : a handbook of black magic.* Prentice Hall, Englewood Cliffs, N.J., 1993.

[4] Bruce Archambeault. *PCB design for real-world EMI control.* Kluwer Academic, Boston, 2002.

[5] Considerations for mixed signal circuit board design. *Application Note AN-404.* Analog Devices Inc.

[6] Susan Pratt. Sensor PCB Design Guidelines for the AD7142 and AD7143 Capacitance-to-Digital Converters. *Application Note AN-854*, 2007. Analog Devices Inc.

[7] LT1016 Ultrafast Precision 10ns Comparator. *Datasheet*, 1991. Linear Technology.

[8] PCB Design Guidelines for Reduced EMI. *Application Note SZZA009*, 1999. Texas Instruments.

[9] J. R. Lakowicz. *Principles of Fluorescence Spectroscopy, 3rd ed.* Springer, New York, 2006.

[10] Jon S. Wilson. *Sensor technology handbook.* Elsevier, Amsterdam; Boston, 2005.

[11] Eric W. Weisstein. *Confidence Interval.* From MathWorld–A Wolfram Web Resource., `http://mathworld.wolfram.com/ConfidenceInterval.html`.

[12] M. L. Meade. *Lock-in amplifiers : principles and applications.* P. Peregrinus on behalf of the Institution of Electrical Engineers, London, 1983.

[13] *GNU ARM Toolchain.* `http://www.gnuarm.com/`.

[14] Randy Yates. *Fixed-Point Arithmetic: An Introduction.* Digital Signal Labs, `http://www.digitalsignallabs.com`.

[15] Erick L. Oberstar. *Fixed-Point Representation and Fractional Math.* Oberstar Consulting, `http://www.superkits.net/.../Fixed%20Point%20Representation%20\&%20Fractional%20Math.pdf`, 2007.

[16] Walt Kester. *Mixed-signal and DSP design techniques.* Newnes, Amsterdam; Boston, 2003.

[17] Steven W. Smith. *The scientist and engineer's guide to digital signal processing.* California Technical Pub., San Diego, Calif., 1997.

[18] Herbert Dawid and Heinrich Meyr. *CORDIC Algorithms and Architectures*, chapter Chapter 22. Digital Signal Processing for Multimedia Systems. Marcel Dekker Inc., New York, 1999.

[19] Steve Kilts. *Advanced FPGA design : optimizing for performance and reliability.* Wiley, Hoboken, N.J., 2007.

[20] AD7643 18 bit analog to digital converter. *Datasheet.* Analog Devices Inc.

[21] Jack G. Ganssle. *Embedded hardware.* Elsevier/Newnes, Amsterdam; Boston, 2008.

Chapter 4

Optical Sensor Platforms

4.1 Overview

An optical probe that yields enhanced sensor performance through the exploitation of anisotropic emission was designed and developed previously at the Optical Sensors Laboratory at DCU by a group of researchers that included the author [1]. An improved design, with increased robustness and which is capable of ratiometric mode operation was developed as part of this work. The design also addresses a number of performance and useability related issues including bubble formation in dissolved applications and the ability to use thicker sample substrates.

The next stage in this work was the design of an enhanced capture element for use in general sensing applications. The basic concept was that the design restrictions imposed on previous element designs due to their parallel use in biosensing applications could be relaxed to achieve increased collection efficiency in general sensing applications. A design process was developed that saw the combined use of ray tracing and optimisation techniques, which resulted in the identification of a capture element geometry that significantly increased capture efficiency over previous designs.

Four probe designs are discussed in the following sections. To avoid confusion both here and in the rest of the thesis, each design has been assigned a label. The original design, as described in [1], is referred to as ‘Probe 1’. The waterproof version of this design is labelled as ‘Probe 2’. The design improvements were implemented in two stages, resulting in two discrete optical probe designs. The first saw the adaptation of the original design for ratiometric-based operation, resulting in ‘Probe 3’. The second stage saw the implementation of all the additional design enhancements alongside ratiometric mode operation. This design is referred to as ‘Probe 4’. The labels that are used are listed in Table 4.1 for reference purposes.

Description	Label
Original Design	Probe 1
Original Design - Waterproof	Probe 2
Ratiometric mode adaptation	Probe 3
Final Design	Probe 4

Table 4.1: The labels that have been assigned to the various optical probe designs that are referred to in this chapter

4.2 Enhanced Capture Probe

The original probe design (Probe 1) uses a parabolic optical element to achieve enhanced luminescence capture. As described in section 2.5.1, luminophores located close to a dielectric interface exhibit an anisotropic emission profile, with the majority of the emitted light being radiated into the higher refractive index medium. The parabolic element, which was designed previously by a co-worker, T. Ruckstuhl, for use in bio-sensing applications, exploits this emission profile to capture a large proportion of the emitted luminescence. A schematic cross-section of the element is shown in Fig. 4.1.

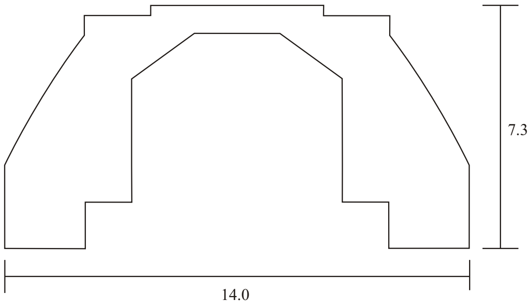

Figure 4.1: Schematic of parabolic element. The element is manufactured from Zeonex (grade 480R), a cyclic olefin polymer with high transmittance and low autofluorescence characteristics. [2]

If luminescent material is placed at the focal point of the parabolic section of the structure, then the substrate radiated luminescence from a small area located at the focal point will undergo total internal reflection at the sides of the element and emerge from its base as a collimated beam. The section of the paraboloid present in the element has been selected to coincide with the peak in the anisotropic emission profile, thus maximising luminescence capture. The process is depicted in the ray trace diagram in Fig. 4.2. The geometric structure in the diagram is a simplified version of the parabolic element. The rays originate at the focus of the paraboloid and are randomly distributed over the angular range of $55° - 75°$.

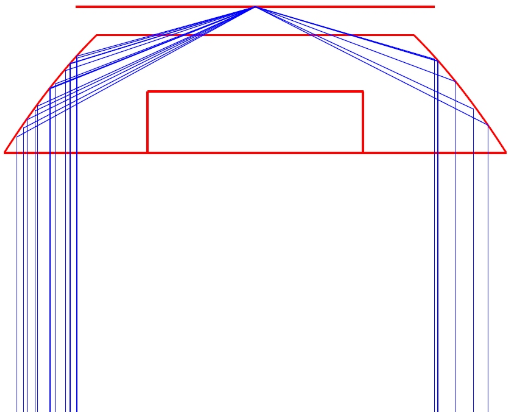

Figure 4.2: Ray trace diagram detailing the action of the parabolic element.

4.2.1 Probe Design

A diagram of the second generation of the original sensor probe design (Probe 2), which is fully waterproof and incorporates a thermistor for ambient temperature measurement, is shown in Fig. 4.3.

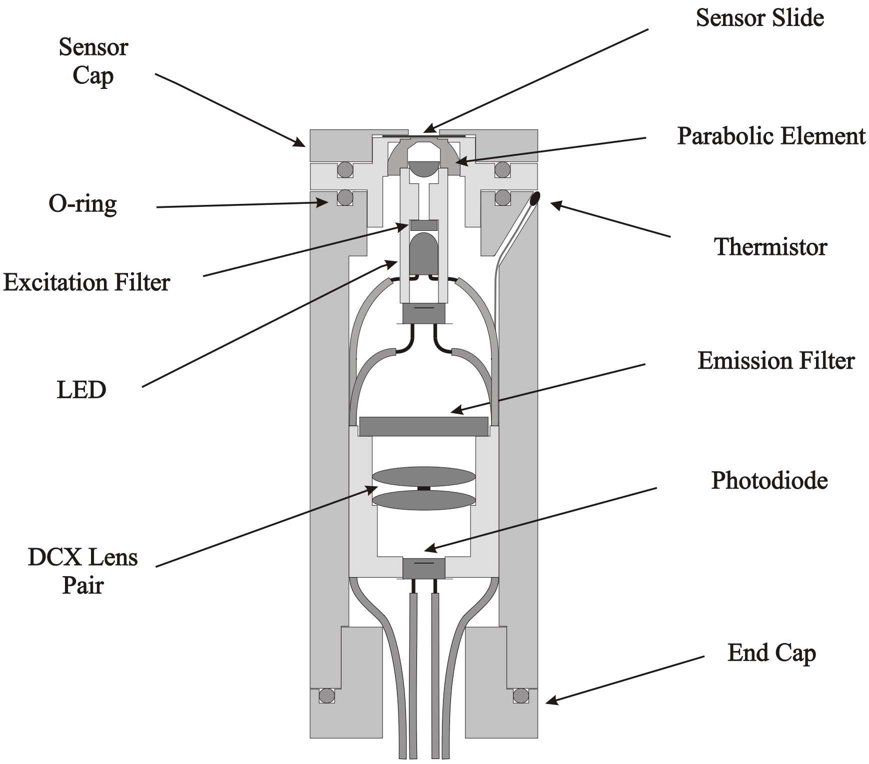

Figure 4.3: The second generation optical sensor probe, which is fully waterproof. This design is referred to as 'Probe 2'.

The probe is an all-in-one system, enabling both luminescence excitation and collection. It has been designed to be used with a $5mm$ LED as the excitation source and a Si-PIN photodiode as the collection element. One of the motivating factors behind the design of the probe was to achieve high performance while using low cost optoelectronic components, thereby making the resulting sensor systems attractive from a commercialisation perspective.

The analyte-sensitive luminophore used is immobilised in a solgel matrix that is deposited on a glass coverslip, which, in turn, is mounted in a detachable sensor cap that screws onto the sensor probe. A small quantity of immersion (or index matching) oil is used to form an optical contact between the sensor slide and the top of the parabolic element, thus minimising reflection/interface losses. The excitation optics, which consists of a $5mm$ LED, an emission filter, and a half-ball lens, is housed in an excitation module that is fixed to the base of the parabolic element. The excitation module incorporates a collimation aperture that partially collimates the light from the LED before it is focused onto the sensor slide by the half-ball lens. Illuminating from underneath the element results in reduced amounts of excitation light reaching the detector in comparison to the various configurations that involve illuminating from the top surface. This reduces the potential for intensity sensitivity (see section 3.2.2.3), and may also lead to reduced noise.

Luminescence emission emerges from the base of the parabolic element, as shown in Fig 4.2, and takes the form of a ring that passes parallel to the excitation module and strikes the emission filter. The emission filter removes any excitation light that was backscattered by the element and/or the sensor slide. The filtered light is then focused onto the photodiode detector using a double convex lens (DCX) pair. A collection module is used to house the emission filter, DCX lens pair and photodiode, with the use of a single module simplifying the probe assembly process. The optoelectronic component connecting cables are routed from the excitation module along the inside wall of the probe through slots that have been machined in the sidewall of the collection module. A slot is also provided for the thermistor cable. An unavoidable consequence of the configuration used is that the cables obstruct some of the luminescence. Approximately 5% of the luminescence signal is lost but this is offset by the advantages of exciting from underneath the element.

The probe is rendered waterproof by the inclusion of nitrile O-rings at the interfaces of each of its sections. The base-cap is compatible with industry standard waterproof conduit fittings, which facilitates the use of flexible waterproof conduit to connect the probe to the electronics enclosure.

A hole is machined in the probe that allows the placement of a bead thermistor close to the top of the probe for the measurement of ambient temperature. The thermistor is fixed in place using a silicone-based adhesive that ensures that the integrity of the probe is not compromised.

4.2.2 Referencing Configuration

In this particular case the probe is configured for dual photodiode referencing, with the reference photodiode being placed at the base of the excitation module, directly behind the LED. It is also possible to configure the probe for use with dual LED referencing by replacing the reference photodiode in Fig. 4.3 with a spectrally suitable LED that faces towards the emission filter.

4.2.3 Assembly

The main parts of the probe, namely the main body, the parabolic element housing, the end cap and the sensor cap, all thread together to form a single module. With the exception of the collection assembly, all of the other parts of the probe, including the parabolic element, are held in place using adhesive. The collection module is designed to be a tight fit in the main body of the probe, and therefore does not require adhesive, which greatly simplifies the disassembly process.

4.3 Ratiometric Configuration (Probe 3)

As discussed in section 2.4.4, ratiometric operation is a commonly used technique that leads to enhanced sensor performance. A ratiometric mode compatible dye, HPTS, was used as the luminophore in a dissolved CO_2 sensor, and it was required that an optical assembly capable of ratiometric operation be developed. This task was undertaken by the author and a colleague (Conor Burke). It was recognised that the use of ratiometric operation in conjunction with the enhanced capture probe would lead to improved performance, and as a result, the feasibility of modifying the probe for ratiometric operation was investigated. In the applications in question the HPTS dye exhibited two absorbtion/excitation peaks and a single emission peak, which meant that dual excitation mode ratiometric operation was required. This involved the addition of a second excitation source to the probe, with a key requirement being that both sources illuminate the centre of the sensor spot with approximately equal intensities. It was determined that a beam-adder type configuration would satisfy this requirement, and it was found that a suitable dichroic beam-splitter, which could be used as an adder, was available commercially. The excitation module was modified to accommodate a second LED and the dichroic beam-splitter, as shown in Fig. 4.4. The dichroic filter element is mounted across the central channel of the excitation module at an angle of 45°. The required shape was not commercially available so a larger element (FF409-Di02-25x36, Semrock) was diced and then manually polished down to the correct shape. The second LED is mounted in the side of

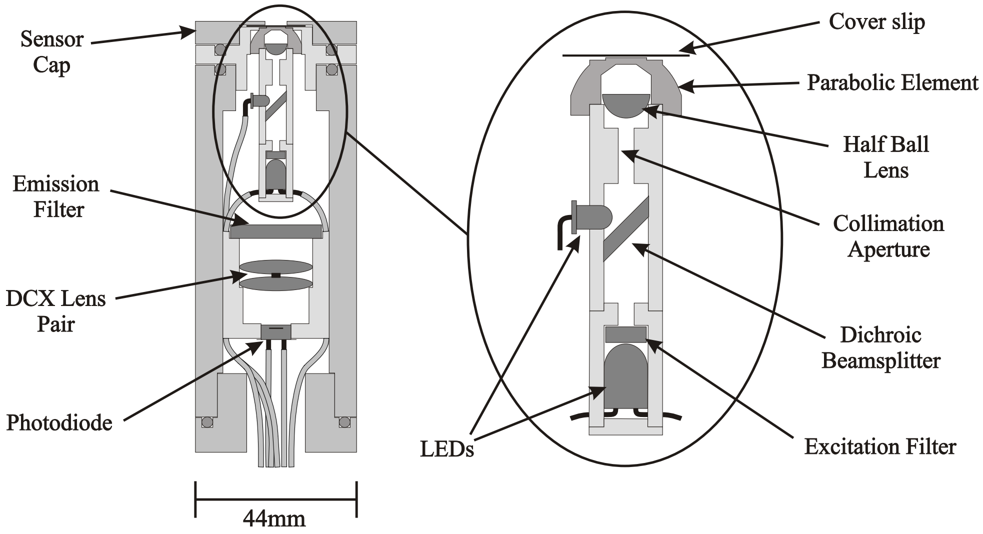

Figure 4.4: Enhanced capture probe with ratiometric operation support (Probe 3).

the excitation module, aligned with the point where the centreline of the module strikes the dichroic filter, resulting in the beams from both LEDs being aligned. The back of the LED is in the path of the luminescence ring, so a $3mm$ LED was used to reduce losses. The luminescence loss due to the presence of the second LED was estimated to be approximately 4%.

The absorption and emission spectra of the HPTS dye, the emission spectra of the chosen excitation LEDs and the spectral response of the dichroic filter used, are shown in Fig. 4.5.

4.4 Design Improvements

A range of design improvements were implemented in order to improve the useability, ruggedness and reliability of the probe, and to simplify the assembly process.

4.4.1 Modified Paraboloid Design

The original parabolic element was designed for use with $200\mu m$ thick sample slides, which were quite fragile and difficult to use in the laboratory. The use of thicker, more robust slides would result in the sensor film being moved away from the focus of the paraboloid, thereby reducing collection efficiency and sensor performance. The effect of film location on collected luminescence is illustrated in Fig. 4.6. Luminescence capture is maximised when the sensor film is located at the focal point of the parabolic element but drops off rapidly as it is moved away from the focus. Given the magnitude of the associated reduction in luminescence

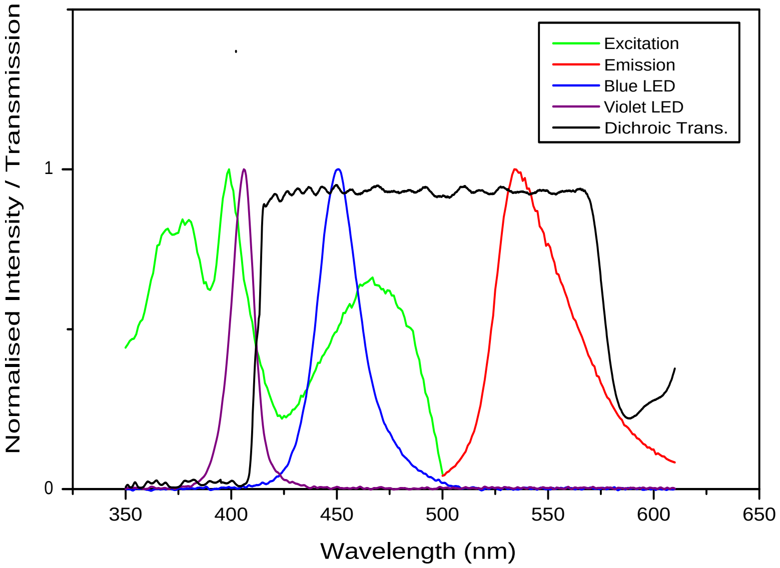

Figure 4.5: The excitation and emission spectra of the CO_2 sensor film [3], the emission spectra of the excitation LEDs, and the transmission curve of the dichroic beam-splitter [4]. The transmission curves of the blue LED excitation filter and the emission filter have been omitted in the interests of clarity.

capture, the use of a thicker film with this element was not feasible. Therefore, a modified parabolic element would have to be designed in order to use thicker slides.

4.4.1.1 Design Procedure

A parabola with its axis of symmetry parallel to the positive z axis, and its vertex located at the origin, is described by the equation:

$$z = ax^2 \tag{4.1}$$

where a is a variable that changes the form of the parabola. The focal point is located a distance F along the positive z axis, where F is given by:

$$F = \frac{1}{4a} \tag{4.2}$$

All parabolic surfaces will collimate an emission source located at the focal point, which means that the parameter a can be adjusted arbitrarily to achieve the desired focal point location and element shape, which define the collection properties of the element. The diagram in Fig. 4.7 details all of the parameters that must be taken into consideration during the design process. The surface of the

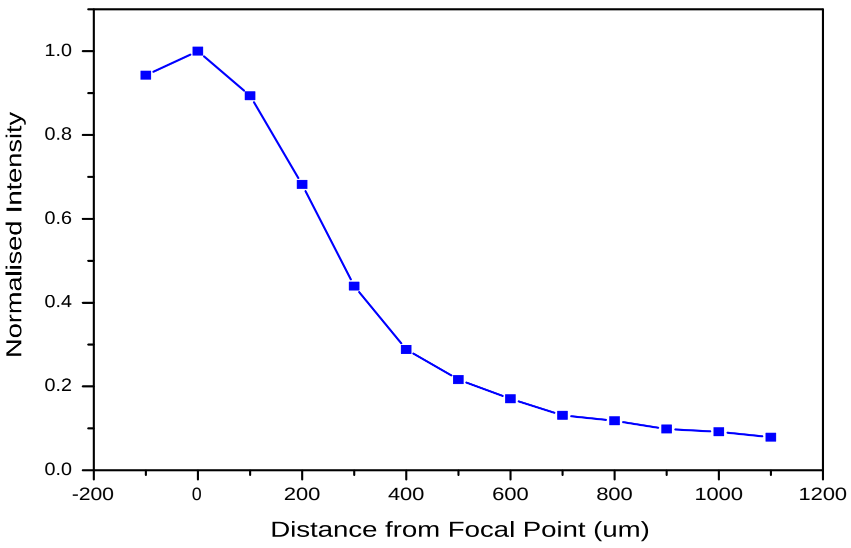

Figure 4.6: The normalised collected luminescence intensity is plotted as a function of the distance of the sensor material from the focal point of the parabolic element. This data was obtained by measuring the angular position of the sensing cap as it was rotated, and translating the angular measurement into displacement by relating it to the thread pitch.

sample slide is positioned at the focal point of the paraboloid and a small space is left between the surface of the element and the slide to accommodate the index matching layer that is required. The overall thickness of the sample slide and index matching layer is denoted by H. In order to match the dimensions of the sensor probe, the width of the base of the element, w had to be less than or equal to a predefined value. The maximum and minimum emission angles that can be captured by the element, which are denoted by ϕ_{max} and ϕ_{min} respectively, had to be taken into consideration as they had to coincide with the peak in the anisotropic emission profile. This brought to a total of four the number of parameters that had to be considered. With the aid of Fig. 4.7, it can be seen that it is possible to satisfy any selection of three of these parameters, but not all four. This implies that a trade-off has to happen between two or more of the parameters. The most desirable slide thickness is $1mm$, as this is the thickness of a range of commercially available slide types. In addition, it is not possible to relax the restriction on the width of the base of the element, which means that the trade-off had to take place between ϕ_{max} and ϕ_{min}. The element that resulted from the design process was also to be used by colleagues for a SAF-based [5, 6] bio-sensing application. The capture of high angle emission is critical in SAF applications, and as a result, ϕ_{max} was selected as the controlling parameter.

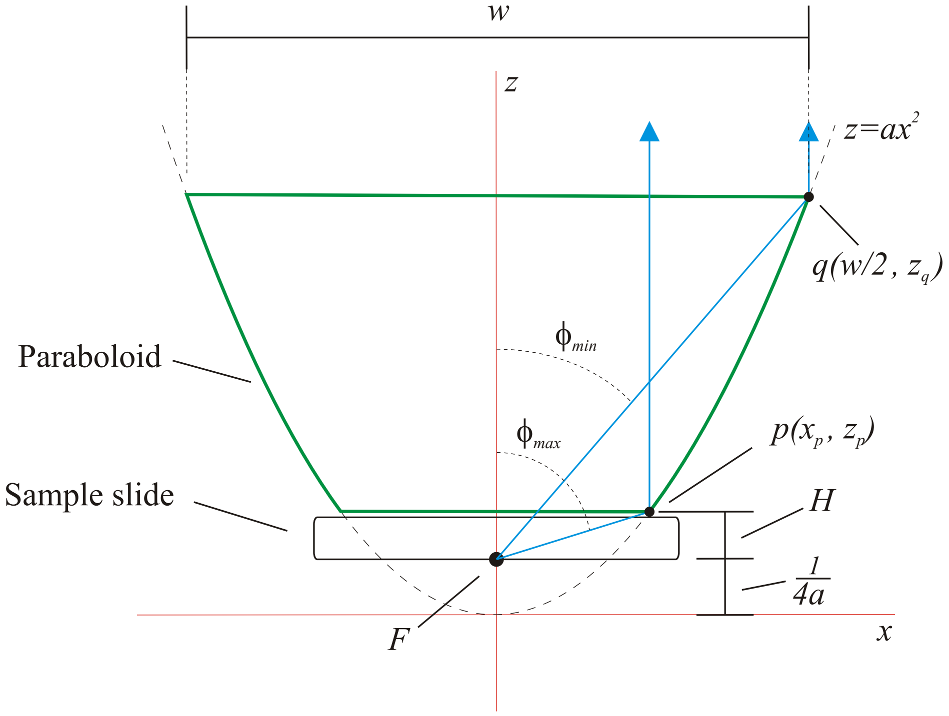

Figure 4.7: The parameters that must be taken into consideration when designing a parabolic element

It is possible to select a using iterative or trial and error techniques. An analytical approach, however, greatly simplifies the process. The following system of equations describe the location of point p (see Fig. 4.7), which is a function of ϕ_{max}, H and a.

$$z_p = ax_p^2 \tag{4.3}$$

$$z_p = H + \frac{1}{4a} \tag{4.4}$$

$$x_p = H\tan(\phi_{max}) \tag{4.5}$$

Combining equations 4.3, 4.4 and 4.5, results in the expression:

$$4H^2\tan^2(\phi_{max})a^2 - 4Ha - 1 = 0 \tag{4.6}$$

which is a quadratic equation in terms of a. Solving this equation for a, results in:

$$a = \frac{1 \pm \sqrt{1+\tan^2(\phi_{max})}}{2H\tan^2(\phi_{max})} \tag{4.7}$$

There are two possible values for a, one positive and one negative. The positive value results in a parabola with its axis of symmetry along the positive z axis, which was the orientation convention chosen in this case. The value of a that allows luminescence at ϕ_{max} to be captured when using a combined sensor slide and index matching layer thickness of H is then:

$$a = \frac{1 + \sqrt{1 + \tan^2(\phi_{max})}}{2H \tan^2(\phi_{max})} \tag{4.8}$$

The minimum emission angle, ϕ_{min} that can be captured, is a function of a and the width of the base of the element, w, and is given by the expression:

$$\phi_{min} = \tan^{-1}\left(\frac{2aw}{a^2w^2 - 1}\right) \tag{4.9}$$

Total Internal Reflection The correct operation of the element requires that total internal reflection (TIR) take place at its surface, and there is a possibility that the requirement for TIR could impose restrictions on the range of a values that can be used. For total internal reflection to occur, the angle of incidence must be greater than the critical angle at the interface in question. The smallest possible angle of incidence, ϕ_i of light from the focal point striking the side of the element occurs for a value of $H = 0$, which results in an angle of incidence of 45°. This situation is depicted in Fig. 4.8. The element is manufactured from Zeonex, which has a refractive index of 1.51, and is operated in air, which results in a critical angle of 41.47°. Therefore, the angle of incidence will always be greater than the critical angle, regardless of the value of a that is selected, which implies that TIR requirements do not impose any restrictions on the element design process.

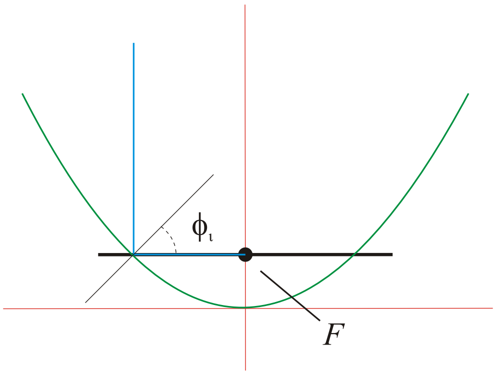

Figure 4.8: The smallest angle of incidence possible is $45°$, which occurs for the theoretical worst case scenario where $H = 0$.

The constraints listed in Table 4.2 were applied to equations 4.8 and 4.9. This resulted in a value of a of 0.1415, and a ϕ_{min} value of 53.6°. This parabolic surface was incorporated in an element that included a number of other design improvements.

Parameter	Value
H	$1.52mm$
w	$14mm$
ϕ_{max}	$72.5°$

Table 4.2: Parameters used in the design of the modified optical element. H includes a contribution from an O-ring that was added to the design to confine the immersion oil to the top surface of the element. Immersion oil seepage was a problem in the previous design.

4.4.2 Glue Free Assembly

In the original design (Probe 1 and Probe 2), all of the internal parts were held in place using adhesive. This led to a lengthy assembly process and was the cause of a considerable number of reliability-related problems that were caused by failure of the adhesive, to the extent that the useability and reliability of the probe was severely compromised. Component misalignment was also a significant problem. To overcome these issues and improve reliability and simplify assembly, a probe was designed that used threaded interfaces throughout. The starting point for this work was Probe 3, the ratiometric mode probe. A retaining lip was added to the base of the parabolic element that allowed it to be held in place using a retaining ring. The interior of the element was threaded to fix the excitation module in place, with flat mating surfaces being provided to ensure correct alignment. The half-ball lens, emission filter, and excitation LED are held in place using a spring-based system that avoided the specification of precise machining tolerances, which would have added significantly to the manufacturing costs of the probe.

4.4.3 Anti-bubble Formation Sensor Cap

In all of the aqueous phase applications in which the original probe was used, bubble formation at the sensor film was a considerable problem. This was especially so when the probe was being used with dissolved gas test and calibration setups as the fully saturated nature of the water in the cell was conducive to bubble formation. The only way to reduce the occurrence of bubbles was to orient the probe at low angles, which caused the system to be difficult to use. The cause of the problem was traced to the rim of the sensor cap, which was found to act both as a trap and as a nucleation point for the formation of bubbles, which grew in size with time until they eventually obstructed the active sensing area of the film. A modified cap was designed, which prevented bubble formation by using a 'fingers'-based approach to hold the sensor slide in place. The new cap design is shown in Fig. 4.9. The sensor slide is held in place by three tapered fingers. The combination of the spaces between the fingers and their tapered edges prevent either the formation or trapping of bubbles.

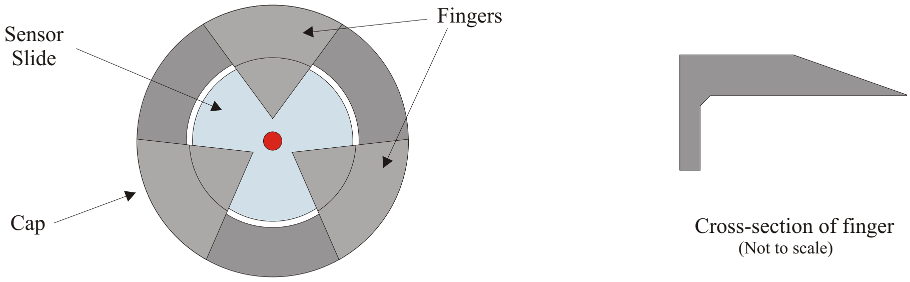

Figure 4.9: Sensor cap that prevents the formation or trapping of bubbles over the active sensor area.

4.4.4 Implementation

A sensor probe that incorporates the improvements that have been listed in the previous sections was designed in conjunction with a colleague (Stephen O'Driscoll). A cross-sectional diagram of the resulting design, which is referred to as 'Probe 4', is shown in Fig. 4.10. The probe was constructed from Acetal and was used for dissolved carbon dioxide sensing. Robustness and reliability were improved considerably, and probe assembly time was reduced from three days to

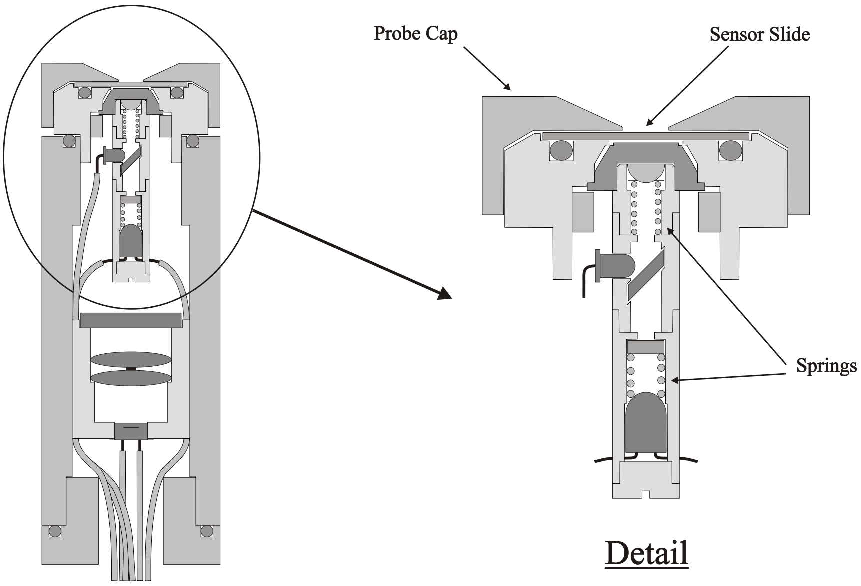

Figure 4.10: The sensor probe design that incorporates the design enhancements that were developed during this work.

approximately fifteen minutes, due to the removal of the multiple adhesive drying steps. Its performance is discussed in more detail in Chapter 7.

4.5 Design of Luminescence Capture Elements for General Sensing Applications

4.5.1 Motivation

The enhanced capture elements described previously were designed to be used in both bio-sensing and general sensing applications. Bio-sensing in this case refers to immunosensing based primarily on sandwich assay techniques while general sensing refers to applications such as gas sensing, where background suppression and surface specificity are not of major concern. In order to achieve optimum performance for bio-sensing, the elements were designed to capture surface confined luminescence from a small area at the focus of the element, and to reject luminescence from the bulk solution above the element and from other areas of the sample slide. The restriction of luminescence capture to a small area is not necessary for general sensing applications and in many cases results in a large proportion of the available luminescence being rejected. If the element was designed to collect luminescence from a larger area, increased signal levels, and consequently, an increased signal to noise ratio would be obtained. Moreover, if current signal levels were adequate, excitation intensity could be reduced, resulting in a reduction in photo-degradation/photobleaching of the luminophore, which would be desirable in many situations.

4.5.2 Overview of Design Process

The basic concept behind the design process was to develop a ray tracing-based model of the system and to use this model to determine what collection structure yielded maximum luminescence collection. While there were a large number of structures that may have performed well, the selection was limited to cone, parabola- and asphere-based elements. Discontinuous and non-analytically definable options were not considered due to difficulties involved in manufacturing such surfaces. The cone and paraboloid are the simplest of the three structures, while the asphere has more degrees of freedom and can take on a wide range of forms. The relationship between the parameters of the collection structures and the collection efficiency are quite complex and non-intuitive. As a result, automated iterative optimisation techniques were used to determine the parameter values that yielded maximum collection efficiency for each of the structures. The optimum versions of each of the structures were then compared to determine the best candidate.

4.5.3 Optical Configuration

It was necessary that the element resulting from the design process be deployable in an optical probe type configuration, with the overall probe dimensions being similar to those of the existing probe. As a result, the same optical configuration as was used for the previous probe design, which is depicted in Fig. 4.11, was used for the modelling process. The luminescence emerging from the base of the collection element is focussed onto a detector, a photodiode for example, using a DCX lens pair. All of the optical components are circularly symmetrical and are aligned along a single axis, which is taken to be the z axis in the following sections.

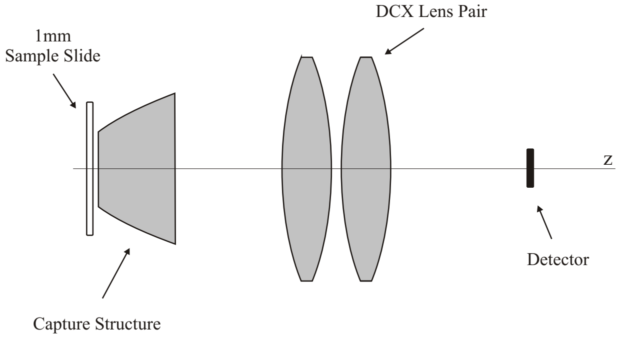

Figure 4.11: Optical configuration used in the element modelling process.

4.5.4 Ray Tracing Engine

Although access was available to commercial ray tracing software, it would have been very difficult to integrate it with the necessary parameter optimisation software. for this reason, a custom ray tracing engine that could be easily integrated into, or used with other software routines, was developed. It also provided full access to, and control over, all of the relevant parameters of the system, which would have been problematic with the commercial ray tracing software.

The ray tracing engine was developed in Matlab in order to leverage its native support for vector and matrix calculations and also due to the availability of built-in routines to perform some of the required mathematical operations.

4.5.4.1 Ray Tracing Basics

Ray tracing involves mathematically tracing the path of a collection of rays through the environment being modelled, taking the various interactions of the rays with the objects they encounter into account. A ray can be described mathematically by the expression:

$$r(t) = R + tD \tag{4.10}$$

where R and D are vectors that describe the origin and direction of the ray respectively, and t is a parameter that varies over the range $\{t > 0, t < 0\}$. In $3D$ space, the vectors R and D are given by:

$$R = \begin{bmatrix} x_R \\ y_R \\ z_R \end{bmatrix}, \qquad D = \begin{bmatrix} x_D \\ y_D \\ z_D \end{bmatrix} \tag{4.11}$$

When a ray intersects an object, reflection, refraction and/or one or more of a number of absorption-based effects can take place. In order to simplify the modelling process, it was assumed that absorption-based effects would not vary significantly between the different collection structures, and therefore were omitted. This was possible due to the fact that all of the structures were constrained to the same width(see section 4.5.5) and would therefore have similar volumes and associated absorption losses. The result was that only reflection and refraction effects had to be taken into account.

Reflection and Refraction Reflection at a surface is depicted in Fig. 4.12a. The incident ray, denoted by $\vec{i}$, strikes the reflecting surface at the point P. The reflected ray is denoted by $\vec{r}$ and the normal to the surface at point P, which is of unit length, is denoted by $\hat{n}$. The process is described, in vector format, by the expression [7]:

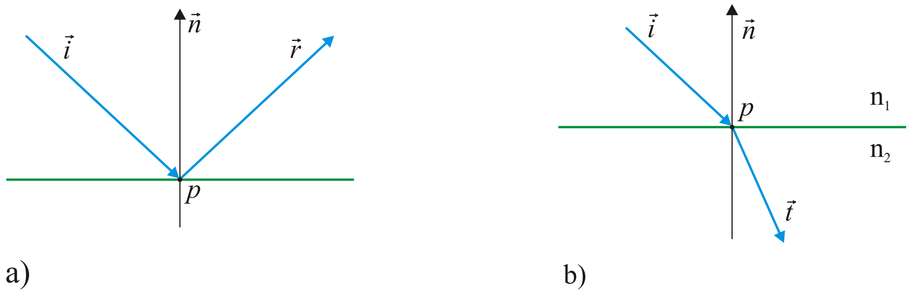

Figure 4.12: Reflection (a) and refraction (b) at an interface

$$\vec{r} = \vec{i} - 2\left(\vec{i} \cdot \hat{n}\right)\hat{n} \tag{4.12}$$

Refraction, which is depicted in Fig. 4.12b, is described by the expression [7]:

$$\vec{t} = \left(\frac{n_1}{n_2}\right)\vec{i} - \left[\frac{n_1}{n_2}\left(\vec{i}\cdot\hat{n}\right) + \sqrt{1 - \left(\frac{n_1}{n_2}\right)^2\left(1 - \left(\vec{i}\cdot\hat{n}\right)^2\right)}\right]\hat{n} \tag{4.13}$$

where $\vec{t}$ is the refracted ray and n_1 and n_2 are the refractive indices of the source and destination media, respectively. When the ray in question is travelling from a more dense to a less dense medium, total internal reflection occurs if the angle of incidence is greater than the critical angle. This corresponds to the square root term in equation 4.13 being less than zero, which occurs when the following inequality is satisfied:

$$\left(\frac{n_1}{n_2}\right)^2\left(1 - \left(\vec{i}\cdot\hat{n}\right)^2\right) > 1 \tag{4.14}$$

In order to evaluate equations 4.12 and 4.13, the point of intersection of the ray with the surface in question, and the normal to the surface at that point, must be evaluated. For a surface that can be described analytically by the expression:

$$z = f(x, y) \tag{4.15}$$

the non-unit length surface normal, $\vec{n}$, at the point (x_0, y_0) is given by [8]:

$$\vec{n} = \begin{bmatrix} \frac{\partial f}{\partial x} \\ \frac{\partial f}{\partial y} \\ -1 \end{bmatrix}_{(x_0, y_0)} \tag{4.16}$$

where $\frac{\partial f}{\partial x}$ and $\frac{\partial f}{\partial y}$ are the partial derivatives of the surface function.

The means of determining the point of intersection of a ray with a surface varies based on the surface in question. In the case of surfaces that can be described analytically by invertible functions of the form of equation 4.15, the point of intersection can be determined by treating the equations describing the ray and the surface as a set of simultaneous equations and solving for the parametric value of the ray, t. If the expression describing the surface is not invertible , then numerical techniques must be used to locate the point of intersection. In the event that the function describing the surface is not differentiable, the normal must also be evaluated numerically.

Intersection with a Plane The simplest case is for the intersection of a ray with a plane, which are used extensively in the modelling process. The equation of a plane in 3D space is:

$$ax + by + cz + d = 0 \tag{4.17}$$

All of the planes used in the modelling process are orthogonal to the z axis (see section 4.5.3), which reduces equation 4.17 to:

$$z + d = 0 \tag{4.18}$$

Combining equations 4.10, 4.11 and 4.18 and solving for t yields:

$$t = \frac{-d - Z_R}{z_D} \tag{4.19}$$

Substituting this value of t into the equation of the ray in question as defined by equations 4.10 and 4.11 allows the intersection point to be calculated.

From equation 4.16, it can be seen that the normal to the plane in the simplified case described by equation 4.18 is simply:

$$\hat{n} = \vec{n} = \begin{bmatrix} 0 \\ 0 \\ -1 \end{bmatrix} \tag{4.20}$$

Intersection with a Sphere The next surface that must be addressed is the sphere, as the surfaces of the lenses used in the system are described by spheres. A sphere is described by the equation:

$$(x - a)^2 + (y - b)^2 + (z - c)^2 = R^2 \tag{4.21}$$

where R is the radius of the sphere and a, b and c define its centre point. Combining equations 4.10, 4.11 and 4.21 results in the expression:

$$(x_R + tx_D - a)^2 + (y_R + ty_D - b)^2 + (z_R + tz_D - c)^2 = R^2 \tag{4.22}$$

Expanding this expression and grouping terms results in a quadratic equation in terms of t, which can be solved using the standard equation:

$$t = \frac{-B \pm \sqrt{B^2 + 4AC}}{2A} \tag{4.23}$$

where A, B and C are given by:

$$\begin{aligned} A &= x_D^2 + y_D^2 + z_D^2 \quad (4.24) \\ B &= 2x_D(x_R - a) + 2y_D(y_R - b) + 2z_D(z_R - c) \quad (4.25) \\ C &= (x_R - a)^2 + (y_R - b)^2 + (z_R - c)^2 - R^2 \quad (4.26) \end{aligned}$$

This results in two values of t, which correspond to the intersection of the ray with both sides of the sphere. The correct value of t must be chosen by comparing the two values obtained and taking the location of the spherical surface relative to the origin of the ray into account. In theory it is possible that the ray does not intersect the sphere, which corresponds to $B^2 - 4AC < 0$, or that only one point of intersection occurs ($B^2 = 4AC$). These possibilities do not have to be considered in this case due to the action of the ray selection strategy that is employed by the ray tracing algorithm (see section 4.5.4.4).

The normal to the sphere at the point of intersection, denoted by (x_0, y_0), is obtained by evaluating equation 4.16. Rearranging equation 4.21 so that is is in the form $z = f(x, y)$, and applying equation 4.16 results in:

$$\vec{n} = \begin{bmatrix} \dfrac{x-a}{\sqrt{R^2 - (x-a)^2 - (y-b)^2}} \\ \dfrac{y-a}{\sqrt{R^2 - (x-a)^2 - (y-b)^2}} \\ -1 \end{bmatrix}_{(x_0, y_0)} \tag{4.27}$$

$\vec{n}$ is scaled to unit length by dividing by its norm, resulting in:

$$\hat{n} = \begin{bmatrix} \vec{n}_x \\ \vec{n}_y \\ \vec{n}_z \end{bmatrix} \frac{1}{\sqrt{n_x^2 + n_y^2 + n_z^2}} \tag{4.28}$$

All of the other surfaces that must be supported by the ray tracing engine are dealt with in the next section.

4.5.4.2 Capture Structures

From a mathematical viewpoint, the capture structures can be considered as a collection of surfaces and the interaction of the rays with all of the surfaces they interact with must be taken into account in order to describe the behaviour of the structure as a whole. The top and bottom of the structures are represented by planes by parallel planes that are orthogonal to the axis of symmetry of the element, in this case the z axis. The sides of the structures are represented by the surface generated by rotating the relevant curve about the z axis.

Conic Element The surface of a cone is obtained by rotating the line:

$$z = \frac{1}{c}x + z_0 \tag{4.29}$$

about the z axis. c is the ratio of the radius to the height of the cone and z_0 is the location of its apex. The rotation about the z axis can be represented mathematically by replacing the x term in equation 4.29 with the expression:

$$\sqrt{x^2 + y^2} \tag{4.30}$$

resulting in:

$$z = \frac{1}{c}\sqrt{x^2 + y^2} + z_0 \tag{4.31}$$

As with the other surfaces that have been analysed, expressions must be obtained for the point of intersection of a ray with the cone and the normal to the cone at that point. Using the same techniques as in section 4.5.4.1, it can be shown that the point of intersection of a ray and the cone is given by:

$$t = \frac{-B \pm \sqrt{B^2 - 4AC}}{2A} \tag{4.32}$$

where:

$$\begin{aligned} A &= x_D^2 + y_D^2 - z_D^2 c^2 && (4.33) \\ B &= 2x_D x_R + 2y_D y_R - 2z_D z_R c^2 + 2z_0 z_D c^2 && (4.34) \\ C &= x_R^2 + y_R^2 - z_R^2 c^2 - z_0^2 c^2 + 2z_R z_0 c^2 && (4.35) \end{aligned}$$

As was the case with the sphere, there are multiple possible values of t, and the correct one must be selected based on the geometry of the problem in question. The normal to the cone at the point (x_0, y_0) is given by:

$$\vec{n} = \begin{bmatrix} -\dfrac{x}{c\sqrt{x^2 + y^2}} \\ -\dfrac{y}{c\sqrt{x^2 + y^2}} \\ -1 \end{bmatrix}_{(x_0, y_0)} \tag{4.36}$$

Paraboloid Following the same approach as for the cone, the equation that describes a parabolic surface is found to be:

$$z = a(x^2 + y^2) + z_0 \tag{4.37}$$

where a is the coefficient that defines the shape of the parabolic surface and z_0 is the location of its apex. The point of intersection of a ray with the parabolic surface is given by equation 4.32, where A, B and C are given by:

$$\begin{aligned} A &= a(x_D^2 + y_D^2) && (4.38) \\ B &= 2a(x_R x_D + y_R y_D) - z_D && (4.39) \\ C &= a(x_R^2 + y_R^2) + c - z_R && (4.40) \end{aligned}$$

The normal to the parabolic surface is given by:

$$\vec{n} = \begin{bmatrix} 2ax \\ 2ay \\ -1 \end{bmatrix}_{(x_0, y_0)} \tag{4.41}$$

Aspheric Element The standard equation for describing the curvature of aspherical optical elements is:

$$z + z_0 = \frac{x^2}{R(1 + \sqrt{1 - (1+k)x^2/R^2})} + A_2 x^2 + A_4 x^4 + A_6 x^6 + \ldots \tag{4.42}$$

where R is the radius of curvature, k is the conic constant, $A_2, A4\ldots$ are the aspheric coefficients, and z_0 is the location of the apex of the curve. Rotating about the z axis results in:

$$z+z_0 = \frac{x^2 + y^2}{R(1 + \sqrt{1 - (1+k)(x^2+y^2)/R^2})} + A_2(x^2+y^2) + A_4(x^2+y^2)^2 + \ldots \tag{4.43}$$

This expression is not invertible, so therefore a numerical technique must be used to solve for t when determining the point of intersection of a ray with the surface. The simplest approach is to use a root finding-based technique. Combining equations 4.10, 4.11 and 4.43 results in an expression of the form:

$$f(t, \ldots) \tag{4.44}$$

The roots of the function f correspond to the values of t that define the intersection points of the ray with the aspheric surface. The root-finding process was implemented using Matlab's numerical root finding algorithm, $fzero$, which de-

termines the location of the nearest root to a user provided starting point by searching for the nearest point where the function goes to zero.
Equation 4.43 is differentiable, and an analytical expression for the normal was evaluated in the same way as for the other surfaces. It is not reproduced here due to the large number of terms involved.

4.5.4.3 Ray Generation

The luminescence source was simulated using a set of anisotropic point sources distributed at random over the specified sensor spot area. Each point source consisted of a group of rays that were distributed so as to match the theoretically predicted emission profile. A model that calculates the emission intensity profile from a collection of randomly oriented luminophore located at or near a dielectric interface was developed previously by Polerecky et. al. [9]. The model described in [9] was implemented by Polerecky as a set of Matlab scripts, and these were used to generate the emission profile of a luminescent layer located at the interface between a substrate with a refractive index of 1.52, and air. A 2D cross-section of the resulting profile, which is circularly symmetrical, is shown in Fig. 4.13. Rays had to be assigned in 3D space to match this profile, and due to the symmetry involved, a spherical coordinate-based approach was used. The emission profile in Fig. 4.13, is provided by the modelling software in discrete form. It can be described mathematically by the expression:

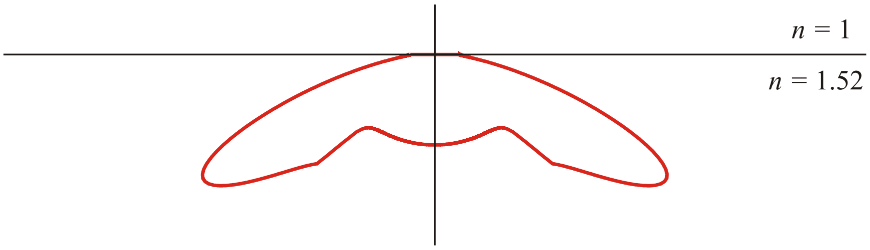

Figure 4.13: The emission profile of a luminescent layer located on the surface of a transparent material with a refractive index of 1.52. The superstrate radiated luminescence has been omitted, as for the purposes of modelling, only the substrate radiated luminescence is of interest.

$$I_{2D}[n] = f(\phi[n]) \tag{4.45}$$

where n is the data index and ϕ is the angle relative to the axis of symmetry indicated in Fig. 4.13. It should be noted that the data is provided for the range $\frac{\pi}{2} \leq \phi \leq \pi$ and has been mirrored to obtain the profile in 4.13.

Using standard mathematical spherical notation, (r, θ, ϕ) [10], the simplest way to generate the rays was to assign the ϕ value of the rays based on the emission profile, and then to assign a random θ value to each ray. In order to be able to use this approach, an expression for the total intensity as a function of ϕ was required. The total intensity can be obtained by rotating the emission profile function about its axis of symmetry and integrating to obtain the resulting area. To express the total area as a function of ϕ, consider an infinitesimal area, dA, defined by $d\theta$ and $d\phi$, which is located a distance r from the origin, at an angle of ϕ. The area of dA is given by $r^2 \sin\phi d\theta d\phi$. When dA is rotated about the axis of symmetry, the area it sweeps out, dA_T, is given by:

$$dA_T = \int_0^{2\pi} r^2 (\sin\phi) d\phi d\theta \tag{4.46}$$

Evaluating the integral results in:

$$dA_T = 2\pi r^2 \sin\phi d\phi \tag{4.47}$$

If r is taken to be the 2D emission intensity, I_{2D}, and equation 4.47 is expressed in discrete form, due to the discrete nature of I_{2D}, the result is:

$$\Delta A_T[n] = 2\pi (I_{2D}[n])^2 \sin(\phi[n]) \Delta\phi \tag{4.48}$$

$\Delta A_T[n]$ can also be written as $\Delta\phi \cdot I_T[n]$, where I_T is a function that describes total intensity as a function of ϕ. Making this substitution in equation 4.48, yields the following expression for I_T:

$$I_T[n] = 2\pi \sin(\phi[n]) (I_{2D}[n])^2 \tag{4.49}$$

This function describes the required distribution of the ϕ values of the rays when the 3D nature of the emission is taken into account. Integrating over the range $\frac{\pi}{2} \leq \phi \leq \pi$ results in the total substrate radiated emission, I_S. The integration has to be carried out numerically and can be described by the expression:

$$I_S = \sum_{n=1}^{N} I_T[n] \cdot \Delta\phi \tag{4.50}$$

where n is the data index, $\Delta\phi$ is the step size of ϕ and N is the number of samples in the discrete function I_T. In order to increase the accuracy of the ray assignment process, and also that of the numerical integral described by equation 4.50, I_T was up-sampled by a factor of 100 using linear interpolation. Equation

4.50 then becomes:

$$I_S = \sum_{n=1}^{M} I_T^u[n] \cdot \Delta\phi_M \qquad (4.51)$$

where M is the number of samples in the up-sampled waveform, I_T^U. The number of rays required per source, N_R, is specified by the user. The intensity per ray, I_R is then:

$$I_R = \frac{I_S}{N_R} \qquad (4.52)$$

The ϕ values of the rays can be determined by dividing the 3D intensity profile, I_T, into N_R regions of size I_R, and taking the ϕ values that correspond to the centre of each I_R segment as the ϕ values for the rays. An accumulation-based algorithm was developed to implement this process, and works by summing the individual elements of I_T^U until the following inequality is satisfied:

$$(j+1)I_R \leq \sum_{n=1}^{k} I_T[n] \qquad (4.53)$$

j is the index of the previously generated ray and k is the current sample index, which is incremented with each iteration. When the inequality is satisfied, $\phi[k]$ is used to generate the ϕ value of the $(j+1)th$ ray using the relation:

$$\phi_{j+1} = \frac{\phi[k] + \phi_j^*}{2} \qquad (4.54)$$

where ϕ_k^* is the upper bound of the jth I_R segment. Once all of the ϕ values are generated, the θ values are selected from a uniform distribution on the range $[0, 2\pi]$. As a ray is defined in terms of its origin and a unit direction vector (see equation 4.10), the r value of the rays was set to 1. The direction vectors were converted from spherical to cartesian coordinates using the relations:

$$\begin{aligned} x &= r\cos\theta\sin\phi \\ y &= r\sin\theta\sin\phi \\ z &= r\cos\phi \end{aligned} \qquad (4.55)$$

If all of the rays are assigned the same origin (R), the result is an anisotropic point source, with the user-defined number of rays.

As mentioned previously, the sensor spot was simulated by placing multiple such sources at uniformly distributed random locations over the defined spot area. Random points, uniformly distributed over a circular area on the xy plane can be generated using the expressions [11]:

$$x = r\sqrt{R_n}\sin\theta \tag{4.56}$$

$$y = r\sqrt{R_n}\cos\theta \tag{4.57}$$

where x and y are the coordinates of the points, R_n is a uniform random variable with the range $[0, 1]$, and θ is a uniform random variable with the range $[0, 2\pi]$. The spot radius, r, and the required number of sources is specified by the user at runtime.

4.5.4.4 Tracing Algorithm

The function of the tracing algorithm was to trace the path of the set of generated rays through the various optical components in the system and to determine how many rays reached the collector element for any given configuration. The optical setup, which is shown in Fig. 4.11, consists of five optical components: a sample slide with a luminescent material on its top surface, a capture structure, two DCX lenses, and a detection element. Each of these components was constructed using the necessary combination of the surfaces that have been described in sections 4.5.4.1 and 4.5.4.2. Once the required surfaces were positioned correctly relative to one another, it was necessary to devise a means of defining the bounds of the component in question. This was achieved through the use of a ray selection algorithm that determined what rays struck the surface in question inside or outside the bounds of the component. The circular symmetry of all of the components in the system, and the fact that they were all aligned along a single axis, allowed a simple, plane-based approach, to be used for this purpose. Determining what rays enter the capture structure can be taken as an example of the operation of the algorithm. The intersection points of all of the rays with the plane that defines the top surface is determined and the distance of each intersection point from the alignment axis of the system, which is taken to be the z axis, is measured. The radius of the top of the element is known and all of the rays that intersect the plane inside this radius are deemed to have entered the structure. The remaining rays, which were not captured, are removed from the set of rays and not processed any further. This ‘plane-radius’ selection process was used for all of the optical components in the system. It was very simple to implement and the process of removing all of the rays that were not captured by each component resulted in significant increases in computational efficiency, and also provided a simple means of defining the boundary of the ray tracing volume.

Graphics A graphical representation of the optical components and the tracing results was required for presentation and debugging purposes. A simple, 2D graphical display was implemented in which the optical components and all of the rays produced by the tracing engine are projected onto the xz plane. Examples of the resulting images can be seen in the next section.

4.5.4.5 Tracing Engine Results

In order to test the operation of the ray tracing engine, it was run with an optical configuration that consisted of a parabolic capture structure with a single anisotropic point source located at its focus. This configuration was chosen as the ray patterns that should be observed are well defined. All of the rays that enter the parabolic capture element should be collimated by the capture element and focussed to a narrow beam waist at the focus of the DCX lens pair. The resulting graphical output from the tracing engine is shown in Fig. 4.14. The expected behaviour is observed, thus validating the operation of the ray tracing software.

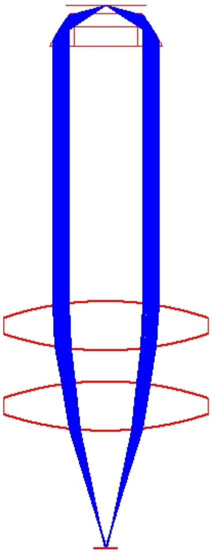

Figure 4.14: Ray trace of selected rays with parabolic capture structure

Performance of Original Element The performance of the previous parabolic element design was determined in order to provide a baseline for the performance of the structures under investigation. The capture efficiency was defined as the percentage of the rays that are radiated into the sample slide that reach the detector. This was evaluated for the parabolic element described in section 4.4.1 for a spot diameter of $3mm$ and was found to be 8.4%.

4.5.5 Structure Optimisation

The aim of this work was to determine the optimum parameters of each of the three structure types that resulted in maximum collection efficiency. The relationship between the various parameters that could be adjusted and the capture efficiency was complex and it was not possible to use analytical techniques to determine them. As a result, a numerical optimisation approach was used. At a high level, the entire ray tracing engine was treated as a black-box function that accepted parameter values and returned the capture efficiency. The optimisation algorithm adjusted the parameters until it determined that an optimum set of parameters have been found. The majority of optimisation algorithms aim to minimise the function in question so in practice the return value of the ray tracing function was the capture inefficiency, or the number of rays that did not reach the detector.

Optimisation algorithms can be grouped into two main types: local and global. Local optimisation algorithms search for a minimum of the function in question in the vicinity of a user provided starting point. Many functions have multiple minima however, and in such cases it is possible that the algorithm may have found a local minimum that is not the global minimum of the function. Global optimisation algorithms attempt to find the global minimum of the function in question. A local approach is the most desirable as they are much faster than their global counterparts. The choice of what type of optimisation algorithm has to be used depends on the nature of the function to be minimised, and whether it possesses multiple local minima. The simplest way to determine if this is the case is to run a local optimisation algorithm a number of times using a wide range of starting points. If the algorithm converges to the same result each time, then it is generally safe to use a local approach. However, if it converges to different results for different starting points, then a global approach should be used.

4.5.5.1 Optimisation Parameters

The relevant optimisation parameters had to be chosen for each of the structures. In each case this included the parameters that defined the form and location of the structure and also the location of the detection element as its optimum location varied for each of the structures and also as a function of the structure parameters. The parameters of each of the structures that were taken into account in the optimisation process are listed in Table 4.3. In line with the design principles applied in section 4.4.1, the width of the base of each of the elements was fixed to the same value. This radius of each of the elements was set to $7mm$ initially but as will be discussed in the next section, it was subsequently increased to $10mm$.

Cone	Paraboloid	Asphere
Apex	Focal point	Apex
Cone angle	‘a’ value	R, k, A_2, A_4..
Detector Location	Detector Location	Detector Location

Table 4.3: Parameters used for the optimisation of each of the structures

4.5.5.2 Local Optimisation

Local optimisation was implemented using Matlab’s built-in function, $fminsearch$, which finds local minima using the Nelder-Mead simplex technique [12]. In order to determine if local optimisation was sufficient in this case, the optimum parameters of a parabola-based structure were determined for a range of starting points. The optimum parameters determined by the algorithm, and the corresponding capture efficiency for three different sets of starting values are listed in Table 4.4. Different optimum parameters and different capture efficiencies were obtained in each case, indicating the presence of multiple local minima. As a result, a global optimisation-based approach had to be undertaken.

Detector Location(mm)	Focal Point (mm)	‘a’ Value(mm)	Capture Efficiency (%)
-71.8	-0.1706	0.0	21.3
-72.6	-0.1842	-0.4	20.9
-75.9	-0.2576	-0.4	15.8

Table 4.4: Optimum parameters and corresponding collection efficiency values obtained by the $fminsearch$ local optimisation algorithm for a range of starting values.

Width Constraint While assessing the suitability of the local optimisation approach, it became apparent that significant increases in the capture efficiency would not be possible without increasing the width of the base of the element. A radius of $7mm$ prevented the capture of luminescence from the edge of the spot, regardless of the capture structure geometry. The element radius was assigned as one of the optimisable parameters and an optimum radius of approximately $14mm$ was obtained, using the local optimisation algorithm. This was deemed to be too large for many of the target applications and a radius of $10mm$ was chosen as a compromise between collection efficiency and capture structure size.

4.5.5.3 Global Optimisation

There are a wide range of optimisation algorithms available commercially, based on a variety of different techniques. For this work, a trial version of Tomlab from Tomlab Optimisation, Sweden was used. It is an extensive suite of optimisation algorithms and solvers with a number of different global optimisation options that integrates seamlessly with Matlab. All of the solvers that were applicable to this work were run on a number of test configurations and it was found that the $glbFast$ solver converged to the consensus global minimum in the shortest amount of time in all cases. The $glbFast$ solver is based on a modified version of the DIRECT global optimisation algorithm [13].

The optimum set of parameters was obtained for each element using $glbFast$. The algorithm required that bounds be provided for all of the optimisable parameters and these were determined based on the physical constraints of the system, e.g. the apex of the cone or asphere could not be below the sample slide. The capture efficiency of the optimum of each of the three structure types are listed in Table 4.5. the spot diameter was set to $3mm$ in each case. The capture efficiencies of all of the optimum structures compares favourably to the that of the original design, at 8.4%. The largest improvement, which was for the parabolic and asphere structures, corresponds to a factor of 3 increase in capture efficiency for a spot size of $3mm$.

Structure	Capture Efficiency %
Cone	14.5
Parabola	25.8
Asphere	25.8

Table 4.5: Capture efficiency of the optimum of each of the three structure types

4.6 Conclusions

A range of design improvements were developed and implemented that have added to the functionality, useability and robustness of an enhanced capture-based optical probe that was previously designed at this laboratory. In the area of functionality, the main development was the design and implementation of a probe configuration that facilitated dual-excitation ratiometric operation. This resulted in the ability to apply the benefits associated with the use of enhanced luminescence capture strategies to ratiometric applications. An additional feature of the design is that, when combined with the functionality of the DSP-based instrumentation electronics, both LEDs can be operated simultaneously. This represents an improvement over the commonly used ratiometric configurations, which require that both light sources be operated alternately. In terms of robustness and useability, a number of design changes have been implemented that overcome issues such as bubble formation, the use of fragile sample substrates and the use of adhesive in the assembly process. These issues were the source of considerable problems from a practical perspective and their resolution has significantly increased the applicability of the enhanced capture probe technology. The second element of this work was the design of enhanced capture elements that were optimised for general sensing, as opposed to bio-sensing applications. In relaxing the bio-sensing-related restrictions imposed on the capture element design, it was possible to achieve significant increases in luminescence capture. The design process saw the use of custom ray tracing software in conjunction with optimisation algorithms. The use of optimisation techniques reduced what would otherwise have been quite a laborious process to one that could be implemented and executed with relative ease.

Going forward one of the areas of interest is the miniaturisation of the optical probe. In the current configuration, the size of the probe is ultimately limited by the thickness of the sensor slide, with a thinner substrate leading to reduced overall probe size. The reduction of sensor slide thickness is not desirable, for the reasons that were outlined previously. A solution to this problem would be to deposit the sensor film directly onto the parabolic element, which would equate to a sample slide thickness of zero. This would facilitate a dramatic reduction in overall probe size without any reduction in capture efficiency. The obvious downside to this approach is that a new capture element would be required for each sensor film, which would potentially have cost implications. This could be avoided, however, through the use of injection moulding techniques that could be used to produce large quantities of the elements at low cost.

The key result of the element modelling work is outlined in Table 4.6.

Structure	Capture Efficiency %
Original Design	8.4
Parabola/Asphere	25.8

Table 4.6: The capture efficiency of the original element design and the optimum design that was developed during the modelling work for a 3mm diameter sensor spot.

The next stage in this work will be to have the optimum structure manufactured and to compare its actual performance to that which was predicted by the ray tracing software. A number of items of future work are also planned from a modelling perspective. The first of these is to investigate the feasibility and performance of composite structures constructed from a small number of sub-surfaces. It is also intended to add support for the calculation of reflection and absorption losses to the ray tracing software in order to increase the accuracy of the results it generates. This was not considered to be a problem for the work that was carried out to date due to the relative similarity of the candidate structures that were tested, however, this may no longer be true if composite structures are used.

Bibliography

[1] Conor S. Burke, Thomas Ruckstuhl, and John P. Moore. *Optical Probe.* Patent, 2008. WO2008029298.

[2] Thomas Ruckstuhl. Parabolic element drawing, 2005. Unpublished.

[3] Dorota Wencel. Excitation and emission spectra of HPTS and Ru(dpp)3, 2010. Personal Communication.

[4] *Semrock Inc.* `http://www.semrock.com`.

[5] D. Kurzbuch, J. Bakker, J. Melin, C. Jnsson, T. Ruckstuhl, and B. D. MacCraith. A biochip reader using super critical angle fluorescence. *Sensors and Actuators B: Chemical*, 137(1):1–6, 2009.

[6] T. Ruckstuhl and D. Verdes. Supercritical angle fluorescence (saf) microscopy. *Optics Express*, 12(18):4246–4254, 2004.

[7] Andrew G. Glassner. *An Introduction to Ray Tracing.* Academic Press Limited, 1989.

[8] Eric W. Weisstein. *Normal Vector.* From Mathworld - A Wolfram Web Resource, `http://mathworld.wolfram.com/NormalVector.html`, 2010.

[9] L. Polerecki, J. Hamrle, and B. D. MacCraith. Theory of the radiation of dipoles placed within a multilayer system. *Applied Optics*, 39(22):3968–3977, 2000.

[10] Eric W. Weisstein. *Spherical Coordinates.* From MathWorld - A Wolfram Web Resource., `http://mathworld.wolfram.com/SphericalCoordinates.html`.

[11] Eric W. Weisstein. *Disk Point Picking.* From MathWorld - A Wolfram Web Resource., `http://mathworld.wolfram.com/DiskPointPicking.html`.

[12] J. A. Nelder and R. Mead. A simplex-method for function minimization. *Computer journal*, 7(4):308–313, 1965.

[13] D. R. Jones, C. D. Perttunen, and B. E. Stuckman. Lipschitzian optimization without the lipschitz constant. *Journal of Optimization Theory and Applications*, 79(1):157–181, 1993.

Chapter 5

Multi-parameter Sensing based on a Numerical Data Processing Technique

5.1 Introduction

As part of this work, a multi-parameter sensing technique that facilitates simultaneous measurement of multiple parameters using a single sensor element has been developed. At the core of the technique is a numerical data processing algorithm that allows the response of the sensor element to the parameters in question to be described using arbitrary mathematical expressions. All of the alternative single-element, multi-parameter approaches reported in the literature require that the expressions used be invertible and/or solvable by analytical means. Avoiding these constraints allows the use of a much wider range of expressions to describe sensor response, which introduces the possibility of increased calibration accuracy.

The arbitrary mathematical expressions that describe sensor response are generated using curve-fitting techniques. The use of this approach, combined with the functionality of the numerical algorithm, eliminates the need to describe the response of the sensor-element using theoretical models, which can be a very time-consuming process. The technique, which was developed in the context of analyte sensitive luminophores, can be considered as a black-box approach that can be applied to any combination of luminophores, without prior knowledge of the theoretical response of the luminophores to the analytes or parameters in question. This allows the rapid development of single-element multi-parameter sensors.

This chapter begins with a description of the concepts involved in single-element, multi-parameter sensing, and then goes on to give a high level description of the technique that has been developed. This is followed by a detailed mathematical description of the technique, and a description of the numerical algorithms that have been developed. An analysis of the factors that govern measurement resolution is then presented. The chapter concludes with an assessment of the performance of the technique using a simulated dataset that represents a single-element dual analyte system.

5.2 Overview of Principle of Operation

The technique that is presented here is based on the concept of analyte-sensitive luminophores, the intensity and/or lifetime of which varies predictably with the magnitude of the analyte of interest. Multiple luminophores that are sensitive to the relevant parameters or analytes are immobilised in the same sensor element. The luminophores that are used are chosen such that they all have different lifetimes, which allows the response of each of the luminophores to be distinguished using frequency or time domain techniques. Although frequency domain techniques involving the use of multi-frequency modulation have been used in this work, time domain techniques, such as that presented in [1, 2], are equally applicable. If possible, the luminophores are also selected such that they have common excitation and emission wavelengths, allowing the use of a single excitation source and single excitation and emission filters, thereby simplifying the design of the optical assembly.

The excitation source is modulated at multiple frequencies, with the number of modulation frequencies corresponding to the number of luminophores, which should also correspond to the number of measurands in question. The presence of a range of lifetimes in the sensor element results in a different response being obtained at each frequency. These multiple responses consist of differing contributions from each of the luminophores and can be described using a system of equations. This system of equations can, in principle, be solved using simultaneous equation techniques to evaluate each of the measurement parameters. This is the approach that has been adopted by other workers [3–5], and requires that the equations used to describe sensor response be solvable using analytical means. In the approach that is presented here, the response of the sensor to the relevant parameter or analyte range at each frequency is described using an arbitrary calibration expression. These expressions are generated from calibration data using curve-fitting techniques. The resulting system of equations is solved numerically using an iterative successive approximation/bisection-based algorithm, in order to determine the value of the parameters or analytes in question. The process is described in detail in the next section.

A multi-parameter technique that also makes use of curve fitting and iterative numerical techniques has recently been developed by Klimant *et al.* [1, 2]. It is inferior to the approach described here, however, as it requires that the expressions describing the sensors response be invertible.

5.2.1 Detailed Description

A two-parameter system is described in the interests of clarity. The technique is inherently scalable, however, with the only limitation to the number of parameters being the availability of multi-dimensional curve fitting tools and the time taken to calibrate the system.

As frequency domain interrogation is being used, the sensor response, S, can be measured in terms of either luminescence intensity or phase angle, with the following being equally applicable to both types of measurements. The sensor response at each frequency, S_{f1} and S_{f2}, can be described by the following system of equations:

$$S_{f1} = F(P_1, P_2) \tag{5.1}$$

$$S_{f2} = G(P_1, P_2) \tag{5.2}$$

where $F()$ and $G()$ are the arbitrary functions that describe the sensor response at each frequency, $f1$ and $f2$ respectively, and P_1 and P_2 are the measurement parameters. For each individual S_{f1} value, which will be denoted $S_{f1}[i]$, there are a range of corresponding pairs of P_1 and P_2 values. If equation 5.1 is represented in 3D space, where equations 5.1 and 5.2 are taken to be of the form $z = f(x, y)$, then these pairs of values will be represented as a curve in the P_1P_2 plane. The curve corresponds to the intersection of the $S_{f1} = S_{f1}[i]$ plane with the surface $S_{f1} = F(P_1, P_2)$. Such curves are referred to mathematically as level curves [6]. The same situation occurs for a value obtained simultaneously at the second frequency, $S_{f2}[i]$, and the surface defined by equation 5.2, resulting in a second curve in the P_1P_2 plane. The intersection point of these two curves gives the parameter values, $P_1[i]$ and $P_2[i]$, that correspond to the sensor values $S_{f1}[i]$ and $S_{f2}[i]$. Mathematically, it can be said that the single set of values of P_1 and P_2 that simultaneously satisfy the following expressions must be found.

$$S_{f1}[i] = F(P_1, P_2) \tag{5.3}$$

$$S_{f2}[i] = G(P_1, P_2) \tag{5.4}$$

A typical set of P_1P_2 curves, which were obtained from a single-element oxygen and temperature sensor, are shown in Fig. 5.1. The numerical data processing

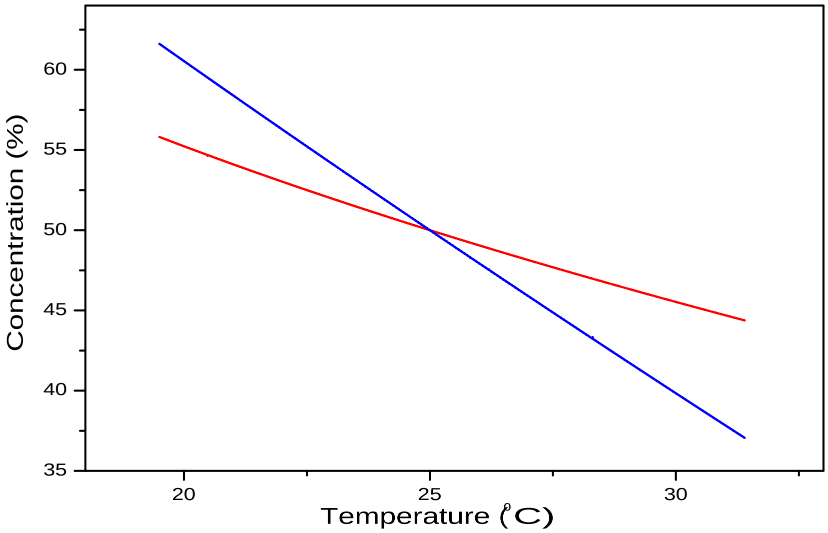

Figure 5.1: Typical P_1P_2 curves that correspond to a single set of sensor values, $S_{f1}[i]$ and $S_{f2}[i]$

algorithm numerically solves equations 5.3 and 5.4 to find the point of intersection discussed above and depicted in Fig. 5.1.

5.3 Implementation

In the implementation of the technique, the sensor is treated as a black-box that is known to respond to the parameters in question in an unknown, monotonic manner. The sensor performance is described by relating the sensor responses directly to the input calibration parameters, without referring to underlying physical parameters (e.g. lifetime) or trying to describe the sensor response with theoretical models of expected behaviour. This leads to a simplified data analysis process that can be easily implemented, provided expressions can be found via curve fitting that accurately describe the sensor's response. As will be seen in sections 5.4.2 and 8.3.2, this is indeed the case.

5.3.1 Calibration Surface Generation

Calibration data are obtained in the usual manner by varying P_1 and P_2 in increments over the relevant ranges and recording the resulting sensor output values. 3D surfaces are then fitted to the datasets (S_{f1}, P_1, P_2) and (S_{f2}, P_1, P_2), using TableCurve3D from Systat Inc, USA. TableCurve3D is a powerful application that rapidly fits a very large number of equations to the dataset in question and returns a list of equations ranked in order of performance. It typically achieves R^2 values of > 0.9999. The highest ranking function that satisfies the requirements detailed in the following section is then selected for the response obtained at each frequency. Typical calibration surfaces for a dual O_2 and temperature sensor are shown in Fig. 5.2.

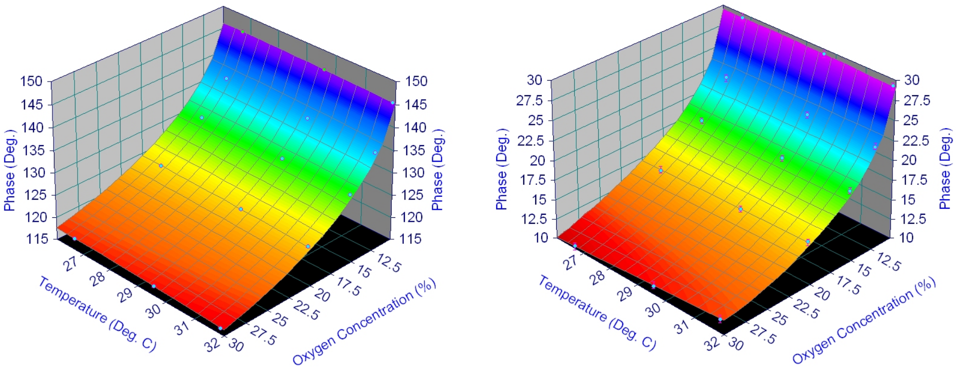

Figure 5.2: Calibration surfaces generated for a dual O_2 and temperature sensor. The surfaces were identified, and rendered, using TableCurve3D

5.3.1.1 Calibration Equation Selection

The highest ranking equation that is returned by TableCurve3D may not necessarily be the best choice. Tablecurve3D ranks the potential equations in terms of R^2 value. There are a number of additional parameters, however, that must be taken into account when selecting the most suitable surface for applications such as this. Tablecurve3D does not test for continuity over the entire calibration range, and it regularly occurs that a function that yields an excellent R^2 value will contain discontinuities. The data processing algorithm will not function correctly if there are any discontinuities present, so the user must ensure that the selected function is continuous over the calibration range. This is typically undertaken using visual inspection of the candidate surfaces. Another parameter that is of importance is the degree of smoothness of the selected function over the calibration range. If the function is not smooth enough, then multiple level curve intersections can occur and incorrect results may be obtained by the data processing algorithm. As is the case with discontinuities, a function that yields an excellent R^2 value can have an unacceptable level of smoothness. The suitability of the candidate functions from a smoothness perspective was assessed by viewing graphical representations the derivative of the calibration surface. If the derivative is monotonic and does not display any points of inflection, then then multiple level curve intersection points are unlikely to occur. The derivatives of candidate functions with acceptable and unacceptable smoothness levels, respectively, are shown in Fig. 5.3. The final parameter relating to fit quality that was taken into consideration was the distribution of the fitting residuals. If it is assumed that the noise in the calibration data is normally distributed, then the ideal calibration function will result in randomly distributed residual values. Visual inspection of a graphical representation of the residual values was carried out to ensure that this was the case.

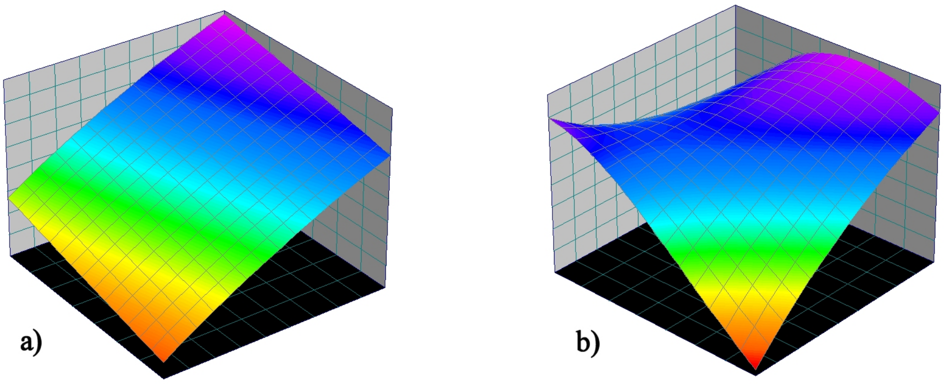

Figure 5.3: Derivatives of candidate calibration functions that both had identical R^2 values. The derivative surface shown in a) satisfies the selection criteria, whereas that in b) does not.

For this work, the surface selection process relied on manual selection by the user. It would be possible to develop algorithms that would fully automate this process. This was not undertaken, however, as the focus of this work was on demonstrating the feasibility of the multi-parameter technique.

5.3.2 Data Processing Algorithm

Given a set of sensor outputs, the data processing algorithm must find the point of intersection of the corresponding P_1P_2 curves. In order to perform this task, two algorithms have been developed that make use of a successive approximation/bisection-based approach. The first implements successive approximation in one dimension, while the second, which is much more computationally efficient, implements two dimensional nested successive approximation. Computational efficiency is determined by the number of operations required to perform a certain operation. The 1D algorithm was used for testing and characterisation purposes due to its simplicity and the nature of its output, while the second was used in any situation where speed of operation was an important factor.

The basic principle of the successive approximation (SA) approach is that a starting range that is known to contain the parameter in question is divided by two with each iteration of the algorithm, with the centre of the range becoming the new parameter estimate. This results in a factor of two reduction in the maximum error in the current estimate with each iteration. The calibration function is evaluated using the the current estimate and a decision is made on whether to stop the algorithm or to perform another iteration-based on the difference between the function value and the supplied sensor measurement value. The maximum permissable difference between these values is specified by the user.

5.3.2.1 1D Successive Approximation Algorithm

The 1D algorithm divides the starting range, R, of one of the parameters into N intervals. The number of intervals is determined by the maximum permissable error in the calculated value, max_error, of the parameter and is given by:

$$N = \frac{2R}{max\_error} \tag{5.5}$$

The algorithm steps through each of the resulting values, determining the value of the other parameter at each using SA. This process results in the P_1P_2 level curve for the sensor measurement in question. The same procedure is repeated for the second sensor measurement value, resulting in a second P_1P_2 curve. the algorithm then determines the point of intersection of the P_1P_2 curves using a search procedure, thereby yielding the set of parameter values that correspond to the supplied sensor measurements. A block diagram representation of the 1D algorithm is shown in Fig. 5.4

Each bisection event that takes place during the SA process results in two ranges. The range that contains the parameter value is identified based on the sign of the slope of the calibration function and the sign of the difference between the function value corresponding to the current estimate and the supplied sensor measurement.

The search procedure that is used to find the point of intersection searches the arrays of P_1P_2 values for the set of points in each array that are closest to each other. The midpoint of these two points is then taken as the result. This approach is quite inefficient and there are a number of more advanced search techniques that could have been used. Efficiency was not a concern, however, for this implementation, and, also, the need for a search step is eliminated in the 2D successive approximation implementation.

5.3.2.2 2D Successive Approximation Algorithm

In this algorithm, the step in the 1D approach where one of the parameters was divided into N intervals is replaced by successive approximation. This algorithm sees the step in the 1D approach where one of the parameters was divided into

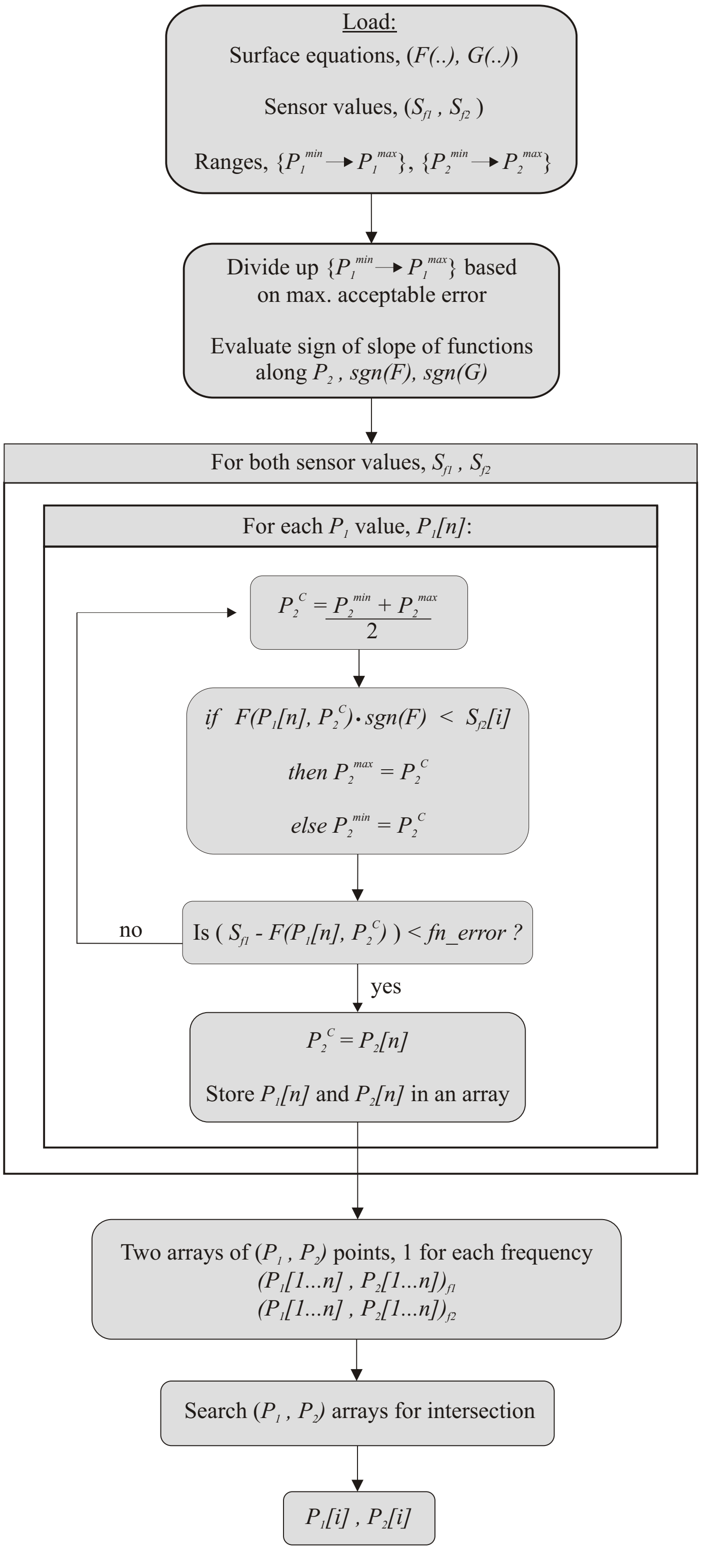

Figure 5.4: Flowchart of 1D successive approximation algorithm. P_2^C is the current estimate of P_2. fn_error is the maximum acceptable difference between the function value corresponding to the current estimate (P_2^C) and the supplied sensor measurement $(S_1$ or $S_2)$

N intervals being with successive approximation. The result is nested, or two dimensional, successive approximation which is substantially more efficient than the 1D approach. A block diagram of the 2D algorithm is shown in Fig. 5.5. The

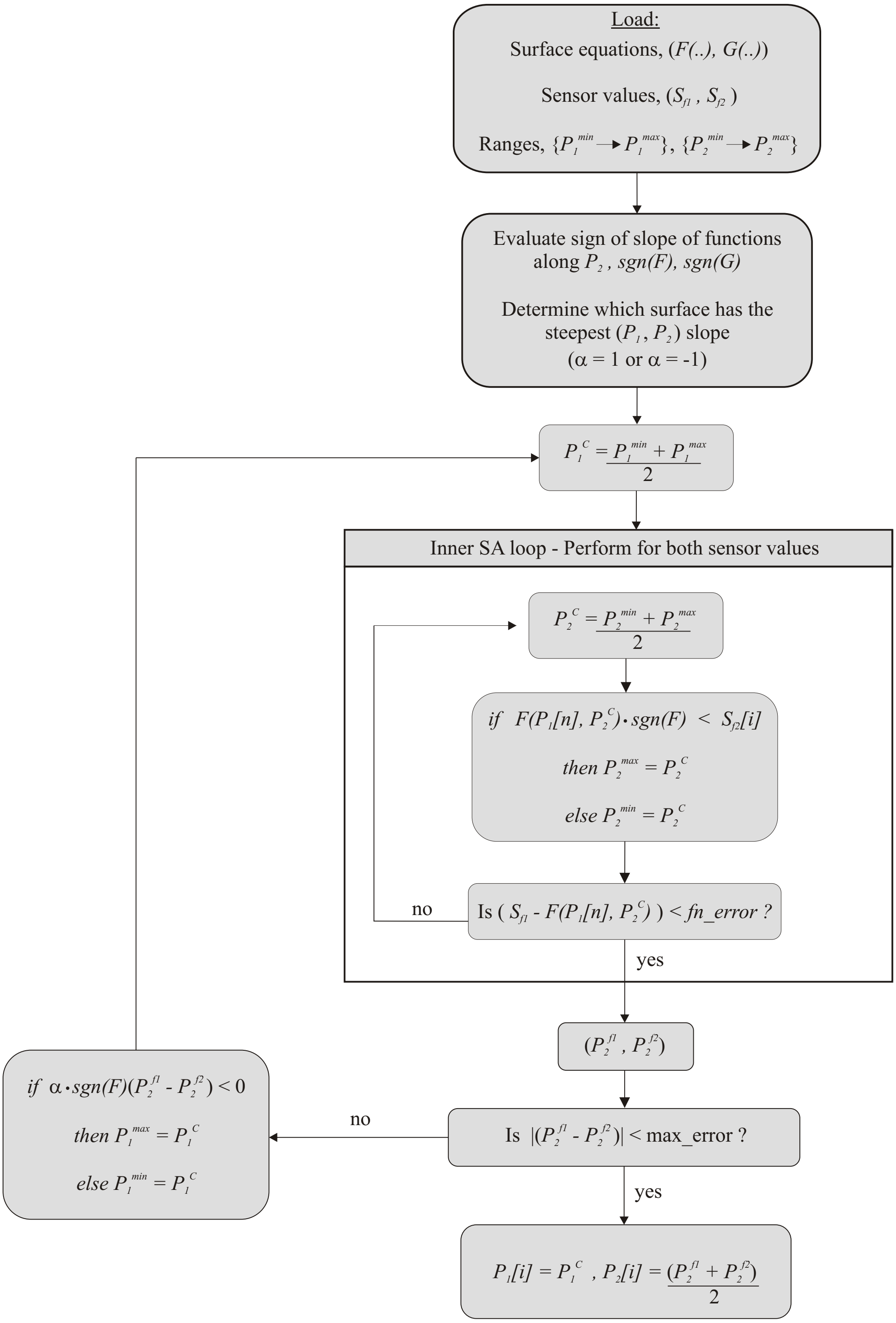

Figure 5.5: Flowchart of 2D successive approximation algorithm. P_1^C and P_2^C are the current parameter estimates.

outer SA loop sets the value of P_1, by dividing the current range in two. The inner SA loop then calculates the corresponding P_2 values for each frequency, P_2^{f1} and P_2^{f2}. The stopping criterion for the outer loop is the magnitude of the difference between these two P_2 values. If they are not close enough, the P_1 range is bisected and the outer loop performs another iteration. The signs of the P_2 slopes for each function, and the relative slopes of the P_1P_2 curves are used to determine which range limit is replaced by P_1^C.

The increase in efficiency over the 1D algorithm comes from the fact that far fewer P_2 values have to be evaluated using the 2D algorithm to achieve the same level of performance. Using the 1D algorithm, if the P_1 range is divided into N intervals, the maximum error in P_1 is given by:

$$max\_error = \frac{2}{N}R \tag{5.6}$$

With the 2D algorithm, the maximum error in P_1 is reduced by a factor of two with each iteration. Therefore, after M iterations of the 2D algorithm, the maximum error is given by:

$$max\_error = \frac{2}{2^M}R \tag{5.7}$$

The number of iterations of the 2D algorithm required to achieve the same maximum error as N iterations of the 1D algorithm is then:

$$M = \log_2 N \tag{5.8}$$

Obtaining the ratio of N and M provides a means of comparing the efficiencies of both algorithms. This yields the expression:

$$\frac{N}{M} = \frac{N}{\log_2 N} \tag{5.9}$$

From this it can be seen that the efficiency improvement is dependent on the required value of N. For $N = 10000$, the 2D algorithm is 750 times more efficient than the 1D algorithm.

5.3.2.3 Coding

Both algorithms were implemented in C using the Microsoft Visual Studio development environment. This approach was chosen over other possibilities as the code that was developed could be easily ported to an embedded system, if realtime application of the technique was required. For the purposes of validation and testing, it was not necessary that the algorithm operate in realtime. As a result, a post-processing-based implementation, in which the sensor data were stored to a file and processed at a later stage, was used.

5.3.3 Selection of Optimum Modulation Frequencies

The optimum modulation frequency for single dye-based phase fluorometry systems has been investigated by a number of researchers. The classic approach, which is presented by Lakowicz [7], takes the optimum frequency to be the value that leads to the maximum system sensitivity, $\frac{d\Phi}{d\tau}$. Zhang et. al. [8] have expanded on this by taking the amplitude, and thus frequency dependence, of the phase noise into account. Kolle [9] has further expanded this by recognising that the majority of phase fluorometry systems make use of photodiodes, which have frequency dependent noise characteristics. He derived an expression that describes the noise characteristics of a photodiode detector and used it to obtain an expression for the optimum modulation frequency that takes the use of photodiode detectors into account. It is quite complex, however, and must be solved numerically. It also requires the measurement or modelling of a number of noise-related system parameters.

Valledor *et al.* [10] have developed a technique for calculating the optimum frequencies for two-dye systems that is based on the classical approach. The mathematical model they have developed is for two dyes with largely different lifetimes, to the extent that the lifetime of one dye can be approximated to zero. This technique also requires the use of numerical techniques to evaluate one of the frequency values.

In the case of a single dye system, the difference between the optimum frequency values calculated using the classical approach and one of the improved approaches (Zhang or Kolle), can be substantial [9]. Given the added complexity of a dual dye system it is then reasonable to expect the accuracy of optimum frequency values calculated using the classically inspired approach developed by Valledor *et al.* to be questionable. A preliminary investigation of the possibility of expanding the approaches developed by Zhang and Kolle to a two dye system was carried out. It was found that the resulting equations were prohibitively complex, and as a result, it was deemed that an empirical approach was the best option.

5.4 Performance

5.4.1 Sensor Resolution

The resolution of a standard single parameter sensor is a function of the measurement noise and the sensitivity of the sensor. The situation with the multi-parameter single element approach that is presented here is more complex however. In addition to noise and sensitivity, resolution is also a function of the relative difference between the responses measured at each frequency.

By considering the graph presented in Fig. 5.1, it can be seen that the resolution of the measurements obtained by the system will depend on the slopes of both P_1P_2 level curves, as well as the slope of the calibration surfaces and the noise in the sensor measurements that are used to generate the P_1P_2 curves. A graphical representation of the factors involved is presented in Fig. 5.6. It was assumed that the level curves are linear on the scale of the noise-induced variations in their positions.

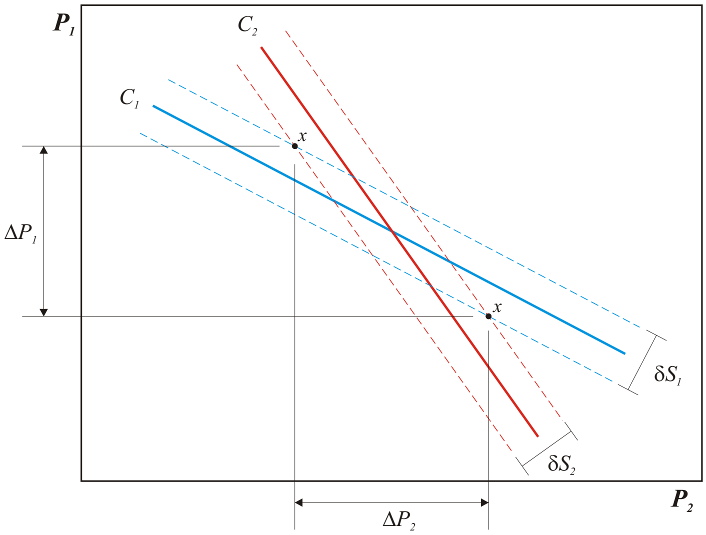

Figure 5.6: This diagram illustrates the factors that govern the resolution of the measurements obtained using the technique that has been developed. The level curves resulting from simultaneous phase measurements at two frequencies are labelled C_1 and C_2. The noise-induced range in the positions of the level curves, δS_1 and δS_2, for a fixed set of parameter values are indicated by the dotted lines.

If the standard peak-to peak noise definition of resolution is used (see section 3.2.3.1), then the resolution is determined by the maximum possible range of the point of intersection of the level curves. This is indicated by the quantities ΔP_1 and ΔP_2 in the diagram. The magnitudes of ΔP_1 and ΔP_2 are determined by the locations of the points marked (x) in Fig. 5.6. The simplest way of quantifying resolution is to measure it in realtime for steady state parameter values. Alternatively, if the peak-to-peak noise in the measurements at each frequency for a given set of parameter values is known, then the maximum and minimum value of each parameter can be used to evaluate the measurement resolution for each parameter using the data processing algorithm. It would have been possible to derive an analytical expression that related resolution to measurement noise using the gradients [11] of the calibration surfaces. There was little benefit in adopting this approach, however, given the fact that the data processing algorithm was already available.

It can be seen from Fig. 5.6 that the values of ΔP_1 and ΔP_2 are considerably larger than the magnitude of the level curve ranges, δS_1 and δS_2. This is an intrinsic property of the technique and implies that the resolution of the parameter values will be larger when measured in a multi-parameter configuration than could be achieved if they were measured separately using single-element techniques. This is an unavoidable consequence of the use of the multi-parameter, single-element technique and should be taken into consideration by the user in situations where resolution is critical.

5.4.2 Simulated Dual Parameter Sensor

In order to evaluate the feasibility of the multi-parameter technique, simulated data were generated using a Matlab model of a simple dual analyte system consisting of two mono-exponential fluorophores with different lifetimes. The model was based around the use of multi-frequency interrogation techniques in conjunction with phase fluorometry.

The relationship between the lifetime of a mono-exponential fluorophore and the phase angle of its emission is given by the expression [7]:

$$\Phi = \tan^{-1}(2\pi f \tau) \tag{5.10}$$

where τ is the lifetime of the fluorophore and f is the modulation frequency. It follows from this expression that the contribution from each of the fluorophores will have different phase angles, and that these phase angles will be different for each of the modulation frequencies. At each of the modulation frequencies, vector addition occurs between the components at each lifetime and it is the properties of the resultant vector that are measured by the instrumentation electronics. The vector addition process is depicted in the phasor diagram shown in Fig. 5.7. The vectors E_1 and E_2 correspond to the shorter-lived and longer-lived of the fluorophores, respectively. The sum of these two vectors, which is denoted by E_T, is what is measured by the phase fluorometry system. By resolving the vectors E_1 and E_2 into their i and j components, the following expressions can

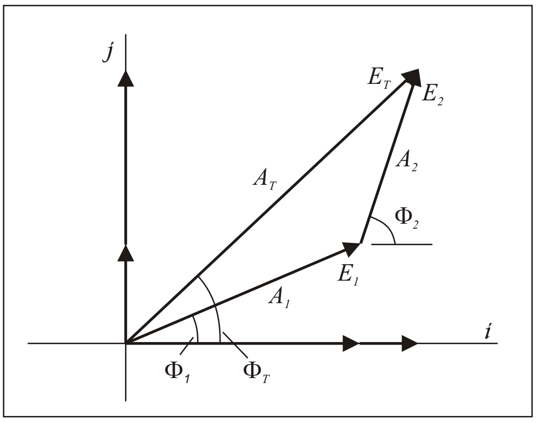

Figure 5.7: Phasor diagram representation of what occurs when two co-immobilised fluorophores with different lifetimes are interrogated at a single frequency. The intensity and phase angle of each of the vectors are denoted by A and Φ respectively.

be obtained for the intensity, A_T, and phase angle, Φ_T, of the vector E_T.

$$A_T = \sqrt{(A_1 \cos\Phi_1 + A_2 \cos\Phi_2)^2 + (A_1 \sin\Phi_1 + A_2 \sin\Phi_2)^2} \tag{5.11}$$

$$\Phi_T = \tan^{-1}\left(\frac{A_1 \sin\Phi_1 + A_2 \sin\Phi_2}{A_1 \cos\Phi_1 + A_2 \cos\Phi_2}\right) \tag{5.12}$$

Equations 5.10, 5.11 and 5.12 form the basis of the set of equations that is required to model the behaviour of the system.

The next step in modelling the behaviour of the system is to introduce the dependence of the lifetime and intensity of each of the fluorophores on the values of the parameters that they are being used to sense. For the purposes of the model it was taken that the relationship between the parameters and the properties of the fluorophores obey the Stern-Volmer model [7], which is described by the expression:

$$\frac{I_0}{I} = \frac{\tau_0}{\tau} = 1 + k\tau_0[Q] \tag{5.13}$$

where I and τ are the intensity and lifetime corresponding to the analyte concentration, $[Q]$, k is the bi-molecular quenching constant and I_0 and τ_0 are the intensity and lifetime values that correspond to an analyte concentration of zero. The purpose of the model was to generate a dataset that could be used to test the multi-parameter algorithm. In order to achieve this, I and τ values were calculated for each fluorophore using equation 5.13 for a number of parameter values in the range $[0.4, 1]$. A lower limit of 0.4 was selected to reflect the fact that real sensors always have a certain amount of unquenchable dye. The value of k was chosen such that the profiles of the resulting I and τ values were similar to those of a typical fluorescence-based oxygen sensor. The intensity values produced by this method reflect a fully modulated fluorescence signal and must be scaled to take the frequency and lifetime dependence on the degree of modulation of the emission into account. The modulation effect is characterised using a quantity referred to as the modulation factor. The modulation factor, m, is defined as the ratio of the excitation light modulation to the emission modulation and is given by [7]:

$$m = \frac{1}{\sqrt{1 + \omega^2 \tau^2}} \tag{5.14}$$

If it is assumed that the excitation source is fully modulated, then the modulation factor can be taken as a measure of the degree of modulation of the fluorescence emission. The corrected or scaled emission intensity, A, is then:

$$A = mI = I \frac{1}{\sqrt{1 + \omega^2 \tau^2}} \tag{5.15}$$

The I values obtained using equation 5.13 were scaled using equation 5.15 and the τ values that were obtained were converted into phase values using equation 5.10. The resulting A and Φ values were then substituted into equation 5.12 to obtain the phase values, Φ_T, that corresponded to the response of the sensor element. This process was carried out for both modulation frequencies. The system parameters that were used during the calculation process are listed in Table 5.1. The simulated data were fitted using TableCurve3D, generating calibration surfaces of the type shown in Fig. 5.2. The corresponding calibration functions were imported into the data processing algorithm, which was operated as described in section 5.3.2.3. In order to test the operation of the algorithm, it had to be supplied with pairs of phase measurement data and the easiest way to achieve this was to use the phase values that were generated by the simulation model and which were used to generate the calibration surfaces. The parameter values calculated by the algorithm are illustrated in Fig. 5.8, alongside the expected values. The analyte values that were used to produce the simulated phase data are shown in blue and the calculated analyte values generated by the algorithm are shown in red. There is excellent agreement between the values calculated by the algorithm and the actual values, which validates the functionality of the algorithm. It was

Parameter	Value
$\tau_0(f_1)$	$5us$
$\tau_0(f_2)$	$300ns$
f_1	$20KHz$
f_2	$60KHz$
N	6

Table 5.1: The values of the various system parameters that were used during the modelling process. N is the number of analyte values that were generated.

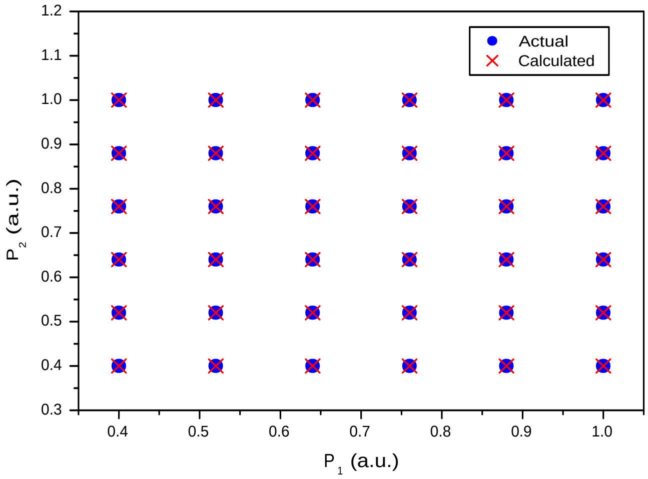

Figure 5.8: This graph represents the results obtained using the multi-parameter technique for a simulated two dye system.

found that the largest discrepancy between the actual and calculated values was 0.0005. No noise was added during the simulation process as its presence may have masked any underlying problems or issues with the algorithm. Once the correct operation of the algorithm was confirmed it would have been possible to add noise to the simulated data in order to assess the resolution of the analyte measurements. However, the results obtained could not be expected to reflect the behaviour of an actual sensor system due to the relative simplicity of the simulation model and as a result of this no such testing was carried out.

5.5 Potential Applications

There are a very wide range of potential applications of the multi-parameter technique that has been presented. The aim of this section is not to attempt to list all, or even a small subset of these potential applications, but rather to identify some of the broad application areas to which it can be applied.

One of the key potential application areas, and the one that has been used as an example throughout this chapter, is a single-element-based sensor that contains luminophores that are sensitive to two different analytes. An example of this would be a combined DO/pH sensor. Another key application area involves the use of luminophores that display cross-sensitivity to a number or all of the target analytes or parameters. An important property of the multi-parameter algorithm is that it can be used with luminophore combinations that display cross-sensitivity to the other analytes of interest. An example of this type of application would be a simultaneous oxygen and temperature sensor that consists of two oxygen and temperature-sensitive dyes that display differing sensitivities to oxygen and temperature. Such a system is presented in chapter 8.

Up to this point, all discussion has referred to the application of the technique to single-element systems. It is also applicable, however, to certain multi-element configurations. In certain situations the development of a single-element approach may not be desirable or feasible, and in such cases it is possible to achieve the same functionality using two sensor elements that are located in close proximity to one another. If the separate sensor elements are chosen such that they are cross-sensitive to the relevant parameters to differing degrees, then the cross-sensitivity principle introduced in the previous paragraph will apply and the multi-parameter technique can be used to measure both parameters. A system that makes use of this technique, which was developed in order to avoid the difficulties involved in developing a single-element sensor during early testing, is described in chapter 8.

5.6 Conclusions and Future Work

A technique has been developed that allows the simultaneous measurement of multiple parameters using single-element and multi-element configurations. It is based on a custom-developed numerical data processing algorithm that overcomes a number of the limitations associated with conventional multi-parameter approaches. Two distinct implementations of the algorithm have been tested, with one having much improved computational efficiency, facilitating its use in embedded realtime applications.

The technique makes use of curve fitting techniques that are applied directly to the raw calibration data. Moreover, they do not rely in any way on a theoretical understanding or description of the behaviour of the luminophores that have been used. The net result of these two factors is that the system represents a powerful black-box type approach that can be rapidly applied to a new sensor system without the necessity for time-consuming and potentially less accurate theoretical work to be carried out.

In order to verify that the technique, and more specifically the data processing algorithm, function correctly, a dual analyte, single-element-based sensor was modelled. The resulting data were processed using the algorithm and it was found that there was excellent agreement between the algorithm results and the expected values.

Although the technique has been presented and explained in terms of a dual-analyte approach, it is inherently scalable, and it is intended that it be expanded to 3 or more analytes in the near future. If this scale-up is successful, it could introduce the ability to apply optical sensors to ‘electronic-nose’ type applications.

Bibliography

[1] C. R. Schroeder, G. Neurauter, and I. Klimant. Luminescent dual sensor for time-resolved imaging of pco(2) and po(2) in aquatic systems. *Microchimica Acta*, 158(3-4):205–218, 2007.

[2] Claudia R. Schroeder, Lubos Polerecky, and Ingo Klimant. Time-resolved pH/pO(2) mapping with luminescent hybrid sensors. *Analytical Chemistry*, 79(1):60–70, 2007.

[3] O. S. Wolfbeis and E. Urbano. Fluorescence quenching method for determination of 2 or 3 components in solution. *Analytical Chemistry*, 55(12):1904–1906, 1983.

[4] S. M. Borisov, G. Neurauter, C. Schroeder, I. Klimant, and O. S. Wolfbeis. Modified dual lifetime referencing method for simultaneous optical determination and sensing of two analytes. *Applied Spectroscopy*, 60(10):1167–1173, 2006.

[5] G. S. Vasylevska, S. M. Borisov, C. Krause, and O. S. Wolfbeis. Indicator-loaded permeation-selective microbeads for use in fiber optic simultaneous sensing of ph and dissolved oxygen. *Chemistry of Materials*, 18(19):4609–4616, 2006.

[6] Eric W. Weisstein. *Level Curve.* From MathWorld–A Wolfram Web Resource, `http://mathworld.wolfram.com/LevelCurve.html`.

[7] J. R. Lakowicz. *Principles of Fluorescence Spectroscopy, 3rd ed.* Springer, New York, 2006.

[8] Z. Y. Zhang, K. T. V. Grattan, and A. W. Palmer. Phase-locked detection of fluorescence lifetime. *Review of Scientific Instruments*, 64(9):2531–2540, 1993.

[9] Christian Kolle. *Development and evaluation of a phase fluorometric instrument for different luminescence based optical oxygen sensor applications.* Ph.D. Thesis, University of Leoben, 1999.

[10] Marta Valledor, Juan Carlos Campo, Israel Snchez-Barragn, Jos M. Costa-Fernndez, Juan Carlos Alvarez, and Alfredo Sanz-Medel. Determination of phosphorescence lifetimes in the presence of high background signals using phase-shift measurements. *Sensors and Actuators B: Chemical*, 113(1):249–258, 2006.

[11] Eric W. Weisstein. *Gradient.* From MathWorld–A Wolfram Web Resource., `http://mathworld.wolfram.com/Gradient.html`.

Chapter 6

An Oxygen Sensor for Realtime Measurements in Breath

6.1 Introduction

A sensor system has been developed at this laboratory that measures breath-by-breath oxygen uptake by human subjects. A considerable amount of the development work was completed by the author as part of this work, with the primary contributions being the instrumentation electronics systems that were used to interrogate the sensor film and the development of the oxygen uptake calculation algorithm. The system is based on an optical oxygen sensor that is placed directly in the subject's airstream. This allows the oxygen concentration to be measured across the full breath profile, and represents a significant improvement over all current instruments, which measure oxygen concentration at only two points in a full breath cycle.

Placing the oxygen sensor directly in the airstream presents a number of challenges due to the necessary response time requirements and the presence of significant, rapidly changing, temperature and humidity gradients. The system developed makes use of the custom-designed phase fluorometry systems described previously, and also utilises the parabolic-element-based optical probe introduced in chapter 4 to maximise fluorescence capture. The use of these high performance component systems, together with a sensor film that was optimised for use in breath monitoring applications, results in the necessary performance criteria to operate in such a challenging measurement environment.

This chapter begins with a brief overview of the motivation for this work and then goes on to describe the basic measurement principle on which it is based. A description of the system and each of its constituent elements is then provided, and this is followed by a high level description of the test and calibration setups that were developed. The key sensor performance criteria are then presented, and the chapter concludes with the presentation and analysis of data from a test subject.

6.2 Motivation/Background

As a result of the fundamental role oxygen plays in human metabolic processes, the measurement of oxygen uptake is clinically relevant in a variety of situations. These range from simple fitness tests, where parameters such as VO_2max [1] provide information on aerobic capacity and fitness levels, to advanced topics in clinical research and applications where the measurement of oxygen uptake plays a key role. These research areas include exercise physiology [2–4] , chronic obstructive pulmonary disorder (COPD) [5, 6] and cystic fibrosis [7] among many others. A search of the literature reveals that > 30 refereed papers that involve the measurement of oxygen uptake have been published in 2010 alone, a clear indicator of its continuing relevance.

Current techniques for the measurement of oxygen uptake rely on the use of either bulky laboratory based equipment (e.g. [8]), or portable systems with electrochemical based oxygen sensors (e.g. [9]). To the best of the author's knowledge, all of these systems rely on the use of sampling techniques, where a plug of air is sampled from each breath and transferred to the gas sensor through dehumidifying tubing. The volume of oxygen in the corresponding breath is then inferred from this single value using look-up table techniques, or similar.

The use of an optical oxygen sensor that could be placed directly in the air stream provides considerable scope for improvements in performance. It would facilitate true breath-by-breath measurement, where the oxygen concentration is measured across the entire breath instead of at just a single point. This would result in simplified measurement algorithms and could potentially lead to increased measurement accuracy. Additionally, electrochemical-sensor-based portable systems have been found to be quite unreliable [10], and it was possible that the inherent advantages associated with optical sensors, which are discussed in chapter 2 would lead to improved system performance.

6.3 Theory of Operation

The basic concept behind the system is that if both oxygen concentration and volumetric flow rate are measured, then the amount of oxygen being consumed can be determined. By combining oxygen concentration and flow rate values, the volume of oxygen in an inhaled breath and the subsequent exhaled breath can be determined. The difference between these two values is the volume of oxygen consumed during the breath cycle. Mathematically, this involves numerically integrating the product of the flow and oxygen concentration values over the breath cycle. The oxygen uptake in a single breath, $VO_2(Br)$ is given by the expression:

$$VO_2(Br) = \sum_{n=1}^{N} F[n] \frac{C[n]}{100} \Delta T \qquad (6.1)$$

where F is volumetric flow rate (L/s), C is oxygen concentration (%), and ΔT is the sampling interval (s). N is the number of sensor samples in the breath cycle. It is possible to integrate over the full breath cycle without separating the inhaled and exhaled portions as the flowmeter values have a different sign for each. Each breath cycle must be identified, which can be accomplished by locating the zero crossing points of the flowmeter data. The standard convention for flowmeters is that exhalation is deemed to be positive flow, while inhalation is negative. This means that a negative-going zero-crossing marks the crossover from exhalation to inhalation, which is the start of a breath cycle. Once two such zero crossings are located, equation 6.1 can be used to evaluate the oxygen uptake during what will then be the previous breath.

6.4 Sensor System

The main components of the breath-by-breath oxygen measurement system that was developed are a fluorescence-based optical oxygen sensor, and a volumetric flowmeter.

The oxygen sensor consists of an oxygen-sensitive fluorescent dye immobilised in a solgel matrix, phase-fluorometry-based interrogation electronics, and an optical assembly that makes use of an enhanced capture structure to maximise fluorescence capture.

A commercially available flowmeter, which was designed specifically for human breath applications, was used for flow measurement.

Each of the constituent elements of the system is described in detail in the following sections.

6.4.1 Oxygen Sensitive Films

The oxygen sensitive films, which are described in detail in [11] and [12], consist of the oxygen sensitive fluorophore [Ru(II)tris(4,7-diphenyl-1,10-phenanthroline)]$^{2+}$ ($[Ru(dpp)_3]^{2+}$), immobilised in a porous solgel matrix. There are a number of oxygen sensitive dyes available, with $[Ru(dpp)_3]^{2+}$ being chosen due to its high quantum efficiency, large Stokes shift and relatively long lifetime. The high quantum efficiency results in high brightness and increased sensor SNR, the large Stokes shift simplifies the design of the optical assembly, and the long lifetime facilitates the use of low cost phase fluorometry-based interrogation electronics.

There are a range of sensor film characteristics that must be optimised for breath oxygen sensing. These include sensitivity in the $15-21\%$ range, response time, and humidity sensitivity. A short response time is important due to the rate at which breath oxygen concentrations change at medium to high breathing rates. Minimal humidity sensitivity is an important requirement due to the large range in humidity levels the sensor film is exposed to during each breath cycle. The humidity of ambient air would be expected to lie in the range $60-90\%$, while that of exhaled air is $\sim 100\%$. Colleagues tested films composed from a range of solgel precursors in order to determine what precursor yielded the best films for breath oxygen sensing purposes. Details of the preparation and characterisation of the various films can be found in [11] and [12]. Films based on the precursor n-propyltriethoxysilane (PTEOS) were found to be the best choice as they exhibited high sensitivity in the required oxygen concentration range and very low humidity sensitivity.

6.4.2 Optical Assembly

An optical assembly that utilised cone-shaped enhanced capture structures was used in the early stages of the project for film testing and characterisation. This early stage system, which is described in [13], was replaced by the original parabolic element-based design (Probe 1). The sensor cap was replaced with an adaptor module that accommodated standard size mouth-pieces on one side and the chosen flowmeter on the other. As the subject breathed in and out, air would pass across the sensor film and through the flowmeter.

A $450nm$ LED (LED450-06U, Roithner Lasertechnik), which matched the absorption peak of $[Ru(dpp)_3]^{2+}$, was used as the excitation source in the probe and a Si-PIN photodiode (S1223-01, Hamamatsu) was used for detection purposes. As discussed in section 2.5, optical emission and excitation filters must be included in the probe. An interference type bandpass filter (FF02-447/60-25, Semrock Inc, USA) with a $60nm$ wide pass-band centred at $447nm$ was used as the excitation filter. An interference type long-pass filter (FF01-519/LP-25 Semrock Inc, USA), which had a cut-on wavelength of $530nm$ was used as the emission filter. Interference-based filters were chosen as they provide the highest level of blocking in the stop-band of any optical filter type, and, as was explained in section 3.2.2.3, this is necessary to minimise intensity sensitivity of the phase measurements. The absorption and emission spectra of $[Ru(dpp)_3]^{2+}$, and the transmission spectra of the excitation and emission filters are shown in Fig. 2.8.

6.4.3 Electronics

Two of the electronics systems that are described in chapter 3 were used over the course of this work. The analog phase fluorometry system described in section 3.2.2 was used for the majority of the work, and the portable digital phase fluorometry system was used in the final stages of the project.

Both systems were used as described in chapter 3, without any modifications. The analog system was operated at a result generation rate of $\sim 8/s$, which corresponds to a sampling interval of $125ms$. The digital system generates results every $40ms$ and these were averaged by the PC interface software to achieve an effective generation rate of $\sim 8/s$. This software consisted of a Labview-based GUI that received raw data from the sensor, carried out any necessary processing and then displayed it on-screen for user inspection. All data was stored to file for later use.

6.4.4 Temperature Compensation

The temperature of exhaled air is $\sim 37°C$, while that of ambient air is typically in the range $15 - 25°C$. This represents a substantial change in temperature over each breath cycle, and when the fact that $[Ru(dpp)_3]^{2+}$ displays significant temperature sensitivity is taken into account, it becomes apparent that temperature compensation is critical. The standard approach, which involves measuring the temperature of the film using a separate temperature sensor and calibrating the sensor response over the range of possible temperatures, was used. Accurately measuring the temperature of the film is complicated by the fact that it changes so rapidly. For athletes at peak exertion, respiratory rates can exceed 60 breaths/min, which corresponds to a full temperature cycle every second. A temperature sensor had to be selected that could respond at these rates of change. In order to be able to measure such changes with reasonable accuracy, a sensor with a T_{10-90} thermal response time in air of $< 150ms$ was required. The t_{10-90} response time of a sensor corresponds to the time taken for the sensor output to change from 10% to 90% of the final value, when exposed to a step change.

Both phase fluorometry systems were designed to be used with resistive temperature sensors. The majority of commercially available resistive sensors have T_{63} thermal response times in air of several seconds, making them totally unsuitable for this application. A hand-made micro-bead thermistor which had a T_{10-90} thermal response time in air of approximately $100ms$ was sourced in small quantities, and was used in this work. A number of options were investigated for achieving good thermal contact between the thermistor and the sensor film and it was found that glueing it to the sensor slide, to one side of the active area, using an epoxy-based adhesive, achieved the best results.

6.4.5 Flowmeter

There are a number of flowmeters available commercially that have been designed specifically for use in breath measurement applications. They all employ thermal, pressure differential, or impeller-based measurement principles. The thermal sensors make use of hot-wire anemometer (HWA) [14] techniques, in which the heat transfer from a heated sensor element is related to flow. The pressure-based sensors measure flow by measuring the pressure differential either side of an obstruction in the flow. In the impeller-based sensors, a lightweight impeller is placed in the flow and is interrogated by optical chopper techniques. The resulting signal is inherently digital and these type of flowmeters are often referred to as digital volume transducers (DVTs). HWA-based sensors are influenced by gas composition, temperature and humidity [14], and suffer from poor stability, requiring frequent recalibration. Pressure-based sensors are sensitive to temperature and humidity and also suffer from poor stability [15]. DVTs are affected to a much lesser extent by these factors and are considerably more stable [16, 17]. As a result they were deemed to be the best choice for this application. A commercial DVT flowmeter, the SpiroUSB from Micro Medical Ltd, UK was purchased and was used for all of the flow measurements carried out during the project.

The original firmware on the sensor allowed for continuous measurements to be obtained for 60 seconds. This was not adequate, so the research and development department of Micro Medical Ltd provided modified firmware that allowed for continuous measurements to be obtained. The interface software for the device was provided in the form of an Activex control. A Labview VI was written that interfaces with the ActiveX control, which provides GUI-based user control over the device and also records the time-stamped flow data returned by the sensor.

6.5 Test and Calibration Systems

Dynamic characterisation of the sensor was required due to the rapid changes in oxygen concentration that the sensor experienced during use. A lung simulator was sourced that allows the dynamic performance of the sensor to be characterised, however it was not suitable for calibration purposes. This was due to the fact that the oxygen concentration in the air leaving the simulator could not be precisely controlled. It was also not possible to control the temperature of the air leaving the device. There were no alternative solutions that would have allowed dynamic calibration of the sensor so instead a static calibration technique was opted for. This saw the sensor element being exposed to steady-state, or static, oxygen concentration and temperature values. The oxygen concentration and temperature were varied in discrete steps over the required ranges, with oxygen concentration and temperature being recorded at each. Temperature control was achieved by heating the calibration gas being flowed over the sensor, which in turn heated the sensor. This approach avoided the cooling related problems that the calibration gas flow would have led to if other heating techniques were used.

6.5.1 Static Calibration Facility

A diagram of the static calibration setup is shown in Fig 6.1. The module adaptor described in section 6.4.2 was converted into a flowcell by fitting end-caps in place of the mouthpiece and flowmeter. Gas tubing fittings were added to the end-caps to allow gas to be flowed through the cell. Oxygen concentration is controlled by delivering precisely metered ratios of nitrogen and oxygen using computer controlled mass flow controllers (MFCs). The metered gases are then introduced to a single gas line where mixing takes place. The MFC flow rates are controlled such that the total delivered volume gas remains constant in order to eliminate the possibility of flow or volume induced inaccuracies. The temperature of the gas is controlled using a resistive type gas heater, with the gas mixture from the MFCs being passed through the heater before entering the flow cell.

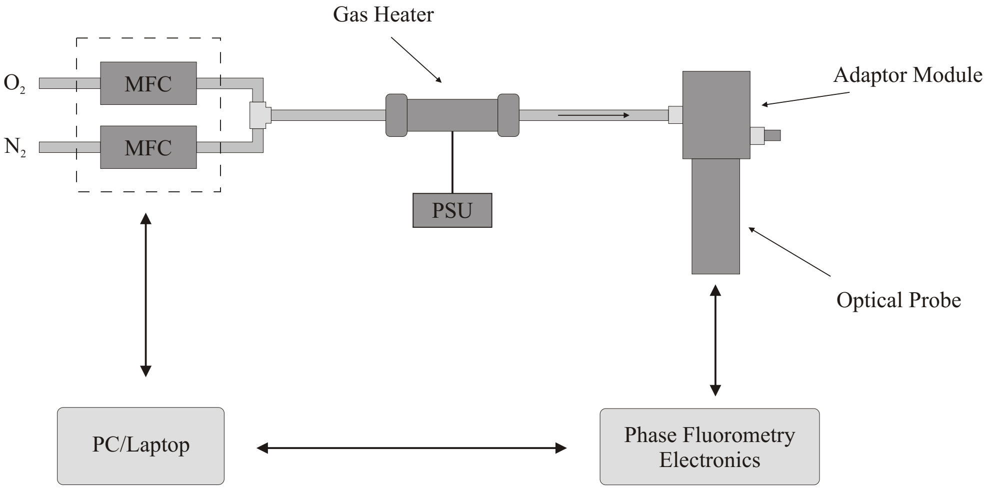

Figure 6.1: Static calibration and test setup.

6.5.2 Lung Simulator

A simple representation of the lung simulator is shown in Fig. 6.2. The lung simulator is a commercially available device and was purchased from Vacumed Inc, USA. It is essentially a large motor driven syringe. It has a maximum capacity of $4L$, which corresponds to the upper limit of tidal volume range found in the general population. Reduced volumes of 1, 2 or $3L$ can also be obtained by changing the position of the piston drive arm on the drive wheel. The speed of the drive motor can be adjusted to achieve a stroke rate range of $< 1 - 60$ $strokes/minute$. Oxygen uptake is simulated by introducing a metered amount of CO_2/N_2 mix into the chamber during the inward stroke. This results in reduced oxygen partial pressure in the air expelled during the following outward stroke. The introduction of the CO_2/N_2 mixture requires the use of a gas storage bladder and a valve system. However, these have been omitted from Fig. 6.2 in the interests of clarity.

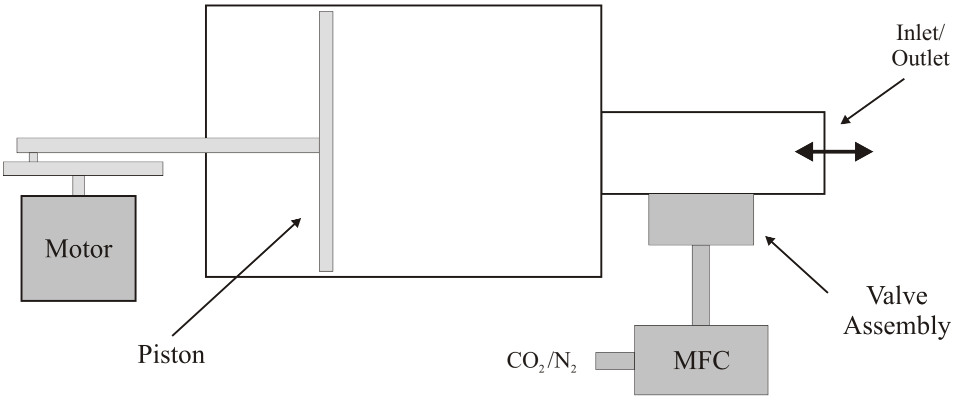

Figure 6.2: Lung simulator used for testing the dynamic performance of the sensor.

6.5.3 Sensor Calibration

As mentioned previously, the sensor was calibrated by varying the oxygen concentration and temperature over the required ranges and recording the resulting sensor outputs. The typical range of oxygen concentration in breath is $16 - 21\%$. However, as will be seen in section 6.7, the volume of the sensor system, or dead-space as it is commonly referred to, causes lower than expected oxygen levels in the exhaled breath of the user. It was therefore necessary to calibrate the sensor over the oxygen concentration range of $13 - 22\%$.

The gas heater that was used to control the temperature of the calibration gas entering the cell was a basic model and did not have temperature control or measurement capabilities. It simply added a certain amount of heat, which was a function of the heater supply voltage, to the gas as it passed through the heater. This meant that the user had to manually set the supply voltage to achieve the required sensor film temperature. Even though the air flowing across the sensor film changed from $\sim 20°C$ to $\sim 37°C$, the temperature of the film did not necessarily change over the same range due to the thermal mass of the probe to which it was attached. In order to avoid calibrating the sensor over an excessive range, the temperature range encountered during a test cycle was determined and used as the calibration range.

It took approximately thirty minutes to achieve a stable film temperature value following a change in the heater supply voltage, while oxygen concentration stabilised within $2-3$ seconds of it being changed. As a result, the sensor was calibrated by setting a particular temperature, and then scanning through all of the required oxygen concentration values at that temperature before moving on to the next temperature setting. Typical calibration data are shown in Fig. 6.3 for four temperature settings and seven oxygen concentration settings. In order

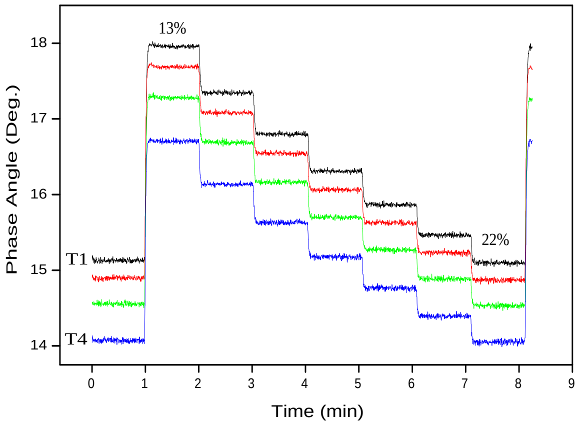

Figure 6.3: Calibration data for four temperature steps, labelled in order of increasing temperature, and seven oxygen settings, which progress in increments of 1.5% from $13-22\%$. The temperature values correspond to the film temperature range encountered during human breathing. This range was evaluated in terms of raw ADC units and as a result the actual temperature values cannot be provided.

to obtain a calibration equation for the sensor from these data, oxygen concentration, temperature and phase angle triplets $(C(\%), T, \Phi)$ were obtained for each oxygen concentration and temperature setting, and a 3D surface was fitted to the resulting dataset. Before obtaining the triplet data from the raw calibration data graphs, the curves were smoothed using 100 point adjacent averaging in order to increase the accuracy of the resulting fit. The 3D fitting process was carried out using TableCurve3D, as described in section 5.3.1, resulting in an arbitrary expression that best described the calibration data. The best fit surface for the data in Fig. 6.3 is shown in Fig. 6.4. The raw temperature readings from the phase fluorometry electronics have not been converted to temperature values as the thermistor calibration process would serve to reduce the overall accuracy of the oxygen measurements. This is due to the finite accuracy that is associated with virtually all curve fitting processes, regardless of the fit quality, and can be prevented by using raw sensor data. In addition, the use of raw ADC values impacts positively on computational efficiency of the oxygen concentration calculation process.

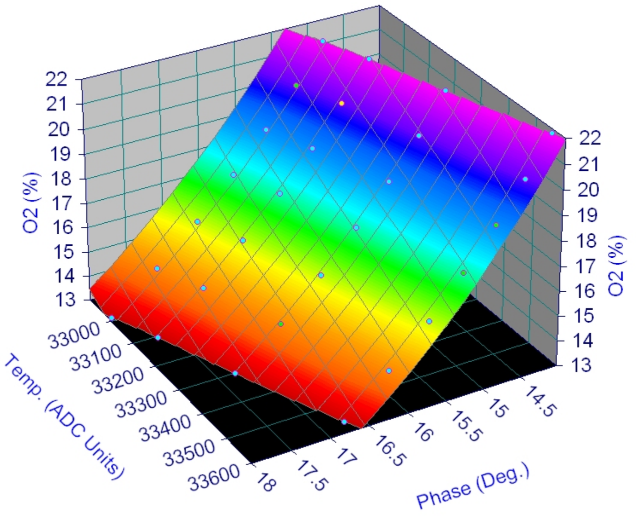

Figure 6.4: Calibration surface for the raw calibration data shown in Fig. 6.3. The temperature data is expressed in terms of raw ADC units. The fit has an R^2 value of 0.999997.

6.6 System Characterisation

The relevant performance criteria of the oxygen sensor have been assessed using the appropriate test setup. The performance of the flowmeter had to be taken to be that which was stated by the manufacturers as the equipment that would have been necessary to characterise its performance was not available.

The key performance criteria for breath oxygen measurements are response time, humidity sensitivity and resolution.

6.6.1 Response Time

The accurate measurement of sensor film oxygen response times is a non-trivial task and requires the use of custom designed test systems based around high speed solenoid valves. The construction of such a system could not be justified in this case so instead of measuring the actual response time of the films, the sensor response characteristics that are influenced by response time were investigated. Response time is an important parameter for breath oxygen measurement, as it is necessary that the film fully respond to the rapid changes in oxygen concentration that it is exposed to. The response of the sensor at a range of breathing rates was assessed using the lung simulator. The simulated oxygen uptake by the lung was kept constant and the breathing rate was varied over the physiologically relevant range. The maximum breathing rate that did not result in a change in the oxygen concentration range measured by the sensor was taken as a measure of the response time.

There is a direct film thickness-induced trade-off between resolution and response time [18]. Thicker films contain more fluorescent material, which impacts positively on resolution, however the increased film thickness decreases response time due to decreased oxygen diffusion rates. A range of sensor film thickness, which were obtained by drop-coating various amounts of the sol onto glass cover-slides, were tested using the technique that has been described. It was found that the film thickness that was obtained when $1\mu L$ of the sol was used did not display any response time-related limitations in oxygen response for breathing rates of up to 40 breaths/min. The results that were obtained are presented in [18].

6.6.2 Humidity Sensitivity

The importance of minimal humidity sensitivity has been discussed previously. The best way to assess the humidity sensitivity of the films would have been to use the lung simulator or a similar dynamic system. This would have resulted in the most accurate representation of the conditions that the sensor would be exposed to in use. However, it was not possible to adapt the lung simulator for use with humidified gas samples, or to develop and alternative approach that would have resulted in the required gas flow rates.

During the process of selecting the optimum sensor film formulation [11, 12], the humidity sensitivity of each of the candidate film compositions was tested using a static approach. This was accomplished by passing the gas mixture emerging from the MFCs in a typical static calibration system, such as that described in section 6.5.1, through a series of gas wash-bottles in order to humidify it. While not an accurate representation of the conditions in which the sensor will be used, the results that were obtained using this approach will still give a good indication of the degree of humidity sensitivity that could be expected. The response of the PTEOS-based film that was selected for this work to humidified and non-humidified calibration gas mixtures is shown in Fig. 6.5. It can be seen that there is negligible humidity sensitivity.

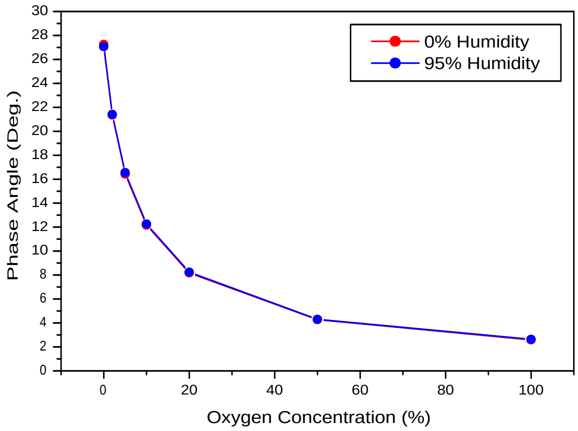

Figure 6.5: The response of the PTEOS-based oxygen sensor film that was used for this work to humid and dry calibration gases [19].

6.6.3 Resolution

As discussed previously, there is a direct trade-off between the response time and resolution of the sensor films, and that the relationship between the two is a function of the film thickness. In this case the film thickness was selected on the basis of achieving a given response time, which meant that it was not possible to have any control over resolution. It is still useful to quantify it, however, as it will provide a means of evaluating alternative film compositions, should the need arise.

The resolution of the system at 22% was evaluated by measuring the peak-to-peak noise in the signal (see section 3.2.3.1). The resulting value is listed in Table 6.1.

Resolution (%)
0.36

Table 6.1: Oxygen measurement resolution of the breath oxygen sensor at an oxygen concentration of 22%.

6.7 Breath Oxygen Measurement

The oxygen sensor and flowmeter were combined to form a single module, which was then fitted with a standard mouthpiece. Correct operation of the system requires precise synchronisation of the flowmeter and oxygen sensor data, which required that the data from both sensors be accurately time-stamped. The flowmeter data are time-stamped by default and the oxygen sensor firmware was modified to incorporate time-stamping functionality, which time-stamped each data point with $< 1ms$ accuracy. A Labview VI was written that interfaced simultaneously with the oxygen sensor and flowmeter and combined their respective data streams. The Labview program also incorporated an interpolation routine that matched the sampling rates of both sensors.

Typical human oxygen sensor and flowmeter data, which were obtained from a test subject who was at rest, are shown in Figs. 6.6 and 6.7. The sensor

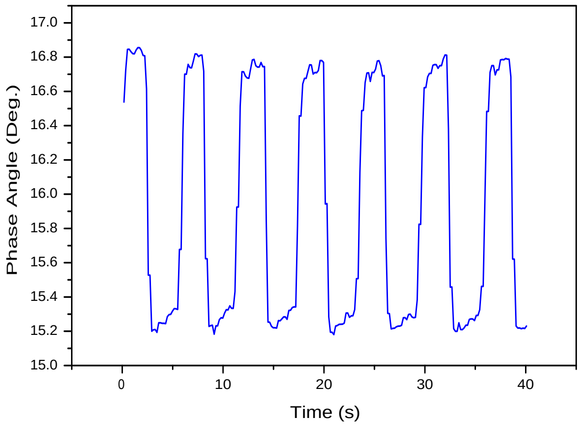

Figure 6.6: Raw, uncalibrated, oxygen sensor data obtained during a human trial, where the subject was at rest.

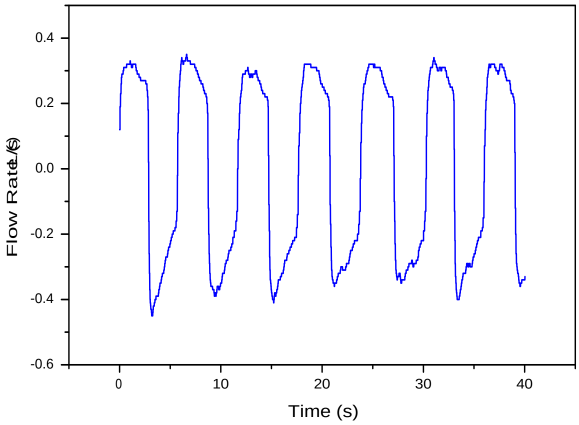

Figure 6.7: Flowmeter data that corresponds to the oxygen sensor data shown in Fig. 6.6.

film temperature sensor value is recorded alongside each oxygen sensor value.

The raw oxygen and temperature sensor data are processed using the calibration equation generated during the calibration process to obtain actual oxygen values. This has been carried out for the raw data in Fig. 6.6 and the resulting oxygen concentration data are shown in Fig. 6.8. There are a number of features in the data presented in Fig. 6.8 that can be associated with the breathing process, which suggests that the system is functioning correctly. When the subject starts to inhale, the oxygen concentration changes rapidly and quickly reaches a plateau, which corresponds to ambient oxygen concentration. When the subject starts to exhale, the oxygen concentration decreases at a slower rate than on inhalation and tapers to a final value. This taper corresponds to increasing CO_2 levels in the air from deeper in the lungs. This is in contrast to the raw oxygen sensor data in Fig. 6.6, where this pattern cannot be observed, indicating the importance of accurate temperature measurement.

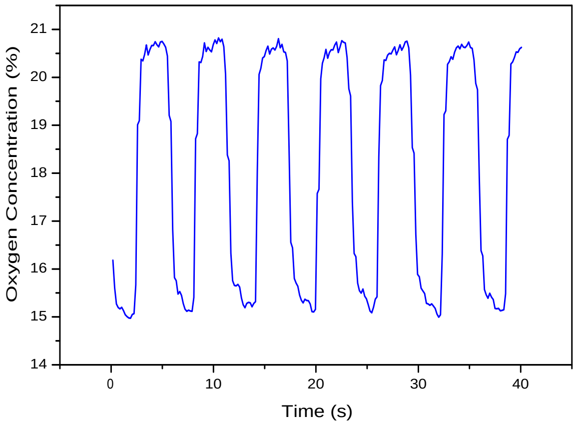

Figure 6.8: Calibrated version of the raw data shown in Fig. 6.6.

For a healthy individual at rest, the oxygen concentration in exhaled breath is expected to be approximately 17%. The oxygen concentration indicated by the sensor can be seen to drop to below 15% in Fig. 6.8, which is significantly below the expected value. At first it was thought that there was a problem with the sensor and that it was returning erroneous values. However, the results were found to be very repeatable and recalibration and diagnostic testing of the system did not reveal any problems. The volume of air contained by the assembled system was quite large and it was suspected that the associated ‘dead-space’ effects may be responsible for the low oxygen values that were being observed. In order to test this hypothesis, the dead-space of the system was substantially reduced by removing the flowmeter and using a shorter mouthpiece. The modifications resulted in the volume of air held by the system being reduced from $392cm^3$ to

$99cm^3$. A test run was completed by the same test subject under identical conditions using the modified system. A segment from the resulting oxygen profile is shown in Fig. 6.9. It can be seen from the data in Fig. 6.9 that reducing the dead-space of the system has a significant impact on measured oxygen concentration, with the exhaled oxygen concentration changing from 15% to 17% as the dead-space was reduced from $392cm^3$ to $99cm^3$. The data presented in Fig. 6.8 and 6.9 suggest that having a large system volume or dead-space, causes changes to the oxygen concentration in the air exhaled by the test subject. This is not a desirable situation and in order to minimise the effect, the system should be designed to have as small a volume as possible.

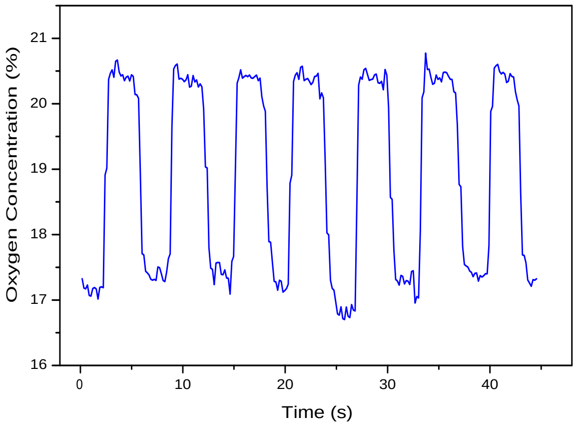

Figure 6.9: Oxygen concentration profile observed when using a system configuration with reduced deadspace.

6.7.1 Oxygen Uptake Measurements

Once the raw oxygen sensor data have been processed using the calibration equation and the resulting calibrated data and the corresponding flowmeter data are synchronised, oxygen uptake can be calculated using equation 6.1. A 7.5 minute human trial was completed with the subject at rest and the oxygen uptake was calculated from the resulting data using equation 6.1. The calculated uptake values per breath are shown in Fig. 6.10. The most striking feature in these data is the presence of positive values, which would indicate oxygen production, instead of consumption. This seems counter-intuitive. It can be understood however by considering that oxygen uptake is being evaluated on a breath by breath basis, and that the data in Fig. 6.10 represent discrete breath events, and not a continuous quantity. If a greater volume of air is exhaled during a breath cycle than was inhaled, then it is possible that more oxygen will be exhaled than was

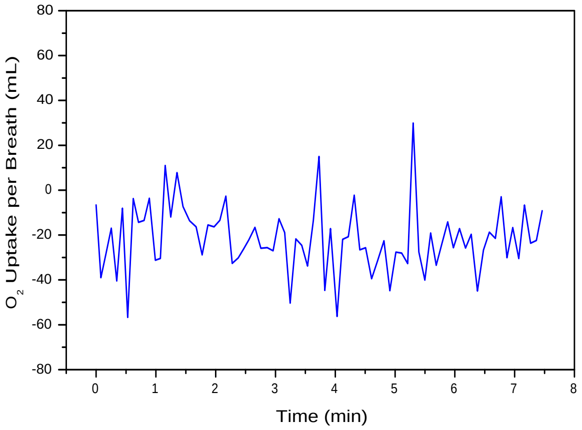

Figure 6.10: Human breath by breath oxygen uptake data for a test subject at rest. The values are negative due to the sign convention used by the flowmeter.

inhaled, which would manifest as oxygen production.

The ideal means of validating the accuracy of the oxygen uptake data would have been to obtain measurements for the same subject under the same measurement conditions using a commercial instrument. Access to such an instrument was not available, however, so the only means of ascertaining the validity of the measurements was to compare them to values quoted in the literature. Oxygen uptake is typically expressed in units of mL/min, so it was necessary to convert the data in Fig. 6.10 to this form. The discrete nature of the breath by breath data, and the fact that the values were not evenly spaced in time, complicated this task. A solution to the problem was to sum individual breath uptake values that corresponded to a length of time of approximately one minute. The resulting values were then scaled based on the actual duration they corresponded to. A Matlab script was written to implement this algorithm. The mL/min representation of the breath uptake data presented in Fig. 6.10 is shown in Fig. 6.11. The typical value for oxygen uptake at rest is taken to be $250mL/min$ [20]. As can be seen, the mean of the data obtained by the sensor coincides with the expected value, thus providing a degree of validation of the sensor system performance.

6.8 Conclusions and Future Work

A breath by breath oxygen uptake measurement system that measures oxygen concentration across the full breath profile has been developed. The key system parameters have been characterised and the measurement of oxygen uptake in a test subject has been demonstrated. Results to date have been promising and the next step, from a validation perspective, is to compare the performance of

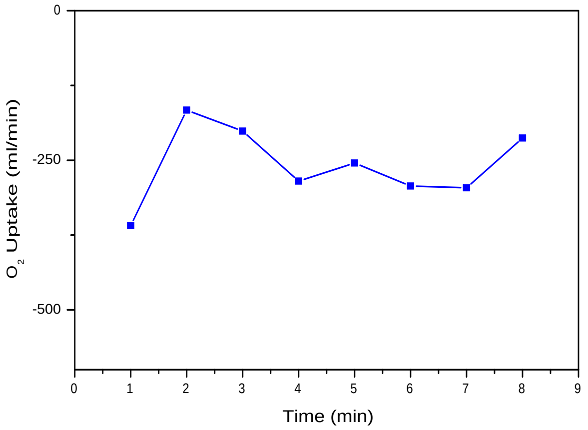

Figure 6.11: The breath uptake data presented in Fig. 6.10, represented in terms of mL/min. The typical mean value for a healthy individual at rest is $250ml/min$.

the system to that of a commercial metabolic analysis system. It may also be worthwhile to carry out Douglas bag-based [21] validation testing.

While the test results obtained to date suggest that it is performing satisfactorily, there are concerns as to the accuracy of the temperature measurements obtained with the thermistor. Accurate measurement of the instantaneous temperature of the sensor film requires that the thermal response times of the thermistor and sensor film be perfectly matched. A reliable method of characterising the thermal response characteristics of the film and the thermistor could not be found, so an estimate of the degree of mismatch, and related measurement inaccuracy, could not be obtained. Even if such measurements were available, adjusting, or tuning the thermal characteristics of either the film or the thermistor would be a very difficult task. A potentially more accurate alternative to thermistor-based measurements would be to co-immobilise a temperature sensitive dye alongside the oxygen sensitive dye in the sensor film. This would ensure that the thermal responses of both films would be intrinsically matched, and that the temperature values obtained would precisely match the instantaneous temperature of the film. This approach is investigated in chapter 8, which reports on the application of the multi-parameter sensing techniques discussed in chapter 5 to the simultaneous measurement of oxygen and temperature.

It was demonstrated that a large system volume, or dead-space, causes changes to the oxygen concentrations in the exhaled breath of the test subject. A key requirement for virtually all sensors and sensor-based systems is that performing a measurement have minimal impact on the system being studied. The flowmeter is the primary contributor to the dead-space of the system (63%), and efforts will be made to source a flowmeter with reduced dead-space for any future work.

Bibliography

[1] William D. McArdle, Frank I. Katch, and Victor L. Katch. *Essentials of exercise physiology.* Lippincott Williams & Wilkins, Baltimore, Mar., 2006.

[2] Christine Hanon, Pierre-Marie Lepretre, David Bishop, and Claire Thomas. Oxygen uptake and blood metabolic responses to a 400-m run. *European journal of applied physiology*, 109(2):233–240, 2010.

[3] Simon Marwood, Dumitru Constantin-Teodosiu, Edel Casey, Martin Whyte, Leslie Boobis, and Jo Bowtell. No acetyl group deficit is evident at the onset of exercise at 90maximal oxygen uptake in humans. *Journal of sports sciences*, 28(3):267–279, 2010.

[4] Audrey Baguet, Katrien Koppo, Andries Pottier, and Wim Derave. beta-alanine supplementation reduces acidosis but not oxygen uptake response during high-intensity cycling exercise. *European journal of applied physiology*, 108(3):495–503, 2010.

[5] S. Bjorgen, J. Helgerud, V. Husby, S. Steinshamn, R. R. Richadson, and J. Hoff. Aerobic high intensity one-legged interval cycling improves peak oxygen uptake in chronic obstructive pulmonary disease patients; no additional effect from hyperoxia. *International Journal of Sports Medicine*, 30(12):872–878, 2009.

[6] Marla K. Beauchamp, Mika Nonoyama, Roger S. Goldstein, Kylie Hill, Thomas E. Dolmage, Sunita Mathur, and Dina Brooks. Interval versus continuous training in individuals with chronic obstructive pulmonary disease-a systematic review. *Thorax*, 65(2):157–164, 2010.

[7] Daniel J. Lesser, Margaret M. Fleming, Carolyn A. Maher, Stephanie B. Kim, Marlyn S. Woo, and Thomas G. Keens. Does the 6-min walk test correlate with the exercise stress test in children? *Pediatric pulmonology*, 45(2):135–140, 2010.

[8] *Oxycon Pro.* CareFusion (Viasys Healthcare), `http://www.viasyshealthcare.com/prod_serv/prodDetail.aspx?config=ps_prodDtl\&prodID=277`.

[9] *K4 b2 Metabolic Analyser.* Cosmed srl, `http://www.cosmed.com/index.php?option=com_content\&view=article\&id=249\&Itemid=174\&lang=en`.

[10] Donal O'Gorman. Performance of portable metabolic analyser during exercise trials, 2009. Personal Communication.

[11] Dorota Wencel. *Sol-gel-derived Optical Oxygen, pH and Dissolved Carbon Dioxide Sensors.* Ph.D. Thesis, Dublin City University, 2008.

[12] Clare Higgins, Dorota Wencel, Conor S. Burke, Brian D. MacCraith, and Colette McDonagh. Novel hybrid optical sensor materials for in-breath o-2 analysis. *Analyst*, 133(2):241–247, 2008.

[13] C. S. Burke, J. P. Moore, D. Wencel, A. K. McEvoy, and B. D. MacCraith. Breath-by-breath measurement of oxygen using a compact optical sensor. *Journal of Biomedical Optics*, 13(1):014027, 2008.

[14] Hans H. Bruun. *Hot wire anemometry : principles and signal analysis.* Oxford Univ. Press, Oxford, 1995.

[15] Y. Q. Tang, M. J. Turner, J. S. Yem, and A. B. Baker. Calibration of pneumotachographs using a calibrated syringe. *Journal of applied physiology*, 95(2):571–576, 2003.

[16] A. Dirksen, F. Madsen, O. F. Pedersen, A. M. Vedel, and A. KokJensen. Long term performance of a hand held spirometer. *Thorax*, 51(10):973–976, 1996.

[17] O. F. Pedersen, M. R. Miller, T. Sigsgaard, M. Tidley, and R. M. Harding. Portable peak flow meters - physical characteristics, influence of temperature, altitude, and humidity. *European Respiratory Journal*, 7(5):991–997, 1994.

[18] Conor S. Burke, John P. Moore, Dorota Wencel, and Brian D. MacCraith. Development of a compact optical sensor for real-time, breath-by-breath detection of oxygen. *Journal of Breath Research*, 2(3):037012, 2008.

[19] Dorota Wencel. Response of PTEOS-based oxygen sensor films to dry and humid conditions. Personal Communication.

[20] Donal O'Gorman. Typical VO2 values for a healthy individual at rest. School of Health and Human Performance, Dublin City University. Personal Communication.

[21] Roger G. Eston and Thomas Reilly. *Exercise physiology: kinanthropometry and exercise physiology laboratory manual.* Routledge, London; New York, 2001.

Chapter 7

Sensors for the Measurement of Dissolved Oxygen and Dissolved Carbon Dioxide

7.1 Introduction

Sensor systems have been developed as a part of this work for the detection of dissolved oxygen and dissolved carbon dioxide. The dissolved oxygen sensor system is made up of the analog phase fluorometry system described in section 3.2.2 and the waterproof version of the original enhanced capture probe design (Probe 2). A number of small modifications were made to the phase fluorometry electronics. These included the addition of a drop-in micro-controller-based module for the calculation of dissolved oxygen concentrations, and the introduction of dual-LED referencing. The carbon dioxide sensor system that was developed, which was ratiometric mode-based, consists of the DSP-based instrumentation electronics described in section 3.4 and one of the two ratiometric enhanced capture probe designs (Probe 3 or Probe 4). Both Probe 3 and Probe 4 were used during the course of this work.

The performance of each of the sensor systems was characterised in suitable laboratory-based test and calibration setups. A number of field trials were then carried out using the DO sensor system at a site on a local river, while the dissolved carbon dioxide sensor was tested in a fish-tank-based test facility.

7.2 Dissolved Oxygen Sensor

7.2.1 Background/Motivation

Oxygen is a vital requirement for almost all aquatic organisms, and as a result, dissolved oxygen (DO) concentration is an important parameter in aquatic environments. It is also an important indicator of water quality and can be used to identify the occurrence of pollution and other events, such as eutrophication, which adversely affect water quality.

Until recently, the standard techniques for the measurement of DO were the Winkler method or the use of electrochemical based oxygen sensors. There are numerous disadvantages associated with both of these techniques. The Winkler method must be performed off-line in a laboratory, however, using time-consuming titration-based techniques. Electrochemical sensors consume oxygen and must therefore be placed in flowing water or must be constantly agitated. They are also prone to drift and require frequent recalibration and membrane and electrolyte changes. A number of luminescence-based DO sensors, some of which are available commercially [1–3], have recently been developed that address these issues. This includes a DO sensor that has been developed previously at the OSL [4] that made use of the precursor to the analog phase fluorometry electronics that have been developed during this work. To the best of the author's knowledge, none of the optical sensors that are either described in the literature, or are available commercially, made use of luminescence capture enhancement techniques. It was felt that the use of such strategies could lead to improved performance and as a result, a DO sensor was developed that consisted of the parabolic element-based probe, and the analog phase fluorometry system described previously. There was also the possibility that the improved design phase fluorometry system would also lead to performance improvements. This could not be investigated before the system was constructed, however, as performance information was not available for the electronics systems used with existing sensors.

7.2.2 Sensor System Description

The main components of the sensor system were a fluorescence-based sensor system, the waterproof optical probe described in detail in section 4.2, and the analog phase fluorometry electronics described in section 3.2.2. The oxygen sensor film consisted of $[Ru(dpp)_3]^{2+}$ immobilised in a PTEOS-based solgel matrix. A bead thermistor was located at the top of the probe to allow accurate measurement of the temperature of the water in the vicinity of the sensor film.

A number of modifications of the phase fluorometry system had to be implemented. It was required that the system output DO concentration readings in terms of milligrams per litre (mg/L). As will be seen in section 7.2.3.1, this involves a number of calculations, and it was found that the PIC microcontroller used in the system did not have the necessary computational capacity. To overcome this problem, a drop-in module based on a more powerful processor was added to the system to perform the required calculations. It was designed so that it could be inserted into the serial line coming from the main circuit, where it would intercept the raw sensor data and convert it into DO concentration. This approach was the quickest and easiest of the possible options to implement as the main circuit board did not have to be modified in any way. The circuit diagram of the drop-in module can be found in appendix B.4. The original configuration of the phase fluorometry electronics, as described in section 3.2.2, was used initially. As will be seen in section 7.2.4, however, it had to be modified to make use of dual LED referencing during the development and testing phase.

The system was designed to be used as part of a sensor array that was to be placed on a wirelessly-enabled data buoy, which in turn would be used to monitor a range of water quality parameters. The electronics were placed in an IP68 rated waterproof enclosure and the probe was connected to this enclosure using IP68 flexible waterproof conduit. A picture of the finished system is shown in Fig. 7.1.

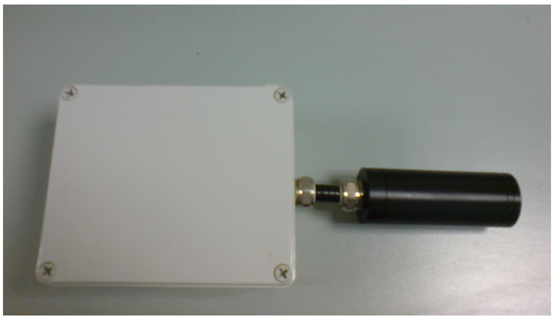

Figure 7.1: Image of DO sensor system. The power and data cable, which is not shown, attaches to the enclosure using an IP68 socket.

7.2.2.1 Non-continuous Operation

All of the instrumentation located on the data buoy was to be operated from on-board solar charged batteries, and as a result, the power consumption of the system was a key parameter. Following consultation with the project partners it was decided that the continuous acquisition of DO measurements was not necessary and that intermittent operation, where one measurement would be obtained every 30 minutes would suffice. The system firmware was altered so as to be compatible with intermittent operation, and to integrate with the buoy control system, which had ultimate control over all of the sensors deployed in the sensor array.

7.2.3 Test and Calibration System

A laboratory-based test and calibration facility was designed and constructed. A diagram of the system is shown in Fig. 7.2. The flowcell is watertight and has an opening in its lid that allows the probe to be inserted. As discussed previously, bubble formation was found to be a considerable problem, especially in test and calibration setups, and as a result the probe was mounted at a low angle to minimise the formation and entrapment of bubbles. The dissolved oxygen concentration of the liquid in the cell is controlled by bubbling an O_2/N_2 mix into the cell through a fitting located at its base. The ratio of O_2 and N_2 in the mixture is controlled using computer-interfaced mass flow controllers (MFCs). The flowcell, which is machined from a single block of aluminium, is placed in a temperature controlled waterbath, allowing precise control over its temperature. A typical sensor calibration curve, which was obtained using the test and calibration system is shown in Fig. 7.3.

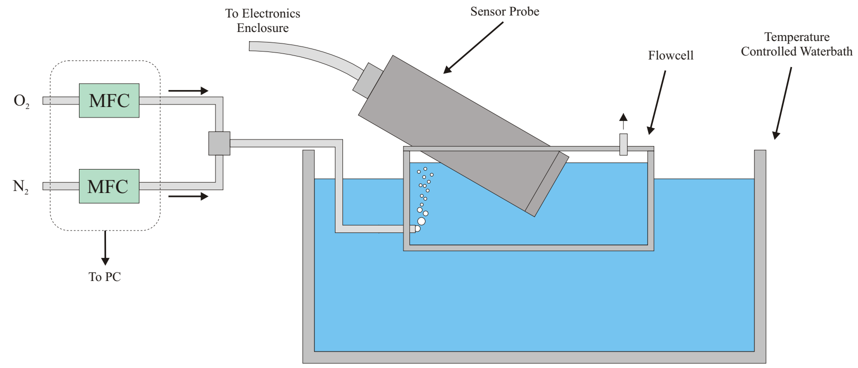

Figure 7.2: Dissolved oxygen sensor calibration setup.

7.2.3.1 DO Calculation

Expressing DO concentration readings in units of mg/L requires a number of steps.

The dissolved oxygen concentration in the liquid in the cell can be described using Henry's Law, which states that the concentration of a gas in a liquid is proportional to the partial pressure of the gas in the headspace above the liquid. This implies that the DO concentration in the liquid in the cell varies linearly as a function of the ratio of O_2 and N_2 being bubbled into the cell. This ratio can be

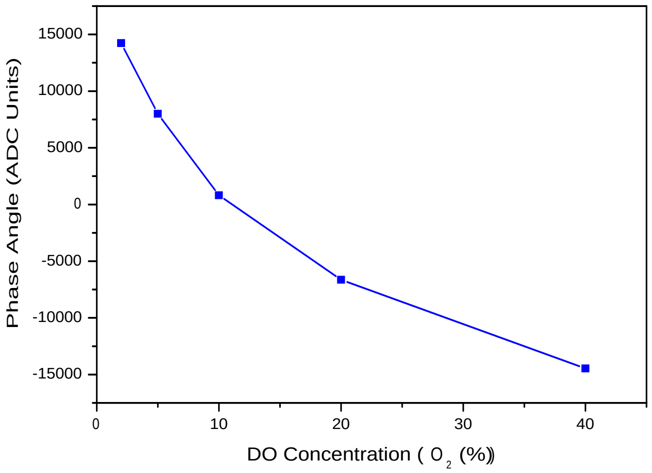

Figure 7.3: Typical DO sensor calibration curve. The phase values are expressed in terms of raw ADC units.

expressed in terms of the partial pressure of either of the gases in the mixture. As a result of the linear relationship between the quantities, if the DO concentration is known in mg/L for a particular oxygen partial pressure, ρO_2, then it can be evaluated for all partial pressure values simply by scaling this known value.

Weiss [5] empirically determined the following expression, which expresses the DO concentration resulting from air saturation, as a function of temperature and salinity.

$$\begin{aligned}\ln(DO) &= A_1 + A_2\frac{100}{T} + A_3\ln\left(\frac{T}{100}\right) + A_4\left(\frac{T}{100}\right) \\ &\quad + S\left(B_1 + B_2\left(\frac{T}{100}\right) + B_3\left(\frac{T}{100}\right)^2\right)\end{aligned} \tag{7.1}$$

DO is dissolved oxygen concentration in mL/L, T is temperature (K), S is salinity and A_1, A_2, A_3, A_4. B_1, B_2 and B_3 are fitting coefficients. Initially, all testing was to be carried out in freshwater, where salinity is zero. Setting the salinity component of equation 7.1 to zero results in:

$$\ln(DO) = A_1 + A_2\frac{100}{T} + A_3\ln\left(\frac{T}{100}\right) + A_4\left(\frac{T}{100}\right) \tag{7.2}$$

Applying Henry's Law, the DO concentration in ml/L that results from a given calibration partial pressure, ρO_2, is then:

$$DO = \exp\left[A_1 + A_2\frac{100}{T} + A_3\ln\left(\frac{T}{100}\right) + A_4\left(\frac{T}{100}\right)\right]\cdot\left(\frac{\rho O_2}{20.83}\right) \tag{7.3}$$

where the O_2 partial pressure in atmospheric air is taken to be 20.83%. Conversion from ml/L to mg/L requires the use of the ideal gas law:

$$PV = nRT \tag{7.4}$$

where P is pressure (Pa), V is volume (m^3), n is the number of moles of the gas in question, R is the ideal gas constant, and T is temperature (K). The mass, m, of a certain volume of the gas in question can be determined from equation 7.4 by taking the molar mass, M, of the gas into account, resulting in:

$$m = \frac{MPV}{RT} \tag{7.5}$$

An expression describing dissolved oxygen concentration, in units of mg/L, as a function of temperature, pressure, and oxygen partial pressure can be obtained by combining equations 7.3 and 7.5:

$$DO = \frac{MP}{20.83RT} \exp\left[A_1 + A_2\frac{100}{T} + A_3 \ln\left(\frac{T}{100}\right) + A_4\left(\frac{T}{100}\right)\right]\rho O_2(\%) \tag{7.6}$$

The values of the various parameters in equation 7.6 are listed in Table 7.1. All of the testing was to be carried out at or near sea level so pressure was assumed to be constant at 1 atmosphere.

Coefficient	Value
A_1	-173.4292
A_2	249.6339
A_3	143.3483
A_4	-21.84920
P	101325.0
R	8.314472
M	32000.00

Table 7.1: The values of the various coefficients in equation 7.6. Note that the molar mass, M, is expressed in units of milligrams.

7.2.3.2 Sensor Calibration

As discussed previously, $[Ru(dpp)_3]^{2+}$ displays considerable temperature sensitivity and as a result it was necessary to calibrate the sensor for temperature as well as DO concentration. This was achieved by varying the DO concentration in, and the temperature of, the flowcell over the required ranges and recording the resulting sensor response. A 3D surface was fitted to the data using TableCurve3D, as described in section 5.3.1, and the resulting calibration equation was programmed into the firmware of the drop-in DO calculation module. The DO concentration calibration range was $2-40\%$, which allowed for the possibility of supersaturated conditions. The sensor was to be used throughout the full year, which corresponded to a potential water temperature range of $0 \sim 18°C$. The lowest temperature that could be reached by the waterbath was $1.8°C$ so the sensor was calibrated over the temperature range of $2-20°C$.

The sensor was calibrated in terms of ρO_2 and the sensor values were converted to units of mg/L using equation 7.6. A typical calibration equation, which was generated from calibration data using TableCurve3D is as follows:

$$\begin{aligned} DO(\rho O_2(\%)) &= a + b\ln T + c\ln\phi + d(\ln T)^2 + e(\ln\phi)^2 + f\ln T\ln\phi \\ &\quad + g(\ln T)^3 + h(\ln\phi)^3 + i\ln T(\ln\phi)^2 + j(\ln T)^2\ln\phi \end{aligned} \tag{7.7}$$

where $a-j$ are calibration coefficients. The R^2 value of the fit that generated this equation was 0.99995, which was typical of the values obtained over multiple calibrations and with multiple sensor units. In order to minimise computational effort, the phase and temperature data is supplied in terms of raw ADC units. This does not have any effect on fit quality and eliminates the mathematical operations that would have been involved in the conversion process.

7.2.4 System Referencing Strategy

The analog phase fluorometry electronics described in section 3.2.2 were initially used 'as-was'. However, early stage testing highlighted the fact that the significant warm-up time of the system (see Fig. 3.7), while not an issue in the breath monitoring application, was not compatible with intermittent operation. There was little scope to improve the warm-up performance of the system while still using dual photodiode referencing, and as a result, dual LED referencing was investigated. This was an option as dual photodiode referencing was employed in the phase fluorometry system in order to achieve the measurement rates that were required by the breath oxygen measurement application, however no such requirements existed in the case of water monitoring. A number of configurations were tested and the best performance was achieved using a configuration in which MOSFET-based switching circuitry was used to switch between the signal and reference LED. A high level diagram of the switching circuit is shown in Fig. 7.4. The circuit switches between both LEDs, with a single logic input controlling its operation. The same current control circuitry is used for both LEDs, maximising their common signal path, and minimising the potential for thermally induced drift. A GPIO pin on the systems microcontroller was used to control LED switching. During operation, the system alternates between both LEDs, with

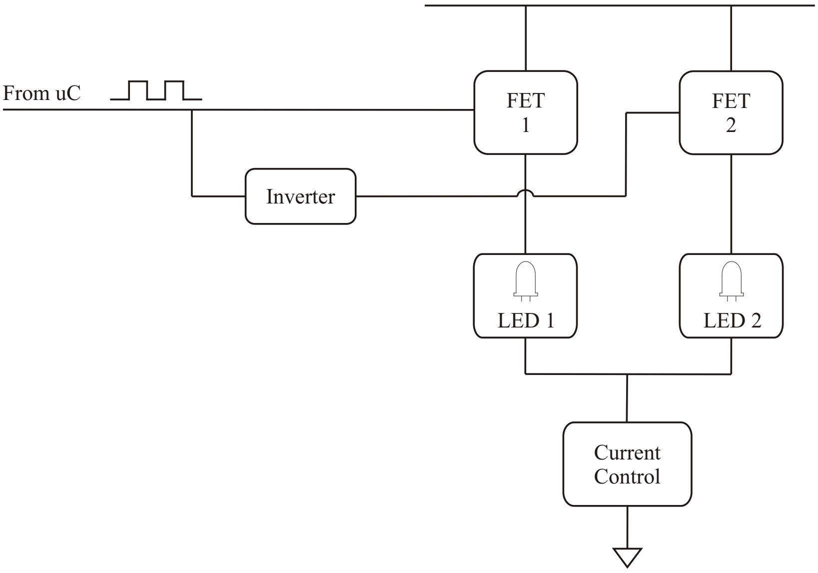

Figure 7.4: Circuit configuration for dual LED referencing.

the data corresponding to the settling time of the low pass filter being discarded. This configuration resulted in substantially reduced warm-up time and warm-up drift, as is illustrated in Fig. 7.5.

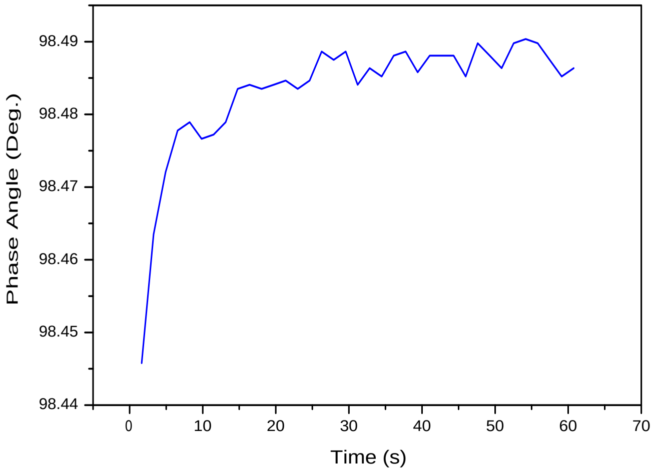

Figure 7.5: Warmup profile of dual LED configuration over a 60 second period.

7.2.5 Sensor Performance

The performance of the sensor was assessed both in the lab and in the field. The laboratory-based testing was carried out using the test and calibration system described previously, and the field trials were carried out at a site on the River Liffey (Dublin).

7.2.5.1 Laboratory-Based Testing

Resolution As can be seen in Fig. 7.3, the response of the sensor to oxygen is non-linear, which implies that its resolution will be concentration dependent. In such cases, resolution at 0%, which is also referred to as the limit of detection (LOD), is commonly used to describe sensor resolution. The resolution at 0% was evaluated by measuring the peak-to-peak noise in the sensor output. The value that was obtained is listed in Table 7.2. The sampling interval was 6 seconds, which, as will be seen in the next section, corresponds to the response time of the sensor.

Limit of Detection ($\mu g/L$)
0.63

Table 7.2: Limit of detection of the dual LED referencing-based system at $20°C$.

The lowest LOD among the commercially available DO sensors is $1\mu g/L$ [1], which means that the performance of the DO sensor that has been developed shows a significant improvement over the current state of the art. The limit of detection of the previous DO sensor designed at the OSL [4] was $6\mu g/L$ for an integration time of 30 seconds. When it is considered that the LOD of this sensor is $0.63\mu g/L$ for an integration time of 6 seconds, it can be seen that there has been a substantial improvement in resolution/LOD. This can be attributed to both the use of luminescence capture enhancement techniques and also to the improvements made to the phase fluorometry electronics.

It should be noted that the use of dual LED referencing has a negative impact on resolution/LOD. This is due to the fact that the non-continuous operation of the signal LED reduces the effective sampling rate of the system when compared to dual photodiode mode, which allows for continuous sampling. This reduction in resolution was not an issue in this case as the resolution of the system in dual LED mode was better than what was required. There is scope, however, to further improve the resolution of the system from that which is listed in Table 7.2 by switching back to dual photodiode referencing, if an application emerges where improved resolution is required.

Response Time Sensor response time is an important parameter for dissolved gas sensors as the reduced gas diffusion rates in liquids compared to gases can lead to much reduced response times in aqueous phase applications. It was not possible to determine the response time of the sensor using the test and calibration system. While the amount of oxygen being bubbled into the cell can be changed very quickly ($< 1s$), the resulting change in DO concentration is limited by the rate of diffusion of the oxygen into the liquid. This diffusion rate is governed primarily by the geometry of the flowcell and is typically much slower than the actual response of the sensor film. An alternative method, which avoids diffusion-related contributions to the measured response time, is to prepare two water samples that have different DO concentrations and to quickly transfer the sensor probe from one sample to the other. This procedure was carried out for the sensor and the resulting response curve can be seen in Fig. 7.6. The T_{10-90} response time was determined from the profile in Fig. 7.6 using graphical techniques. The measured value is listed in Table 7.3. The response times of commercially available DO sensors are in the region of 60 seconds in all cases. The response time of the sensor at 5.9 seconds represents a substantial improvement, and is likely due to reduced sensor film thickness compared to that of the commercial systems. If shorter response times were required, for example for depth profiling applications, this could be achieved by reducing the thickness of the sensor films, at the cost of decreased resolution.

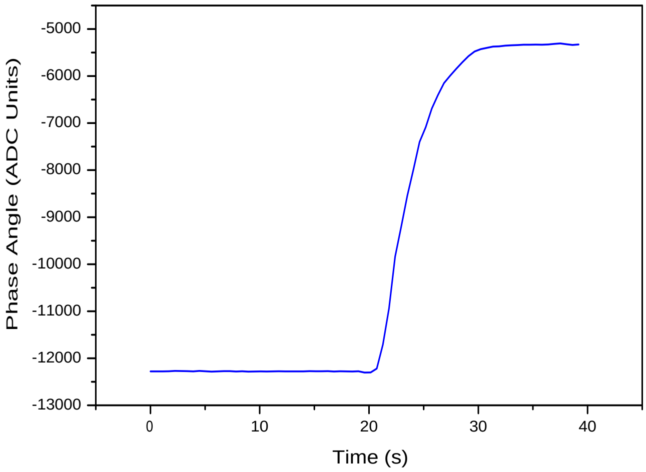

Figure 7.6: Response profile of the sensor when it is transferred from water with a DO concentration of $7.95mg/L$ to water with a DO concentration of $9.1mg/L$. Both water samples were at $20°C$.

Response Time (s)
5.9

Table 7.3: The T_{10-90} response time of the sensor.

7.2.5.2 Field Trials

A number of field trials were carried out before the sensor was deployed in the sensor network. An easily accessible site with moderate flow rates was chosen on the River Liffey. An image of the sensor in-situ during one of the trials is shown in Fig. 7.7. It was not possible to find an accessible test site that was secure so tests were limited to one day in length. The system was set up to acquire one measurement every thirty minutes. Typical field trial data are shown in Fig. 7.8. The trial was started early in the morning and the expected increase in DO concentration as the day progresses can be observed. A number of such trials were conducted in order to assess the robustness of the system and no problems were encountered. In order to investigate the possibility of the occurrence of

Figure 7.7: DO sensor in the field at a site on the River Liffey. The electronics enclosure, a battery pack and a laptop for logging the sensor data are located on the river bank. The flow velocity of the river was approximately $1m/minute$

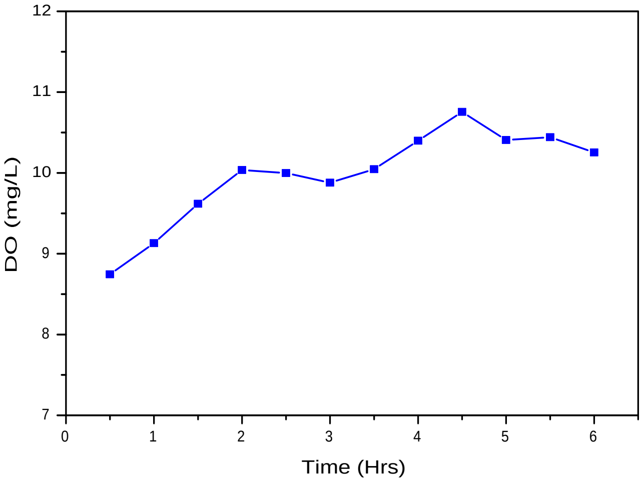

Figure 7.8: DO sensor data for a six hour field trial.

sensor drift, the response of the sensor was tested in the laboratory-based test system following a number of the trials and it was found that no observable drift in response had occurred.

7.3 Ratiometric Dissolved DCO_2 Sensor

7.3.1 Background/Motivation

Carbon dioxide is highly soluble in water and its dissolved concentration levels are important in a range of areas including bio-processing, environmental monitoring, and in the beverage industry. In bio-processing applications, dissolved CO_2 levels must be closely controlled in order to provide optimum culture conditions and obtain high yields. In the beverage industry, the measurement of dissolved CO_2 is an important parameter in quality control, and is also required during the fermentation process. As a result of the current focus on climate change and global warming, there is a considerable amount of research being conducted into the carbon sinking capacity of the oceans and other large bodies of water. Accurate dissolved CO_2 measurement is a vital part of this research. Dissolved CO_2 levels are also used as an indicator of water quality, and for the identification of pollution and eutrophication.

The commercially available dissolved CO_2 (DCO_2) sensors are based on one of three measurement principles: thermal conductivity, non dispersive infrared (NDIR) absorption, or pH measurement. In the thermal conductivity-based sensors, CO_2 diffuses through a porous membrane and changes the thermal conductivity of the gas mixture in the chamber behind the membrane. The measurement chamber is periodically flushed with a purge gas and CO_2 concentration is determined from the rate of change of thermal conductivity in the chamber immediately following the purge event. The NDIR-based sensors make use of the fact that CO_2 exhibits an absorption band in the mid-infrared. Such systems typically consist of a broadband IR source and an IR detector, which are used to determine the absorption of the gas in a test cell at the appropriate wavelength. The pH-based sensors operate on the principle that when CO_2 dissolves in water, a weak acid, carbonic acid, is formed. CO_2 diffuses through an ion impermeable membrane into an aqueous environment containing a pH sensor, with the pH of the environment being related to the amount of CO_2 that has diffused through the membrane. Although the majority of pH-based CO_2 sensors available commercially make use of electrochemical Severinghaus pH electrodes, a number of optical CO_2 sensors that use a luminescent or colorimetic pH sensor have been developed, with such sensors recently coming onto the market.

The aim of this work was to develop an optical dissolved CO_2 sensor that could be used for environmental monitoring applications but that could also be applied to other application areas at a later stage. There are a range of problems associated with each of the other types of sensors that makes the optical pH sensor-based approach the most attractive choice for DCO_2 measurements in environmental applications. Thermal conductivity-based sensors require the availability of a purge gas and as such are limited to fixed installations. NDIR-based sensors are widely used for gas phase CO_2 measurement. They are not well suited to dissolved measurements, however, as a relatively large sample cell is required to obtain adequate sensor resolution. The use of a large cell results in response time limitations of sensor performance. Electrochemical pH sensor-based systems have long response times and require frequent maintenance and recalibration.

An optical DCO_2 sensor that makes use of a luminescence-based pH sensitive dye as the pH sensing element has been developed. It makes use of a waterproof enhanced capture probe that has been configured for ratiometric operation. The sensor is interrogated using the multi-purpose electronics described in section 3.4, which was configured for intensity-based ratiometric operation.

7.3.2 Sensor System Description

As was discussed in section 2.4.3, lifetime-based measurements lead to improved sensor performance compared to direct intensity measurements. The lifetime values of all of the suitable pH sensitive dyes are in the low nanosecond region, however, which rules out the use of lifetime-based measurements due to the cost and complexity of the required instrumentation. This means that intensity-based techniques must be used. A number of techniques can be used in intensity-based applications that overcome many of the problems associated with direct intensity measurement, with the two most common being dual-luminophore-referencing (DLR) and ratiometric operation. Because the DLR technique is protected by a patent [6], ratiometric operation was chosen as the most viable alternative. The details of ratiometric operation are discussed in section 2.4.4.

The DCO_2 sensor that has been developed consists of a luminescence-based pH sensitive dye, 8-hydroxy-1,3,6-pyrene trisulfonic acid (HPTS), which has been immobilised in a solgel-based matrix. This dye was chosen as its pKa value is in the required range and it is compatible with ratiometric operation. The sensor film is incorporated into an enhanced capture probe that has been adapted for ratiometric operation, and is interrogated using the DSP-based multi-function interrogation electronics described in section 3.4. Each of the constituent components of the sensor system is described in detail in the following sections.

7.3.2.1 Sensor Films

The sensor film composition and fabrication process are described in [7]. Briefly, HPTS and a base are co-immobilised in a MTEOS/PTEOS-based solgel matrix. The base is required in order to achieve reversible operation. A mixture consisting of uncured solgel, HPTS and base was prepared and coated onto glass slides using spin-coating techniques. The coated slides are then cured in an oven and once cured, the slides are coated in a Teflon layer. The Teflon layer acts as a proton/ion impermeable barrier that prevents cross-sensitivity to the pH of the test medium by ensuring that only gas molecules can diffuse into the solgel matrix.

7.3.2.2 Optics

The system made use of the ratiometric mode enhanced capture configuration described in chapter 4. Two of the probe designs that were developed were used over the course of the project. The basic design (Probe 3) was used for all of the film characterisation testing that was carried out, while the improved design (Probe 4) was introduced in the latter stages of the project and used for the fish-tank-based testing. Details of the two designs can be found in sections 4.3 and 4.4, respectively. A Si-PIN photodiode (S1223-01, Hamamatsu (UK) Ltd.), was used as the detector element.

7.3.2.3 Electronics

The DSP-based instrumentation electronics described in section 3.4 were used to interrogate the sensor film. Two of the systems excitation channels, one for each LED, and a single input channel, were used. A diagram of the active parts of the DSP electronics is shown in Fig. 7.9. The sensor slide is illuminated simulta-

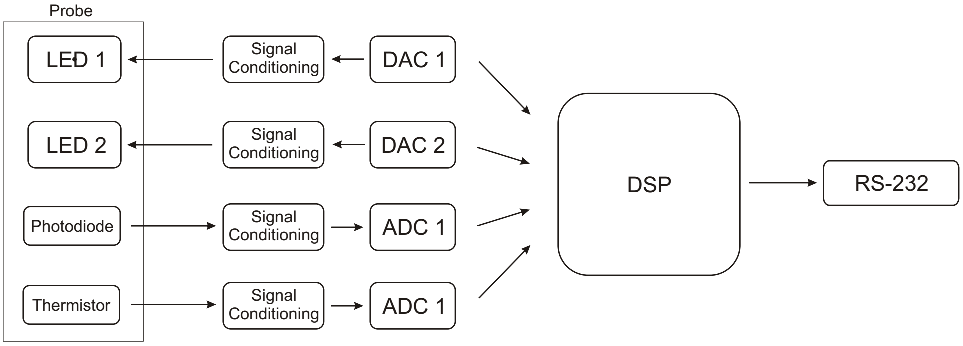

Figure 7.9: The elements of the DSP electronics that were used for the ratiometric DCO_2 sensor.

neously by both LEDs, with each LED being modulated at different frequencies. The resulting emission intensity is measured at both modulation frequencies using synchronous demodulation, as described in section 3.3.2. The ratio of both intensities is obtained and taken as the sensor output. In this instance, the ratio was calculated by the PC-side software in order that the raw data from both LEDs be available for test and characterisation purposes. The 405nm LED was modulated at $1000Hz$ and the 450nm LED was operated at $3508Hz$. In order to achieve optimum performance, it was necessary to choose frequencies that were not harmonically linked and that were sufficiently separated to ensure that there was no crosstalk during the synchronous demodulation process. Low modulation frequencies were chosen in order to facilitate increased over-sampling and thus reduce measurement noise. A lower limit of $1000Hz$ was chosen, however, in order to avoid the area of the spectrum that contains $50Hz$ and $100Hz$ components and their harmonics. It has been found that significant amounts of each are introduced to the signal by mains interference and artificial lighting.

A thermistor was used to measure the temperature of the test liquid, as was the case in the DO sensing application. It was connected to the electronics using one of the passive bridge inputs, which is in turn connected to the auxiliary ADC.

LED Drive Current The LED brightness has a direct impact on the rate of photo-degradation of the sensor film. As will be seen in section 7.3.4.3, it was necessary to minimise photo-degradation, and in order to achieve this, LED intensity was reduced. The maximum rated current for both of the LEDs used in the probe is $30mA$. It was found that the LED drive current could be set as much as a factor of 40 below this value at $0.7mA_{rms}$, while still achieving adequate resolution and LOD performance.

7.3.3 Test and Calibration System

Despite the efforts that were made to minimise the occurrence of bubble formation when designing the DO test facility, bubble formation was still a significant problem. As a result, a new flow cell was designed that allowed the probe to be mounted horizontally. It was used as part of a test and calibration system that included a number of design enhancements over previous systems. A diagram of the new design is presented in Fig. 7.10. The flow cell was machined from a single block of aluminium. A circular port was placed in the side of the cell that allows the sensor probe to be mounted horizontally. A Wilson seal configuration, which is used extensively in vacuum systems, was used to form a seal around the probe. The main element in the seal is a tapered ring that forces two O-rings against the

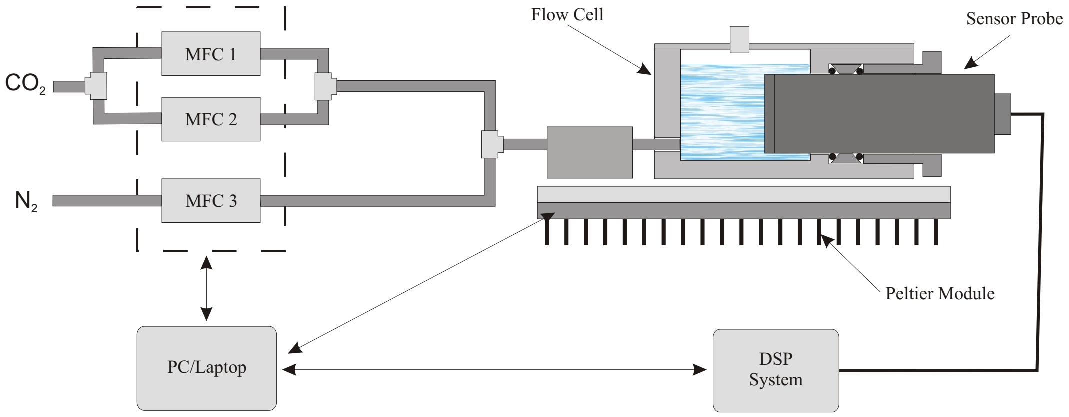

Figure 7.10: The test and calibration setup developed for testing and characterising the DCO_2 sensor.

sides of the probe and the cell when placed under compression by a compression ring. As in previous systems, gas delivery is controlled using PC-interfaced MFCs. It was necessary, however, to use two CO_2 MFCs in order to achieve the required gas concentration range with a suitable level of accuracy. Temperature control was achieved through the use of a thermoelectric Peltier module. A Peltier module was selected over the waterbath used previously primarily to avoid having to immerse the probe fully during laboratory testing. It also provided a number of additional advantages including reduced response time and a larger temperature range. The temperature of the module is controlled using a computer-controlled PID controller, which provides setpoint accuracy of $0.1°C$.

A Labview VI was written that incorporated gas control, temperature control, and the DSP interface into a single GUI. It was designed to operate in either fully automated mode, which was useful during the calibration process, or manual mode which facilitated specific testing.

Sensor calibration was carried out in the usual manner, namely by varying temperature and gas concentration over the required ranges, with the resulting data being fitted with a 3D surface using TableCurve3D.

7.3.4 Sensor Performance

One of the objectives of the project from a sensor film perspective was to determine the optimum sensor film composition and as a result a large number of formulations were tested. The optimum composition was identified and was used for the remainder of the project. Details of the test results and the optimum film formulation can be found in [8]. The response of a sensor consisting of the optimum formulation over the DCO_2 concentration range of $0 - 30\%$, at a fixed temperature of $20°C$, is shown in Fig. 7.11. It can be seen in Fig. 7.11 that

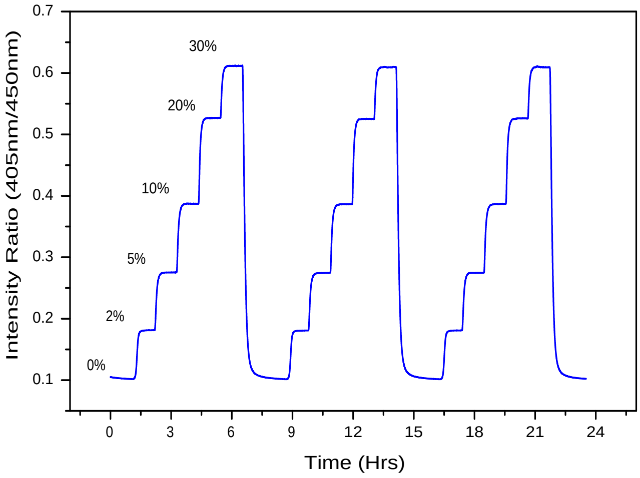

Figure 7.11: Sensor response for a range of DCO_2 concentrations. The sensor response is expressed in terms of the ratio of 405nm LED induced luminescence to that induced by the 450nm LED.

the response of the sensor is fully reversible and repeatable. The apparently long response time can be attributed to the volume in the cell, and, as will be seen below, the actual response time of the sensor is substantially shorter.

7.3.4.1 LOD/Resolution

The LOD of the sensor was evaluated as described previously and is listed in Table 7.4. This value compares favourably with those of the commercially available DCO_2 sensors. The non-optical sensor types typically have LODs in the region of 0.1% [9, 10], with the exception of a specialised electrical conductivity-based system developed by Martek Instruments, USA [11] for the measurement of DCO_2 in ultra-pure water. Although an LOD of $5.7 \times 10^{-6}\%$ is quoted for this system, it can only be used in ultra-pure water and is therefore not a valid benchmark for the performance of the sensor that has been developed. At the time of writing, there are two optical DCO_2 sensor available commercially, one from PreSens [12] and the other from Fluorometrix [13]. There is no performance information available for the Fluorometrix system and the PreSens system does not provide LOD data but instead quotes resolution at 2%. For comparison purposes the resolution of the sensor at 2% CO_2 was evaluated and was found to be 0.008%. The resolution

Limit of Detection
0.002%

Table 7.4: The limit of detection of the sensor for a sampling interval of $2.5s$.

of the PreSens sensor at 2% is 0.06%, which is 7.5 times poorer than the system developed here. The system also compares favourably with the DCO_2 sensors that have been described in the literature, such as Rao et. al. [14] who describe a sensor with an LOD of $\sim 0.03\%$ and colleagues at the OSL [15], who built a system with an LOD of 0.017%. Wolfbeis et. al. [16] have developed a DCO_2 sensor with an LOD of 0.0013%. It uses a PMT for luminescence detection, however, instead of a photodiode. The noise performance of a PMT is several orders of magnitude better than that of a photodiode, but they are much more expensive, larger and require a high voltage source, rendering them unsuitable for many portable sensing applications.

The sensor system that has been developed outperforms all comparable sensors on the market or in the literature, despite the fact that it has not been optimised for resolution. Although the current LOD/resolution performance is adequate for the application in question, there is substantial scope for achieving improved LOD/resolution performance, should it be required. The LEDs are driven a factor of 40 below their maximum rated current, while a sampling interval of $2.5s$ is being used. This could be increased by an order of magnitude without imposing any restrictions on the quality of the data produced by the sensor. These changes could theoretically result in a factor of 120 improvement in LOD/resolution.

7.3.4.2 Response Time

The response time of the films were assessed by a colleague as part of the film optimisation process. It was was determined using the technique described in section 7.2.5.1, and was found to be 4 minutes for a change in DCO_2 concentration from 5% to 25%.

7.3.4.3 Fish-Tank Trial

In order to assess the performance of the sensor in realistic operating conditions while still having some degree of control over its operating environment, a test setup consisting of a temperature-controlled fish tank containing a range of plants was put in place. A typical test run involved submerging the sensor probe in the tank at a low angle and monitoring the DCO_2 concentration over a number of days. Both the original waterproof probe design and the improved design that incorporated the anti-bubble formation assembly described in section 4.4.3 were used during testing. It was found that bubble formation was a problem with the original design, however it did not occur at all when using the improved design.

Data from a 3 day tank test are shown in Fig. 7.12. The expected diurnal

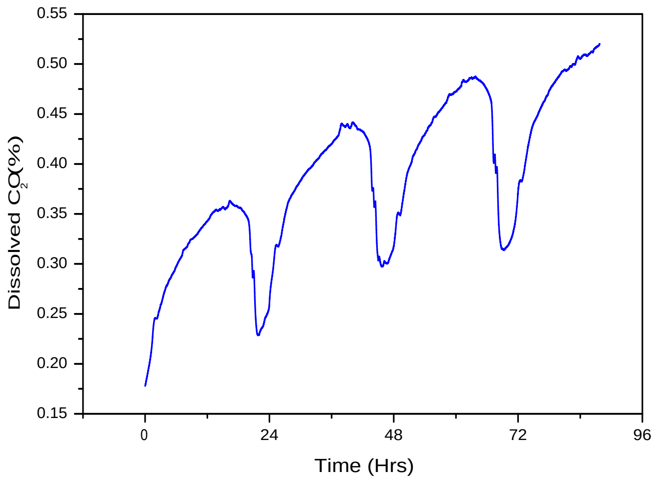

Figure 7.12: Dissolved CO_2 concentration in the fish tank over a 3 day period.

changes due to photosynthesis can be clearly observed, but there is also a considerable drift in sensor output. The most likely causes are photo-degradation or sensor film evolution, or a combination of both. The purpose of ratiometric operation is to remove effects such as this. A measure of its effectiveness can be obtained by viewing the raw intensity data resulting from either of the excitation LEDs. The raw intensity data for the 450nm LED corresponding to the data in Fig. 7.12 is plotted in Fig. 7.13. It can be seen that the drift is substantially

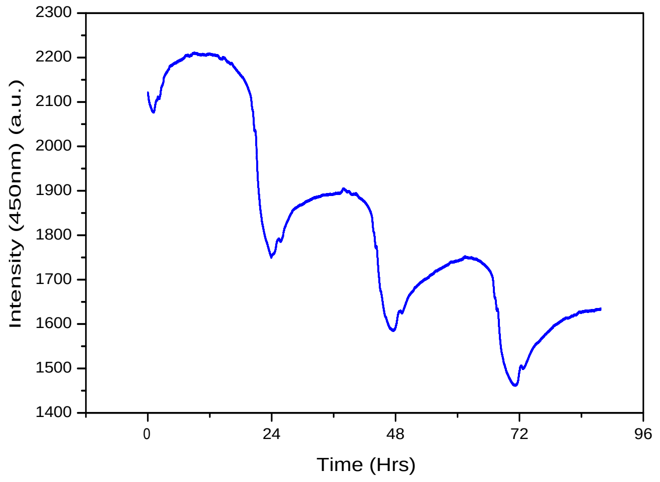

Figure 7.13: Raw intensity data corresponding to the fish tank DCO_2 data presented in Fig. 7.12. The data is for the 450nm excitation LED.

worse in the raw data in Fig. 7.13 than in the data in fig. 7.12, indicating that ratiometric operation reduces the magnitude of the drift but does not remove it completely. While the level of drift that is present may not pose a problem for a bio-processing application where the working range of the sensor would be much larger, it introduces unacceptable inaccuracy to the results at environmental levels. A means of overcoming the effects of drift in a HPTS-based ratiometric pH sensor has recently been published by Hakonen et. al. [17]. They have developed a temporal calibration procedure that allows the sensor output to be compensated for drift. Sensor drift is characterised as a function of time, resulting in an expression that describes the temporal evolution of the film. Extrapolation techniques can be used to predict the post calibration evolution of the film or alternatively, if the in-batch repeatability is adequate, a single sensor from each batch can be temporally calibrated and the resulting expressions used to describe the response of the remaining sensors in the batch. Time and funding constraints meant that the development of the sensor has been put on hold for the time being. The implementation of such a strategy is a key element of the future work that is planned, however.

7.4 Conclusions/Future Work

Dissolved gas sensor systems were developed for sensing both dissolved oxygen and dissolved carbon dioxide. Both systems make use of enhanced capture optical probes. The dissolved oxygen sensor is based on the oxygen sensitive fluorophore $[Ru(dpp)_3]^{2+}$ and is interrogated using the analog phase fluorometry system. With a limit of detection of $0.63 \mu g/L$, it out-performs all previously reported dissolved oxygen sensors that have a similar dynamic range. The carbon dioxide sensor is based on the pH-sensitive luminophore HPTS and is interrogated using the DSP-based system configured in dual-excitation ratiometric mode. The multi-frequency capabilities of the instrumentation electronics allow the excitation LEDs to be operated simultaneously, which results in an inherent advantage over other dual-excitation systems which must operate the LEDs alternately. The limit of detection of the dissolved carbon dioxide sensor was found to be 0.002%, which outperforms all of the comparable sensors that have been reported. There is considerable scope to improve this value through the use of higher excitation intensities and increased sampling times.

A number of elements of future work are planned. The first of these is the application of a temporal calibration procedure in order to improve the stability of the dissolved carbon dioxide sensor. This will be carried out in parallel with efforts to improve the stability of the sensor films from a formulation perspective. The dissolved oxygen sensor was implemented using the analog phase fluorometry system and it is intended to migrate to the DSP-based system in the near future in order to optimise the performance of the system.

Bibliography

[1] *D-Opto Dissolved Oxygen Sensor.* Zebra-Tech Ltd., `http://www.d-opto.com/`.

[2] *ROX DO Sensor.* YSI Inc., `http://www.ysi.com/accessoriesdetail.php?6150-ROX-Optical-Dissolved-Oxygen-Sensor-6-Series-90`.

[3] *FOXY/neoFox Oxygen Sensor.* Ocean Optics Inc., `http://www.oceanoptics.com/Products/neofox.asp`.

[4] C. McDonagh, C. Kolle, A. K. McEvoy, D. L. Dowling, A. A. Cafolla, S. J. Cullen, and B. D. MacCraith. Phase fluorometric dissolved oxygen sensor. *Sensors and Actuators B: Chemical*, 74(1-3):124–130, 2001.

[5] R. F. Weiss. Solubility of nitrogen, oxygen and argon in water and seawater. *Deep-Sea Research*, 17(4):721, 1970.

[6] Ingo Klimant. *Method and Device for Referencing Fluorescence Intensity Signals.* Patent, 1999. WO9906821 (A1).

[7] Dorota Wencel. *Sol-gel-derived Optical Oxygen, pH and Dissolved Carbon Dioxide Sensors.* Ph.D. Thesis, Dublin City University, 2008.

[8] Dorota Wencel. The characteristics of various dissolved carbon dioxide sensor film formulations and details of the optimum film composition, 2010. Personal Communication.

[9] *InPro5000 Dissolved Carbon Dioxide Sensor.* Mettler Toledo, `http://ie.mt.com/ie/en/home.html`.

[10] *ORBISPHERE 31XXX, CO2 Thermal Conductivity (TC) Sensor.* Hach Company, `http://www.hach.com/`.

[11] *Martek Dissolved Carbon Dioxide Analyzer.* Martek Instruments, `http://www.martekinstruments.com/pdfs/co2.pdf`.

[12] *CellPhase pH, DO and DCO2 non-invasive sensors*. Fluorometrix Inc., `http://www.fluorometrix.com`.

[13] *Carbon Dioxide Sensors*. PreSens Precision Sensing GmbH, `http://www.presens.de`.

[14] Xudong Ge, Yordan Kostov, and Govind Rao. High-stability non-invasive autoclavable naked optical co2 sensor. *Biosensors and Bioelectronics*, 18(7):857–865, 2003.

[15] Conor S. Burke, Adam Markey, Robert I. Nooney, Patrick Byrne, and Colette McDonagh. Development of an optical sensor probe for the detection of dissolved carbon dioxide. *Sensors and Actuators B: Chemical*, 119(1):288–294.

[16] Gerhard Neurauter, Ingo Klimant, and Otto S. Wolfbeis. Microsecond lifetime-based optical carbon dioxide sensor using luminescence resonance energy transfer. *Analytica Chimica Acta*, 382(1-2):67–75, 1999.

[17] Aron Hakonen and Stefan Hulth. A high-precision ratiometric fluorosensor for ph: Implementing time-dependent non-linear calibration protocols for drift compensation. *Analytica Chimica Acta*, 606(1):63–71, 2008.

Chapter 8

Simultaneous Measurement of Oxygen Concentration and Temperature

8.1 Introduction

As discussed in chapter 6, the acquisition of temperature-compensated oxygen measurements using a single sensor element is desirable as it would eliminate the possibility of thermal-response-time induced errors. As a result, the multi-parameter technique that is described in chapter 5 was applied to the simultaneous measurement of oxygen concentration and temperature using a single sensor film.

This work was completed in two stages. The first saw the development of a multi-element based system that was used to test the feasibility of the multi-parameter technique for temperature compensation. A multi-element approach was used in the first instance in order to be able to investigate feasibility without having to address the formulation challenges associated with the development of a suitable single-element-based sensor. Promising results were obtained using this system, and as a result, a single-element-based system was designed and implemented.

This chapter begins with a description of the multi-element system, and this is followed with a treatment of the single-element approach that led from it. The results obtained with both systems are presented and are used to identify focus areas for future work.

8.2 Multi-Element Approach

The principle of operation of the multi-element approach was introduced in chapter 5.5. It requires that the sensor elements, two in this case, display different degrees of cross-sensitivity to the analytes in question. This was achieved through the use of two solgel-based sensor films that both contained the oxygen sensitive fluorophore $[Ru(dpp)_3]^{2+}$, but which were fabricated using different solgel precursors. The oxygen sensitivity of a solgel-based sensor film is precursor-dependent [1], as the precursor that is used influences the micro-structure of the sensor film, which in turn affects the accessibility of the dye molecules. The films were interrogated using phase fluorometry techniques and were calibrated and tested using a custom flowcell-based system that allowed both films to be interrogated simultaneously.

8.2.1 System Description

Each of the constituent components of the system is described in the following sections.

8.2.1.1 Sensor Elements

As discussed, two different solgel precursors, methyltriethoxysilane (MTEOS) and n-propyltriethoxysilane (PTEOS) were used for the sensor elements. The sols were formulated using the same recipe and procedure (albeit with different precursors), the details of which can be found in [2]. The sols were aged for a number of weeks and then dip-coated onto glass microscope slides. The slides were cured in an oven and then left to age for a number of weeks before use. Typical oxygen response curves for both sensor films are presented in Fig. 8.1. It can be seen that the films have significantly different oxygen responses, and as such are a suitable choice for use with the multi-parameter technique.

8.2.1.2 Phase Fluorometry Electronics

The sensor films were interrogated using the analog phase fluorometry system described in section 3.2.2, with a separate system being used for each film. The use of two separate systems would not be practical in a finished sensor system. As this work was being carried out for proof of concept purposes, however, it was not an issue in this case. It was found during operation that if the same modulation frequency setting was used for both systems that the systems would interfere with each other. Due to the nature of the flowcell that was used for testing, it was not possible to achieve optical isolation between both systems.

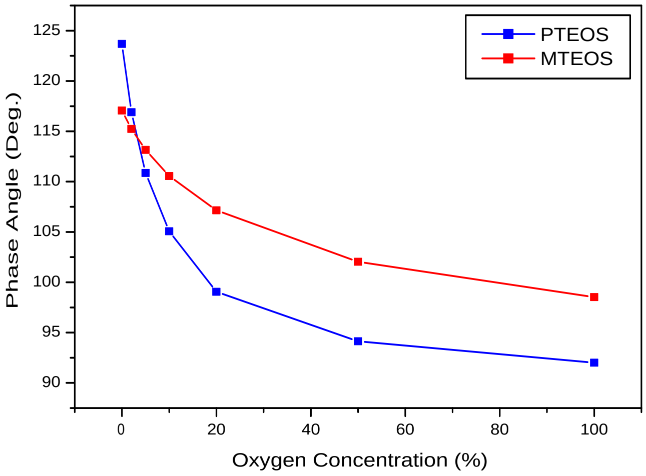

Figure 8.1: Calibration curves for MTEOS and PTEOS-based oxygen sensors. Both curves were obtained at $20°C$.

The resulting crosstalk led to beat frequency effects appearing in the outputs of both systems, which was caused by a slight mismatch in the frequency of each system. The problem was overcome by operating the systems at two different frequencies ($20KHz$ and $25KHz$). The operation of the systems at two different frequencies should not be confused with the multi-frequency operation that is an intrinsic part of the single-element approach.

8.2.1.3 Multi-element Flowcell and Experimental Setup

A dual right-angle flowcell that was capable of accommodating two sensor films simultaneously was designed for testing the films. A diagram of the cell is shown in Fig. 8.2. The sensor films are fixed on either side of a mounting plate that is placed at the centre of the cell. Excitation and detection is achieved through ports in the sides of the cell that are oriented at right angles to one another. The excitation and emission filters are held in place using the LED and photodiode mounting blocks. Gas entry and exit ports are placed at opposite corners of the cell.

An experimental setup similar to that which was used for the breath oxygen sensor (see section 6.5.1) was used to control the oxygen concentration and temperature in the cell. The gas concentration was controlled using computer-controlled mass flow controllers and a resistive type gas heater was used to change the temperature of the gas and thus the cell. The temperature in the cell was measured using a thermocouple.

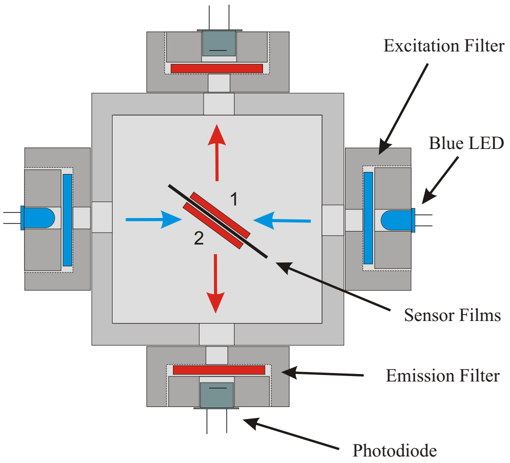

Figure 8.2: The flowcell that was designed for calibration and testing purposes. The cell, which has been machined from an opaque polymer (Acetal) can accommodate two sensor elements simultaneously.

8.2.1.4 Sensor Calibration

The sensor elements were calibrated by varying the oxygen concentration and temperature in the cell over suitable ranges. As was the case with the breath monitoring work, the oxygen concentration could be changed much more rapidly than the temperature in the cell. For this reason, the oxygen concentration was cycled through the full range of calibration values at each temperature before moving to the next temperature setting. The raw calibration data for both films were fitted using TableCurve3D as described in section 5.3.1, in order to generate the calibration functions required by the multi-parameter algorithm.

8.2.2 Results

The performance of the multi-element system was investigated by processing the data obtained during the calibration process using the 1D algorithm that is described in section 5.3.2.1. The calibration data were used instead of obtaining new sensor measurements in order to eliminate the possibility of drift and measurement-related errors masking the baseline performance of the multi-parameter technique. A representative selection of the results that were obtained is presented in Table 8.1. It can be seen from the data presented that the technique generates the expected values for certain oxygen concentration and temperature values but that there are large errors in the calculated values for others. In order to determine why the technique did not function correctly for certain values, the level curves generated by the algorithm were inspected. In the cases where the algorithm generated results that were close to the expected values it was found that the level curves had significantly different slopes in the P_1P_2

Actual O_2 (%)	Calculated O_2 (%)	Actual Temp. ($^{\circ}C$)	Calculated Temp. ($^{\circ}C$)
10.3	10.4	40.3	40.3
20.3	20.3	30.0	30.0
10.3	10.2	36.5	36.9
2.4	4.4	38.6	31.0
5.4	3.4	33.1	39.2
5.4	3.9	36.6	40.7

Table 8.1: The actual oxygen concentrations are listed in columns 1 and 3 and the measured values are listed in columns 2 and 4. The samples listed are representative of a dataset that contains 36 points.

plane and displayed a single point of intersection at or close to the expected point. However, in the cases where large errors occurred, it was found that the level curves had very similar slopes and in some cases displayed multiple points of intersection. An example of the level curves obtained in both scenarios is presented in Fig. 8.3. The level curves provide insight into the behaviour of the algorithm. In order to function correctly, the algorithm requires that the slopes of the level curves be significantly different. As can be seen in Fig. 8.3, however, this is not always the case. The relative slopes of the level curves are governed by the relative sensitivity of the sensor elements to the parameters being measured. The fact that the curves are coincident in certain cases indicates that both sensor elements display identical sensitivity for certain oxygen concentration and temperature combinations. The implication of this is that the multi-parameter technique will function correctly in certain regions, or zones, of the calibration

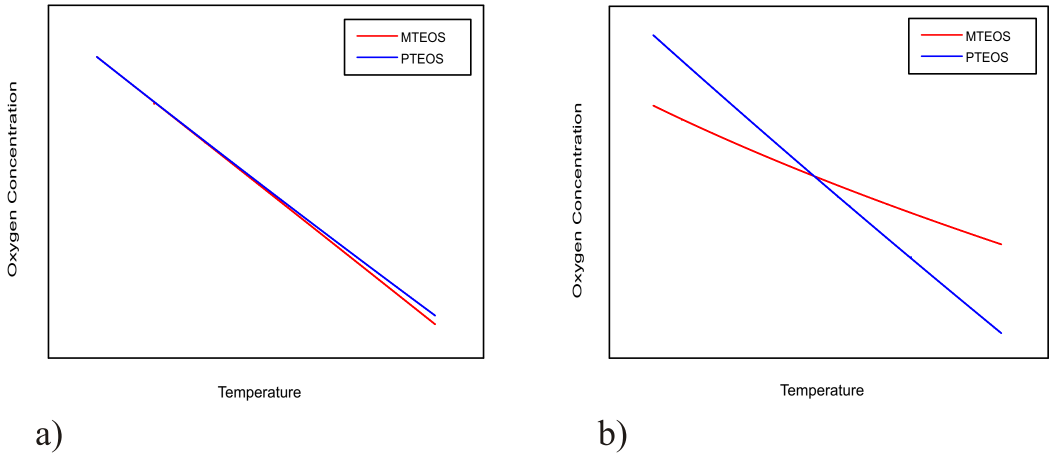

Figure 8.3: The level curves presented in b) correspond to a situation in which the correct results were obtained while those presented in a) were for a set of measurement values that resulted in large errors.

plane, but not others, which means that the sensor element combination that was selected was not a good choice for the oxygen concentration and temperature ranges that were used. This highlights a consideration that must be taken into account when using the multi-element implementation of the multi-parameter technique, and perhaps also the single-element version.

The fact that correct results were obtained using the technique verifies that the algorithm and the multi-parameter technique in general functions correctly when used with experimental data. Additionally, a calibration plane region where the technique was viable was identified and the results obtained from that region were used to demonstrate that the technique can be used to achieve temperature compensation of oxygen sensor measurements. Temperature-compensated data from this region are presented in Fig. 8.4. The oxygen concentration values that would have been obtained if temperature compensation was not carried out are included for reference.

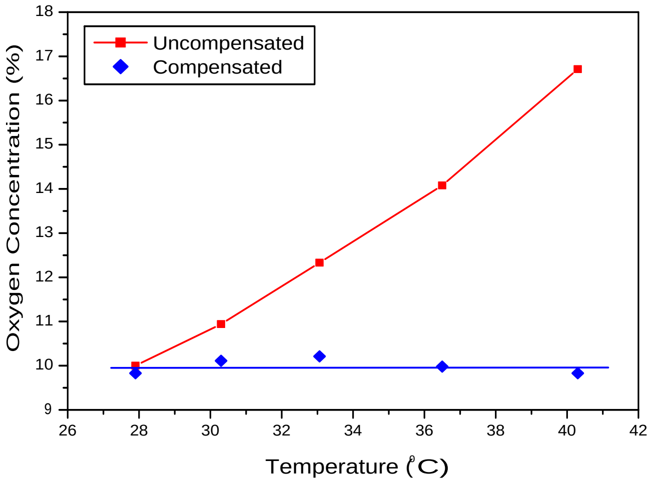

Figure 8.4: Oxygen concentration data that were obtained at an oxygen concentration setting of 10% and a range of temperatures. The oxygen values that would have been obtained if temperature was not accounted for are also shown.

Despite the fact that the sensor elements that were chosen were not suitable for the oxygen concentration and temperature ranges that were used, the system successfully demonstrated the feasibility of the multi-parameter technique when used with experimental data. As a result, it was decided to move on to the development of a single-element-based oxygen and temperature measurement system.

8.3 Single Element Approach

A single-element-based system for simultaneously measuring oxygen concentration and temperature was implemented. It consisted of a sensor film that contains two oxygen-sensitive dyes, $[Ru(dpp)_3]^{2+}$ and Ruthenium(II)tris(2,2-bipyridyl)$^{2+}$ ($[Ru(bpy)_3]^{2+}$), which have unquenched lifetimes of $\sim 5\mu s$ and $\sim 300ns$, respectively. The optical platform that was used in the breath monitoring project, which is described in section 6.4, was used to accommodate the sensor element. The DSP-based electronic system described in section 3.4 was used to interrogate the sensor. Each part of the system is described in greater detail in the next section.

The motivation for this work was two-fold. Firstly, as discussed in section 6.8, the accuracy of the oxygen measurements obtained in a breath oxygen measurement system will be maximised if the sensor used for temperature compensation is co-located with the oxygen film. Maximising the accuracy of the breath oxygen system that was described in chapter 6 is a key focus moving forward in order that the technology may be applied to challenging application areas such as monitoring the status of COPD patients. The second motivation for this work was to demonstrate the feasibility of implementing the multi-parameter technique using a single sensor element-based configuration.

8.3.1 System Description

8.3.1.1 Sensor Element

In order for the multi-parameter technique to work it was required that the sensor element contain two fluorophores with different lifetimes that displayed differing sensitivities. Although there are a range of oxygen sensitive fluorophores available that satisfy this requirement, the majority do not have overlapping excitation and emission bands. The use of dyes for which this is the case is desirable as it allows the use of a single excitation LED and emission filter. Two of the ruthenium-based dyes, $[Ru(dpp)_3]^{2+}$ and $[Ru(bpy)_3]^{2+}$ were found to be suitable in this regard. Once suitable fluorophores were identified, the next challenge was to co-immobilise them in a single film. This aspect of the work was carried out by a laboratory colleague but is summarised briefly here.

The simplest option was to simply mix both dyes together and immobilise the resulting mixture in a suitable matrix. A PTEOS-based solgel was used for this purpose. Due to the mechanism of operation of the multi-parameter technique, it was felt that the ratio of the emission intensities from each of the fluorophores could impact on its performance. As a result, a range of sensor elements were fabricated using different fluorophore ratios. The range of elements that were fabricated are listed in Table 8.2.

$[Ru(dpp)_3]^{2+}$	:	$[Ru(bpy)_3]^{2+}$
5	:	1
1	:	1
1	:	5

Table 8.2: The molar fluorophore ratios that were used in the sensor elements.

The sensor elements were fabricated by spin-coating the uncured sol onto $16mm$ diameter glass coverslips. These were chosen as they were compatible with the optical assembly that was being used. Following the spin-coating process, the sensor elements were cured at $110°C$ and then aged for 4 - 6 weeks before use, in order to allow the sensor films to stabilise.

8.3.1.2 Electronics

A single-element implementation of the multi-parameter technique requires that the sensor film be interrogated using multi-frequency techniques. The DSP-based electronic system that was developed during the course of this work, and which is described in detail in section 3.4, is capable of simultaneous multi-frequency operation. The DSP-based system modulates the excitation source using a composite waveform containing components at the required frequencies and then carries out synchronous demodulation on the resulting composite emission waveform, at each of the modulation frequencies, in order to evaluate the intensity and phase of the emission at each frequency. As discussed in section 5.3.2.3, a post-processing-based implementation of the the multi-parameter algorithms were used for this work. In order to log the raw sensor data to file, the DSP system GUI, which is described in section 7.3.3, was used. Both the intensity and phase-angle values were stored in all cases.

8.3.1.3 Optical Assembly and Experimental Setup

It was decided to use an "enhanced capture" optical probe to optimise the capture of fluorescence from the sensor element in order to maximise SNR. The optical assembly that was developed for the breath monitoring project was used without any modifications. This allowed the test and calibration system that was developed for that application to be used, a description of which can be found in section 6.5.1. The only change that was made to the calibration system is that the analog MFCs that were used previously were replaced with digital MFCs, which have higher setpoint accuracy.

8.3.2 Results

Each of the various sensor formulations that were prepared was tested in order to determine its performance. The DSP system was operated in multi-frequency mode at frequencies of $18181.2Hz$ and $40000Hz$. Phase values at each frequency were obtained for a number of points in the oxygen concentration range of $0-20\%$ and the temperature range of $(\sim 26- \sim 32^\circ)$. Using the phase data obtained, calibration surfaces were generated for each frequency using TableCurve3D. The 1D algorithm was then used to process sensor data using the generated surfaces. As with the multi-element system, the sensor data that were obtained during the calibration process were used for testing the feasibility of the algorithm.

A minor issue that was encountered during the curve fitting process, and the resulting solution that was devised, are worth noting. The issue was caused by the fact that the oxygen concentration range extended to zero in this case. A significant number of the candidate functions in Tablecurv3D's database contain discontinuities at 0 or 1, which renders them unsuitable. This had an adverse effect on the fit quality that could be obtained, which had a knock-on effect on the performance of the multi-parameter algorithms. It was found that offsetting the oxygen concentration values such that 0 or 1 no longer lay in the range was an effective solution. 10% was added to the oxygen concentration calibration data, before they were processed by TableCurve3D, which led to the availability of a much wider range of candidate functions and higher quality fits. The 10% offset is accounted for by subtracting 10% from the oxygen concentration values calculated by the algorithm.

A high level assessment of the performance of each of the formulations that was tested is presented in Table 8.3. The performance of each of the films was assessed in terms of the oxygen concentration and temperature values that were calculated by the algorithm. A subjective, rating-based method is used to describe the performance of each of the films in the first instance, in order to avoid having to list large amounts of numerical data that would be quite unpalatable to the reader. If the values that were obtained were in no way related to the expected values then the performance was deemed as being "very poor", whereas, if there was

Element no.	Element Composition	Performance
1	$[Ru(dpp)_3]^{2+} + [Ru(bpy)_3]^{2+}$ (5:1)	Very poor
2	$[Ru(dpp)_3]^{2+} + [Ru(bpy)_3]^{2+}$ (1:1)	Poor
3	$[Ru(dpp)_3]^{2+} + [Ru(bpy)_3]^{2+}$ (1:5)	Good

Table 8.3: High level assessment of comparative performance of each of the sensor film formulations that were tested.

some correlation between the calculated values and the expected results, but the errors were large, the performance was described as being “poor”. Situations such as that encountered by the multi-element system, where acceptable results were only obtained for certain regions of the calibration plane, were also described as “poor”. A rating of “good” required that there were no regions in the calibration plane in which the technique did not function satisfactorily, and also that the errors in the calculated values were small. In addition to assessing the calculated results, the level curves generated by the algorithm were also inspected. As was the case with the multi-element system (section 8.2.2), there was a clear relationship between the level curves and the quality of the results that were obtained. In all of the cases where the technique performed poorly it was found that the level curves were very similar or in some cases fully coincident, thus providing an explanation for the poor performance that was obtained.

As can be seen from Table 8.3, only one of the sensor element formulations that were tested performed to an acceptable level. There is a clear trend in the performance of the elements that made use of a $[Ru(dpp)_3]^{2+}$ + $[Ru(bpy)_3]^{2+}$ mixture. As the relative amount of $[Ru(bpy)_3]^{2+}$ is increased, the performance of the multi-parameter algorithm improves, with good performance being achieved for a ratio of $[Ru(bpy)_3]^{2+}$ to $[Ru(dpp)_3]^{2+}$ of 5 : 1. It is likely that this is related to the relative quantum efficiencies of the two fluorophores, with that of $[Ru(bpy)_3]^{2+}$ being considerably lower than that of $[Ru(dpp)_3]^{2+}$. In order to achieve similar emission intensities from both fluorophores, there would have to be a larger amount of $[Ru(bpy)_3]^{2+}$ in the mixture. The calculated and expected oxygen and temperature values that were obtained with sensor element 3 are listed in Table 8.4. It can be seen that the oxygen values that were calculated by the system are in very close agreement with the expected values but that there are significant errors associated with some of the calculated temperature values. This is not of major concern in this case as the sensor system is being used for temperature compensation purposes, which do not require that the temperature measurements that are obtained are accurate. It was necessary, however, that the cause of this behaviour be investigated, as it may lead to limitations in applications involving different analytes or parameters. Once again, the level curves served to provide an explanation. The level curves that were generated by the algorithm when calculating the parameters listed in row 8 of Table 8.4 are shown in Fig. 8.5. The fact that the oxygen concentration values were calculated more accurately than the temperature values can be understood by considering the relative sensitivities of the level curves shown in Fig. 8.5 to each of the parameters. It can be seen that a given measurement error, which manifests as a change in the location of the level curve, in the direction perpendicular to the curve, (see

Actual O_2 (%)	Calculated O_2 (%)	Actual Temp. ($°C$)	Calculated Temp. ($°C$)
0.00	0.01	26.7	26.1
2.00	1.97	26.7	27.4
5.00	4.98	26.7	26.7
10.00	10.04	26.7	26.1
20.00	19.96	26.7	27.0
0.00	0.01	29.6	28.9
2.00	1.99	29.6	29.8
5.00	4.98	29.6	29.8
10.00	10.04	29.6	29.6
20.00	20.06	29.6	29.4
0.00	-0.04	31.9	33.0
2.00	2.05	31.9	31.4
5.00	5.06	31.9	31.7
10.00	9.85	31.9	32.3
20.00	20.11	31.9	31.8

Table 8.4: The actual oxygen concentrations are listed in columns 1 and 3 and the measured values are listed in columns 2 and 4. The samples listed correspond to a dataset that contained 15 points.

section 5.4.1), will cause a considerably larger error in the calculated temperature value than in the oxygen value. The relative sensitivities of the level curves are a function of the parameters that govern optimum frequency selection (see section 5.3.3), in addition to the intrinsic sensitivity of each of the fluorophores to both parameters. It was not possible to carry out an analysis of these factors, either from a theoretical or empirical standpoint, as part of this work, and it remains as a key component of the future work that is planned in this area.

8.3.2.1 Resolution

The resolution of the system is given by the peak-to-peak noise present in the calculated parameter values for steady-state conditions. This measurement was carried out for an oxygen concentration of 5% and a temperature of $29.6°C$. The values that were obtained are listed in Table 8.5. These values are in line with those which are presented in Table 8.4, in that the oxygen measurement resolution is well within acceptable levels whereas the temperature measurement

Oxygen (%)	Temperature ($°C$)
0.36	3.8

Table 8.5: The oxygen concentration and temperature measurement resolution of the system at an oxygen concentration of 5% and a temperature of $29.6°C$.

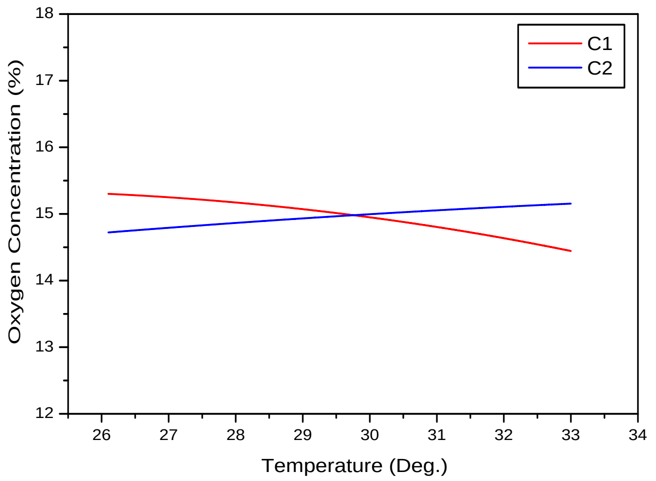

Figure 8.5: The level curves $(C_1,\ C_2)$ that were generated by the 1D algorithm when calculating the values displayed in row 8 in Table 8.4. Note that the 10% offset that was discussed earlier in this section is reflected in the level curves.

resolution is not. Due to the nature of this particular application, this is not of concern, however the potential for this type of behaviour must borne in mind if the technique is applied to other analyte or parameter combinations.

8.3.2.2 Discussion

Despite the errors present in the temperature data, the data presented in Table 8.4 clearly demonstrates the feasibility of using the multi-parameter technique in a single-element configuration for temperature compensation purposes. It also demonstrates the feasibility of the single-element implementation of the multi-parameter technique in general, and leaves the way clear for the technique to be used for the measurement of other analytes or parameters.

8.4 Conclusions and Future Work

The feasibility of using the multi-parameter technique that was developed during this work for obtaining temperature-compensated oxygen concentration measurements using a single sensor element has been demonstrated. In order to test the feasibility of the technique at a basic level, while avoiding the difficulties involved in fabricating a suitable single element, a dual-element implementation was designed and implemented. The results obtained using the dual-element system indicated that the multi-parameter technique functioned correctly with real, physical data, and that it could be used for the purposes of temperature compensation. Following on from this, a single-element implementation was designed and tested. A suitable sensor element composition was identified and testing revealed that accurate temperature compensated oxygen concentration values could be obtained.

A number of elements of future work are planned for the single-element temperature-compensated oxygen sensor that has been described. The first of these is to develop a methodology for optimising the performance of the sensor. This will involve the sensitivity-related analysis that is described in section 5.4.1, and also the development of a means of empirically identifying the optimum modulation frequencies, as discussed in section 5.3.3. Also, a number of additional sensor formulations that may lead to improved performance have been identified by laboratory colleagues, and once formulated, these will be tested and fully characterised.

To date, the application of the multi-parameter technique has been limited to the measurement of temperature compensated oxygen values. It is intended that the single-element multi-parameter technique be applied to additional analyte combinations. One particular analyte combination that was identified for future investigation is dissolved oxygen/pH. The target application for this sensing combination is bio-process monitoring, where the ability to simultaneously measure dissolved oxygen and pH offers a number of advantages over current approaches.

The final area of future work that is under consideration is the extension of the technique to three or more parameters. A potential application in this area is the development of a three-in-one sensor for the measurement of dissolved oxygen, pH and dissolved carbon dioxide.

Bibliography

[1] Dorota Wencel. *Sol-gel-derived Optical Oxygen, pH and Dissolved Carbon Dioxide Sensors*. Ph.D. Thesis, Dublin City University, 2008.

[2] Clare Higgins, Dorota Wencel, Conor S. Burke, Brian D. MacCraith, and Colette McDonagh. Novel hybrid optical sensor materials for in-breath o-2 analysis. *Analyst*, 133(2):241–247, 2008.

Chapter 9

Conclusions and Further Work

The primary aim of this work, which was the development of luminescence-based sensor systems with increased performance and/or functionality over the current state of the art, was realised. Each of the specific research objectives, which are outlined in chapter 1, were satisfied.

Three instrumentation electronics systems were developed. The first is an analog phase fluorometry system that was designed specifically for a range of oxygen sensing applications, including real-time breath oxygen measurement. The second system is a digital implementation of the first, which was designed with reduced size in mind. The resulting system was battery-powered and was incorporated into a belt-mountable enclosure for use in the measurement of breath oxygen concentration. The third system, which represents the culmination of the instrumentation electronics-related design efforts, is based on a high performance DSP and is capable of multi-frequency operation in intensity, phase or ratiometric-intensity measurement modes. It has improved functionality and noise-and drift-related performance characteristics compared to any systems which are reported in the literature or which are available commercially.

An enhanced luminescence capture-based optical probe that was designed previously at this laboratory was incorporated into sensing systems for a number of applications. A range of design improvements were developed and implemented that added functionality to, and increased the robustness and useability of, the original probe design. From a functionality perspective, a dual-excitation-based ratiometric probe configuration was developed that allowed the advantages associated with enhanced luminescence capture to be applied to ratiometric mode sensing. The robustness and useability of the original design was limited by the use of thin sample slides, the formation of bubbles and the mechanical instability of the probe. Design improvements were implemented that addressed each of these issues and led to a much improved design from a user perspective.

As part of the optical sensor platform work, an enhanced capture element that was optimised for general sensing applications was designed. Custom ray tracing software was developed and used in conjunction with optimisation algorithms to identify the optimum capture structure design. The optimum design resulted in a factor of three increase in luminescence capture from a typical sensor spot compared to the original design.

A multi-parameter technique was developed that allows the simultaneous measurement of multiple parameters using a single sensor element. The technique is based on the use of a successive approximation-based numerical data processing algorithm that overcomes the limitations associated with alternative approaches. An intrinsic element of the multi-parameter technique that was developed is the use of curve-fitting techniques. this results in a black-box-based approach that allows multi-element systems to be rapidly developed without the need for time-consuming theoretical modelling.

A key part of the work that was completed was the development of sensor systems for a range of specific applications. Sensor systems were developed for the following:

- Real-time breath oxygen measurement
- Dissolved oxygen measurement
- Dissolved carbon dioxide
- Simultaneous measurement of oxygen concentration and temperature

The breath oxygen system that was developed sees the sensor element being placed directly in the airflow, which allows the full oxygen concentration profile to be measured in real-time. This represents a significant improvement over the gas sampling-based approaches that are currently used. The system was used to measure the oxygen consumption of an individual at rest and good agreement with the expected values was observed.

Both of the dissolved sensors that were developed display resolution/LOD performance that exceeds that of any of the comparable systems that are reported in the literature and were available commercially. The dissolved carbon dioxide sensor is operated in ratiometric mode and makes use of the ratiometric optical probe and the DSP-based electronics. The multi-frequency capabilities of the DSP electronics facilitates the constant illumination of the sample with both excitation sources, which represents an improvement over the standard approach in which the light sources must be operated alternately.

The multi-parameter technique that was developed during this work was used to develop a system that simultaneously measures oxygen concentration and temperature using a single sensor element. The intended application of the system is the acquisition of accurately temperature compensated oxygen concentration measurements in applications that are exposed to rapidly changing temperatures, such as in the breath oxygen application. The system was tested over a range of oxygen concentration and temperature values and the feasibility of the multi-parameter technique for use in this application was verified.

A considerable amount of future work is planned and has been outlined at the end of each chapter. There are a number of key focus areas going forward. The first is the development of a miniaturised breath oxygen measurement system that incorporates the following:

- Miniaturised DSP-based electronics
- Lightweight and robust optical probe that incorporates the relevant subset of the design improvements that were developed, including the optimised element design.
- Single element-based measurement of oxygen and temperature

The second key focus area is the expansion of the multi-parameter technique to other analyte combinations and to move to three or more analytes. One area that is of particular interest is the development of multi-parameter sensors for use in bio-reactors and fermenters.

List of Publications and Conference Presentations

Oral Presentations

- *"Exploiting sensor cross sensitivity: Achieving temperature compensation via a dual-element optical oxygen sensor"*. Advanced Environmental, Chemical, and Biological Sensing Technologies IV ,Optics East, 1 - 4th October 2006 , Boston, USA

Poster Presentations

- John P. Moore, John P. Moore, Ross N. Gillanders, Conor S. Burke, Brian D. MacCraith and Colette McDonagh, *"Development of an Optical Dissolved Oxygen Sensor for Wireless Environmental Monitoring"*. Europtrode IX, Dublin, March 2008
- John P. Moore, Maja Sourdaine, Dorota Wencel, Niall Stevenson, Colette McDonagh, Conor S. Burke, Brian D. MacCraith, *"A Novel Technique for Multi-parameter Sensing using a Single Sensor Spot"*. Europtrode X, Prague, March 2010

Patents

- Conor S. Burke, John P. Moore, *"Single Element Sensor With Multiple Outputs"*. PCT/EP2008/056643, WO2008/148703, 2008
- Conor S. Burke, Thomas Ruckstuhl, John P. Moore, *"Optical Probe"*. US2009191092 (A1), WO2008029298 (A2), 2006

Conference Proceedings

- John P. Moore, Clare Higgins, Orla McGaughey, Brian G. Lawless, Brian D. MacCraith, *"Exploiting sensor cross sensitivity: Achieving temperature compensation via a dual-element optical oxygen sensor"*. Proceedings of the SPIE, vol:6377, Advanced Environmental, Chemical, and Biological Sensing Technologies IV, Optics East, 2006

Peer-reviewed Publications

- Conor S. Burke, John P. Moore, Dorota Wencel, Brian D. MacCraith, *"Development of a compact optical sensor for real-time, breath-by-breath detection of oxygen"*. Journal of Breath Research, 2, 3, 037012, 2008
- Conor S. Burke, John P. Moore, Dorota Wencel, Aishling K. McEvoy, Brian D. MacCraith, *"Breath-by-breath measurement of oxygen using a compact optical sensor"*. Journal of Biomedical Optics, 13, 1, 014027, 2008
- Juncal Estella, Dorota Wencel, John P. Moore, Maja Sourdaine, Colette McDonagh, *"Fabrication and performance evaluation of highly sensitive hybrid solgel-derived oxygen sensor films based on a fluorinated precursor"*. Analytica Chimica Acta, 666, 1-2, 83-90, 2010

Appendix A

Derivation of Power in Square and Sine wave Modulation Waveforms

The power, P, in a waveform is given by $P = V_{rms} I_{rms}$ The rms amplitude, A_{rms}, of a sine wave of amplitude A centred on zero is given by $A/\sqrt{2}$ while that of a similar square wave is given by A. The power dissipated by the waveform in a load of resistance R (assume resistive load only. Ok for comparison purposes) is:

$$P = V_{rms}^2 / R \tag{A.1}$$

Therefore the power in a square wave, P_{sq}, is given by:

$$P_{sq} = A_{sq}^2 \tag{A.2}$$

and that of a sine wave is:

$$P_{si} = A_{si}^2 / 2 \tag{A.3}$$

Taking the fact that the waveforms aren't centred on zero into account, and omitting the R term as it will cancel later yields:

$$P_{sq} = (A_{sq}/2)^2 + A_{sq}^2 = 1.25 A_{sq}^2 \tag{A.4}$$

$$P_{si} = (A_{si}/2)^2 + A_{si}^2/2 = 0.75 A_{si}^2 \tag{A.5}$$

Setting both powers equal yields:

$$A_{si} = 1.29 A_{sq} \tag{A.6}$$

This equality was used to generate the data shown in Fig. 3.3.

Appendix B

Circuit Diagrams

This appendix contains the circuit diagrams of the systems that were developed during this work. All of the design work was carried out using Altium Designer 2004 (Service Packs 3 and 4).

B.1 Analog Phase Fluorometry System Circuit diagrams

The schematic diagram for this system is divided over four pages (Fig. B.1 - B.4).

B.2 Digital Phase Fluorometry System - Innovada Circuit Diagrams

The schematic diagram for this system was prepared by Innovada, the company that the system was designed in conjunction with. The schematic diagram of a two-channel photodiode amplifier that was designed for use with the system is shown in Figs. B.6, B.7 and B.8.

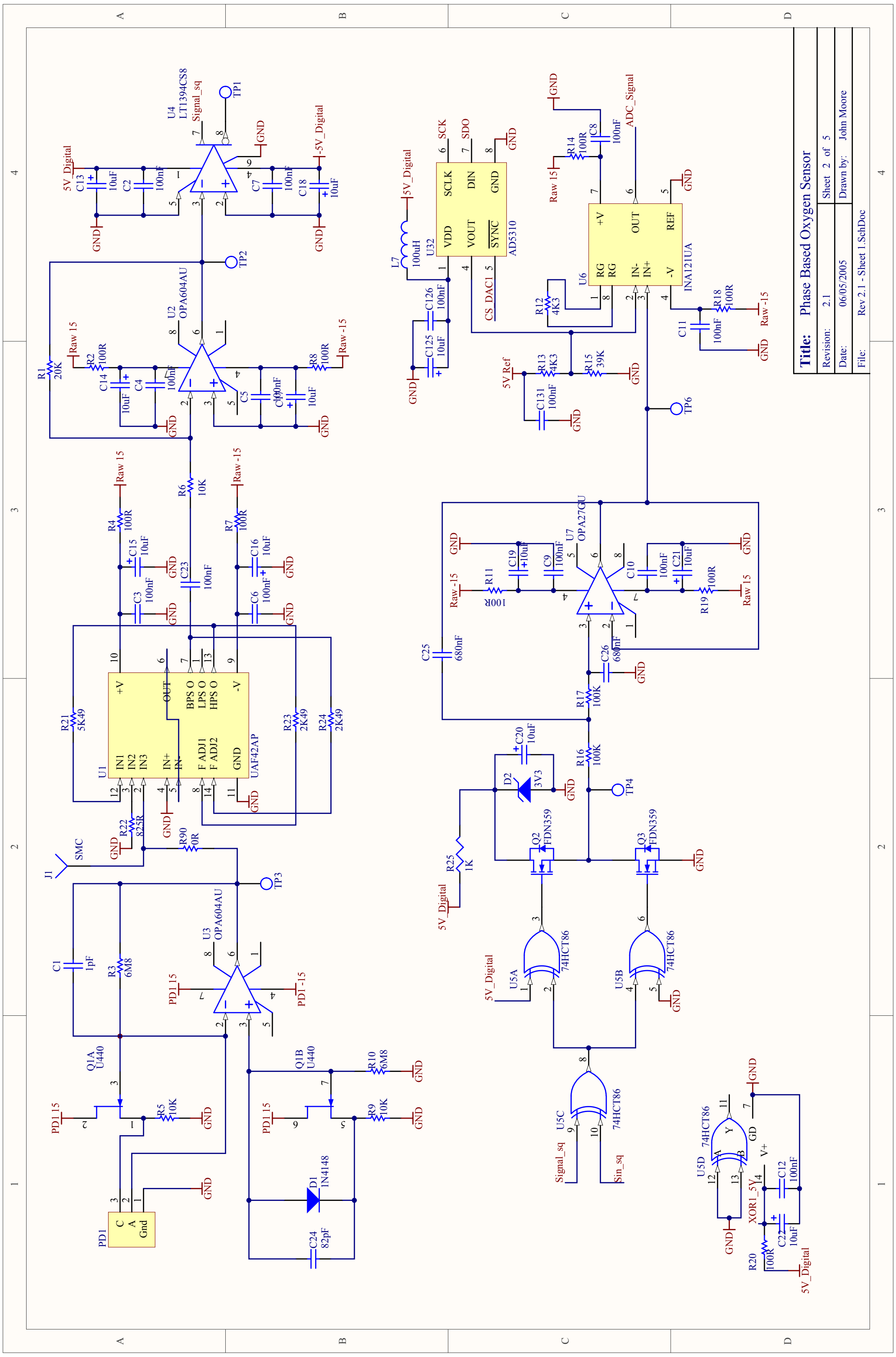

Figure B.1: Analog phase fluorometry system - Signal Channel

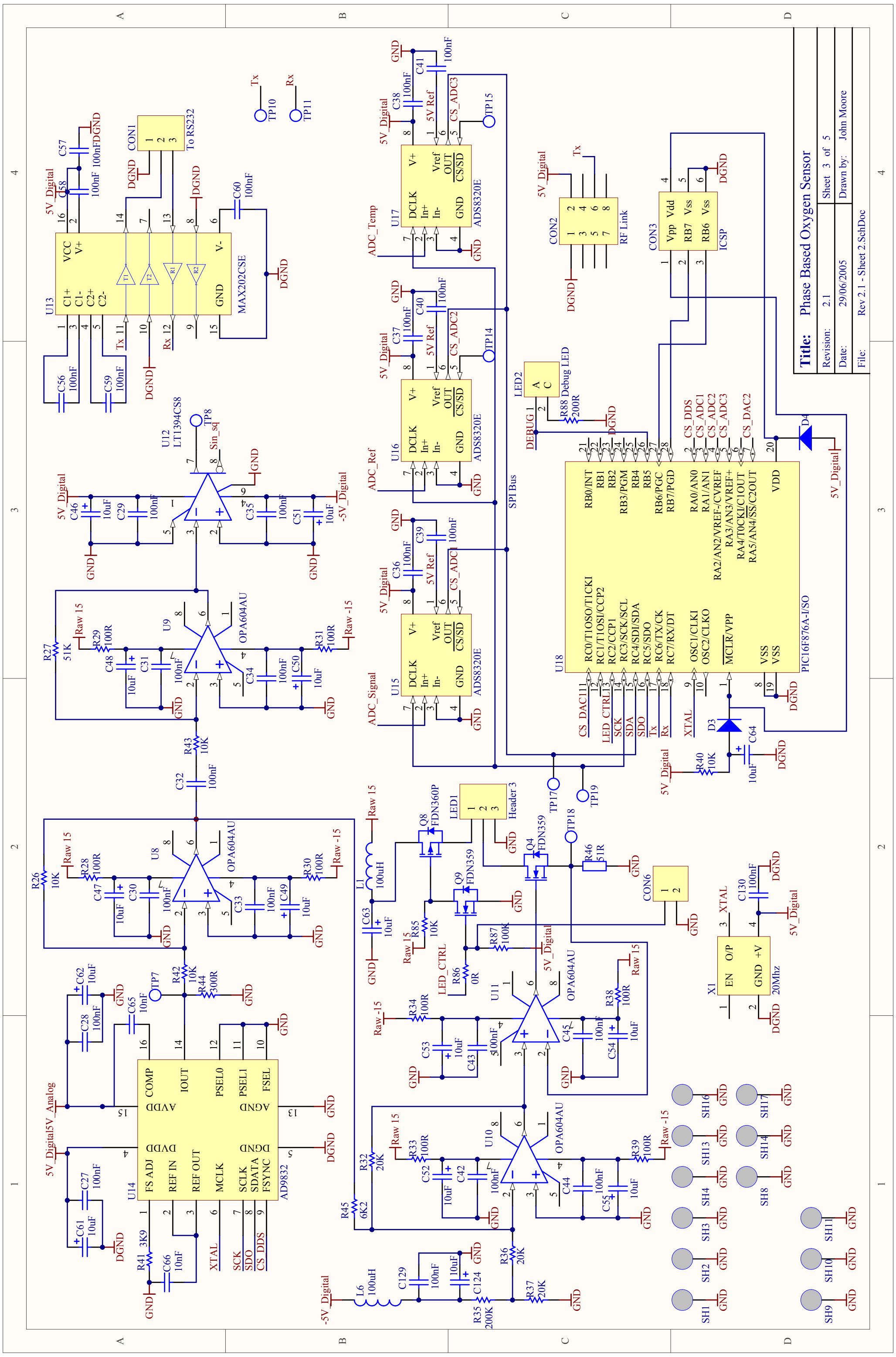

Figure B.2: Analog phase fluorometry system - Digital Components

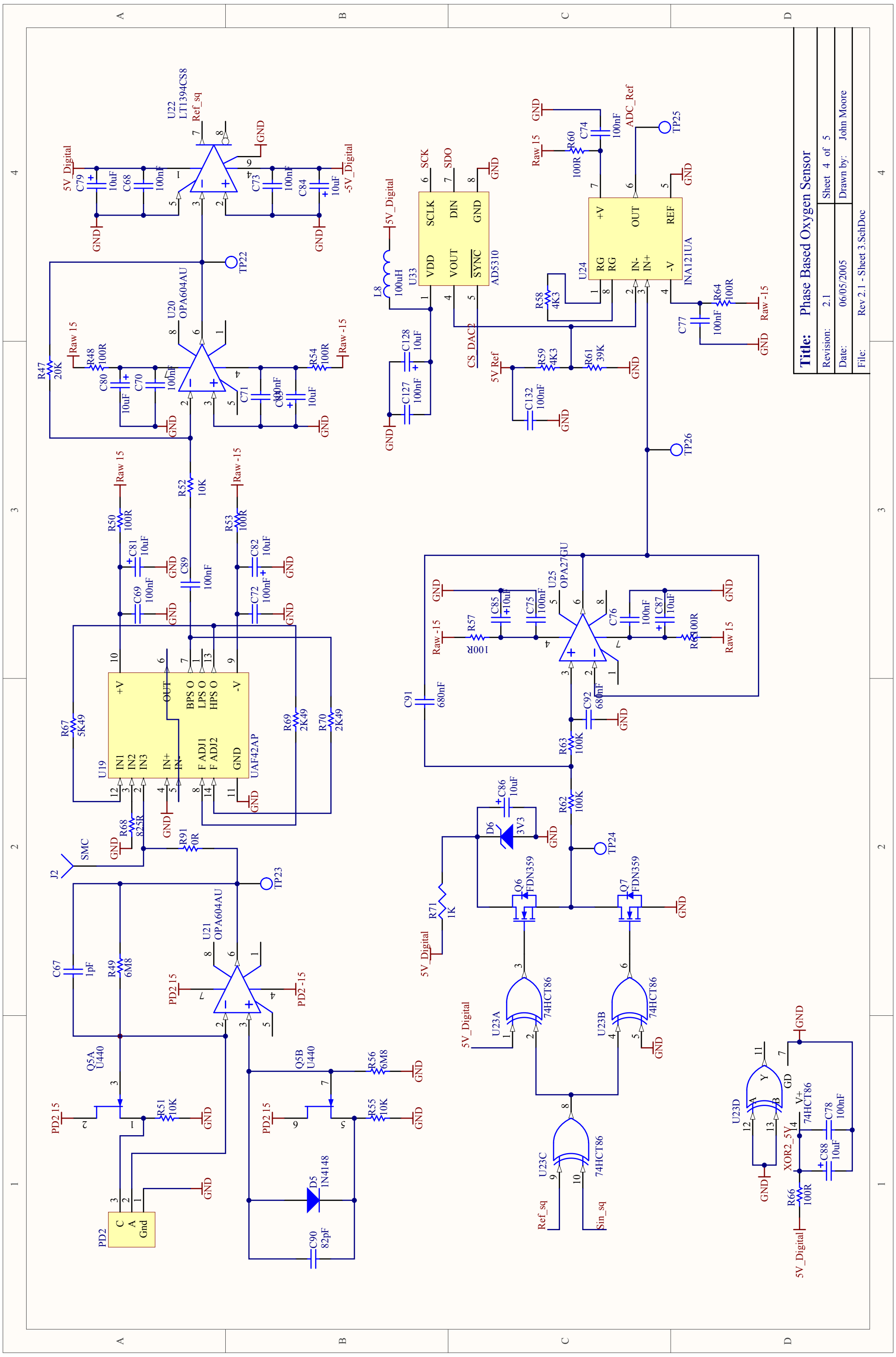

Figure B.3: Analog phase fluorometry system - Reference Channel

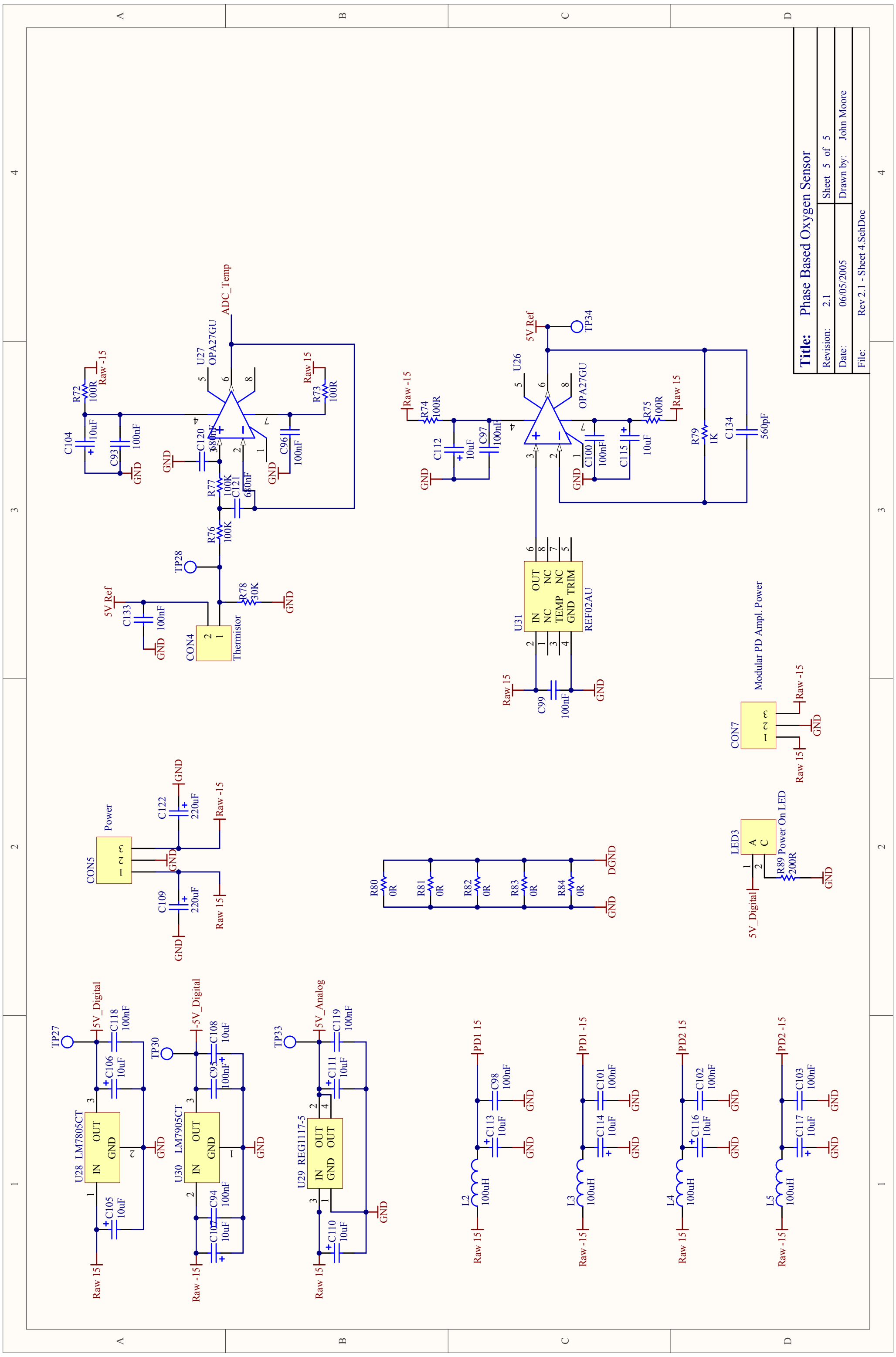

Figure B.4: Analog phase fluorometry system - Power

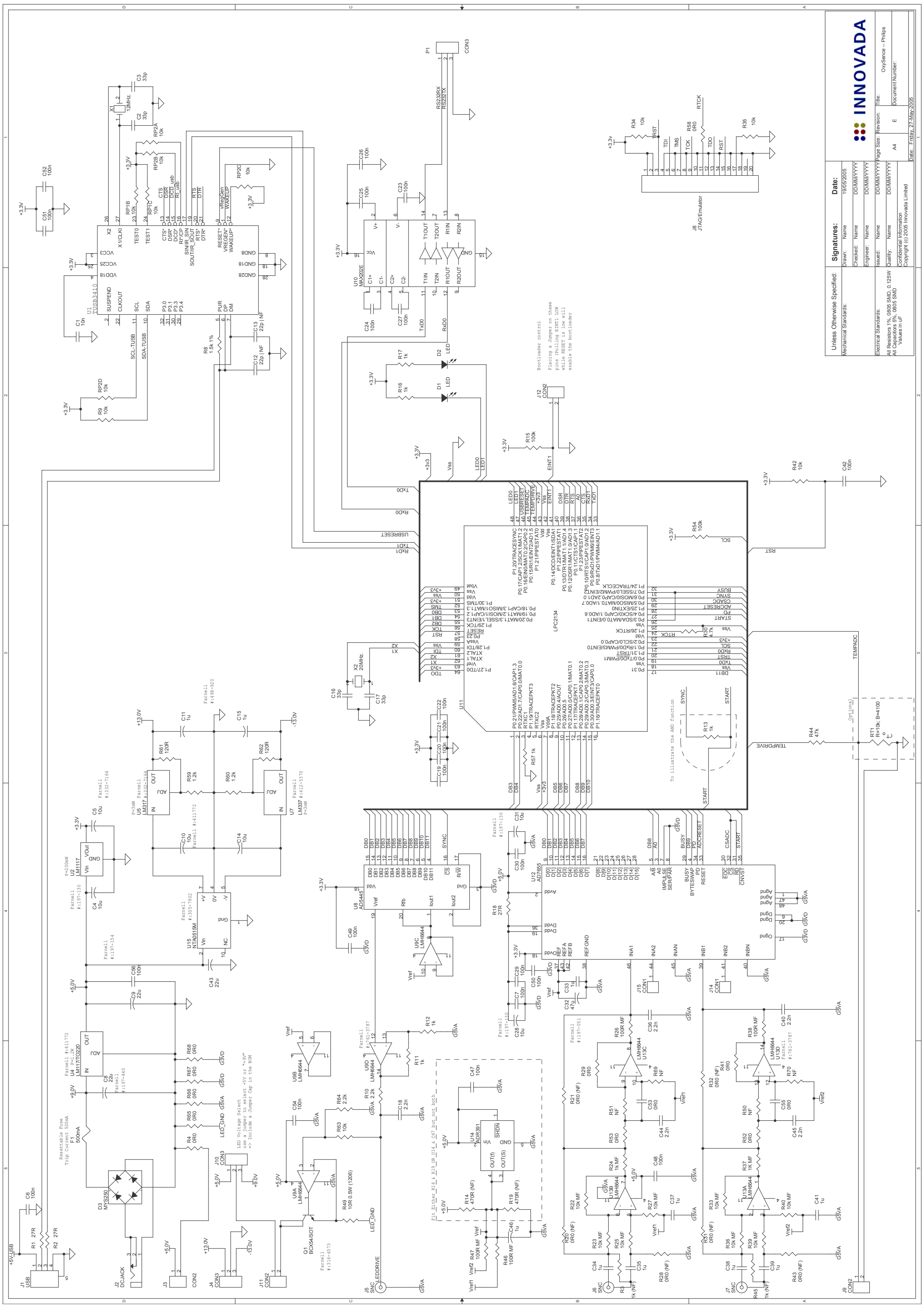

Figure B.5: Digital Phase Fluorometry System

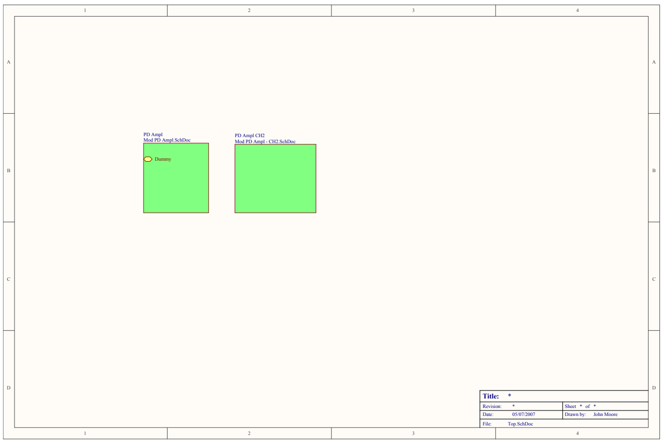

Figure B.6: Photdiode Amplifier - Top Level

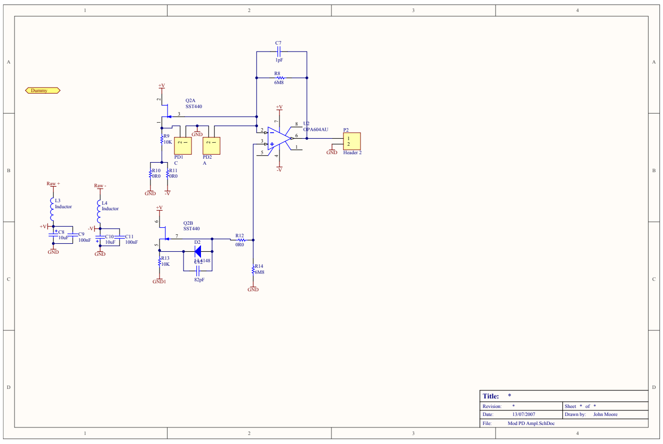

Figure B.7: Photodiode Amplifier - Channel 1

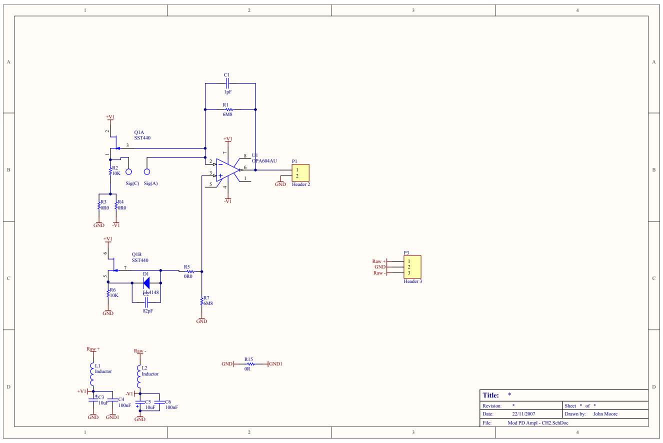

Figure B.8: Photodiode Amplifier - Channel 3

B.3 DSP System Circuit Diagrams

The schematic diagram for the DSP-based system is divided over 12 pages (Figs. B.9 - B.20). The multi-channel design capabilities of Altium Designer 2004 were used in the design of the multi-channel elements of the system. This functionality is controlled using the ‘Repeat($\cdots$)’ command that can be seen on the top level diagram B.9.

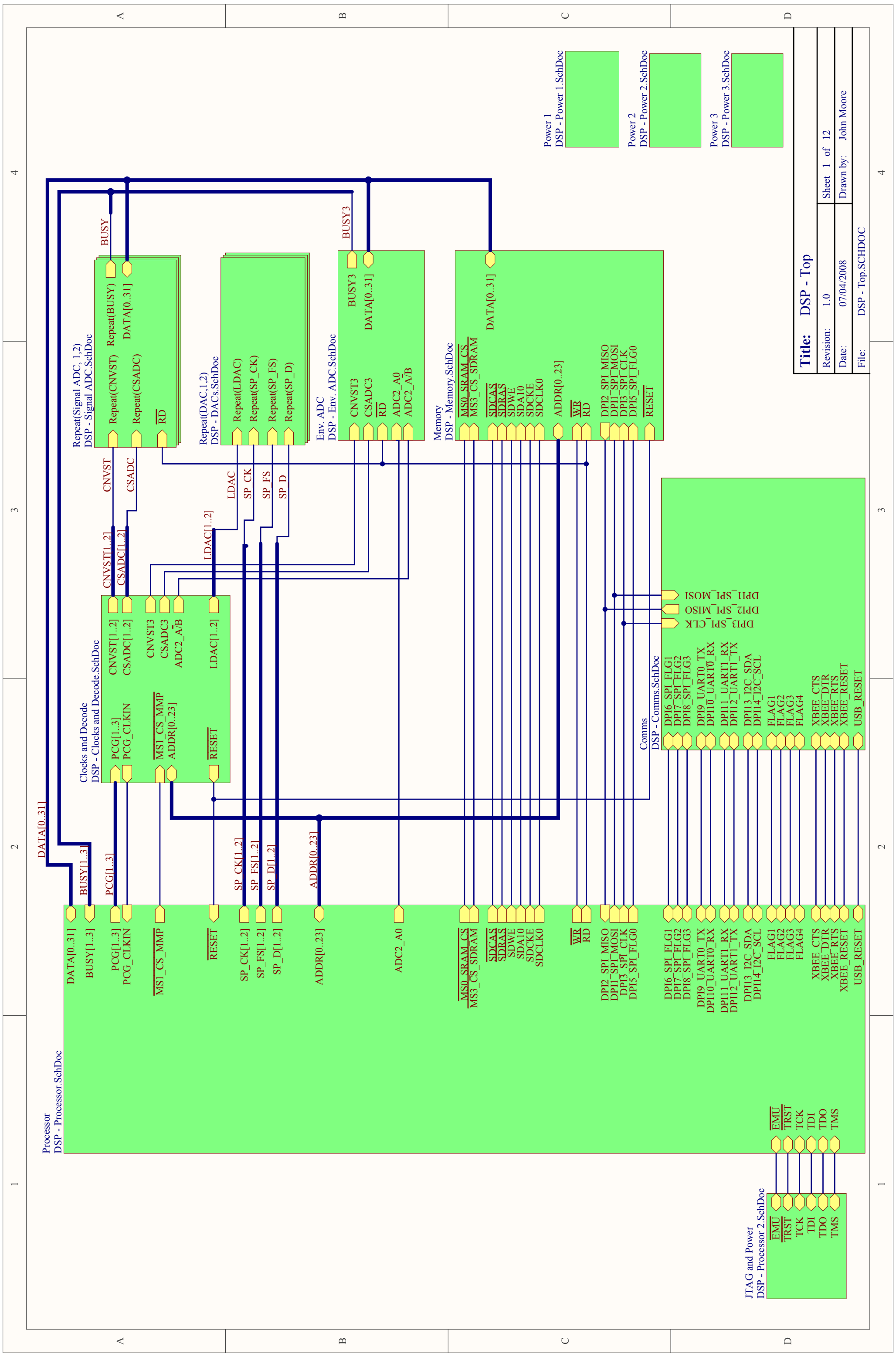

Figure B.9: DSP-based System - Top Level

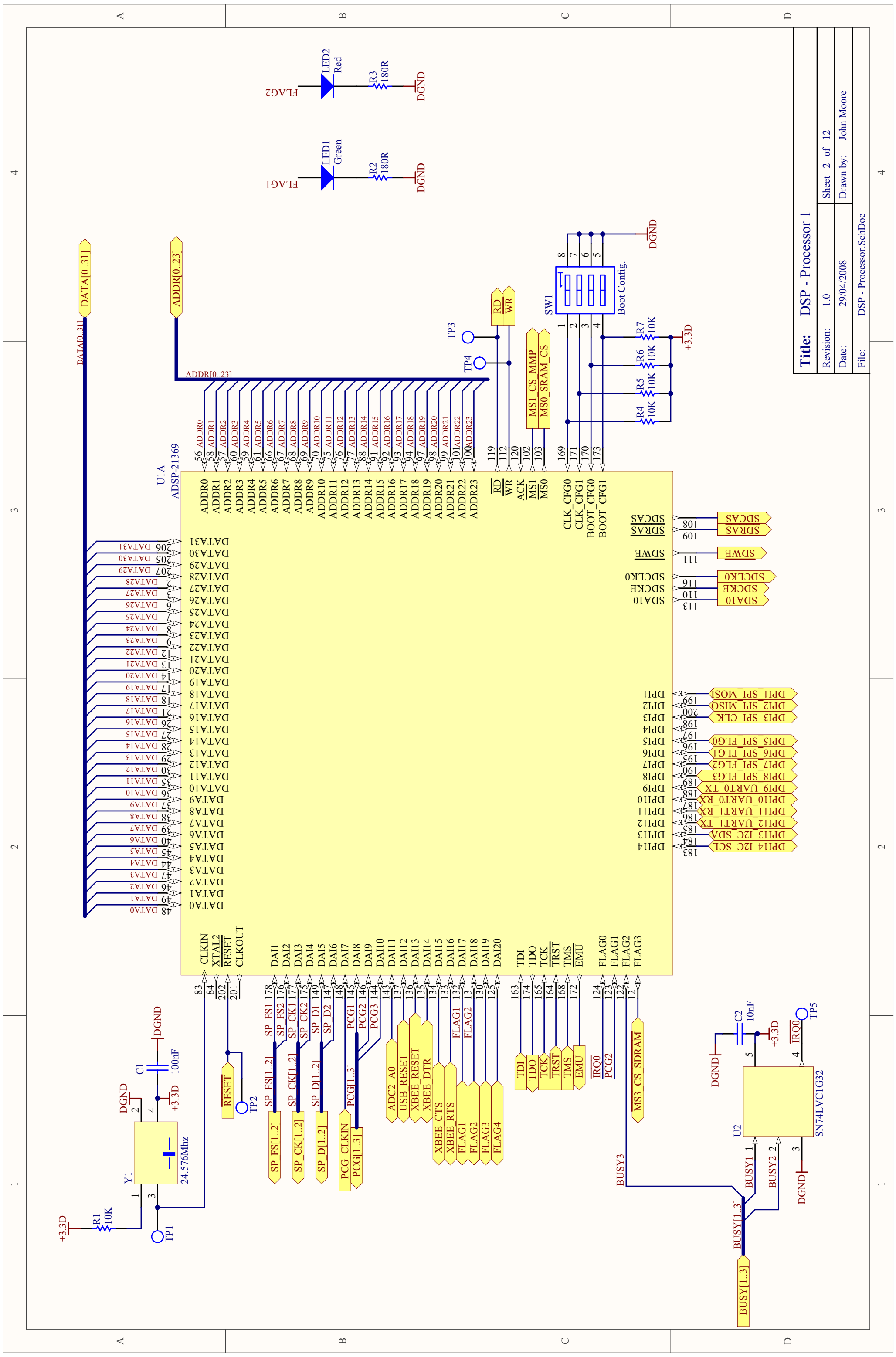

Figure B.10: DSP-based System - Processor

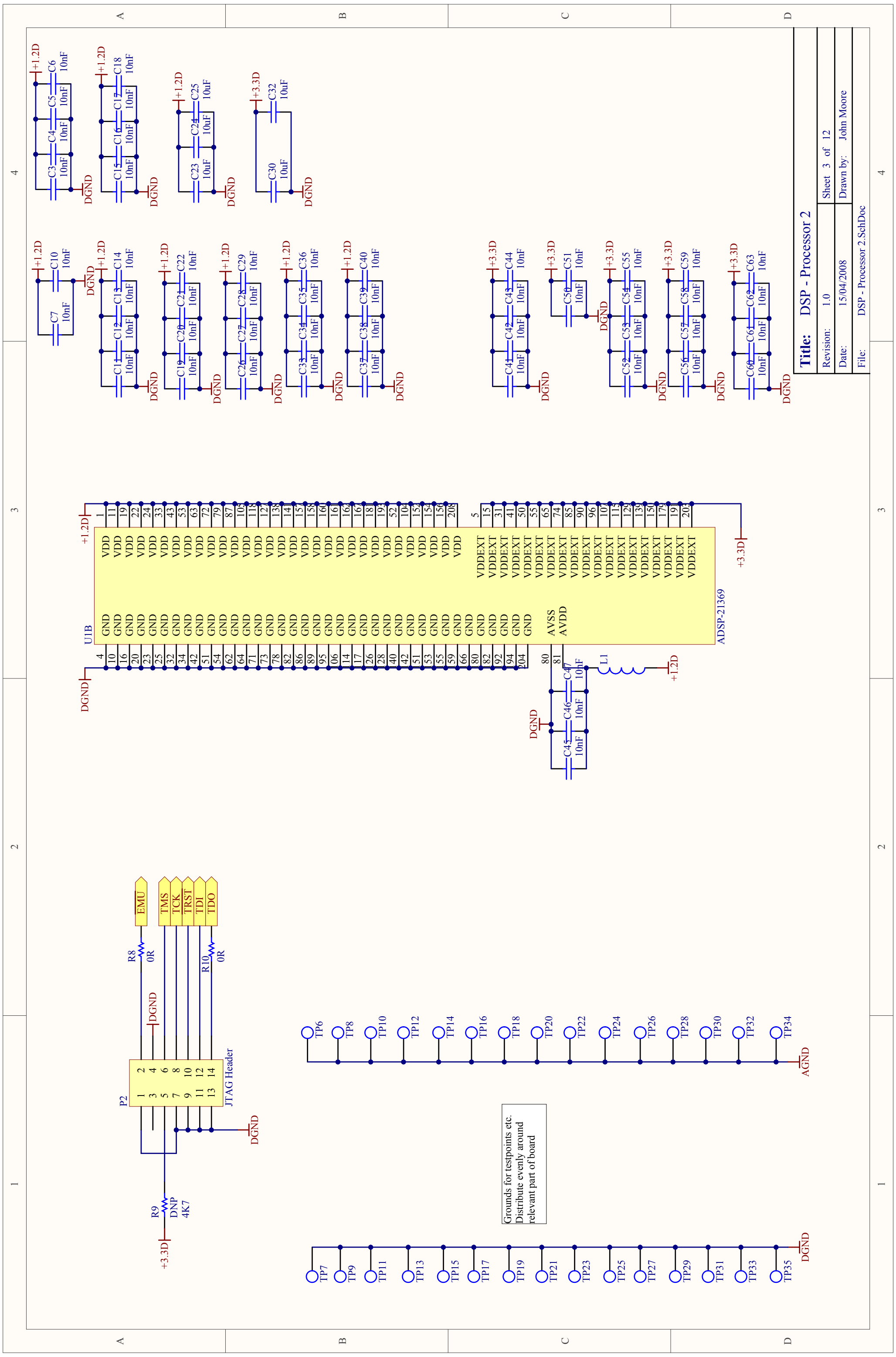

Figure B.11: DSP-based System - Processor Support

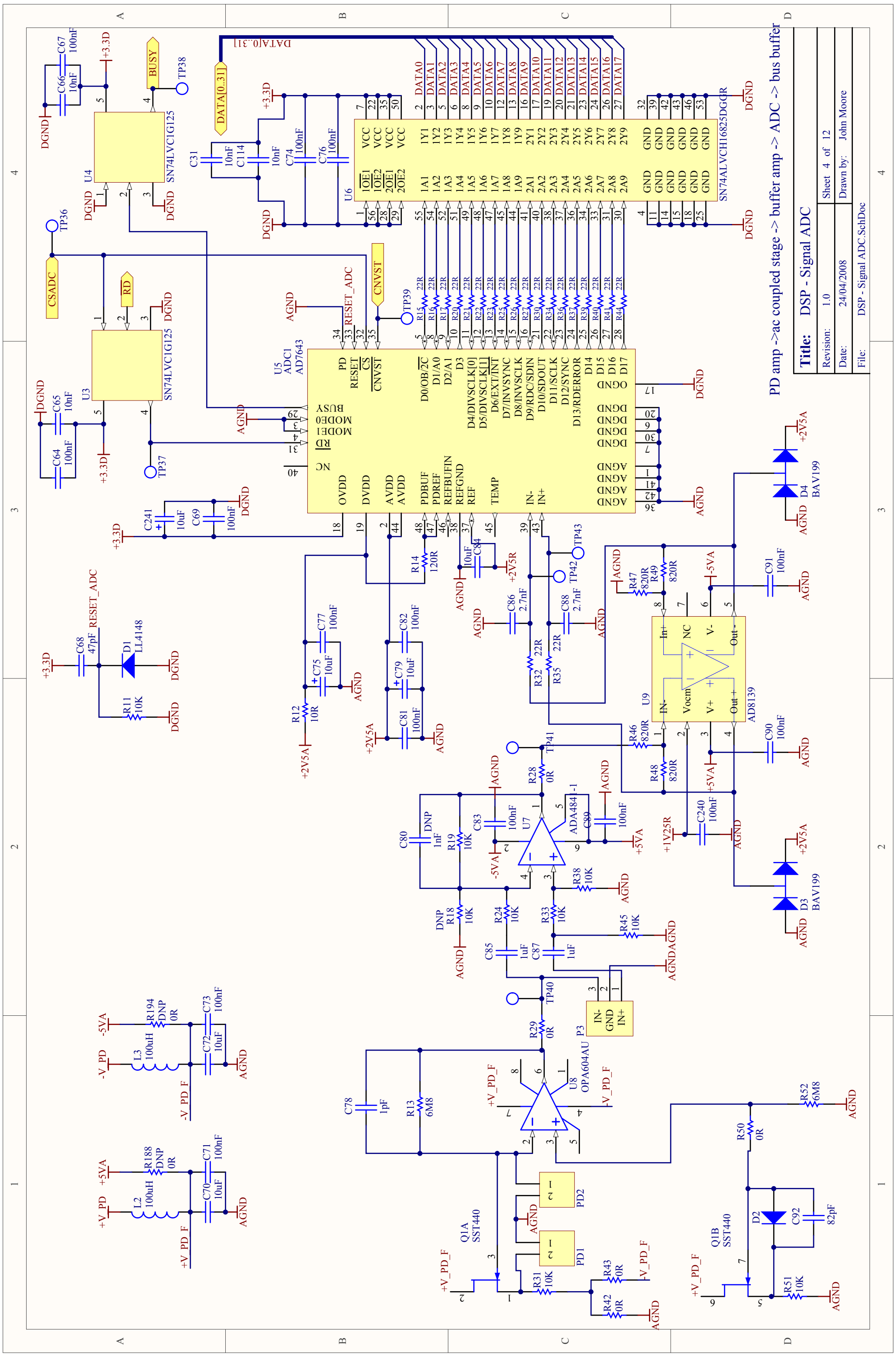

Figure B.12: DSP-based System - Signal Detection Channel

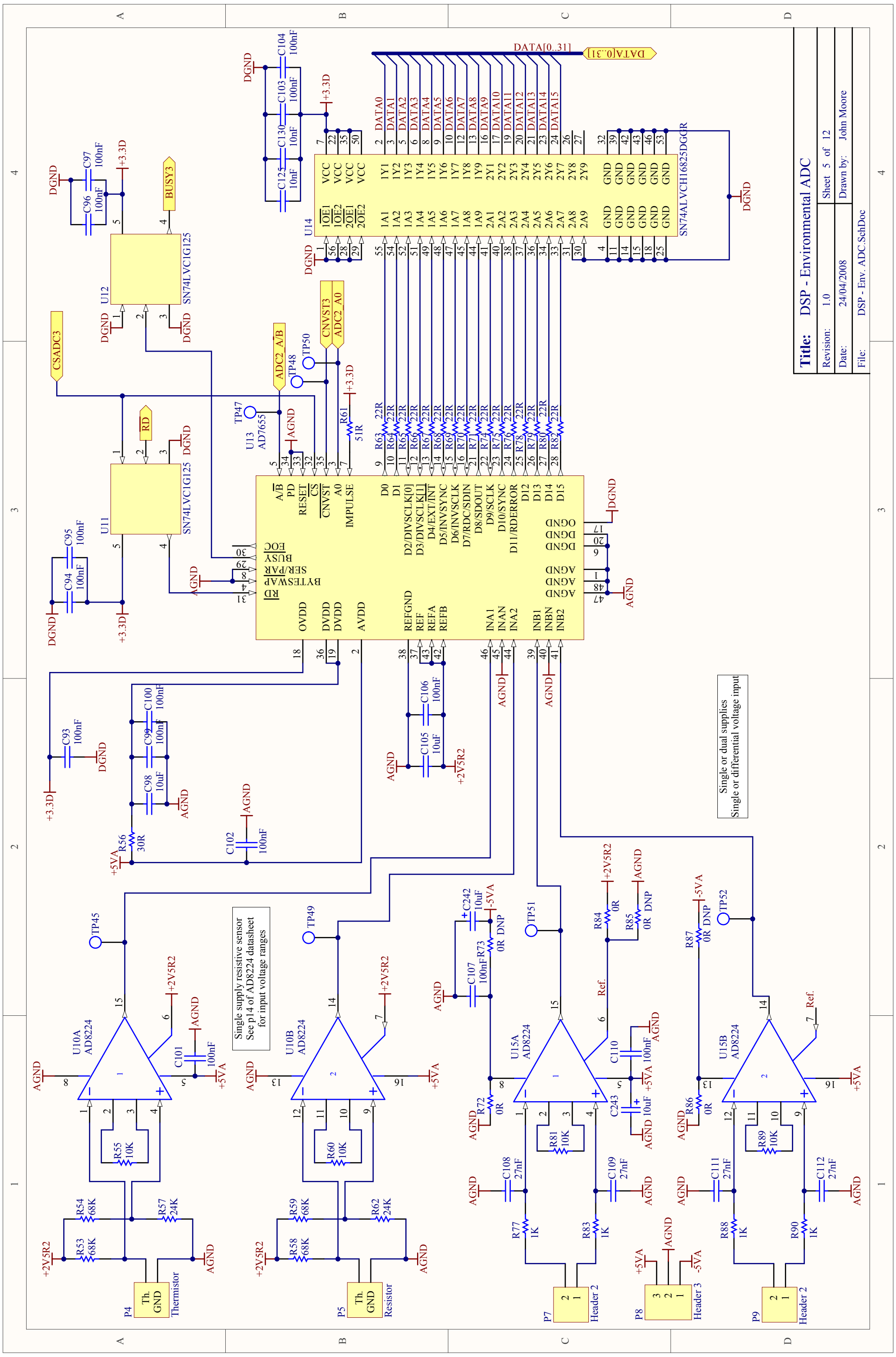

Figure B.13: DSP-based System - Auxiliary Sensors Channel

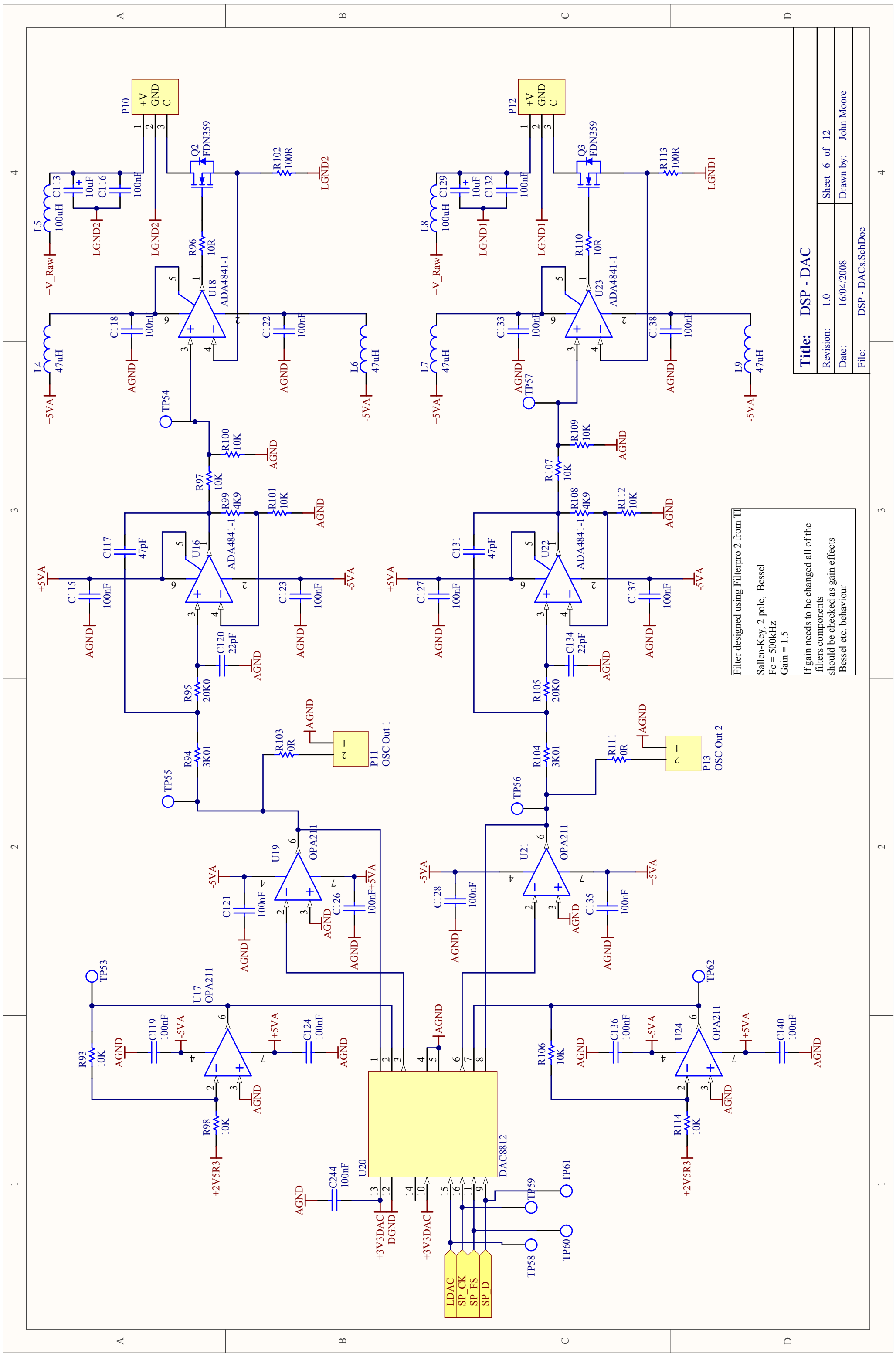

Filter designed using Filterpro 2 from TI

Sallen-Key, 2 pole, Bessel
Fc = 500kHz
Gain = 1.5

If gain needs to be changed all of the filters components should be checked as gain effects Bessel etc. behaviour

Figure B.14: DSP-based System - Excitation Channel

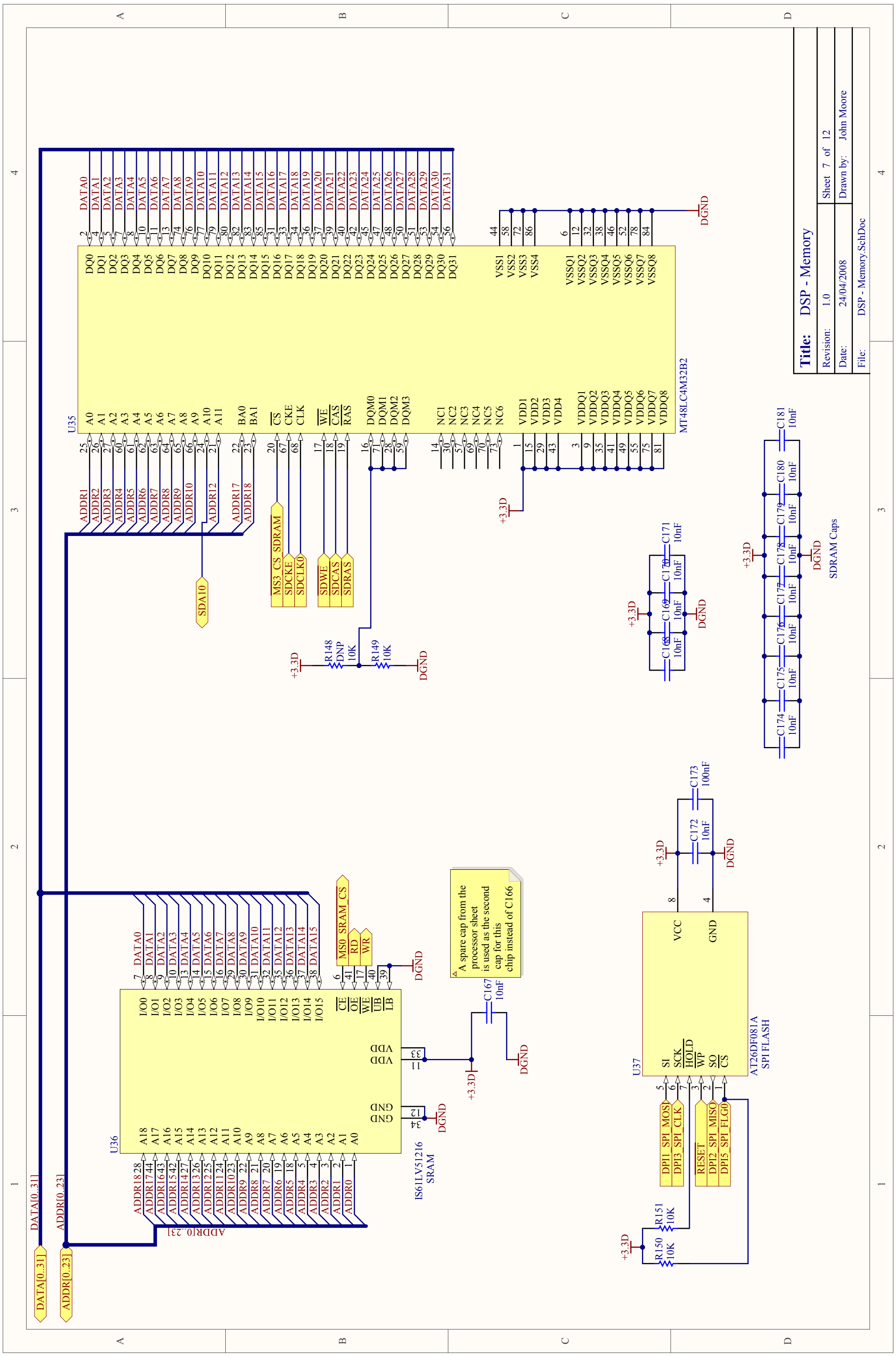

Figure B.15: DSP-based System - System Memory

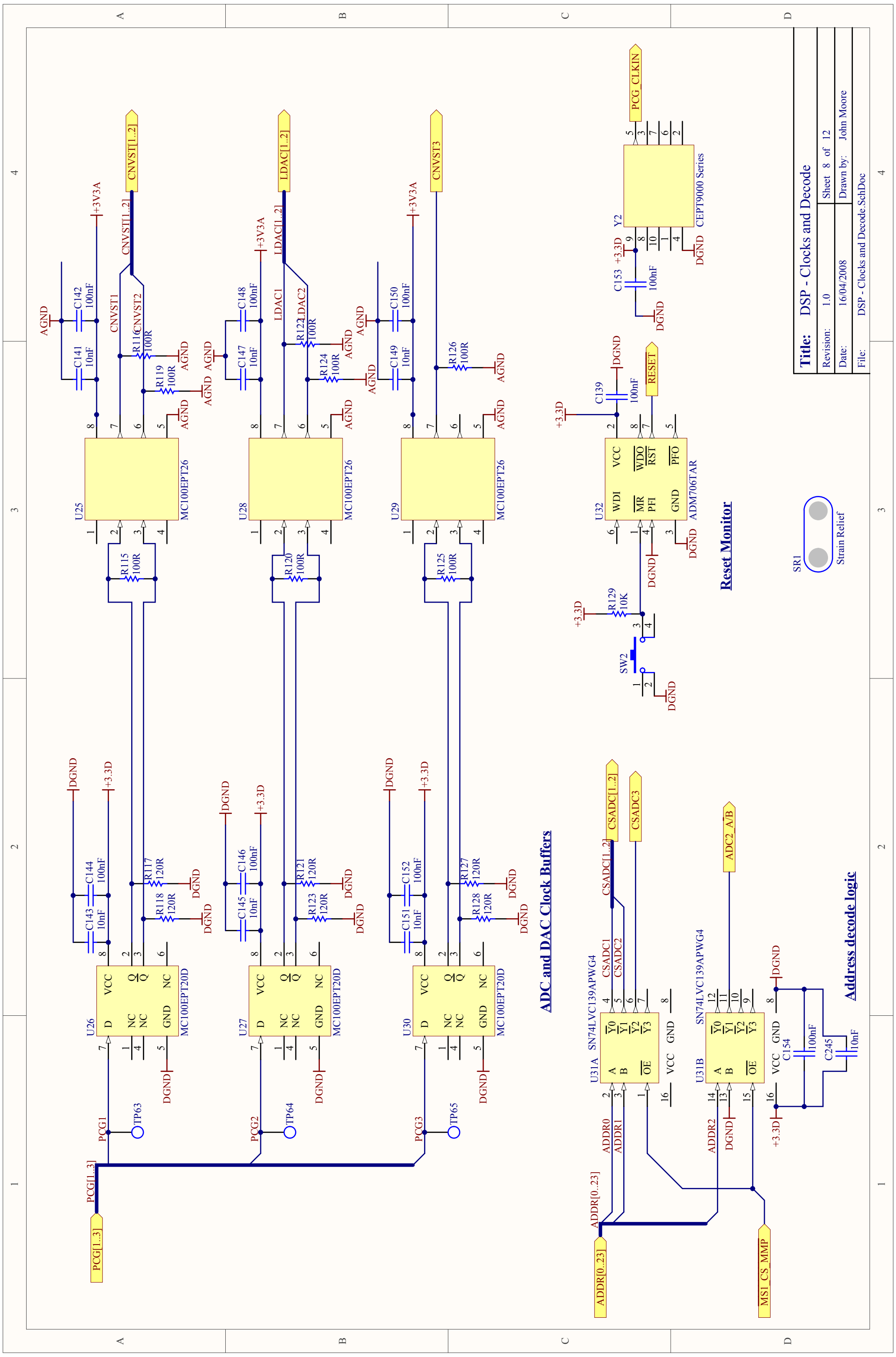

Figure B.16: DSP-based System - Clock Distribution

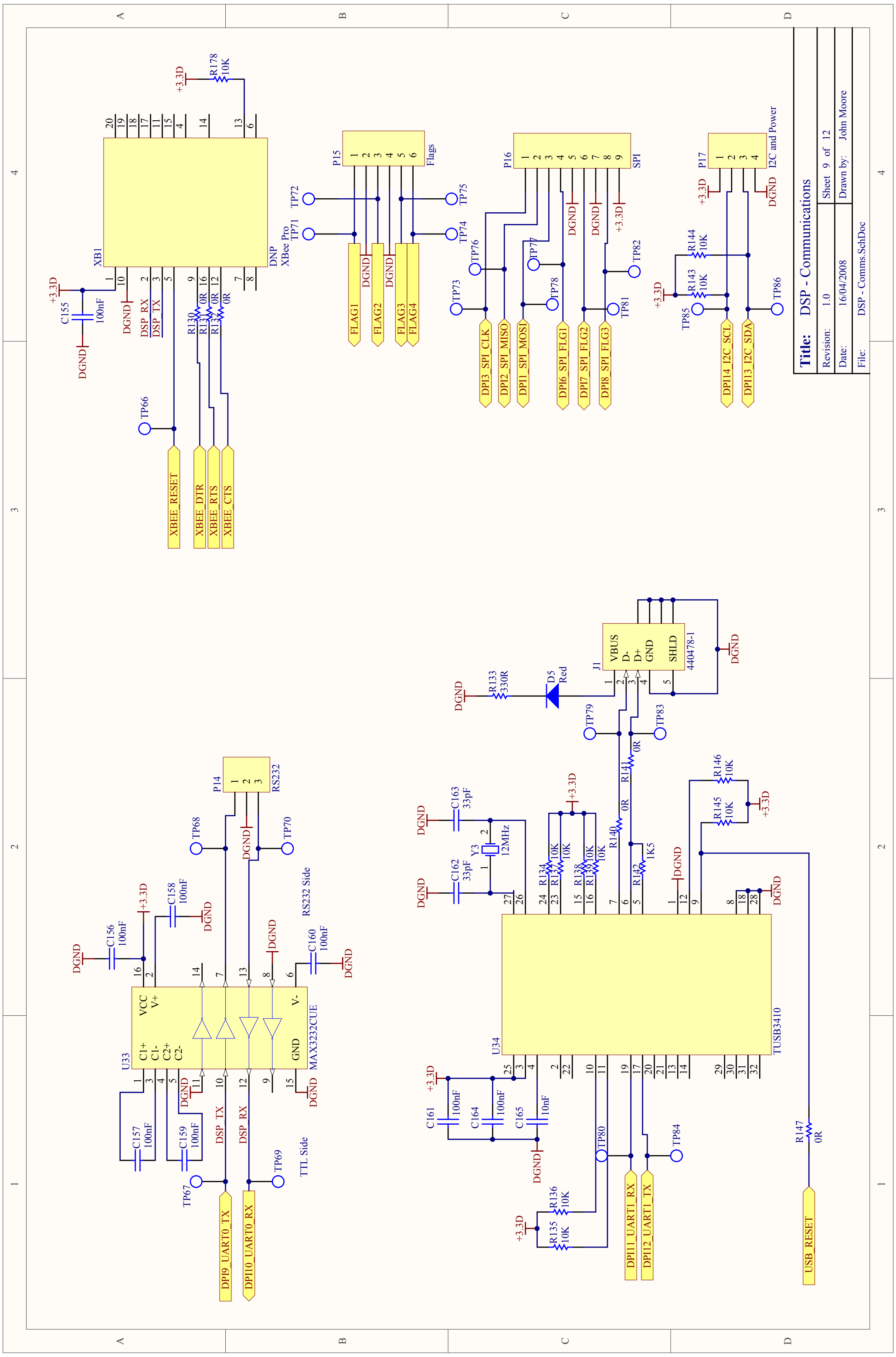

Figure B.17: DSP-based System - Interface

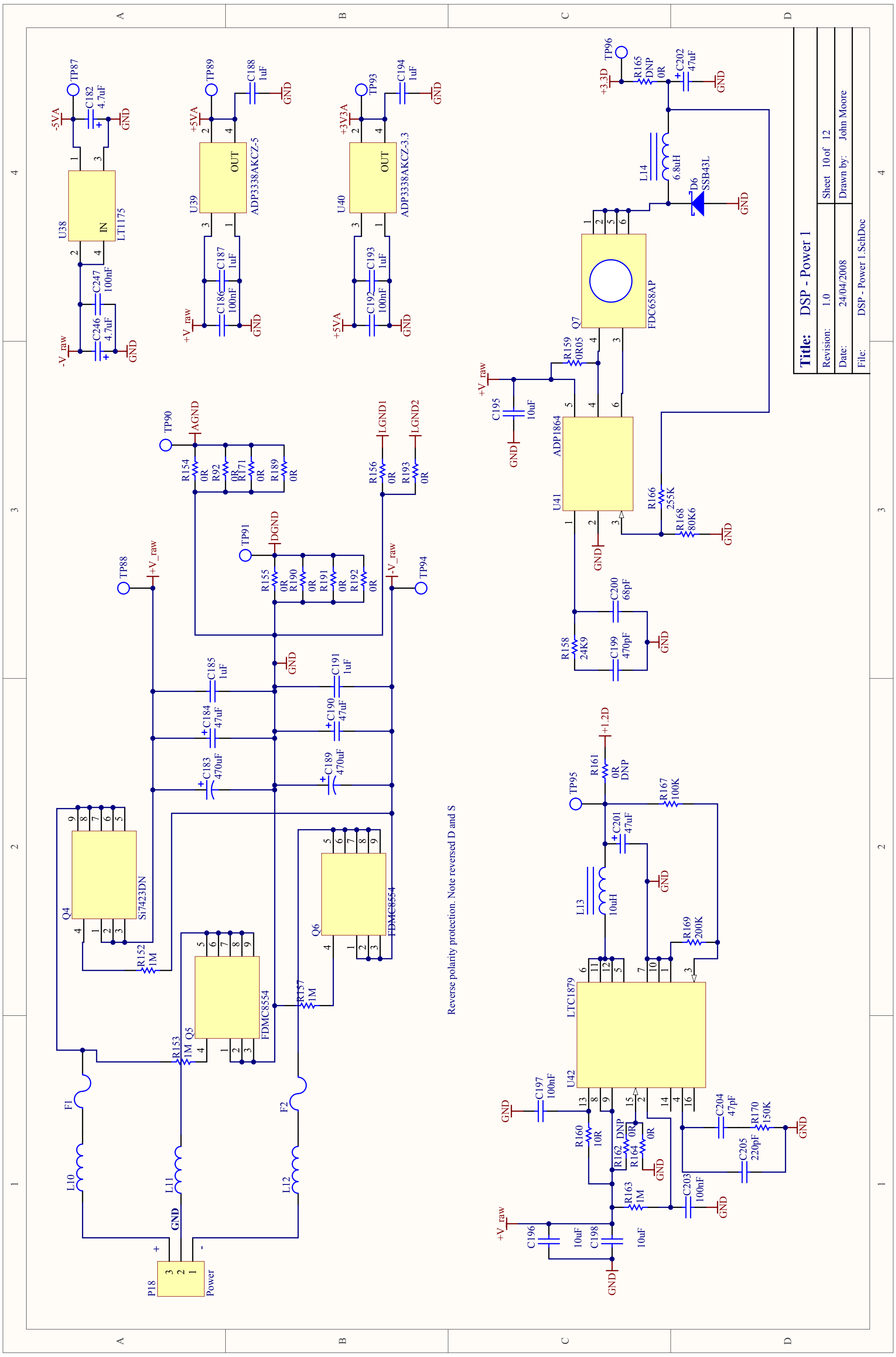

Figure B.18: DSP-based System - Power 1

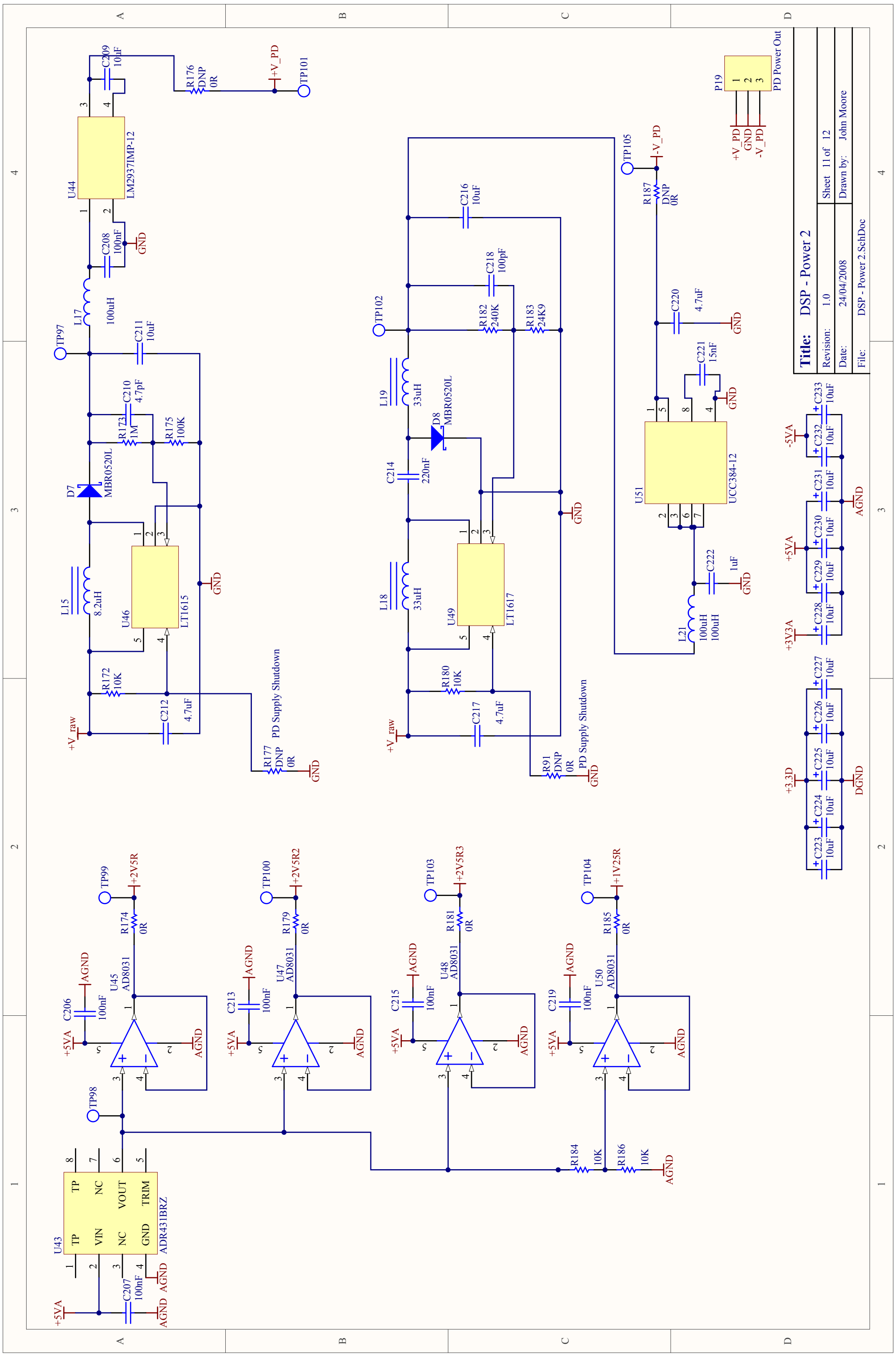

Figure B.19: DSP-based System - Power 2

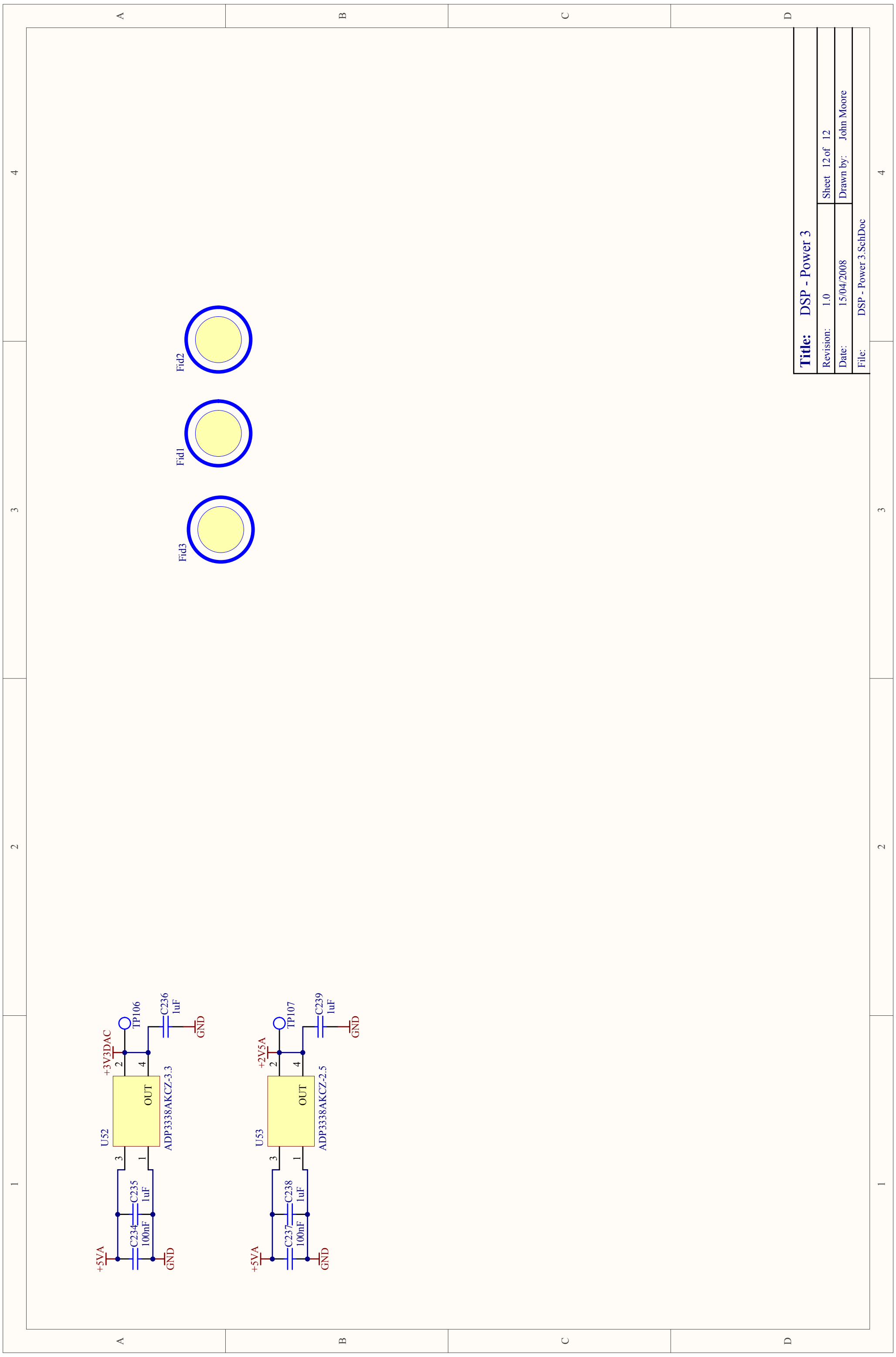

Figure B.20: DSP-based System - Power 3

B.4 DO Sensor Drop-in Module Circuit Diagram

The schematic diagram of the drop-in module that was designed for the dissolved oxygen sensor is shown in Figs. B.21 and B.22. The micro-controllers I/O pins were routed to headers and a number number of 16-bit ADCs were added to allow the module to be used in other applications.

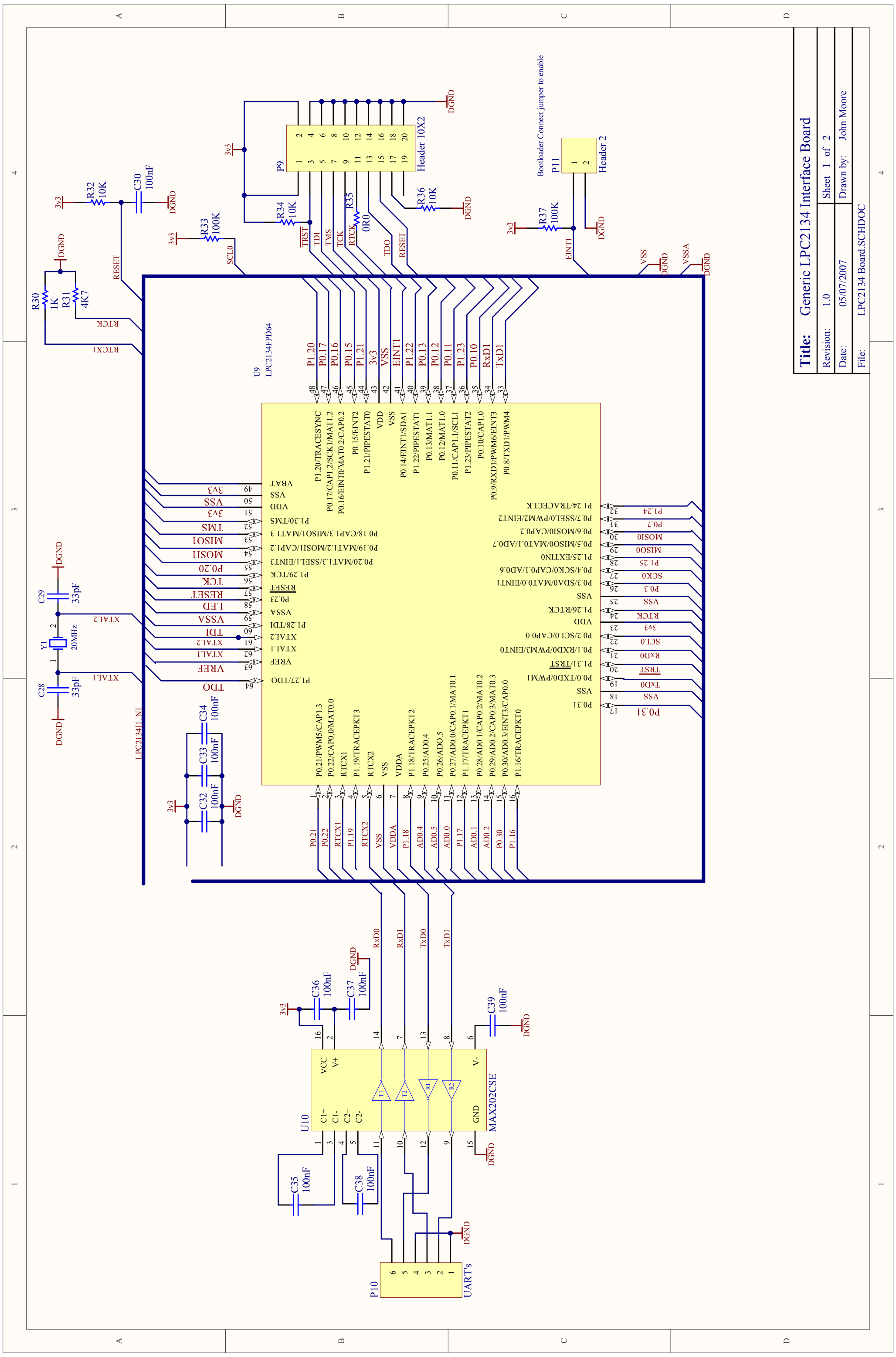

Figure B.21: Drop-in System - Microcontroller

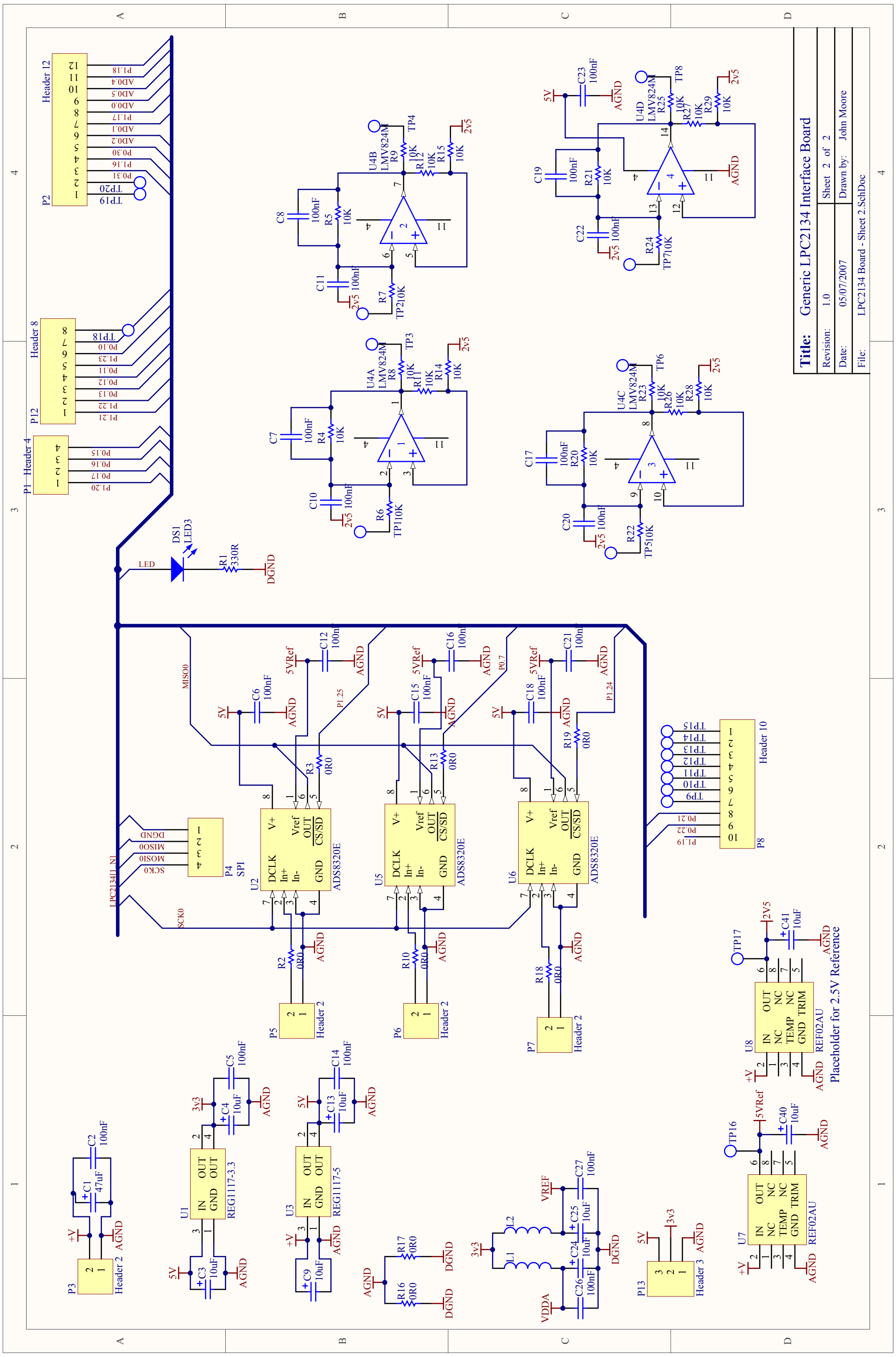

Figure B.22: Drop-in system - Expansion